Numerical implementation of Hadamard renormalization in black hole spacetimes

Lorenzo Pisani, MSc



Supervisors: Assistant Prof. Peter Taylor
Prof. Brien Nolan

Dissertation submitted for the award of Doctor of Philosophy

School of Mathematical Sciences
Dublin City University

August 2026

Declaration

I hereby certify that this material, which I now submit for assessment on the programme of study leading to the award of Doctor of Philosophy is entirely my own work, and that I have exercised reasonable care to ensure that the work is original and have conformed to the regulations on the use and declaration of Generative AI, and does not to the best of my knowledge breach any law of copyright, and has not been taken from the work of others save and to the extent that such work has been cited and acknowledged within the text of my work. I hereby certify that no Generative Artificial Intelligence (Gen AI) tools have been used in the creation of the thesis.

Signed: Lorenzo Pisani

ID No.: 21267355

Date: 26-08-2026

Acknowledgements

I would like to thank Prof. Claudio Dappiaggi and Assist. Prof. David Long for generously taking the time to carefully read my thesis and for providing such useful comments that greatly improved this work.

I owe my deepest gratitude to my supervisor, Assist. Prof. Peter Taylor. This thesis would not have been possible without your guidance, expertise, support, and patience. I really enjoyed our numerous discussions, which showed me what research is about. I have grown so much, both as a person and as a researcher, by working with you. Thank you for always being available to help; it was a privilege and a pleasure to work with you.

I would like to give special thanks to Julio Arrechea. Collaborating with you has been amazing, both professionally and personally. I learned so much from you, and I would like to thank you for all your work and advice. Thank you for always being available when I needed help or had questions.

I would also like to thank my Master's thesis supervisor, Antonio Ferreiro. Thank you for introducing me to the topic of Quantum Field Theory in Curved Spacetime and for your patience and all your explanations. Your knowledge and passion have truly inspired me and provided great motivation for pursuing this PhD. Thank you also for your kind hospitality in Nijmegen.

I thank Prof. Brien Nolan for his inspiring lectures, which made me fall in love with general relativity. Thank you also for always being available when I needed advice.

I would also like to thank my collaborators Cormac Breen, Marc Casals, and Adrian Ottewill for our numerous discussions and for their work and advice. Working together has been a real pleasure.

Thanks also to all the staff members of the School of Mathematical Sciences and CfAR for being so welcoming.

To my friends in the School of Mathematical Sciences: Ole, Emmet, Ciara, Ran, Jack, Evan, Brian, Aditya, Valentin, Eneko, Lucy, Ben, Josh, Conor, Abbie. You really made this PhD journey special. I will miss seeing you at DCU.

I am also grateful to DCU's School of Mathematical Sciences and to Research Ireland for funding my PhD research during these years.

I extend my gratitude to my family - my mom, dad, and brother - for giving me the opportunity to pursue my studies and for always being there for me, even when we were far apart. I feel lucky to have a family like you.

I give special thanks to my girlfriend, Valentina. Your care and love have made this journey lighter. Thank you for your patience and for always being there for me, especially in the most difficult times. Thank you for making me believe in myself and for always making me happy. I am lucky to have you by my side.

I thank all my friends in Italy. Thank you for making me feel at home whenever I came back, and thank you also for visiting me. I truly miss having you around.

Living in Ireland also allowed me to meet so many amazing new friends. Thank you for all the laughs, experiences, and support. This PhD journey would have been way harder without you all.

Contents

Declaration ii

Acknowledgements iii

List of Figures xi

Abbreviations xii

Notation xiii

Publications xiv

Abstract xv

Preface xvi

1 Introduction 1

1.1 Quantum field theory in curved spacetime 1

1.2 Canonical quantization 2

1.2.1 Minkoski spacetime 2

1.2.2 Curved spacetime 5

1.3 Green's functions 8

1.3.1 Green's functions in flat spacetime and Wick rotation 10

1.4 Hadamard construction of the Green's function and Hadamard parametrices 12

1.5 The renormalized stress-energy tensor 17

1.6 The semiclassical Einstein equations 20

1.7 Implementing Hadamard renormalization in black hole spacetimes . . 22

1.7.1 The extended coordinate method 27

1.8 Towards a semiclassical toolkit 30

2 Adapting the extended coordinate method to zero-temperature states 32

2.1 The need for a direct renormalization prescription in the Boulware vacuum state . . . 32
2.2 The Boulware vacuum as a zero temperature Euclidean state . . . 33
2.3 A direct renormalization prescription in the Boulware state . . . 35
2.3.1 Regularization Parameters for the Direct Part . . . 37
2.3.2 Regularization Parameters for the Logarithmic Terms in the Tail . . . 41
2.3.3 Mode-sum expression for the parametrix . . . 47
2.4 Vacuum polarization and components of the RSET . . . 48
2.5 Conclusions . . . 52

3 Computing the RSET in non-extremal and extremal Reissner-Nordström black holes 53
3.1 Introduction . . . 53
3.2 Numerical Implementation . . . 54
3.2.1 Non-Extremal Modes . . . 54
3.2.2 Extremal Modes . . . 56
3.2.3 Accuracy Issues . . . 57
3.3 Results . . . 59
3.3.1 Non-Extremal Results . . . 59
3.3.2 Extremal Results . . . 60
3.4 Backreaction in extremal black holes . . . 64
3.5 Conclusions . . . 70

4 Application of the extended coordinate method to thin shells 72
4.1 Introduction . . . 72
4.2 The extended coordinate method . . . 74
4.3 Thin shells in equilibrium . . . 76
4.3.1 General Formalism . . . 76
4.3.2 Matching Minkowski to Schwarzschild Spacetimes . . . 80
4.4 Numerical Approach . . . 81
4.4.1 Euclidean Modes . . . 81
4.4.2 Schwarzschild modes . . . 82
4.4.3 Minkowski modes . . . 84
4.4.4 Matching conditions at the surface . . . 85
4.4.5 Tests of convergence . . . 86
4.5 Analytical near-shell approximations . . . 90
4.5.1 WKB approximation . . . 90
4.5.2 Weak field approximation . . . 94
4.6 Numerical results . . . 99

4.7 Backreaction effects at the surface of the shell . . . 101
4.8 Conclusions . . . 104

5 Vacuum polarization and renormalized stress-energy tensor on the interior of a Reissner-Nordström black hole 106
5.1 Introduction . . . 106
5.2 The two-point function for a massive field inside a Reissner-Nordström black hole . . . 108
5.2.1 A Basis of Separable Modes . . . 108
5.2.2 The Boulware State . . . 112
5.2.3 The Unruh state on the interior . . . 113
5.2.4 The Hartle-Hawking state on the interior . . . 123
5.3 The Extended coordinate method inside a black hole (Lorentzian spacetime) . . . 124
5.4 Numerical considerations . . . 128
5.5 Convergence of the mode-sums . . . 130
5.6 The renormalized vacuum polarization inside a Reissner-Nordström black hole . . . 132
5.7 The renormalized stress-energy tensor inside a Reissner-Nordström black hole . . . 134
5.8 Conclusions . . . 137

6 Quantum effects near the Cauchy horizon of a Reissner-Nordström black hole 141
6.1 Introduction . . . 141
6.2 The numerical challenges for obtaining near-Cauchy horizon results . 142
6.3 The renormalized vacuum polarization near the Cauchy horizon . . . 145
6.3.1 Numerical results . . . 145
6.3.2 Analytic derivation of the near-Cauchy horizon behaviour . . . 146
6.4 The RSET on the Cauchy horizon . . . 157
6.4.1 Analytical results . . . 157
6.4.2 Numerical results . . . 164
6.5 Conclusions . . . 165

7 Conclusions and outlook 170

Appendices: 176

A The extended coordinate method for zero-temperature states 177
A.1 Cut-off independence . . . 177
A.2 Other representations for direct and tail regularization parameters . . 178

A.3 Hadamard coefficients . . . 179
A.4 Numerical and analytical parts of the RSET . . . 181
A.5 Regularization of $|\omega|^{-2j-1}$ as a generalized function . . . 183

B Thin shells **185**
B.1 Hadamard coefficients . . . 185
B.2 Weak field approximation . . . 189

C The Reissner-Nordström interior **193**
C.1 Hadamard Coefficients on the interior . . . 193
C.2 Small frequency asymptotics for l=0 in the large mass regime . . . 194
C.2.1 The interior scattering coefficients . . . 195
C.2.2 The exterior reflection coefficient . . . 200
C.2.3 The coefficient of the logarithmic divergence . . . 201
C.3 Near-Cauchy horizon, other expressions . . . 202
C.3.1 Frequency integrals of the Hadamard renormalization counterterms . . . 202
C.3.2 Contribution of the Hadamard renormalization counterterms to $(\tilde{w})^t_t$ . . . 202

References **214**

List of Figures

1.1 Two-point functions contours. 11

2.1 Analysis of the convergence of $g_{\omega l}(r) - k^{(n)}_{\omega l}(r)$ for a massless scalar field on the exterior of a Schwarzschild black hole at different orders of expansion n for fixed l and large ω. 51
2.2 Analysis of the convergence of $g_{\omega l}(r) - k^{(n)}_{\omega l}(r)$ for a massless scalar field on the exterior of a Schwarzschild black hole at different orders of expansion n for fixed ω and large l. 51

3.1 RSET components in the Boulware state for a massless, minimally coupled scalar field on a non-extremal Reissner-Nordström spacetime 59
3.2 RSET components in the Boulware state for a massless, conformally coupled scalar field on an extremal Reissner-Nordström spacetime . . 62
3.3 RSET components in the Boulware state for a minimally coupled scalar field with mass $\mu M = 1/10$ on an extremal Reissner-Nordström spacetime 63
3.4 Cancellation of the divergence in the numerical and analytical contributions to the quantity $\langle \hat{\mathcal{E}} \rangle$ for a minimally coupled massless field . . 63
3.5 Cancellation of the divergence in the numerical and analytical contributions to the quantity $\langle \hat{\mathcal{E}} \rangle$ for a minimally coupled field with mass $\mu = M/10$ 64
3.6 Position of the perturbed horizon and its surface gravity for a semi-classically corrected extremal black hole 68
3.7 Solutions for the perturbations $\mathcal{R}(r)$ of the redshift function $\mathcal{M}(r)$ and the Misner-Sharp mass in terms of the radial coordinate z 69

4.1 Analysis of the convergence of $g_{\omega l}(r) - k^{(n)}_{\omega l}(r)$ for a massless scalar field on the exterior of the thin shell for $r \gg r_0$ at different orders of expansion n for fixed l and large ω. 88
4.2 Analysis of the convergence of $g_{\omega l}(r) - k^{(n)}_{\omega l}(r)$ for a massless scalar field on the exterior of the thin shell for $r \gg r_0$ at different orders of expansion n for fixed ω and large l. 88

4.3 Analysis of the convergence of $g_{\omega l}(r) - k^{(0)}_{\omega l}(r)$ for a massless scalar field on the Minkowski interior of the thin shell at different radial points for fixed l and large ω. 89
4.4 Analysis of the convergence of $g_{\omega l}(r) - k^{(0)}_{\omega l}(r)$ for a massless scalar field on the Minkowski interior of the thin shell at different radial points for fixed ω and large l. 90
4.5 Vacuum polarization and renormalized stress-energy tensor of a massless, minimally coupled scalar field near the surface of a spherical thin shell from the interior. 100
4.6 Vacuum polarization and renormalized stress-energy tensor of a massless, minimally coupled scalar field near the surface of a spherical thin shell from the exterior. 100
4.7 Renormalized vacuum polarization and renormalized stress-energy tensor of a massless, minimally coupled scalar field inside spherical thin shells of different radii. 101
4.8 Renormalized vacuum polarization and renormalized stress-energy tensor of a massless, minimally coupled scalar field outside spherical thin shell of different radii. 102

5.1 Exterior separable "in" and "up" modes 111
5.2 Penrose diagram of the Reissner-Nordström black hole 114
5.3 Unruh "in" and "up" modes 116
5.4 Interior separable "L" and "R" modes 118
5.5 Analysis of the convergence of $g_{\omega l}(r) - k^{(n)}_{\omega l}(r)$ inside a charged black hole at different orders of expansion n for fixed l and large ω 131
5.6 Analysis of the convergence of $g_{\omega l}(r) - k^{(n)}_{\omega l}(r)$ inside a charged black hole at different orders of expansion n for fixed ω and large l 131
5.7 $\langle\hat{\Phi}^2\rangle_{\rm ren}$ for a massless scalar field in the interior of a Reissner-Nordström spacetime 133
5.8 Comparison of $\langle\hat{\Phi}^2\rangle_{\rm ren}$ in the interior of a Reissner-Nordström spacetime for a massless and a massive $\mu M = 0.1$ scalar field 134
5.9 RSET components for a massless field in the Hartle-Hawking state in the region across the event horizon of a Reissner-Nordström black hole 135
5.10 RSET components for a massless field in the Unruh state in the region across the event horizon of a Reissner-Nordström black hole 136
5.11 RSET components for massless and massive fields in the Hartle-Hawking state inside a Reissner-Nordström black hole 138
5.12 RSET components for massless and massive fields in the Unruh state inside a Reissner-Nordström black hole 139

6.1 $\langle\hat{\Phi}^2\rangle_{\rm ren}$ for a massless scalar field in the Hartle-Hawking and Unruh states in the vicinity of the inner horizon 146
6.2 $\langle\hat{\Phi}^2\rangle_{\rm ren}$ for a massive $\mu M = 0.1$ scalar field in the Hartle-Hawking and Unruh states in the vicinity of the inner horizon 147
6.3 $\langle\hat{\Phi}^2\rangle_{\rm ren}$ in the Hartle-Hawking and Unruh state in the vicinity of the inner horizon for different values of the mass of the scalar field μ. . . 147
6.4 $\langle\hat{\Phi}^2\rangle_{\rm ren}$ in the Hartle-Hawking and Unruh states in the vicinity of the inner horizon for different values of the charge of the black hole Q. . . 148
6.5 Different l-modes contributions to $\langle\hat{\Phi}^2\rangle_{\rm ren}$ for a massive scalar field in the Hartle-Hawking state in the vicinity of the inner horizon 149
6.6 Low frequency behavior of $g_{\omega 0}(r)$ as $r \to r_-$ 150
6.7 Coefficient of the logarithmic divergence $h_l(\mu)$ plotted as a function of the mass of the scalar field 156
6.8 Coefficient of the logarithmic divergence $h_0(\mu)$ as a function of the mass of the scalar field 157
6.9 $\langle\hat{T}^-_{uu}\rangle^{\rm H}$, $\langle\hat{T}^-_{uu}\rangle^{\rm U}$ and $\langle\hat{T}^-_{vv}\rangle^{\rm U}$ at the Cauchy horizon for a minimally coupled massive scalar field varying the mass of the scalar field μ 165
6.10 $\langle\hat{T}^-_{uu}\rangle^{\rm H}$ on the Cauchy horizon for a massive scalar field varying the mass μ and the coupling ξ 166
6.11 $\langle\hat{T}^-_{uu}\rangle^{\rm H}$, $\langle\hat{T}^-_{uu}\rangle^{\rm U}$ and $\langle\hat{T}^-_{vv}\rangle^{\rm U}$ at the Cauchy horizon for a minimally coupled massive scalar field varying the charge of the black hole Q 166
6.12 $\langle\hat{T}^-_{uu}\rangle^{\rm H}$ at the Cauchy horizon for a massive scalar field varying the charge of the black hole Q and the coupling ξ 167

C.1 Examples of the potential for the Schrödinger-type equation in the interior of a charged black hole. 195

Abbreviations

ADM Arnowitt–Deser–Misner

AHS Anderson-Hiscock-Saumel

GR General Relativity

KMS Kubo-Martin-Schwinger

ODE Ordinary differential equation

PMR Pragmatic mode-sum regularization

QFTCS Quantum field theory in curved spacetime

RNdS Reissner-Nordström-de Sitter

RSET Renormalized stress-energy tensor

RVP Renormalized vacuum polarization

WKB Wentzel–Kramers–Brillouin

Notation

Throughout the thesis, we adopt units in which $G = c = \hbar = 1$ and the metric sign convention $\{-, +, +, +\}$. We use Greek letters α, β, γ, δ,... for general spacetime indices. We also adopt the notation $[A, B] = AB - BA$ for the commutator and $\{A, B\} = AB + BA$ for the anticommutator.

Publications

1. J. Arrechea, C. Breen, A. Ottewill, L. Pisani, P. Taylor, Renormalized stress-energy tensor for scalar fields in the Boulware state with applications to extremal black holes, *Physical Review D*, 111, 085009 (2025) [1].

2. J. Arrechea, C. Breen, A. Ottewill, L. Pisani, P. Taylor, Vacuum polarization and renormalized stress-energy tensor of spherical thin shells, *arXiv*:2607.07583 (2026) [2].

Numerical implementation of Hadamard renormalization in black hole spacetimes

Lorenzo Pisani

Abstract

Quantum field theory in curved spacetimes provides the foundation of the semiclassical theory of gravity, which is governed by the semiclassical Einstein equations. Usually, one attempts to solve these equations perturbatively about a fixed background solution, whence the quantum correction to the geometry is sourced by the expectation value of the stress-energy tensor for the quantum field on the classical background. This quantity is formally divergent, and this divergence can be removed with the Hadamard renormalization procedure. While conceptually understood for decades, its practical implementation in black hole spacetimes is notoriously difficult, with efficient schemes developed only in recent years.

One of the most powerful of such schemes is the extended coordinate method, whose applicability is however limited to quantum scalar fields in the Hartle-Hawking state on the exterior of static, spherically symmetric black holes. In this thesis, we extend this method in several directions and compute renormalized expectation values in various scenarios of interest.

First, we generalize the method to directly compute the renormalized stress-energy tensor (RSET) for massive scalar fields in the Boulware state, thereby enabling the study of semiclassical effects in spacetimes where the Hartle-Hawking state does not exist, for example, in extremal black holes. We demonstrate the accuracy of this method by calculating the RSET in sub-extremal and extremal Reissner-Nordström spacetimes.

Beyond black holes, we apply the method to compute the renormalized vacuum polarization (RVP) and RSET outside and inside a thin shell joining a Schwarzschild exterior to a Minkowski interior. We also derive analytical expressions for their leading-order divergences at the shell.

Additionally, we extend the method to the interior of spherically symmetric black holes that possess a Cauchy horizon. We obtain the RVP and RSET in the Hartle-Hawking and Unruh states inside a Reissner-Nordström black hole and derive their behavior on the inner horizon analytically.

Finally, we show how these very accurate RSET prescriptions can be used to compute the semiclassical backreaction in these contexts.

Preface

Chapter 1 presents a literature review on the quantization of a scalar field in curved spacetimes and on the Hadamard renormalization. The material in the remaining Chapters is original.

The material presented in Chapters 2-3-4 is a result of a collaboration of the author with Julio Arrechea, Cormac Breen, Adrian Ottewill, and the author's primary supervisor, Peter Taylor. The material presented in Chapter 5 was developed in collaboration with Marc Casals, Gabriel Freitas Silva, and Peter Taylor, while the material presented in Chapter 6 was developed in collaboration with Marc Casals and Peter Taylor.

A summary of this thesis and of my main contributions follows. In Chapter 2, we develop a generalization to the extended coordinate method for a direct computation of the renormalized stress-energy tensor for massive quantum scalar fields in the Boulware state. While previous calculations of the RSET in the Boulware state using the extended coordinate method relied on a state-subtraction approach, the new method allows for a direct calculation. This is essential in spacetimes that do not admit a Hartle-Hawking state to use as a reference state. I made substantial contributions to all aspects of this Chapter.

In Chapter 3, we validate the new method by computing the RSET in the Boulware state on the exterior of a sub-extremal Reissner-Nordström spacetime and by comparing the results against existing ones obtained with the indirect state subtraction approach [3]. In addition, we compute the RSET for massless and massive scalar fields in the Boulware state on the exterior of an extremal Reissner-Nordström black hole, providing numerical evidence of its regularity at the extremal horizon. Finally, we make use of the RSET results to compute the semiclassical backreaction in the context of extremal black holes. The near-horizon analytical results were obtained by Cormac Breen. The backreaction equations were derived by Julio Arrechea, Cormac Breen, and Peter Taylor.

In Chapter 4, we shift our attention away from black holes to consider a simple example of a horizonless spacetime: a spherical thin shell joining a Schwarzschild exterior to a Minkowski interior. We compute the renormalized vacuum polarization and the RSET in this spacetime over a wide range of parameters. In addition, we

employ both a WKB and a weak-field approximation to obtain analytical expressions for the leading-order divergences of these quantities at the shell. Finally, we make use of these analytical expressions to compute the semiclassical backreaction on the shell. The WKB approximation near the surface of the shell was carried out by Cormac Breen. The backreaction equations were derived by Julio Arrechea, Cormac Breen, and Peter Taylor.

In Chapter 5, we turn our attention back to black holes, now focusing on their interiors. In particular, we derive, through analytic continuation of the exterior expressions, mode-sum representations for the Wightman functions for massive scalar fields in the Unruh and Hartle-Hawking states on the interior of a Reissner-Nordström spacetime. We then show how the extended coordinate method can be applied in this context and compute the renormalized vacuum polarization and RSET on the interior for both massless and massive scalar fields. This Chapter marks the first application of the extended coordinate method directly in the Lorentzian spacetime. I made substantial contributions to all aspects of this Chapter.

In Chapter 6, we then focus on the region near the Cauchy horizon. We compute numerical results for the renormalized vacuum polarization for massless and massive scalar fields and complement these with analytical expressions. In addition, we obtain semi-analytical expressions for the leading-order RSET components on the Cauchy horizon and compute them numerically over a wide parameter space, providing evidence that these quantities diverge there. I made substantial contributions to all aspects of this Chapter.

Finally, in Chapter 7, we draw some conclusions and provide an outlook.

Chapter 1

Introduction

1.1 Quantum field theory in curved spacetime

General relativity and quantum field theory are two of the main theoretical frameworks underlying our understanding of the fundamental nature of reality. Despite describing physical processes at very different scales, both general relativity and quantum theory are expected to be important in certain physical scenarios, for instance, when quantum fields propagate on strongly curved backgrounds, such as black-hole spacetimes. Thus, combining general relativity and quantum mechanics into a unified theory of quantum gravity is regarded as one of the most important problems of fundamental physics. While several approaches to quantum gravity have been proposed (see [4] for a review), the lack of experimental and observational data makes it challenging to constrain the different proposals. There are, however, robust low-energy approximations to quantum gravity that are expected to provide useful insights into the interaction between the quantum theory and general relativity. One such approximation is the semiclassical approximation underpinned by quantum field theory in curved spacetime, which describes quantum fields propagating on a classical curved spacetime background. This approximation is considered to be valid in regimes in which the spacetime curvature is small compared to the Planck scale.

One of the earliest and most important results of quantum field theory in curved spacetime was Leonard Parker's work on particle creation in expanding universes [5–7], which demonstrated that quantizing a scalar field on a classical curved background describing an expanding universe can lead to spontaneous particle creation. Parker's original Ph.D. thesis was recently reedited in [8]; see also [9] for a historical review. Parker's studies were particularly influential for Hawking's famous discovery of black hole radiation [10]. Motivated by these earlier works, Unruh later showed that a uniformly accelerated observer in Minkowski spacetime perceives the

Minkowski vacuum as filled with a thermal bath of radiation [11]. These important early results played a central role in shaping the development of the field.

Before discussing the details of quantum field theory in curved spacetimes, it is necessary to introduce the classical Einstein field equations, which describe the interaction between the spacetime geometry and the classical matter content,

$$G_{\alpha\beta} + \Lambda g_{\alpha\beta} = 8\pi\, T^{(\mathrm{cl})}_{\alpha\beta}, \tag{1.1}$$

where $g_{\alpha\beta}$ is the metric of spacetime, Λ is the cosmological constant and $G_{\alpha\beta}$ is the Einstein tensor. The Einstein tensor $G_{\alpha\beta}$ is defined by $G_{\alpha\beta} = R_{\alpha\beta} - \frac{1}{2} g_{\alpha\beta} R$, where $R_{\alpha\beta}$ is the Ricci tensor, R is the Ricci scalar and $T^{(\mathrm{cl})}_{\alpha\beta}$ is the stress-energy tensor of the classical matter.

In quantum field theory in curved spacetime, the spacetime geometry is treated classically, while some fields are quantized, and the expectation value of the stress-energy tensor associated with these quantum fields contributes to the overall stress-energy that appears as the source term on the right hand side of the so-called semiclassical Einstein equations. Discussing the semiclassical Einstein equations requires the technical notions of quantization of a field on curved spacetimes and renormalization of expectation values on curved spacetimes, which will be the focus of Sections 1.2-1.5. We will then introduce the semiclassical Einstein equations in Sec. 1.6.

1.2 Canonical quantization

In this Section, we briefly summarize the canonical quantization formalism. We first consider the case of a flat Minkowski background and later generalize the formalism to a curved spacetime. In doing so, we follow standard textbook material [12–16].

1.2.1 Minkoski spacetime

We consider a scalar field $\Phi(x) = \Phi(t, \mathbf{x})$ in four-dimensional Minkowski spacetime, where t denotes the time coordinate and $\mathbf{x}$ a three-dimensional vector containing the spatial coordinates, defined by the action

$$\mathcal{S} = -\frac{1}{2} \int d^4x \{\eta^{\alpha\beta} \partial_\alpha \Phi\, \partial_\beta \Phi + \mu^2 \Phi^2\}. \tag{1.2}$$

In this expression, μ is the field mass, $\eta_{\alpha\beta}$ is the Minkowski metric and the Lagrangian density is given by

$$\mathcal{L} = -\frac{1}{2}\{\eta^{\alpha\beta}\partial_\alpha\Phi\,\partial_\beta\Phi + \mu^2\Phi^2\}. \tag{1.3}$$

By requiring that

$$\frac{\delta\mathcal{S}}{\delta\Phi} = 0, \tag{1.4}$$

one obtains the Klein-Gordon equation describing the propagation of the scalar field on a Minkowski background,

$$(\partial^\alpha\partial_\alpha - \mu^2)\Phi = 0. \tag{1.5}$$

A convenient set of solutions to this equation is

$$u_{\mathbf{k}}(t,\mathbf{x}) = N_{\omega_{\mathbf{k}}}\, e^{i\mathbf{k}\cdot\mathbf{x} - i\omega_{\mathbf{k}}t}, \tag{1.6}$$

where $N_{\omega_{\mathbf{k}}}$ is a normalization factor, $\mathbf{k}$ is the 3-momentum and the frequency $\omega_{\mathbf{k}}$ is defined as

$$\omega_{\mathbf{k}}^2 = |\mathbf{k}|^2 + \mu^2. \tag{1.7}$$

When $\omega_{\mathbf{k}} > 0$, the modes $u_{\mathbf{k}}$ are called positive frequency modes with respect to the time coordinate t, while $u_{\mathbf{k}}^*$ are called negative frequency modes. In fact, these modes are eigenfunctions of the operator ∂/∂_t, with $\omega_{\mathbf{k}} > 0$,

$$\begin{aligned}\frac{\partial}{\partial t}u_{\mathbf{k}}(t,\mathbf{x}) &= -i\omega_{\mathbf{k}}u_{\mathbf{k}}(t,\mathbf{x}),\\ \frac{\partial}{\partial t}u_{\mathbf{k}}^*(t,\mathbf{x}) &= i\omega_{\mathbf{k}}u_{\mathbf{k}}^*(t,\mathbf{x}).\end{aligned} \tag{1.8}$$

Given two solutions Φ_1 and Φ_2 to Eq. (1.5), we define the Klein-Gordon scalar product as

$$\langle\Phi_1,\Phi_2\rangle = -i\int_{\Sigma_t}\left[\Phi_1\partial_t\Phi_2^* - \Phi_2^*\partial_t\Phi_1\right]d^3x, \tag{1.9}$$

where $\Sigma_t := \{t = \text{constant}\}$ is a constant-time hypersurface. The integrand is a conserved quantity and therefore the value of $\langle\Phi_1,\Phi_2\rangle$ is independent of the choice of Σ_t [12]. Introducing Eq. (1.6) into the scalar product (1.9) and requiring the

orthornomality condition $\langle u_{\mathbf{k}}, u'_{\mathbf{k}}\rangle = \delta^3(\mathbf{k}-\mathbf{k}')$ yields the normalization constant,

$$N_{\omega_{\mathbf{k}}} = \frac{1}{\sqrt{2|\omega_{\mathbf{k}}|(2\pi)^3}}. \tag{1.10}$$

We also define the canonical conjugate momentum as

$$\pi(x) \equiv \frac{\partial \mathcal{L}}{\partial(\partial_t \Phi)} = \partial_t \Phi(x). \tag{1.11}$$

To quantize the field we promote $\Phi(x)$ and $\pi(x)$ to operators and impose the following equal time commutations relations

$$\begin{aligned}
[\hat{\Phi}(t,\mathbf{x}), \hat{\Phi}(t,\mathbf{x}')] &= 0, \\
[\hat{\pi}(t,\mathbf{x}), \hat{\pi}(t,\mathbf{x}')] &= 0, \\
[\hat{\Phi}(t,\mathbf{x}), \hat{\pi}(t,\mathbf{x}')] &= i\delta^3(\mathbf{x}-\mathbf{x}').
\end{aligned} \tag{1.12}$$

The positive frequency $u_{\mathbf{k}}$ modes, together with the negative frequency $u^*_{\mathbf{k}}$ modes, form a complete orthonormal basis with respect to the scalar product (1.9). We then expand $\hat{\Phi}$ as

$$\hat{\Phi}(t,\mathbf{x}) = \int_{\mathbb{R}^3} d^3\mathbf{k} \left(\hat{a}_{\mathbf{k}} u_{\mathbf{k}}(t,\mathbf{x}) + \hat{a}^\dagger_{\mathbf{k}} u^*_{\mathbf{k}}(t,\mathbf{x}) \right) \tag{1.13}$$

where $\hat{a}_{\mathbf{k}}$ and $\hat{a}^\dagger_{\mathbf{k}}$ are known as the annihilation and creation operator respectively, defined by

$$\hat{a}_{\mathbf{k}} = \langle \hat{\Phi}, u_{\mathbf{k}} \rangle \tag{1.14a}$$

$$\hat{a}^\dagger_{\mathbf{k}} = -\langle \hat{\Phi}, u^*_{\mathbf{k}} \rangle. \tag{1.14b}$$

These operators satisfy the following commutation relations

$$[\hat{a}_{\mathbf{k}}, \hat{a}_{\mathbf{k}'}] = [\hat{a}^\dagger_{\mathbf{k}}, \hat{a}^\dagger_{\mathbf{k}'}] = 0, \qquad [\hat{a}_{\mathbf{k}}, \hat{a}^\dagger_{\mathbf{k}'}] = \delta^3(\mathbf{k}-\mathbf{k}'). \tag{1.15}$$

The Hilbert space of the quantum field theory is the Fock space

$$\mathcal{F} = \mathbb{C} \oplus \left(\bigoplus_{n=1}^{\infty} \mathcal{H}^{(n)} \right), \tag{1.16}$$

where $\mathcal{H}$ is the single-particle Hilbert space and $\mathcal{H}^{(n)}$ is the Hilbert space of n-particle states. We define the vacuum state $|0\rangle \in \mathcal{F}$ as the state annihilated by all

annihilation operators

$$\hat{a}_{\mathbf{k}}|0\rangle = 0, \quad \forall\, \mathbf{k}. \tag{1.17}$$

This state contains no particles for all inertial observers. In Minkowski spacetime, the existence of the Poincaré symmetry provides a natural set of modes (see Eq. (1.13)) and a preferred choice of vacuum state for all inertial observers (see Eq. (1.17)) that is invariant under the action of the Poincaré group [12]. Note, however, that a non-inertial observer may still perceive the vacuum in Eq. (1.17) as containing particles. This is, in fact, the origin of the Unruh effect [11]. We will see that this notion of a preferred vacuum will break down entirely in curved spacetime.

A one-particle state can be constructed by acting on the vacuum state $|0\rangle$ with a creation operator $\hat{a}^{\dagger}_{\mathbf{k}}$

$$|1_{\mathbf{k}}\rangle = \hat{a}^{\dagger}_{\mathbf{k}}|0\rangle. \tag{1.18}$$

This concept is generalized to construct an n-particle state as

$$|1_{\mathbf{k}_1}, 1_{\mathbf{k}_2}, ..., 1_{\mathbf{k}_n}\rangle = \hat{a}^{\dagger}_{\mathbf{k}_1} a^{\dagger}_{\mathbf{k}_2} ... a^{\dagger}_{\mathbf{k}_n}|0\rangle. \tag{1.19}$$

1.2.2 Curved spacetime

Let us assume a C^{∞} globally hyperbolic fixed background spacetime $(\mathcal{M}, g)$ [17], equipped with a Lorentzian metric $g_{\alpha\beta}$. We introduce a scalar field on this background by generalizing the action in Eq. (1.2) to curved spacetimes, replacing normal derivatives with covariant derivatives,

$$\mathcal{S} = -\frac{1}{2}\int d^4x\sqrt{g}\left\{g^{\alpha\beta}\nabla_{\alpha}\Phi\nabla_{\beta}\Phi + \mu^2\Phi^2 + \xi R\,\Phi^2\right\}, \tag{1.20}$$

where we define $g \equiv |\det(g_{\alpha\beta})|$, and

$$\mathcal{L} = -\frac{1}{2}\sqrt{g}\left\{g^{\alpha\beta}\nabla_{\alpha}\Phi\nabla_{\beta}\Phi + \mu^2\Phi^2 + \xi R\,\Phi^2\right\} \tag{1.21}$$

is the Lagrangian density of the field. Note that in Eq. (1.20) we also introduced a coupling ξ to the gravitational background curvature. Two values of the coupling ξ are particularly relevant: minimal coupling $\xi = 0$ and conformal coupling $\xi = 1/6$. In the minimally coupled case, the scalar field is not directly coupled to the Ricci scalar. For conformal coupling, in the massless case, the action and field equation are invariant under conformal transformations [14].

The Klein-Gordon equation in curved spacetime can be obtained by varying the

action with respect to the scalar field and applying the principle of stationary action

$$\frac{1}{\sqrt{g}}\frac{\delta \mathcal{S}}{\delta \Phi} = (\Box - \mu^2 - \xi\, R)\Phi = 0, \tag{1.22}$$

where $\Box$ is the d'Alembertian operator $\Box \equiv g^{\alpha\beta}\nabla_\alpha \nabla_\beta$. Global hyperbolicity ensures that the Cauchy problem associated with the Klein-Gordon equation is well-posed. That is, given suitable initial data on a Cauchy surface, the solution to the Klein-Gordon equation is uniquely determined.

We define the Klein-Gordon scalar product as

$$\langle \Phi_1, \Phi_2 \rangle = -i \int_\Sigma \left[\Phi_1 \nabla_\alpha \Phi_2^* - \Phi_2^* \nabla_\alpha \Phi_1\right] n^\alpha d\Sigma, \tag{1.23}$$

where the integral is over a Cauchy surface Σ with unit future-directed normal n^α. The value of $\langle \Phi_1, \Phi_2 \rangle$ is independent of the choice of Σ [18].

We then assume that a complete set of mode solutions $\{u_i\}$, where i is a symbolic placeholder for a set of mode numbers that label a complete set of solutions, that are orthonormal with respect to the Klein-Gordon product exists such that,

$$\langle u_i, u_j \rangle = \delta_{ij}, \qquad \langle u_i^*, u_j^* \rangle = -\delta_{ij}, \qquad \langle u_i, u_j^* \rangle = 0. \tag{1.24}$$

As in Minkowski spacetime, we quantize the field by promoting it to an operator and expanding the field operator as

$$\hat{\Phi}(x) = \sum_i (\hat{a}_i u_i + \hat{a}_i^\dagger u_i^*), \tag{1.25}$$

where the symbolic sum over i could involve integrals if any of the mode-numbers is continuous, and where the annihilation and creation operators $\hat{a}_i$ and $\hat{a}_i^\dagger$ are defined by

$$\hat{a}_i = \langle \hat{\Phi}, u_i \rangle, \tag{1.26a}$$
$$\hat{a}_i^\dagger = -\langle \hat{\Phi}, u_i^* \rangle, \tag{1.26b}$$

and satisfy the commutation relations

$$[\hat{a}_i, \hat{a}_j] = [\hat{a}_i^\dagger, \hat{a}_j^\dagger] = 0, \qquad [\hat{a}_i, \hat{a}_j^\dagger] = \delta_{ij}. \tag{1.27}$$

We can then define the vacuum state $|0_a\rangle$ as the state annihilated by all the annihilation operators $\hat{a}_i$

$$\hat{a}_i |0_a\rangle = 0, \quad \forall\, i. \tag{1.28}$$

We have seen that in Minkowski spacetime, there is a natural set of modes (1.13) arising from the Poincaré symmetry. This is no longer true in general curved spacetimes, due to the absence of Poincaré symmetry in this context. Therefore, we can expand the field in a different complete set of orthonormal (with respect to the scalar product (1.23)) modes $\{v_i\}$,

$$\hat{\Phi}(x) = \sum_i (\hat{b}_i v_i + \hat{b}_i^\dagger v_i^*), \tag{1.29}$$

where $\hat{b}_i$ and $\hat{b}_i^\dagger$ are the annihilation and creation operators for this new set of modes and are defined as

$$\hat{b}_i = \langle \hat{\Phi}, v_i \rangle, \tag{1.30a}$$
$$\hat{b}_i^\dagger = -\langle \hat{\Phi}, v_i^* \rangle, \tag{1.30b}$$

with commutation relations

$$[\hat{b}_i, \hat{b}_j] = [\hat{b}_i^\dagger, \hat{b}_j^\dagger] = 0, \qquad [\hat{b}_i, \hat{b}_j^\dagger] = \delta_{ij}. \tag{1.31}$$

In addition, a second vacuum state $|0_b\rangle$ can be defined as the state annihilated by all annihilation operators $\hat{b}_i$

$$\hat{b}_i |0_b\rangle = 0, \quad \forall\, i. \tag{1.32}$$

It is possible to express the modes $\{v_i\}$ in terms of the modes $\{u_i\}$ (and vice versa),

$$v_i = \sum_j (\alpha_{ij} u_j + \beta_{ij} u_j^*), \tag{1.33}$$

where α_{ij} and β_{ij} are known as the Bogoliubov coefficients, obtained from

$$\alpha_{ij} = \langle v_i, u_j \rangle, \qquad \beta_{ij} = -\langle v_i, u_j^* \rangle. \tag{1.34}$$

Employing the definition of annihilation operators in Eq. (1.30), introducing Eqs. (1.33) and (1.25) and exploiting the orthonormality of the modes $\{u_i\}$ yields

$$\begin{aligned} \hat{b}_i = \langle \hat{\Phi}, v_i \rangle &= \Big\langle \sum_k (\hat{a}_k u_k + \hat{a}_k^\dagger u_k^*), \sum_j (\alpha_{ij} u_j + \beta_{ij} u_j^*) \Big\rangle \\ &= \sum_j \left[\alpha_{ij}^* \hat{a}_j - \beta_{ij}^* \hat{a}_j^\dagger \right]. \end{aligned} \tag{1.35}$$

Thus this relation allows us to express the annihilation operators $\hat{b}_i$ in terms of the annihilation and creation operators $\hat{a}_i$ and $\hat{a}_i^\dagger$ and the Bogoliubov coefficients α_{ij}

and β_{ij}. Evaluating the vacuum state $|0_a\rangle$ with the annihilation operator $\hat{b}_i$, making use of Eq. (1.35), yields

$$\hat{b}_i|0_a\rangle = -\sum_j \beta^*_{ij}\hat{a}^\dagger_j|0_a\rangle, \tag{1.36}$$

which is, in general, nonzero.

In addition, it is useful to compute the expectation value of the number operator $\hat{N}_i = \hat{b}^\dagger_i\hat{b}_i$ in different vacuum states. Note that for the vacuum state $|0_b\rangle$

$$\langle 0_b|\hat{N}_i|0_b\rangle = 0, \tag{1.37}$$

meaning that an observer associated with the mode decomposition $\{v_i\}$ detects zero particles in this vacuum state. On the other hand,

$$\langle 0_a|\hat{N}_i|0_a\rangle = \sum_j |\beta_{ji}|^2. \tag{1.38}$$

Therefore, the vacuum state $|0_a\rangle$ contains particles when described in terms of the mode basis $\{v_i\}$. This analysis shows that in curved spacetimes, there is, in general, no unique choice of vacuum state and that the notion of particles is observer-dependent. This is also true in Minkowski spacetime: the vacuum state defined in Eq. (1.17) contains particles as measured by a uniformly accelerated observer [11]. Different choices of vacuum are relevant for different physical scenarios. For example, in Section 1.7, we will discuss the three vacuum states most commonly considered in black hole spacetimes and their physical interpretation.

1.3 Green's functions

A Green's function is an inhomogeneous solution of a linear differential equation sourced by a delta distribution, subject to specified boundary conditions. Green's functions provide a powerful method for constructing solutions to partial differential equations. In quantum field theory, different Green's functions and two-point functions can be constructed from vacuum expectation values of various products of field operators. While Green's functions satisfy the inhomogeneous equation with a delta source, some of the two-point functions that we will introduce in this Section are solutions to the homogeneous equation. Different two-point functions can be constructed by imposing different boundary conditions tailored to the physical problem under consideration. These objects will prove particularly useful in the context of renormalization. For completeness, we will introduce the most important two-point functions of the Klein-Gordon equation, although some will not be

specifically relevant to this thesis.

In this section, we introduce a coordinate system $\{x^0, x^1, x^2, x^3\}$ (not necessarily globally defined) on the globally hyperbolic spacetime $(\mathcal{M}, g)$ and assume that the coordinate $x^0 \equiv t$ is associated with a timelike vector field ∂_t, meaning that hypersurfaces $\Sigma_t := \{t = \text{constant}\}$ are spacelike [13]. We generically refer to x and x' as different points in the spacetime.

We first introduce the Schwinger (or Pauli-Jordan) two-point function $G_{\rm S}$ and the Hadamard two-point function $G_{\rm H}$, defined respectively by the expectation value of the commutator and anticommutator of the fields [12]

$$iG_{\rm S}(x,x') = \langle 0|[\hat{\Phi}(x), \hat{\Phi}(x')]|0\rangle, \tag{1.39}$$
$$G_{\rm H}(x,x') = \langle 0|\{\hat{\Phi}(x), \hat{\Phi}(x')\}|0\rangle, \tag{1.40}$$

and the Wightman functions

$$G^+(x,x') = \langle 0|\hat{\Phi}(x)\hat{\Phi}(x')|0\rangle, \tag{1.41}$$
$$G^-(x,x') = \langle 0|\hat{\Phi}(x')\hat{\Phi}(x)|0\rangle. \tag{1.42}$$

Despite the conventional notation $G(x,x')$, the Schwinger, Hadamard, and Wightman two-point functions are not Green's functions, since they satisfy, from Eq. (1.22), the homogeneous equation (in x and x'), e.g.,

$$(\Box_x - \mu^2 - \xi\, R)G(x,x') = 0. \tag{1.43}$$

The Feynman Green's function is defined as

$$\begin{aligned} iG_{\rm F}(x,x') &= \langle 0|\mathcal{T}(\hat{\Phi}(x)\hat{\Phi}(x'))|0\rangle \\ &= \Theta(t-t')G^+(x,x') + \Theta(t'-t)G^-(x,x') \end{aligned} \tag{1.44}$$

where $\Theta(t-t')$ is the Heaviside function and $\mathcal{T}$ denotes the time ordering operator

$$\mathcal{T}(\hat{\Phi}(x)\hat{\Phi}(x')) = \begin{cases} \hat{\Phi}(x)\hat{\Phi}(x'), & \text{if} \quad t > t', \\ \hat{\Phi}(x')\hat{\Phi}(x), & \text{if} \quad t' > t. \end{cases} \tag{1.45}$$

In addition, we define the advanced and retarded Green's functions

$$G_{\rm adv}(x,x') = \Theta(t'-t)G_{\rm S}(x,x'), \tag{1.46}$$
$$G_{\rm ret}(x,x') = -\Theta(t-t')G_{\rm S}(x,x'). \tag{1.47}$$

The Feynman, advanced, and retarded Green's functions are true Green's functions

in the sense that they satisfy the inhomogeneous equations

$$(\Box_x - \mu^2 - \xi\, R)G_{\rm F}(x,x') = -\frac{1}{\sqrt{g}}\delta^4(x-x'), \tag{1.48}$$

$$(\Box_x - \mu^2 - \xi\, R)G_{\rm adv/ret}(x,x') = \frac{1}{\sqrt{g}}\delta^4(x-x'). \tag{1.49}$$

1.3.1 Green's functions in flat spacetime and Wick rotation

It is instructive to consider the Green's functions in Minkowski spacetime, where the Green's function equation simplifies to

$$(\Box_x - \mu^2)G(x,x') = -\delta^4(x-x'), \tag{1.50}$$

where now $\Box_x = \eta^{\alpha\beta}\nabla_\alpha\nabla_\beta$. This equation can be solved in momentum space, making use of the integral representation for the delta function

$$\delta^4(x-x') = \frac{1}{(2\pi)^4}\int_{\mathbb{R}^4} e^{i\mathbf{k}\cdot(\mathbf{x}-\mathbf{x}')-ik^0(t-t')}d^4k, \tag{1.51}$$

where $k=(k^0,\mathbf{k})$ is the four-momentum. Introducing Eq. (1.51) into Eq. (1.50), we obtain the following integral representation for the Green's function

$$G(x,x') = \frac{1}{(2\pi)^4}\int_{\mathbb{R}^4} \frac{e^{i\mathbf{k}\cdot(\mathbf{x}-\mathbf{x}')-ik^0(t-t')}}{-(k^0)^2+\mathbf{k}^2+\mu^2}d^4k. \tag{1.52}$$

Clearly, the k^0 integral has poles when $k^0 = \pm\sqrt{\mathbf{k}^2+\mu^2}$. As a result, the k^0 integral should be taken along a contour in the complex k^0 plane. The various Green's functions previously defined are associated with different choices of this contour, as reported in Fig. 1.1. While the two-point functions that are solutions to the homogeneous wave equation are associated with closed contours, the actual Green's functions satisfying the inhomogeneous equation are represented by open contours. Note, however, that these open contours should be visualized as closed by infinite semicircles.

The Feynman Green's function is of particular relevance as it possesses several important properties. First, the other two-point functions and Green's functions defined in this section can be obtained from the Feynman Green's function [12]. The contour of the Feynman Green's function can be equivalently understood to be taken along the real axis if one introduces an infinitesimal negative imaginary contribution '$i\epsilon$' to the denominator of the integral representation of the Green's

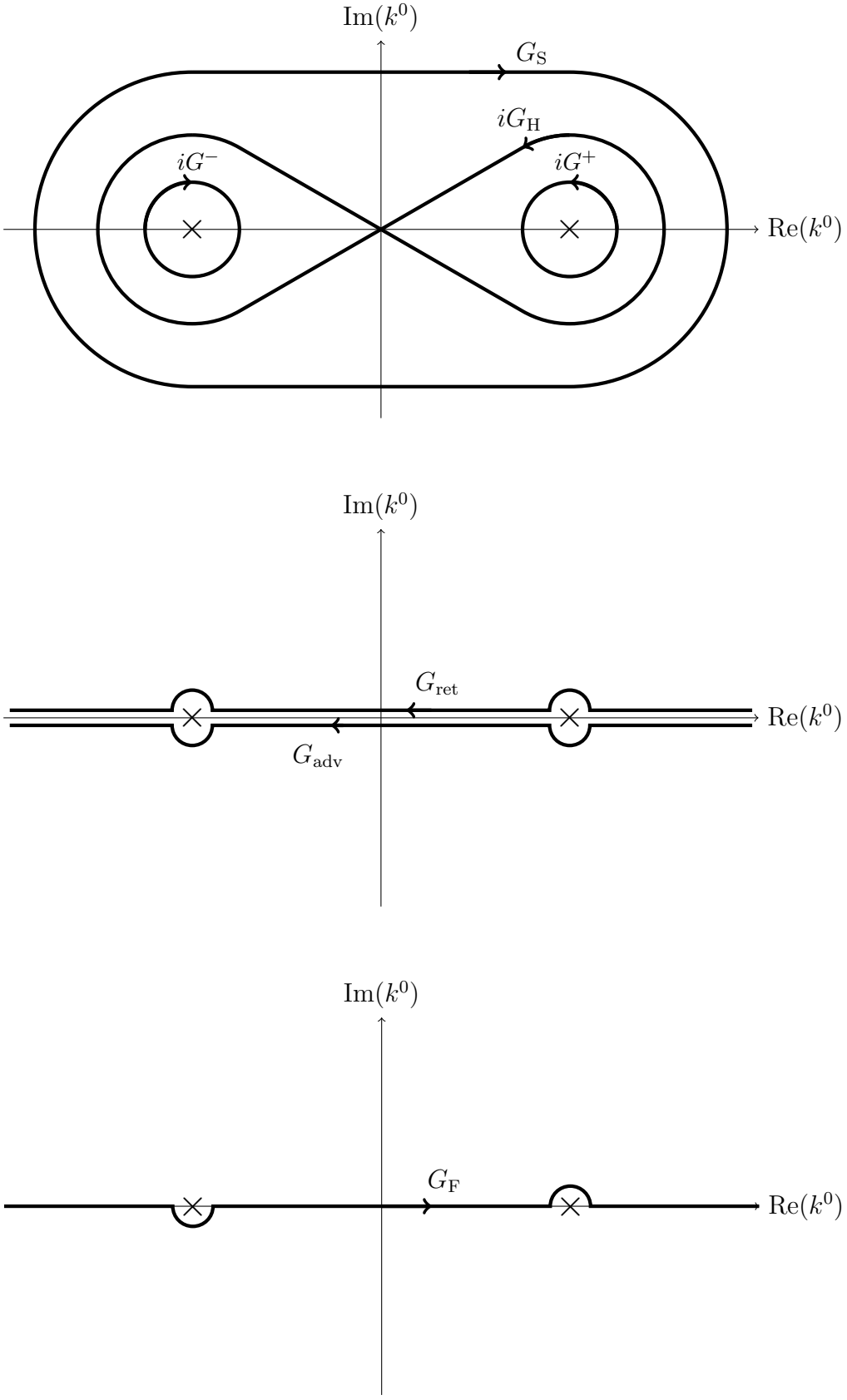


Figure 1.1: *In this Figure, we report the contours associated with the different two-point functions. The poles, occurring on the real axis at* $k^0 = \pm\sqrt{\mathbf{k}^2 + \mu^2}$*, are represented with crosses.*

function

$$G_{\mathrm{F}}(x,x') = \frac{1}{(2\pi)^4}\int_{\mathbb{R}^4} \frac{e^{i\mathbf{k}\cdot(\mathbf{x}-\mathbf{x}')-ik^0(t-t')}}{-(k^0)^2+\mathbf{k}^2+\mu^2-i\epsilon}d^4k. \tag{1.53}$$

In addition, inspecting the contours in Fig. 1.1, one notices that the Feynman contour is unique in that it is the only contour that admits a Wick rotation. In fact, the Feynman contour can be rotated by a counterclockwise rigid rotation of 90 degrees without intersecting the poles so that the integral runs along the imaginary axis. We can generalize the Wick rotation to curved (static) spacetimes by adopting $t \to -i\tau$ and

$$G_{\mathrm{F}}(t,\mathbf{x};t',\mathbf{x}') = -i\,G_{\mathrm{E}}(i\tau,\mathbf{x};i\tau',\mathbf{x}'), \tag{1.54}$$

instead of rotating frequency contours [19]. G_{E} is the Euclidean Green's function which satisfies the equation

$$(\Box_x^{\mathrm{E}} - \mu^2 - \xi\,R)G_{\mathrm{E}}(x,x') = -\frac{1}{\sqrt{g}}\delta^4(x-x'), \tag{1.55}$$

where $\Box_x^{\mathrm{E}}$ is the elliptic Euclidean differential operator. The advantage of working with the Euclidean Green's function is that, for a sufficiently regular boundary and under appropriate boundary conditions, the elliptic operator has a unique, well-defined inverse [12]. As a result, the Klein-Gordon equation admits a unique solution. In addition, we will discuss in the next Section that the distributional nature of the singularity structure of the Euclidean Green's function is simpler than that of the Feynman Green's function.

1.4 Hadamard construction of the Green's function and Hadamard parametrices

In the coincident limit $x' \to x$, the Green's functions introduced in Sec. 1.3 are ill-defined and divergent, as they involve squares of operator-valued distributions. This divergence only depends on the local geometry of the spacetime and on the field parameters. As discussed in the previous section, the Feynman Green's function plays a central role in quantum field theory. Therefore, in what follows, we focus on analyzing the singularity structure of this particular Green's function, recalling that all the other Green's functions can be readily constructed from it. For two spacetime points x and x' within a normal neighborhood (meaning that x and x' must be connected by a unique geodesic), the divergence structure is encoded in the universal Hadamard form of the Feynman Green's function [20], which in four

dimensions is

$$G_{\rm F}(x,x') = \lim_{\epsilon\to 0^+} \frac{i}{8\pi^2}\left\{\frac{\Delta^{1/2}(x,x')}{\sigma_\epsilon(x,x')} + V(x,x')\log\left(\frac{2\sigma_\epsilon(x,x')}{\ell^2}\right) + W(x,x')\right\}. \tag{1.56}$$

In this expression, $\sigma_\epsilon(x,x') = \sigma(x,x') + i\epsilon$, where $\sigma(x,x')$ is Synge's world function, measuring half the square of the geodesic distance between x and x' [21]. This function satisfies the equation

$$2\sigma = \sigma_{;\alpha}\sigma^{;\alpha}, \tag{1.57}$$

where we adopt the notation $\sigma_{;\alpha} \equiv \nabla_\alpha\sigma$, when $x \neq x'$. The world function σ is negative, positive, or zero whenever the points x and x' are, respectively, timelike-, spacelike-, or null- separated. The '$i\epsilon$' prescription is introduced so that Eq. (1.56) is a well-defined distribution even when the spacetime points are null-separated, i.e., when $\sigma(x,x') = 0$. Other Green's functions or two-point functions possess different '$i\epsilon$' prescriptions. The biscalars $\Delta^{1/2}(x,x')$, $V(x,x')$ and $W(x,x')$ are symmetric and regular in the coincidence limit $x' \to x$. Moreover, $\Delta^{1/2}(x,x')$, $V(x,x')$ only depend on the local geometry and the field parameters, and do not carry any global information, such as the details of the quantum state. The global information is instead fully encoded in $W(x,x')$. The parameter ℓ is an arbitrary lengthscale required to make the argument of the logarithm dimensionless and is associated with the renormalization ambiguity.[1]

The biscalar $\Delta(x,x')$ is known as the Van Vleck-Morette determinant [22]

$$\Delta(x,x') \equiv -g^{-1/2}(x)\det(-\sigma_{;\alpha\beta'})g^{-1/2}(x') \tag{1.58}$$

and is related to the world function via the transport equation

$$2\sigma^{;\alpha}\nabla_\alpha\Delta^{1/2} = (4 - \Box_x\sigma)\Delta^{1/2}, \tag{1.59}$$

with initial condition

$$\lim_{x'\to x}\Delta(x,x') = 1. \tag{1.60}$$

The Van Vleck Morrette determinant $\Delta(x,x')$ contains information about whether neighboring geodesics in a geodesic congruence are converging or diverging. In Minkowski spacetime, geodesics are straight lines and $\Delta(x,x) = 1$. The biscalar $V(x,x')$ contains information about waves scattering off the spacetime curvature.

[1] Throughout this thesis, unless explicitly stated otherwise, the notation log denotes the natural logarithm ln.

Introducing the Hadamard representation (1.56) into Eq. (1.48) with $x \neq x'$, it can be shown that the biscalars $V(x,x')$ and $W(x,x')$ satisfy the equations [23]

$$(\Box_x - \mu^2 - \xi^2 R)V(x,x') = 0, \tag{1.61}$$

and

$$\begin{aligned}\sigma(\Box_x - \mu^2 - \xi R)W = &-(\Box_x - \mu^2 - \xi R)\Delta^{1/2} \\ &- 2V - 2V_{;\alpha}\sigma^{;\alpha} + 2V\Delta^{-1/2}\Delta^{1/2}_{;\alpha}\sigma^{;\alpha}.\end{aligned} \tag{1.62}$$

The biscalars $V(x,x')$ and $W(x,x')$ are normally expanded using the Hadamard ansätz

$$\begin{aligned}V(x,x') &= \sum_{p=0}^{\infty} V_p(x,x')\,\sigma^p, \\ W(x,x') &= \sum_{p=0}^{\infty} W_p(x,x')\,\sigma^p,\end{aligned} \tag{1.63}$$

in order to construct series solutions to the equations (1.61) and (1.62) yielding a recursive set of transport equations for V_p and W_p [24, 25]

$$\begin{aligned}(p+1)(2p+4)V_{p+1} + 2(p+1)\sigma^{;\alpha}\nabla_\alpha V_{p+1} - 2(p+1)V_{p+1}\Delta^{-\frac{1}{2}}\sigma^{;\alpha}\nabla_\alpha\Delta^{\frac{1}{2}} \\ + (\Box_x - \mu^2 - \xi\, R)V_p = 0,\end{aligned} \tag{1.64}$$

$$\begin{aligned}&(p+1)(2p+4)\,W_{p+1} + 2(p+1)\,W_{p+1;\alpha}\sigma^{;\alpha} - 2(p+1)\,W_{p+1}\Delta^{-1/2}\Delta^{1/2}_{;\alpha}\sigma^{;\alpha} \\ &\quad + (4p+6)\,V_{p+1} + 2V_{p+1;\alpha}\sigma^{;\alpha} - 2V_{p+1}\Delta^{-1/2}\Delta^{1/2}_{;\alpha}\sigma^{;\alpha} + (\Box_x - \mu^2 - \xi R)W_p = 0,\end{aligned} \tag{1.65}$$

together with the boundary condition for V_0

$$2V_0 + 2\sigma^{;\alpha}\nabla_\alpha V_0 - 2V_0\Delta^{-\frac{1}{2}}\sigma^{;\alpha}\nabla_\alpha\Delta^{\frac{1}{2}} + (\Box_x - \mu^2 - \xi\, R)\Delta^{\frac{1}{2}} = 0. \tag{1.66}$$

The biscalars $\Delta^{1/2}(x,x')$ and $V(x,x')$ can be determined by solving equations (1.59) and (1.64), with boundary conditions (1.60) and (1.66), as covariant Taylor series by introducing [23, 25, 26]

$$\Delta^{1/2}(x,x') = u(x) + \sum_{k=1}^{\infty}\frac{1}{k!}u_{\alpha_1\ldots\alpha_k}(x)\sigma^{;\alpha_1}(x,x')..\sigma^{;\alpha_k}(x,x'), \tag{1.67a}$$

$$V_p(x,x') = v_p(x) + \sum_{k=1}^{\infty}\frac{1}{k!}v_{p\,\alpha_1\ldots\alpha_k}(x)\sigma^{;\alpha_1}(x,x')..\sigma^{;\alpha_k}(x,x'). \tag{1.67b}$$

When the metric is analytic in a neighborhood of $x \in \mathcal{M}$, there always is a sufficiently small neighborhood of x in which these series converge. Since we are ultimately interested in taking the coincident limit, it is sufficient for the domain of convergence to be small. Additionally, in practice, we truncate the series and only make use of the first few coefficients. Equating the terms in the resulting equations at each order of σ yields the coefficients of these expansions. While the coefficients for the first few orders of $\Delta^{1/2}$ can be found in [23, 25], it is particularly relevant to report here the explicit expressions for the first couple of orders of V. Expanding V as

$$V = V_0 + V_1\,\sigma + O(\sigma^{3/2}), \tag{1.68}$$

introducing the covariant Taylor expansions for V_0 and V_1 at the required orders

$$V_0 = v_0 - v_{0\alpha}\,\sigma^{;\alpha} + \frac{1}{2!}\,v_{0\alpha\beta}\,\sigma^{;\alpha}\sigma^{;\beta} + O(\sigma^{3/2}), \tag{1.69a}$$

$$V_1 = v_1 + O(\sigma^{1/2}), \tag{1.69b}$$

and substituting into the relevant equations yields the following coefficients [23, 25]

$$v_0 = \tfrac{1}{2}\left[\left(\xi - \tfrac{1}{6}\right) R + \mu^2\right], \tag{1.70a}$$

$$v_{0\alpha} = \tfrac{1}{2} v_{0;\alpha} = \tfrac{1}{4}\left(\xi - \tfrac{1}{6}\right) R_{;\alpha}, \tag{1.70b}$$

$$\begin{aligned} v_{0\alpha\beta} = {} & -\tfrac{1}{180} R_{\gamma\delta\epsilon\alpha} R^{\gamma\delta\epsilon}{}_{\beta} - \tfrac{1}{180} R_{\alpha\gamma\beta\delta} R^{\gamma\delta} + \tfrac{1}{90} R_{\alpha\gamma} R^{\gamma}{}_{\beta} - \tfrac{1}{120} \Box R_{\alpha\beta} \\ & + \left(\tfrac{1}{6}\xi - \tfrac{1}{40}\right) R_{;\alpha\beta} + \tfrac{1}{12}\left(\xi - \tfrac{1}{6}\right) R\, R_{\alpha\beta} + \tfrac{1}{12}\mu^2 R_{\alpha\beta}. \end{aligned} \tag{1.70c}$$

$$\begin{aligned} v_1 = {} & \tfrac{1}{720} R_{\alpha\beta\gamma\delta} R^{\alpha\beta\gamma\delta} - \tfrac{1}{720} R_{\alpha\beta} R^{\alpha\beta} - \tfrac{1}{24}(\xi - \tfrac{1}{5}) \Box R \\ & + \tfrac{1}{8}(\xi - \tfrac{1}{6})^2 R^2 + \tfrac{1}{4}\mu^2(\xi - \tfrac{1}{6}) R + \tfrac{1}{8}\mu^4. \end{aligned} \tag{1.70d}$$

Clearly, in the coincident limit, one has

$$\lim_{x' \to x} V(x, x') = v_0. \tag{1.71}$$

Interestingly, v_0 vanishes for massless scalar fields propagating in spacetimes in which the Ricci scalar $R = 0$. As a result, in this case, the Feynman Green's function is free of logarithmic divergences, as follows from Eq. (1.56) with $V(x, x) = 0$.

We have seen that the biscalars $\Delta^{1/2}(x, x')$ and $V(x, x')$ are uniquely determined by the local Hadamard expansion. On the other hand, the equations introduced above do not uniquely determine W. In fact, the equations do not fix the boundary conditions for W_0. This reflects the global nature of the biscalar $W(x, x')$, which depends on the quantum state under consideration. Another way of expressing this is that the indeterminate nature of W_0 reflects the failure of the local Hadamard expansion to capture global information.

We note that the state-independent terms are singular in the coincidence limit, and this singular structure is geometrical and completely independent of global boundary conditions that the Green's function might satisfy. The state-independent component of Eq. (1.72) is known as the Hadamard parametrix

$$K(x,x') = \lim_{\epsilon\to 0^+} \frac{i}{8\pi^2}\left\{\frac{\Delta^{1/2}(x,x')}{\sigma_\epsilon(x,x')} + V(x,x')\log\left(\frac{2\sigma_\epsilon(x,x')}{\ell^2}\right)\right\}, \tag{1.72}$$

which satisfies the wave equation with a smooth source and, as we will discuss in the next Section, will play a central role in the renormalization procedure. The terms involving $\Delta^{1/2}/\sigma_\epsilon$ and $V\log\sigma_\epsilon$ on the right-hand side of Eq. (1.72) are usually referred to as, respectively, the direct and tail parts of the Hadamard form. Inspecting Eq. (1.61) also clarifies the origin of the renormalization ambiguity ℓ. This ambiguity arises because $V(x,x')$ is a solution to the homogeneous wave equation, so that arbitrary multiples of $V(x,x')$ can be added to Eq. (1.72) while it remains a parametrix for the wave operator.

Finally, although we focused our discussion on the Hadamard form and parametrix of the Feynman Green's function, we introduce the Hadamard parametrix for the Euclidean Green's function

$$K(x,x') = \frac{1}{8\pi^2}\left\{\frac{\Delta^{1/2}(x,x')}{\sigma(x,x')} + V(x,x')\log\left(\frac{2\sigma(x,x')}{\ell^2}\right)\right\}. \tag{1.73}$$

Note that in the Euclidean version of the Hadamard parametrix, the '$i\epsilon$' prescription is not required, since there is no light cone in a Riemannian manifold. In addition, in the Euclidean case, the parametrix in Eq. (1.73) is actually known as the DeWitt parametrix. In this thesis, however, for simplicity, we use the term Hadamard parametrix for both the Lorentzian and Euclidean version of the parametrix, as is commonly done in the literature. We will see that this significantly simplifies the construction of a renormalization prescription in black hole spacetimes.

The treatment outlined in this Section is not generically valid for any quantum state. We therefore introduce the concept of a Hadamard state. A Hadamard state is a quantum state whose Wightman function possesses a short-distance singularity structure of the Hadamard form:

$$G^+(x,x') = \lim_{\epsilon\to 0^+} \frac{1}{8\pi^2}\left\{\frac{\Delta^{1/2}(x,x')}{\sigma_\epsilon(x,x')} + V(x,x')\log\left(\frac{2\sigma_\epsilon(x,x')}{\ell^2}\right) + W(x,x')\right\}, \tag{1.74}$$

equipped with the '$i\epsilon$' prescription $\sigma_\epsilon(x,x') = \sigma(x,x') + i\epsilon(t-t') + \epsilon^2$. Hadamard states are widely considered as the physically acceptable quantum states [14]. Throughout this thesis, we restrict our analysis to Hadamard states.

1.5 The renormalized stress-energy tensor

As discussed in Section 1.1, the fundamental quantity of interest for the purpose of solving the semiclassical Einstein equations is the expectation value of the stress-energy tensor operator of a quantum field, which encodes the energy-momentum density of the quantum field.

In the classical theory, the stress-energy tensor of a massive scalar field satisfying the Klein-Gordon equation (1.22) is defined by the variation of the action (1.20) with respect to the metric

$$T_{\alpha\beta} := \frac{2}{\sqrt{g}}\frac{\delta \mathcal{S}}{\delta g_{\alpha\beta}} = (1-2\xi)\nabla_\alpha\Phi\nabla_\beta\Phi + (2\xi-\tfrac{1}{2})g_{\alpha\beta}\nabla^\gamma\Phi\nabla_\gamma\Phi - 2\xi\,\Phi\nabla_\alpha\nabla_\beta\Phi + 2\xi\, g_{\alpha\beta}\Phi\nabla^\gamma\nabla_\gamma\Phi + \xi G_{\alpha\beta}\Phi^2 - \frac{\mu^2}{2}g_{\alpha\beta}\Phi^2. \tag{1.75}$$

This tensor satisfies the conservation relation, namely its divergence vanishes $\nabla_\alpha T^{\alpha\beta} = 0$ by virtue of the twice-contracted Bianchi identities, when Φ satisfies the equation of motion (1.22).

If the quantum fields were promoted to operator-valued distributions, as they are in the quantum theory, then the classical expression would be ill-defined, involving terms that are quadratic in an operator-valued distribution evaluated at the same spacetime point. Christensen [27] introduced a covariant point-splitting prescription to circumvent this problem. Following this prescription, the expectation value of the stress-energy tensor operator is defined as the coincident limit of a differential operator acting on the Feynman Green's function

$$\langle \mathrm{A}|\hat{T}_{\alpha\beta}|\mathrm{A}\rangle := -i \lim_{x'\to x} \hat{\tau}_{\alpha\beta}\, G_\mathrm{A}(x,x'), \tag{1.76}$$

where $G_\mathrm{A}(x,x')$ is the Feynman Green's function for a quantum field in a Hadamard state $|\mathrm{A}\rangle$. Of course, this naive definition for the expectation value of the stress-energy tensor is still ill-defined when one actually takes the coincident point limit and hence needs to be renormalized before one computes such limit. The Feynman Green's function $G_\mathrm{A}(x,x')$ possesses a short-distance structure of the universal Hadamard form

$$G_\mathrm{A}(x,x') = \lim_{\epsilon\to 0^+}\frac{i}{8\pi^2}\left\{\frac{\Delta^{1/2}(x,x')}{\sigma_\epsilon(x,x')} + V(x,x')\log\left(\frac{2\sigma_\epsilon(x,x')}{\ell^2}\right) + W_\mathrm{A}(x,x')\right\}, \tag{1.77}$$

and $\hat{\tau}^{\alpha\beta}$ is the differential operator

$$\hat{\tau}^{\alpha\beta} = (1-2\xi)\, g_{\beta'}{}^{\beta}\, \nabla^{\alpha}\nabla^{\beta'} + \left(2\xi - \frac{1}{2}\right) g^{\alpha\beta}\, g^{\gamma}{}_{\gamma'}\, \nabla_{\gamma}\nabla^{\gamma'} - 2\xi\, \nabla^{\alpha}\nabla^{\beta} + 2\xi\, g^{\alpha\beta}\, \nabla_{\gamma}\nabla^{\gamma} + \xi\left(R^{\alpha\beta} - \frac{1}{2}g^{\alpha\beta}R\right) - \frac{1}{2}\mu^{2}g^{\alpha\beta}, \tag{1.78}$$

where $g_{\beta'}{}^{\beta}$ is the bivector of parallel transport, defined by the differential equation $\sigma^{;\gamma} g_{\beta'}{}^{\beta}{}_{;\gamma} = 0$, subject to the boundary condition $\lim_{x'\to x} g_{\beta'}{}^{\beta} = \delta^{\beta}_{\beta'}$ [22, 23, 28]. Note, once again, that the information about the quantum state is fully encoded in the biscalar $W_{\mathrm{A}}(x,x')$, while the other terms in Eq. (1.77) are state independent and identical for all Hadamard states.

Provided that we do not take the coincident limit in Eq. (1.76), the expression on the right-hand side is well-defined and regular. However, in the coincident limit, the expression diverges and requires renormalization. In Minkowski spacetime, this divergence can be removed by renormalizing the zero-point energy by an infinite amount. This is done through a normal ordering procedure and is acceptable because only energy differences are physically observable [12]. This argument is no longer valid in gravitational physics, where the energy density itself acts as a source of gravity. A different renormalization prescription is therefore required.

To renormalize the stress-energy tensor in curved spacetimes, we implement the Hadamard renormalization prescription on the point-split stress-energy tensor. This prescription was originally proposed by Adler, Lieberman, and Ng [29, 30], subsequently corrected by Wald [31] and further developed by Brown and Ottewill [23, 24]. This approach consists of subtracting the Hadamard parametrix from the Feynman Green's function, thus obtaining a quantity that is regular in the coincident limit. This prescription allows us to define what is known as the renormalized vacuum polarization for the field $\hat{\Phi}(x)$ in the state $|\mathrm{A}\rangle$ as

$$\langle \mathrm{A}|\hat{\Phi}^{2}|\mathrm{A}\rangle_{\mathrm{ren}} := -i \lim_{x'\to x}\{G_{\mathrm{A}}(x,x') - K(x,x')\} = \frac{1}{8\pi^{2}} \lim_{x'\to x} W_{\mathrm{A}}(x,x') \tag{1.79}$$

where $K(x,x')$ is the Hadamard parametrix defined in Eq. (1.72). A similar procedure yields an expression for the stress-energy tensor operator that is finite in the coincident limit

$$\langle \mathrm{A}|\hat{T}_{\alpha\beta}|\mathrm{A}\rangle_{\mathrm{finite}} = -i \lim_{x'\to x}\{\hat{\tau}_{\alpha\beta}\,(G_{\mathrm{A}}(x,x') - K(x,x'))\} = \frac{1}{8\pi^{2}} \lim_{x'\to x} \hat{\tau}_{\alpha\beta} W_{\mathrm{A}}(x,x'). \tag{1.80}$$

This expression, however, is not conserved and therefore violates one of Wald's axioms for a physically meaningful stress-energy tensor [31, 32]. A conserved renor-

malized stress-energy tensor can then be defined as [23]

$$\begin{aligned}\langle \mathrm{A}|\hat{T}_{\alpha\beta}|\mathrm{A}\rangle_{\mathrm{ren}} :&= -i \lim_{x'\to x} \left\{\hat{\tau}_{\alpha\beta}\left(G_{\mathrm{A}}(x,x') - K(x,x')\right)\right\} + \frac{v_1 g_{\alpha\beta}}{4\pi^2} \\ &= \frac{1}{8\pi^2}\left(\lim_{x'\to x} \hat{\tau}_{\alpha\beta} W_{\mathrm{A}}(x,x') + 2v_1 g_{\alpha\beta}\right). \end{aligned} \tag{1.81}$$

where v_1 is defined in Eq. (1.70d). The addition of the v_1 term in the definition of the RSET gives rise to the so-called trace anomaly. On the contrary to the classical case in which $T^{\alpha}_{\ \alpha}$ vanishes for conformally invariant fields ($\xi = 1/6$ and $\mu = 0$), the trace of the RSET with $\xi = 1/6$ and $\mu = 0$ is instead nonvanishing [14, 23]:

$$\langle \mathrm{A}|\hat{T}^{\alpha}_{\ \alpha}|\mathrm{A}\rangle_{\mathrm{ren}}\Big|_{\xi=\frac{1}{6},\mu=0} = \frac{1}{4\pi^2} v_1. \tag{1.82}$$

Another important aspect to highlight is that the renormalization prescription is not uniquely defined. We have already seen the existence of an ambiguity in the parameter ℓ in the Hadamard parametrix. Additionally, Wald [32] showed that different renormalization procedures yield renormalized stress-energy tensors that differ by the addition of a local, conserved tensor of the form

$$\Theta_{\alpha\beta} = \mathfrak{b}_1\, \mathsf{g}_{\alpha\beta} + \mathfrak{b}_2 \mathsf{G}_{\alpha\beta} + \mathfrak{a}_1\, \mathsf{H}^{(1)}_{\alpha\beta} + \mathfrak{a}_2\, \mathsf{H}^{(2)}_{ab}, \tag{1.83}$$

where $\mathfrak{a}_1, \mathfrak{a}_2, \mathfrak{b}_1, \mathfrak{b}_2 \in \mathbb{R}$ are some constants. Thus, one is free to add tensors of this form to the renormalized stress-energy tensor.

Once the renormalization is performed for a quantum field in a Hadamard state $|\mathrm{A}\rangle$, it is possible to compute renormalized quantities in a different Hadamard state $|\mathrm{B}\rangle$ by state subtraction. For instance, the renormalized vacuum polarization in a state $|\mathrm{B}\rangle$ is defined as

$$\langle \mathrm{B}|\hat{\Phi}^2|\mathrm{B}\rangle_{\mathrm{ren}} :\, = -i \lim_{x'\to x} \left\{G_{\mathrm{B}}(x,x') - K(x,x')\right\} = \frac{1}{8\pi^2} W_{\mathrm{B}}(x,x). \tag{1.84}$$

However, because of the universal singular structure of Hadamard states, one finds

$$-i \lim_{x'\to x} \left\{G_{\mathrm{B}}(x,x') - G_{\mathrm{A}}(x,x')\right\} = \frac{1}{8\pi^2} W_{\mathrm{B}}(x,x) - \frac{1}{8\pi^2} W_{\mathrm{A}}(x,x), \tag{1.85}$$

so that, if one has already obtained the renormalized vacuum polarization in one state $\langle \mathrm{A}|\hat{\Phi}^2|\mathrm{A}\rangle_{\mathrm{ren}}$, then $\langle \mathrm{B}|\hat{\Phi}^2|\mathrm{B}\rangle_{\mathrm{ren}}$ can be readily computed by state subtraction as

$$\langle \mathrm{B}|\hat{\Phi}^2|\mathrm{B}\rangle_{\mathrm{ren}} = -i \lim_{x'\to x} \left\{G_{\mathrm{B}}(x,x') - G_{\mathrm{A}}(x,x')\right\} + \langle \mathrm{A}|\hat{\Phi}^2|\mathrm{A}\rangle_{\mathrm{ren}} = \frac{1}{8\pi^2} W_{\mathrm{B}}(x,x). \tag{1.86}$$

This procedure can be straightforwardly extended to the renormalized stress-energy

tensor.

Finally, although we have defined the renormalized vacuum polarization and RSET in terms of the Feynman Green's function, these quantities can also be computed from the Wightman function $G^+(x,x')$, by noting that we are free to point-split in any direction so that we can always choose a spacelike point separation. In fact, by noting that $iG_{\rm F}(x,x') = G^+(x,x') - iG_{\rm adv}(x,x')$ and that $G_{\rm adv}(x,x')$ vanishes if the points are spacelike separated, then $iG_{\rm F}(x,x') = G^+(x,x')$ in this case. Additionally, when the spacetime admits an Euclidean section, the renormalized vacuum polarization and RSET can be computed from the difference between the Euclidean Green's function and its Hadamard parametrix in Eq. (1.73). In all cases, the renormalized quantities are determined by $W_{\rm A}(x,x')$.

1.6 The semiclassical Einstein equations

We now have all the necessary ingredients to introduce the self-consistent semiclassical Einstein equations

$$G^{-1}\mathsf{G}_{\alpha\beta} + \Lambda\,\mathsf{g}_{\alpha\beta} + \mathfrak{a}_1\,\mathsf{H}^{(1)}_{\alpha\beta} + \mathfrak{a}_2\,\mathsf{H}^{(2)}_{\alpha\beta} = 8\pi\left(\mathsf{T}^{(\rm cl)}_{\alpha\beta} + \langle\hat{\mathsf{T}}_{\alpha\beta}\rangle_{\rm ren}\right). \tag{1.87}$$

In these equations, it is assumed that all the tensors depend on an unknown metric $\mathsf{g}_{\alpha\beta}$. The tensor $\mathsf{T}^{(\rm cl)}_{\alpha\beta}$ denotes the classical stress-energy tensor, while $\langle\hat{\mathsf{T}}_{\alpha\beta}\rangle_{\rm ren}$ is the renormalized stress-energy tensor associated with the quantum fields. Unlike in the fixed background calculations discussed in Sec. 1.5, the renormalized stress-energy tensor is now a functional of the same unknown metric that appears on the right-hand side of the semiclassical equations. $\mathfrak{a}_1, \mathfrak{a}_2 \in \mathbb{R}$ are some constants and $\mathsf{H}^{(1)}_{\alpha\beta}$ and $\mathsf{H}^{(2)}_{\alpha\beta}$ are geometrical tensors defined by

$$\begin{aligned}\mathsf{H}^{(1)}_{\alpha\beta} =& \tfrac{2}{3}\nabla_\alpha\nabla_\beta\mathsf{R} - 2\Box\mathsf{R}_{\alpha\beta} + \tfrac{1}{3}\mathsf{g}_{\alpha\beta}\Box\mathsf{R} - \tfrac{1}{3}\mathsf{g}_{\alpha\beta}\mathsf{R}^2 \\ &+ \tfrac{4}{3}\mathsf{R}\,\mathsf{R}_{\alpha\beta} + (\mathsf{R}_{\gamma\delta}\mathsf{R}^{\gamma\delta})\mathsf{g}_{\alpha\beta} - 4\mathsf{R}_{\alpha\gamma\beta\delta}\mathsf{R}^{\gamma\delta}, \qquad (1.88a)\\ \mathsf{H}^{(2)}_{\alpha\beta} =& 2\nabla_\alpha\nabla_\beta\mathsf{R} - 2\mathsf{g}_{\alpha\beta}\Box\mathsf{R} + \tfrac{1}{2}\mathsf{R}^2\mathsf{g}_{\alpha\beta} - 2\mathsf{R}\,\mathsf{R}_{\alpha\beta}. \qquad (1.88b)\end{aligned}$$

Note that we have reinstated Newton's constant G and expressed it on the left-hand side of the equations, hence Λ here has the interpretation of the cosmological constant divided by Newton's constant. Although we work in units where $\hbar = 1$, the contribution of $\langle\hat{\mathsf{T}}_{\alpha\beta}\rangle_{\rm ren}$ to the semiclassical equations should be understood to carry an explicit factor of $\hbar$. This makes it clear that the term is explicitly quantum in nature.

We have discussed in the previous Section how the renormalization prescription is not unique since one is free to add tensors of the form in Eq. (1.83) to the

renormalized stress-energy tensor. As a result, these terms then appear in the semiclassical equations (1.87). Different renormalizations of the quantum stress-energy tensor are degenerate with different renormalizations of the constants $\mathfrak{a}_1$, $\mathfrak{a}_2$, Λ, and G^{-1} [33].

When attempting to solve the exact semiclassical equations in Eq. (1.87), one is faced with several difficulties. The tensors $\mathsf{H}^{(1)}_{\alpha\beta}$ and $\mathsf{H}^{(2)}_{\alpha\beta}$, together with the renormalized stress-energy tensor, contain fourth-order time derivatives of the metric. As a result, the semiclassical equations admit additional solutions that are not present in the classical equations, which are of second order. These extra solutions include runaway solutions, which are generally deemed as unphysical [34]. Moreover, the renormalized stress-energy tensor associated with quantum fields can typically be calculated only on a fixed background spacetime, and there is, in general, no methodology for computing it on an unknown geometry. For these reasons, the semiclassical equations are usually treated perturbatively about a classical solution and solved recursively order by order, or by means of an order-reduction procedure [34–36].

The perturbative approach removes the unphysical runaway solutions while allowing the methodologies outlined in the previous sections to be employed to compute the renormalized stress-energy tensor on a fixed classical background. The metric is expanded as $\mathsf{g}_{\alpha\beta} \sim g_{\alpha\beta} + \epsilon\, h_{\alpha\beta}$, where we introduce a bookkeeping parameter ϵ to keep track of quantum corrections. To keep track of the corrections to the constants coming from the RSET, we write the constants as $\mathfrak{a}_1 \to \mathfrak{a}_1 + \epsilon\delta\mathfrak{a}_1$ etc., where now $\mathfrak{a}_1$ is considered to be the background value. Similarly, the tensors in Eq. (1.87) are also expanded in the form $\mathsf{G}_{\alpha\beta} \sim G_{\alpha\beta} + \epsilon\,\delta G_{\alpha\beta}$. At zeroth order in ϵ, assuming $\mathfrak{a}_1 = \mathfrak{a}_2 = 0$ and reinstating $G = 1$, the semiclassical equations are effectively the classical Einstein equations for the background metric $g_{\alpha\beta}$

$$G_{\alpha\beta} + \Lambda g_{\alpha\beta} = 8\pi\, T^{(\mathrm{cl})}_{\alpha\beta}. \tag{1.89}$$

At first order in the expansion in ϵ, one finds

$$\delta G_{\alpha\beta} + \delta G^{-1}\, G_{\alpha\beta} + \Lambda h_{\alpha\beta} + \delta\Lambda\, g_{\alpha\beta} + \delta\mathfrak{a}_1\, H^{(1)}_{\alpha\beta} + \delta\mathfrak{a}_2\, H^{(2)}_{\alpha\beta} = 8\pi \left(\delta T^{(\mathrm{cl})}_{\alpha\beta} + \langle\hat{T}_{\alpha\beta}\rangle_{\mathrm{ren}}\right), \tag{1.90}$$

where the perturbation of the Einstein tensor is given by

$$\delta G_{\alpha\beta} = -\frac{1}{2}(\Box\bar{h}_{\alpha\beta} + g_{\alpha\beta}\nabla^\gamma\nabla^\delta\bar{h}_{\gamma\delta} - 2\nabla^\gamma\nabla_{(\alpha}\bar{h}_{\beta)\gamma} - g_{\alpha\beta}R^{\gamma\delta}\bar{h}_{\gamma\delta} + R\,\bar{h}_{\alpha\beta}), \tag{1.91}$$

and where

$$\bar{h}_{\alpha\beta} = h_{\alpha\beta} - \tfrac{1}{2}g_{\alpha\beta}g^{\gamma\delta}h_{\gamma\delta} \tag{1.92}$$

is the trace-reversed metric perturbation. Note that all the derivatives in Eqs. (1.90) and (1.91) are now with respect to the background metric $g_{\alpha\beta}$.

In the equations at first order (1.90), the source term is the renormalized expectation value of the stress-energy tensor operator for a quantum field in a given quantum state on a fixed classical background spacetime. By solving these equations to obtain the metric perturbation $h_{\alpha\beta}$, one determines the so-called semiclassical backreaction, at first order, of the quantum fields on the background geometry. Clearly, to achieve this, one first needs a prescription to accurately compute the renormalized stress-energy tensor on a fixed classical background spacetime. Although this quantity can be formally obtained by Hadamard renormalization (see Eq. (1.81)), its practical computation in most situations of interest is technically challenging. In the next Section, we will discuss these difficulties in the context of black hole spacetimes.

1.7 Implementing Hadamard renormalization in black hole spacetimes

Hadamard renormalization addresses the conceptual problem of how to remove the divergences in a physically meaningful way, but we will see that there is still a computational challenge with its practical implementation in black hole spacetimes.

Before discussing the details of renormalization in black hole spacetimes, it is, however, useful to introduce the quantum states of interest. In static, spherically symmetric black hole spacetimes, there are three important quantum states:

1. *The Hartle-Hawking state* [37]: The Hartle-Hawking state corresponds to a black hole in thermal equilibrium with thermal radiation at the Hawking temperature. An ingoing flux of thermal radiation from past null infinity is exactly balanced by an outgoing flux at future null infinity at the same temperature. This quantum state is regular across both the past and future event horizons and can be extended to black hole interiors that possess a Cauchy horizon.

2. *The Boulware state* [38]: The Boulware state is defined to be empty at past and future null infinity. It is known to be singular on the black hole event horizon [39], making it unsuitable for describing quantum fields inside the black hole. It is considered the natural vacuum state for static, spherically symmetric horizonless equilibrium configurations, such as stars.

3. *The Unruh state* [11]: The Unruh state describes a black hole formed by the gravitational collapse of a spherically symmetric object. It is empty at past null infinity and exhibits an outgoing flux of Hawking radiation at future null

infinity. This state is singular on the past event horizon, but regular on the future event horizon. It can therefore be extended to the black hole interiors that possess a Cauchy horizon.

Earlier approaches to the renormalization computation focused primarily on the exterior of static, spherically symmetric black holes and on the Hartle-Hawking and Boulware states. These states are, in fact, suitable for Euclidean methods, since the computations can be performed on the Wick-rotated Riemannian manifold. Working with the Hartle-Hawking state offers a significant computational advantage since one can employ Euclidean techniques that enforce a discretization of the frequency spectrum. The Hartle-Hawking and Boulware states are treated as Hawking-temperature and zero-temperature Euclidean states, respectively. In earlier renormalization approaches, the direct renormalization of the Unruh state was not considered, since the Unruh state cannot be defined on the Wick-rotated manifold. Nonetheless, the Unruh state is arguably the most physically relevant state in the context of black holes, as it provides a model for a black hole formed by gravitational collapse that emits Hawking radiation at future null infinity. Therefore, developing a method for the renormalization of the Unruh state is of particular physical interest.

To outline the computational challenge of applying Hadamard renormalization in black hole spacetimes, let us consider, as an example, a quantum scalar field in the Hartle-Hawking state propagating on the exterior of a Schwarzschild black hole with line element

$$ds^2 = -f(r)dt^2 + dr^2/f(r) + r^2(d\theta^2 + \sin^2\theta d\phi^2), \tag{1.93}$$

where

$$f(r) = 1 - \frac{2M}{r}, \tag{1.94}$$

and M is the black hole mass. The Hartle-Hawking state is most naturally and conveniently defined on the Wick-rotated Riemannian manifold ($t \to -i\tau$) with Euclidean line-element

$$ds^2 = f(r)d\tau^2 + dr^2/f(r) + r^2(d\theta^2 + \sin^2\theta d\phi^2). \tag{1.95}$$

Working on the Wick-rotated Riemannian manifold is convenient for two main reasons. First, the singularity structure of the Green's function in a Riemannian manifold is simpler: the Euclidean Green's function is only singular in the coincidence limit ($x' \to x$), as opposed to the Feynman Green's function in the original spacetime, which is also singular along the lightcone (compare Eqs. (1.72) and (1.73)).

The static nature of the metric guarantees that the Euclidean two-point function for the quantum scalar field satisfying appropriate boundary conditions is equivalent to the Feynman propagator computed on the Lorentzian line-element [19]. Secondly, a periodicity condition in imaginary time, with periodicity equal to the inverse Hartle-Hawking temperature $1/T_{\rm H}$, $\tau = \tau + 1/T_{\rm H}$ is imposed to avoid the formation of a conical singularity at $r = 2M$ in the Riemannian manifold, where $T_{\rm H} = \kappa/(2\pi)$ and $\kappa = 1/(4M)$ is the surface gravity of the black hole's event horizon. This periodicity in imaginary time is inherited in the two-point function for the quantum scalar field in the Hartle-Hawking state on the Euclidean geometry, resulting in a discrete frequency spectrum, which is a significant computational advantage. The Hartle-Hawking state is, in fact, a thermal equilibrium state at the same temperature as the event horizon. The Kubo–Martin–Schwinger (KMS) condition implies that thermal equilibrium Green's functions are periodic in imaginary time [12]. The Green's function, which satisfies regularity boundary conditions at the event horizon, then corresponds to the Hartle-Hawking state [37, 40].

The Euclidean Green's function in the Hartle-Hawking state is conveniently expressed as a mode-sum [39]

$$G_{\rm H}(x,x') = \frac{1}{8\pi^2}\sum_{l=0}^{\infty}(2l+1)P_l(\cos\gamma)\sum_{n=-\infty}^{\infty}e^{i\,n\kappa\,\Delta\tau}g_{nl}(r,r'), \tag{1.96}$$

where $\cos\gamma = \cos\theta\cos\theta' + \sin\theta\,\sin\theta'\,\cos(\phi'-\phi)$, $P_l(z)$ is the Legendre polynomial of the first kind and $\Delta\tau = \tau' - \tau$. The bi-distribution $g_{nl}(r,r')$ is the one-dimensional radial Green's function satisfying

$$\left\{\frac{d}{dr}\left(r^2 f\frac{d}{dr}\right) - \left[\frac{(n\kappa)^2 r^2}{f} + l(l+1) + r^2(\mu^2 + \xi\,R)\right]\right\} g_{nl}(r,r') = -\delta(r-r'). \tag{1.97}$$

This is a Sturm-Liouville problem. The Green's function can be constructed as an ordered normalized product of homogeneous solutions

$$g_{nl}(r,r') = \frac{p_{nl}(r_<)q_{nl}(r_>)}{N_{nl}}, \tag{1.98}$$

where $p_{nl}(r_<)$ is a homogeneous solution regular at the horizon and $q_{nl}(r_>)$ is a homogeneous solution regular at infinity. We have adopted the ordering notation $r_< = \min\{r,r'\}$, $r_> = \max\{r,r'\}$. The normalization constant N_{nl} is obtained by the Wronskian condition

$$N_{nl} = -r^2 f(r)\mathcal{W}\{p_{nl}, q_{nl}\}, \tag{1.99}$$

where $\mathcal{W}\{p_{nl}, q_{nl}\}$ is the Wronskian of the two solutions

$$\mathcal{W}\{p_{nl}, q_{nl}\} = \left(\frac{d\,q_{nl}}{dr} p_{nl} - \frac{d\,p_{nl}}{dr} q_{nl}\right). \tag{1.100}$$

The radial functions are determined numerically, and information about the quantum state is encoded in the boundary conditions on these mode functions.

We will discuss in Sec. 2.2 that for the Boulware state, which is a zero temperature pure state, the periodic identification of imaginary time is not possible. As a result, the frequency spectrum in the mode-sum expression for the Boulware Green's function remains continuous. This means that, in the expression for the Boulware Green's function, the n-sum in Eq. (1.96) is replaced by a continuous integral over the frequency ω.

The mode-sum expression for the Green's function in the Hartle-Hawking state in Eq. (1.96) is divergent in the coincident limit and requires renormalization. Specifically, in the coincident limit, the l- and n-sums in Eq. (1.96) do not converge. As discussed in Sec. 1.5, this expression can be formally renormalized by subtracting the Hadamard parametrix defined in Eq. (1.73) before taking the coincident limit. However, the computational challenge of applying the Hadamard renormalization in practice is that the divergence encoded in the Hadamard parametrix is purely local and geometrical: $\sigma(x, x') \to 0$ as $x' \to x$, making $K(x, x')$ in Eq. (1.73) singular at the coincidence point limit. On the other hand, the divergence in the Euclidean Green's function manifests in the non-convergence of the l- and n-sums. We are then left with the following computational issue: how can the Hadamard parametrix be subtracted from the Green's function in a way that the coincidence limit can be meaningfully taken?

Candelas and Howard [41–43] provided the first practical implementation of Hadamard renormalization in black hole spacetimes. They considered a massless, minimally coupled quantum scalar field in the Hartle-Hawking state propagating on the exterior of a Schwarzschild black hole. As discussed in Sec. 1.4, for massless fields and in spacetimes with vanishing Ricci scalar, the leading-order logarithmic contributions in the Hadamard parametrix vanish (see Eq. (1.70a)), thus simplifying the divergent structure of the Hadamard parametrix in Eq. (1.73). This method relies on the idea of point-splitting the stress-energy tensor operator along a single direction. It is particularly convenient to point-split along a symmetry of the metric. For this reason, this method involves point-splitting in the temporal direction. For simplicity, we consider here the computation for the renormalized vacuum polarization [41], although the method was later generalized to the computation of the RSET [42, 43]. Following the Candelas-Howard approach, the Euclidean Green's function for the Hartle-Hawking state in Eq. (1.96) point-split only in the temporal

direction can be expressed as [41]

$$G_{\rm H}(\Delta\tau, r) = \frac{1}{4\pi^2}\sum_{n=1}^{\infty}\cos(n\kappa\Delta\tau)\sum_{l=0}^{\infty}\left((2l+1)\frac{p_{nl}(r)q_{nl}(r)}{N_{nl}} - \frac{\kappa}{rf^{1/2}}\right). \tag{1.101}$$

Considering only the leading-order divergent term in Eq. (1.73), the temporal-split Hadamard parametrix takes the form

$$K(\Delta\tau, r) = \frac{1}{4\pi^2}\frac{1}{f(r)\Delta\tau^2} + \mathcal{O}(1), \tag{1.102}$$

where we have used $2\sigma = f(r)\Delta\tau^2 + \mathcal{O}(\Delta\tau^4)$. Now, we can employ the identity

$$\frac{1}{\Delta\tau^2} = -\kappa^2\sum_{n=1}^{\infty} n\cos(n\kappa\Delta\tau) + \mathcal{O}(1), \tag{1.103}$$

to write the leading order divergent term in the Hadamard parametrix as an n-sum analogous to that of the Green's function (1.101). To compute the renormalized vacuum polarization, we can then subtract each n-mode expression of the parametrix from the Euclidean Green's function

$$\begin{aligned}\langle {\rm H}|\hat{\Phi}^2|{\rm H}\rangle_{\rm ren} &= \lim_{\Delta\tau\to 0}\left(G_{\rm H}(\Delta\tau, r) - K(\Delta\tau, r)\right)\\ &= \frac{1}{4\pi^2}\sum_{n=1}^{\infty}\left\{\sum_{l=0}^{\infty}\left((2l+1)\frac{p_{nl}(r)q_{nl}(r)}{N_{nl}} - \frac{\kappa}{rf^{1/2}}\right) + \frac{n\kappa^2}{f}\right\} + \mathcal{O}(1).\end{aligned} \tag{1.104}$$

It is clear from Eq. (1.104), that the Candelas-Howard approach does not lead to a complete mode-by-mode subtraction of the Hadamard parametrix from the Euclidean Green's function, since the singular part of the Hadamard parametrix is only expanded in the frequency modes n and not in the angular modes l. As a result, the renormalized mode-sum expression in Eq. (1.104), despite being formally finite in the limit $\Delta\tau \to 0$, is not suitable for numerical implementation as is. In fact, for the n-sum to converge, it requires a cancellation between the infinite l-sum, which converges very slowly, being of $\mathcal{O}(l^{-2})$ at large l, and the $n\kappa^2/f$ term. As a result, it requires sophisticated analytical methods, including the use of WKB approximations and the Watson-Sommerfeld transform, to make the numerical evaluation possible.

Anderson, Hiscock, and Samuel [44, 45] later improved and consistently generalized the Candelas-Howard method. The AHS method allows the computation of the RSET for massless and massive scalar fields in both the Hartle-Hawking and Boulware states on any static, spherically symmetric spacetime. The AHS method improved the Candelas-Howard method by introducing a systematic WKB subtrac-

tion scheme that makes the renormalization procedure more convenient for numerical calculations.

There are several drawbacks related to these approaches. Firstly, they depend on the use of high-order WKB approximations, which are computationally expensive to implement. These approximations are also not uniform, which results in very poor convergence near the horizon, meaning that computing renormalized quantities there may require a very large number of numerical modes. In addition, there is no control over the order of convergence. Finally, these methods are also constrained to spacetimes that admit a Euclidean section and are difficult to generalize to other scenarios.

Despite these drawbacks, the Candelas-Howard and the AHS methods remained the standard methods for computing renormalized quantities until very recently, when two new independent methods were proposed: Levi and Ori's "pragmatic mode-sum" regularization prescription [46–50] and the Taylor-Breen-Ottewill "extended coordinate" method [51–53].

The pragmatic mode-sum regularization method was developed directly in Lorentzian spacetime and relies on point splitting in a single direction, chosen according to the symmetries of the spacetime. Specifically, three different variants were developed: t-splitting [46], designed for stationary backgrounds, θ-splitting [48], for spherically symmetric backgrounds, and ϕ-splitting [47], for axially symmetric backgrounds. The main advantage of this renormalization scheme is that it is formulated directly in Lorentzian spacetime and requires a single spacetime symmetry for point-splitting, thus making it applicable to a wide range of physically relevant spacetimes. Notably, the pragmatic mode-sum has been used to compute the RSET both outside [49] and inside [54] a Kerr black hole. The main drawback of this method is that subtracting the Hadamard parametrix does not generally yield convergent mode-sums directly. Instead, additional "pragmatic" prescriptions are required to obtain finite results. This makes the procedure less direct and computationally expensive. Moreover, the convergence rate of the mode sums cannot be explicitly controlled. In addition, the method has only been applied to massless, minimally coupled fields.

In this thesis, we will adopt the extended coordinate prescription and provide some generalizations to it. The details of this method will be the focus of the next Section.

1.7.1 The extended coordinate method

In this Section, we present a review of the extended coordinate prescription [51–53]. The principle of the method is to write the Hadamard parametrix as a mode-sum

in the same form as that of the Euclidean Green's function and then perform the subtraction mode by mode [51–53]. This renormalized mode-sum will converge in the coincidence limit. This method was developed for a quantum scalar field in the Hartle-Hawking state propagating on the exterior of static, spherically symmetric black holes, exploiting the fact that, as discussed in the previous Section, one can employ Euclidean methods that discretize the frequency spectrum of the Euclidean Green's function (1.96).

The extended coordinate method is based on two core ideas:

1. Point-split in multiple directions;
2. Expand the Hadamard parametrix in a judiciously chosen set of "extended" coordinates.

The extended coordinates for the Hartle-Hawking state on the exterior are [51, 52]

$$\varpi^2 = \frac{2}{\kappa^2}(1-\cos\kappa\Delta\tau), \qquad s^2 = f(r)\,\varpi^2 + 2r^2(1-\cos\gamma). \tag{1.105}$$

We note that the quantities ϖ and s are $\mathcal{O}(\Delta x)$, where $\Delta x \equiv x' - x$ generically refers to the coordinate separations $\Delta\tau = \tau' - \tau$, $\Delta r = r' - r$, $\Delta\theta = \theta' - \theta$ and $\Delta\phi = \phi' - \phi$. The extended coordinates are defined such that, to leading order, $\sigma = \frac{1}{2}(s^2 + \frac{\Delta r^2}{f}) + \mathcal{O}(\Delta x^3)$. It is important to note that rather than defining $\bar{s}^2 := f(r)\Delta\tau^2 + r^2\Delta\theta^2 + r^2\sin\theta\sin\theta'\Delta\phi^2$, the definition in Eq. (1.105) encodes the angular separation in $\cos\gamma = \cos\theta\cos\theta' + \sin\theta\sin\theta'\cos\Delta\phi$ and makes the periodicity of the Euclidean time explicit in ϖ^2. These definitions reflect the structure of the mode-sum representation of the Euclidean Green's function, in which the angular separation appears as $\cos\gamma$ in the Legendre polynomials and in which the Euclidean time is periodic. This choice is crucial, as it enables a mode-sum representation of the Hadamard parametrix in the same form as that of the Green's function.

For clarity, we now restrict our analysis to the case of a massless scalar field in Schwarzschild spacetime. As discussed previously, in this case $v_0 = 0$ so that the leading order contribution to the logarithmic tail in the Hadamard parametrix vanishes. Note, however, that the extended coordinate method is generically applicable to physical contexts in which $v_0 \neq 0$. In addition, we focus on obtaining a mode-sum representation only for the divergent terms in the Hadamard parametrix. Under these assumptions, when expanded in terms of extended coordinates up to the order containing divergent terms, the Hadamard parametrix takes the form

$$K(x,x') = \frac{1}{8\pi^2}\frac{2}{s^2} + \mathcal{O}(1). \tag{1.106}$$

Note that, for simplicity, we set the coordinate separation $\Delta r = 0$. To express the leading-order divergence in the parametrix as a mode-sum in the same form as the

Euclidean Green's function, we assume

$$\frac{1}{s^2} = \sum_{l=0}^{\infty}(2l+1)P_l(\cos\gamma)\sum_{n=-\infty}^{\infty} e^{in\kappa\Delta\tau}\Psi_{nl}(r). \tag{1.107}$$

We refer to $\Psi_{nl}(r)$ as the regularization parameters. The judicious choice of extended coordinates in Eq. (1.105) makes it possible to invert this expression to obtain a double-integral representation for the regularization parameters. Specifically, setting $\mathfrak{u} = \cos\gamma$, multiplying each side by $e^{-in'\kappa\,\Delta\tau}P_{l'}(\mathfrak{u})$ and integrating yields

$$\Psi_{nl}(r) = \frac{\kappa}{4\pi}\int_0^{2\pi/\kappa}\int_{-1}^{1}\frac{1}{s^2}e^{-in\kappa\Delta\tau}P_l(\mathfrak{u})d\mathfrak{u}\,d\Delta\tau, \tag{1.108}$$

where we made use of the completeness relations

$$\begin{aligned}\int_0^{2\pi/\kappa} e^{-i(n-n')\kappa\,\Delta\tau} &= \frac{2\pi}{\kappa}\delta_{nn'},\\ \int_{-1}^{1} P_l(\mathfrak{u})P_{l'}(\mathfrak{u})d\mathfrak{u} &= \frac{\delta_{ll'}}{l+1/2}.\end{aligned} \tag{1.109}$$

Remarkably, the integrals in Eq. (1.108) can be computed in closed-form in terms of known functions [51, 52]

$$\Psi_{nl}(r) = \frac{(-1)^n}{2r^2}P_l^{-|n|}\left(\sqrt{1+\frac{f(r)}{\kappa^2r^2}}\right)Q_l^{|n|}\left(\sqrt{1+\frac{f(r)}{\kappa^2r^2}}\right), \tag{1.110}$$

where $P^{\mu}_{\nu}(z)$ and $Q^{\mu}_{\nu}(z)$ are the associated Legendre functions of the first and second kind, respectively. As a result, the renormalized vacuum polarization in the Hartle-Hawking state is then readily obtained by subtracting mode-by-mode the expansion for the Hadamard parametrix (1.106) from the Green's function (1.96), and taking the coincident limit

$$\langle \mathrm{H}|\hat{\Phi}^2|\mathrm{H}\rangle_{\mathrm{ren}} = \frac{1}{8\pi^2}\sum_{l=0}^{\infty}\sum_{n=-\infty}^{\infty}(2l+1)\left[g_{nl}(r) - 2\Psi_{nl}(r)\right] + \mathcal{O}(1). \tag{1.111}$$

Note that, as opposed to the Candelas-Howard method, the renormalized mode-sum expression for the vacuum polarization (1.111) involves now a complete mode-by-mode subtraction. The mode-sums converge as $\mathcal{O}(n^{-3})$ at large n for fixed l, and as $\mathcal{O}(l^{-2})$ at large l for fixed n. In this section, we have outlined the method by expanding the Hadamard parametrix only to the order required to capture the divergences in the coincidence limit. However, the convergence can be accelerated to any order by subtracting mode-sum representations for higher-order terms in the parametrix. This freedom of defining the convergence rate of the mode-sums by

setting an expansion order for the parametrix constitutes one of the main advantages of the extended coordinates method.

Notably, although we have here focused on a four-dimensional spacetime, the extended coordinate method is practically agnostic to the number of dimensions and has been implemented to compute renormalized quantities in spacetimes with a generic number of odd [51] and even [52] dimensions. In addition, this prescription has been later generalized for the computation of the renormalized stress-energy tensor [53].

1.8 Towards a semiclassical toolkit

We have discussed how the extended coordinate method serves as a powerful framework for implementing Hadamard renormalization in practice, as it enables a full mode decomposition of the parametrix. The method is well-suited to numerical calculations, and the convergence rate of the mode-sums can be controlled by increasing the order of the expansion of the parametrix. The main disadvantage of this method, in its present form, is that its applicability is constrained to static, spherically symmetric spacetimes for quantum fields in the Hartle-Hawking state.

Although in Ref. [3], the method was applied on the exterior of a Reissner-Nordström black hole to compute RSET in the Unruh, Boulware, and Hartle-Hawking states, only the Hartle-Hawking state was directly renormalized; the RSET for the other two states were computed by state subtraction (see Eq. (1.86)). Therefore this approach is not viable in spacetimes that do not admit a Hartle-Hawking state, such as extremal black holes, the spacetimes of stars, or other horizonless equilibrium configurations [55].

Moreover, if one is interested in studying the semiclassical effects in black hole interiors, the extended coordinate method in its original development is not applicable. For instance, in the region between the horizons of a spherically symmetric Reissner-Nordström black hole, the spacetime is not static. Therefore, the standard Euclidean continuation used in the construction of the Hartle–Hawking state is not possible, and alternative approaches are therefore required to compute the RSET.

This thesis is part of a broader research program aimed at developing a semiclassical toolkit for computing renormalized quantities, particularly the RSET, in a wide variety of spacetimes and physical settings, with the ultimate goal of computing the semiclassical backreaction in these contexts. In light of this, the work presented in this thesis focuses on overcoming some of the limitations of the original version of the extended coordinate method. Specifically, in the first part of the thesis, we generalize the renormalization prescription to the direct renormalization of quantum scalar fields in the Boulware state and apply it to different scenarios of interest. In

the second part of the thesis, we also provide the first extension of the method to the non-static interior region of spherically symmetric black holes, working directly in Lorentzian spacetime.

We note that the method has also been recently extended to charged quantum scalar fields and applied for computing the renormalized scalar condensate and the RSET in the exterior region of a Reissner-Nordström spacetime [56, 57]. Possible avenues for extending the method to rotating black holes have been discussed in [58, 59].

Chapter 2

Adapting the extended coordinate method to zero-temperature states

The material in this chapter is based on the following article:

1. J. Arrechea, C. Breen, A. Ottewill, L. Pisani, P. Taylor, Renormalized stress-energy tensor for scalar fields in the Boulware state with applications to extremal black holes, *Phys. Rev. D*, 111, 085009 (2025) [1].

2.1 The need for a direct renormalization prescription in the Boulware vacuum state

In this Chapter, we generalize the extended coordinate method to directly compute the renormalized stress-energy tensor for a scalar field in the Boulware state. A natural question then is: if the RSET for a field in the Boulware state can be computed by first renormalizing in the Hartle-Hawking state and employing a state subtraction scheme, then why do we need a direct method for renormalizing in the Boulware state? There are several justifications for a direct renormalization prescription for Boulware. First, when employing the indirect method one needs to compute both the Euclidean modes (to do the renormalization in the Hartle-Hawking state) and the Lorentzian modes (to do the state subtraction scheme). Employing a direct method for Boulware requires only one set of modes and hence is computationally less expensive. Second, there are black hole spacetimes that do not admit a Hartle-Hawking state, for example, the extremal Reissner-Nordström spacetime, and hence one requires a direct method for computing the RSET in such situations. Finally, moving away from black hole spacetimes, if we consider semiclassical effects in the spacetime of a compact star, then the natural vacuum state is the Boulware state (there is, in fact, no other reference state). Hence this Chapter sets the foundation for renormalization in those contexts.

The approach we take is similar to that taken in the extended coordinate method for the Hartle-Hawking state [51–53]. We take an arbitrarily high-order expansion of the Hadamard parametrix which encodes the short-distance behaviour of the two-point function, and we rewrite the terms in this expansion as mode-sums of the same form as the Boulware propagator. While the spirit is the same, the mathematical development is significantly trickier because the frequency spectrum is continuous, rather than the discrete frequency spectrum that one obtains in the Euclidean approach to defining the Hartle-Hawking state. As well as presenting a computational challenge, the continuous frequency spectrum also means that the Fourier transform of the terms in the Hadamard parametrix, which is needed to express these as mode-sums, yields functions of the frequency that are not ordinary functions but rather generalized functions. One of the interesting outcomes of treating these mode-sums rigorously as generalized functions is that it becomes completely transparent how an infra-red cutoff appears in these ω integrals, and indeed it is completely explicit that the RSET is independent of the choice of this cutoff. A similar cutoff was introduced in Ref. [45] but it was introduced in an ad-hoc way and by necessity to render the mode-sums finite at low frequency. While the overall results are ultimately equivalent, it is clear here that the source of the cutoff is a consequence of treating rigorously the generalized functions that arise in the Fourier transform of the Hadamard parametrix.

This Chapter is organized as follows. First, in Sec. 2.2, we present the Green's function representation of the Boulware state in the context of a spherically symmetric black hole, when treated as a zero temperature Euclidean state. In Sec. 2.3, we show how we express the expansion of the Hadamard parametrix as a mode-sum of the same type as the Boulware propagator for a scalar field in a static, spherically symmetric spacetime. In Sec. 2.4, we give the explicit expressions for the renormalized expectation values for the vacuum polarization and the stress-energy tensor for a scalar field in the Boulware state. Finally, we conclude in Sec. 2.5.

2.2 The Boulware vacuum as a zero temperature Euclidean state

The Boulware state is vacuum according to a stationary observer far from the black hole. It is useful to treat the Boulware state as a thermal state at zero temperature outside the event horizon and to employ Euclidean methods. Outside the event horizon, we consider Euclidean line elements of static, spherically symmetric spacetimes

of the form:

$$ds^2 = f(r)d\tau^2 + dr^2/f(r) + r^2(d\theta^2 + \sin^2\theta d\phi^2). \tag{2.1}$$

If this line element describes a black hole spacetime with event horizon $r = r_+$ and surface gravity $\kappa = \frac{1}{2}f'(r_+)$, then the geometry possesses a conical singularity at the horizon unless the Euclidean time is periodic with periodicity $\tau = \tau + 2\pi/\kappa$. If we wished to consider a quantum field in the Hartle-Hawking state, this identification would be the appropriate one. Moreover, imposing a periodicity discretizes the frequency spectrum of the field modes, which is a major computational advantage. For computing the renormalization counter-terms, all that matters is the geometry, and so there is no obligation to make any particular identification on the Euclidean time; nevertheless, the renormalized mode-sum is most conveniently derived and computed when we impose the same periodicity on the mode-sum representation of the renormalization counter-terms as we do on the quantum field in the Hartle-Hawking state. In this Chapter, we are interested in the case where the quantum field is in the Boulware state, which is a zero temperature pure state. We make no periodic identification in Euclidean time which implies that the frequency spectrum of the quantum field (and the mode-sum representation of the renormalization counter-terms) will be continuous and that our geometry retains the conical singularity at the event horizon, at least for non-extremal black holes. Given that one of the main motivations for adopting Euclidean techniques in the Hartle-Hawking case is the computational advantage obtained by the discrete frequency spectrum, one might be tempted to discard the Euclidean approach for computing quantum expectation values in the Boulware state, where the spectrum remains continuous. However, the Euclidean approach is still useful since, unlike the Lorentzian framework, the Euclidean Green function does not require an '$i\,\epsilon$' prescription to define the bi-distribution along the lightcone (see Sec. 1.5 for a detailed discussion). In particular, on a Euclidean geometry, the Klein-Gordon equation for the scalar field is elliptic

$$(\Box^{\mathrm{E}} - \mu^2 - \xi\, R)\Phi = 0. \tag{2.2}$$

The corresponding Euclidean Green's function has the following mode-sum representation (with $r = r'$ for simplicity) on this black hole spacetime,

$$G(x, x') = \frac{1}{8\pi^2}\sum_{l=0}^{\infty}(2l+1)P_l(\cos\gamma)\int_{-\infty}^{\infty} d\omega\, e^{i\omega\Delta\tau} g_{\omega l}(r), \tag{2.3}$$

We have denoted by $g_{\omega l}(r) = p_{\omega l}(r)\, q_{\omega l}(r)/N_{\omega l}$ the one-dimensional radial Green function evaluated at the same radius. The radial modes $p_{\omega l}(r)$, $q_{\omega l}(r)$ are solutions

of the homogeneous equation:

$$\left[\frac{d}{dr}\left(r^2 f(r)\frac{d}{dr}\right) - r^2\left(\frac{\omega^2}{f(r)} + (\mu^2 + \xi R)\right) - l(l+1)\right]\Upsilon_{\omega l}(r) = 0, \tag{2.4}$$

with $p_{\omega l}(r)$ the solution regular at the horizon and $q_{\omega l}(r)$ regular at spatial infinity. The normalization constant is given by

$$N_{\omega l} = -r^2 f(r)\,\mathcal{W}\{p_{\omega l}(r), q_{\omega l}(r)\}, \tag{2.5}$$

where $\mathcal{W}\{p_{\omega l}, q_{\omega l}\}$ is the Wronskian of the two solutions.

2.3 A direct renormalization prescription in the Boulware state

In this section, we will outline the extended coordinate approach to calculating the RSET for a quantum scalar field in the Boulware quantum state [38], propagating on a static, spherically symmetric spacetime. In the coincidence limit $\Delta x \to 0$ (i.e. $\gamma \to 0$ and $\Delta\tau \to 0$), the mode sum in Eq. (2.3) diverges. For a quantum state satisfying the Hadamard condition, the local singularity structure of the two-point function when x and x' are sufficiently close is encapsulated in the Hadamard parametrix of the Euclidean propagator in Eq. (1.73). The fact that the mode-sum in Eq. (2.3) does not converge at coincidence is because the two-point function possesses singularities precisely of the type in Eq. (1.73) in the short-distance limit. The goal is to subtract $K(x, x')$ from $G(x, x')$ in such a way that the coincidence limit can be meaningfully taken. The only way to proceed in this approach is to express $K(x, x')$ as a mode-sum of the same type as the mode-sum representation of Eq. (2.3) and then to subtract mode-by-mode. This renormalized mode-sum will converge in the coincidence limit.

Expressing the Hadamard parametrix as a mode-sum is non-trivial. As outlined in Section 1.7.1, the approach of Refs. [51, 52] is to expand the parametrix in a judiciously chosen set of extended coordinates. In that context, it was assumed the field was in the Hartle-Hawking state and the extended coordinates were adapted to that state by ensuring the time dependence had the appropriate thermal periodicity. This must be amended here for the Boulware state. We define the set of extended coordinates $\{s, \Delta\tau, \Delta r\}$, where

$$s^2 = f(r)\,\Delta\tau^2 + 2r^2(1 - \cos\gamma). \tag{2.6}$$

As for the Hartle-Hawking state, this quantity is defined such that, to leading order,

$\sigma = \frac{1}{2}(s^2 + \frac{\Delta r^2}{f}) + \mathcal{O}(\Delta x^3)$. Note that, differently from Eq. (1.105), the coordinate separation $\Delta\tau$ is left as is, because in the Euclidean Green's function for the Boulware state the Euclidean time is not periodic.

Thus, to solve the defining equations for the biscalars order by order, we treat $\Delta\tau \sim s \sim \Delta r \sim \mathcal{O}(\Delta x)$, and instead of expanding the biscalars in the usual coordinate separations Δx, we expand them in terms of the new set of extended coordinates

$$\sigma(x,x') = \sum_{a,b,c} \sigma_{abc}(r)\Delta\tau^a \Delta r^b s^c, \tag{2.7a}$$

$$\Delta^{1/2}(x,x') = \sum_{a,b,c} u_{abc}(r)\Delta\tau^a \Delta r^b s^c, \tag{2.7b}$$

$$V_p(x,x') = \sum_{a,b,c} v^{(p)}_{abc}(r)\Delta\tau^a \Delta r^b s^c. \tag{2.7c}$$

where $a, b, c \in \mathbb{N}$. Substituting the expansions (2.7) into equations (1.57), (1.59) and (1.64) and solving order by order yields the coefficients $\sigma_{abc}(r)$, $u_{abc}(r)$ and $v^{(p)}_{abc}(r)$. Finally, we expand the Hadamard parametrix to an arbitrary truncation order n, where this means we neglect the terms that vanish in the coincidence limit at least as fast as $\mathcal{O}(\Delta x^{2n}\log\Delta x)$, by appropriately combining the resulting series (2.7) to construct the direct and tail terms in the Hadamard form (1.73). Taking the radial points together ($\Delta r = 0$) for convenience and simplifying, yields an expansion of the form

$$\begin{aligned} K(x,x') = \frac{1}{8\pi^2}\Bigg(&\sum_{a=0}^{n}\sum_{b=0}^{a} \mathcal{D}^{(\mathrm{r})}_{ab}(r)\frac{\Delta\tau^{2a+2b}}{s^{2b+2}} + \sum_{a=1}^{n}\sum_{b=1}^{a} \mathcal{D}^{(\mathrm{p})}_{ab}(r)\Delta\tau^{2a-2b}s^{2b-2} \\ &+ \sum_{a=1}^{n-1}\sum_{b=0}^{a-1} \mathcal{T}^{(\mathrm{r})}_{ab}(r)\frac{\Delta\tau^{2a+2b+2}}{s^{2b+2}} + \sum_{a=0}^{n-1}\sum_{b=0}^{a} \mathcal{T}^{(\mathrm{l})}_{ab}(r)s^{2a-2b}\Delta\tau^{2b}\log\left(\frac{s^2}{\ell^2}\right) \\ &+ \sum_{a=1}^{n-1}\sum_{b=0}^{a} \mathcal{T}^{(\mathrm{p})}_{ab}(r)s^{2a-2b}\Delta\tau^{2b}\Bigg) + \mathcal{O}(\Delta x^{2n}\log\Delta x). \end{aligned} \tag{2.8}$$

The coefficients $\mathcal{D}^{(\mathrm{r})}_{ab}(r)$ and $\mathcal{D}^{(\mathrm{p})}_{ab}(r)$ come from the expansion of the direct part of the parametrix $\Delta^{1/2}/\sigma$ and correspond to the coefficients of terms in the expansion that are rational in $\Delta\tau^2$ and s^2 and those that are polynomial in $\Delta\tau^2$ and s^2, respectively. Similarly, $\mathcal{T}^{(\mathrm{r})}_{ab}(r)$ and $\mathcal{T}^{(\mathrm{p})}_{ab}(r)$ are the coefficients of terms that are rational and polynomial coming from the tail $V\,\log(2\sigma/\ell^2)$ of the parametrix, while $\mathcal{T}^{(\mathrm{l})}_{ab}(r)$ is the coefficient of terms in the tail that contain a logarithm. We refer to these coefficients as the Hadamard coefficients. Expressions for the first few of these coefficients are given in Appendix A.3. These coefficients may also be obtained by taking the limit $\kappa \to 0$ in the corresponding coefficients for the Hartle-Hawking state

reported in expression (A1) of [53].

Formally speaking, this expansion need only be computed up to $n = 1$ in order to remove the divergences from the Green function. Nevertheless, by expanding up to higher order terms, including terms that formally vanish in the coincidence limit, and expressing these terms as a mode-sum permits us to have precise control over the rate of convergence of the renormalized mode sum. On the other hand, if we only subtract the singular terms, the mode sum would indeed converge, however, it would converge very slowly. Furthermore, the distinction between the different types of terms that occur in the expansion is an important one. In particular, the terms that are polynomial in the variables $\Delta\tau^2$ and s^2 do not require a mode-sum representation. For example, a multipole expansion of terms that are polynomial in s^2 would involve finite multipole moments and hence cannot affect the large l behaviour. Similarly, their Fourier-mode decompositions yield terms of the form $\int_{-\infty}^{\infty} d\Delta\tau\ e^{i\omega\Delta\tau}\Delta\tau^{2k} = 2\pi(-1)^k\delta^{(2k)}(\omega)$, which produce derivatives of delta distributions. Therefore, these terms also do not present contributions at large ω. Hence the terms above that are polynomial in the expansion parameters are left as-is. The rational and logarithmic terms will be expressed as mode sums. This is the focus of the next sections.

2.3.1 Regularization Parameters for the Direct Part

Starting with the direct part of the Hadamard parametrix, which involves terms of the form $\Delta\tau^{2a+2b}/s^{2+2b}$ for $a \geq b \geq 0$. We write this term in the following mode-sum representation

$$\frac{\Delta\tau^{2a+2b}}{s^{2+2b}} = \sum_{l=0}^{\infty}(2l+1)P_l(\cos\gamma)\int_{-\infty}^{\infty} d\omega e^{i\omega\Delta\tau}\Psi_{\omega l}(a,b|r), \tag{2.9}$$

where the generalized functions $\Psi_{\omega l}(a,b|r)$ we call the regularization parameters for the direct part. The goal is to invert the above representation and hence obtain an explicit closed-form representation for the regularization parameters. A double integral expression for the regularization parameters follows immediately from the completeness of the Legendre polynomials and the Fourier transform of the delta distribution, yielding

$$\Psi_{\omega l}(a,b|r) = \frac{1}{4\pi}\int_{-1}^{1} d\mathfrak{u}\int_{-\infty}^{\infty} dt\frac{e^{-i\omega t}t^{2a+2b}P_l(\mathfrak{u})}{(f\,t^2+2r^2(1-\mathfrak{u}))^{1+b}}, \tag{2.10}$$

where we have relabeled the integration variables by $\mathfrak{u} = \cos\gamma$ and $t = \Delta\tau$. The integrand has a pole at $\mathfrak{u} = 1$ and $t = 0$ (and/or $f(r) = 0$). However, we highlight that point-splitting was assumed in Eq. (2.9) (and that the renormalization method

is not applied exactly on the horizons).

We note that the double integrals in Eq. (2.10) can be performed in various equivalent ways. The following derivation is the polished result of an accurate analysis, in which the goal was to obtain closed-form representations for the regularization parameters that could be computed numerically in an efficient way. To obtain these closed-form expressions, we considered different procedures, computing either the t or $\mathfrak{u}$ integral first, adopting different integral representations for such integrals and determining a posteriori which approach was the most suitable. For example, some integral representations of the t-integral did not allow us to compute the following $\mathfrak{u}$ integral in closed form, but would instead have required us to compute the $\mathfrak{u}$ integral numerically. This, for instance, would have been extremely inefficient for the subsequent computation of the modes. As a result, we obtained various closed-form expressions for such regularization parameters, which we report in Appendix A.2. In what follows, we report the derivation that allowed us to obtain the representation which we deemed to be the most numerically efficient. A similar procedure has been implemented for the derivation of the mode-sum representation for the logarithmic terms in the tail reported in Sec. 2.3.2.

If we define

$$\rho^2 = \frac{f}{2r^2}, \tag{2.11}$$

then we can rewrite our integral expression above as

$$\Psi_{\omega l}(a,b|r) = \frac{1}{4\pi}\frac{1}{(2r^2)^{b+1}}\int_{-1}^{1} d\mathfrak{u}\, P_l(\mathfrak{u})\frac{(-1)^b}{b!2^b}\left(\frac{1}{\rho}\frac{\partial}{\partial\rho}\right)^b \int_{-\infty}^{\infty} dt \frac{e^{-i\omega t}t^{2a}}{(\rho^2\, t^2+1-\mathfrak{u})}. \tag{2.12}$$

Now it is this t-integral that distinguishes the regularization parameters in the Hartle-Hawking and the Boulware states. In the former, the t-integral above would be over a finite domain on account of the time periodicity of a thermal state. But in this case, the integral is over the entire real line which means that for $a \geq 1$, the integral does not converge in the sense of ordinary functions and must be considered in the sense of generalized functions. The most straightforward way to proceed is to start with the $a = 0$ integral which is an ordinary function and is given by

$$\int_{-\infty}^{\infty} dt \frac{e^{-i\omega t}}{(\rho^2\, t^2+1-\mathfrak{u})} = \pi\, \frac{e^{-|\omega|\sqrt{1-\mathfrak{u}}/\rho}}{\rho\sqrt{1-\mathfrak{u}}}. \tag{2.13}$$

For $a \geq 1$, we can take $(2a)$-derivatives with respect to ω of the result above. Since the exponent on the right-hand side involves $|\omega|$ and not ω, we pick up delta

distributions and their derivatives. The result is

$$\int_{-\infty}^{\infty} dt \frac{e^{-i\omega t} t^{2a}}{(\rho^2 t^2 + 1 - \mathfrak{u})} = \pi (-1)^a e^{-|\omega|\sqrt{1-\mathfrak{u}}/\rho} \frac{(1-\mathfrak{u})^{a-1/2}}{\rho^{2a+1}} - 2\pi(-1)^a \sum_{p=1}^{a} \frac{(1-\mathfrak{u})^{a-p}}{\rho^{2a-2p+2}} \delta^{(2p-2)}(\omega), \tag{2.14}$$

which is clearly not an ordinary function of ω. We note also that in these expressions we always assume $\rho \neq 0$, which is justified if we do not evaluate these expressions at $f(r) = 0$. Substituting this back into Eq. (2.12) gives

$$\Psi_{\omega l}(a, b|r) = \frac{1}{(2r^2)^{b+1}} \frac{(-1)^{a+b}}{b! 2^{b+2}} \left(\frac{1}{\rho}\frac{\partial}{\partial \rho}\right)^b \left\{ \frac{1}{\rho^{2a+1}} \mathcal{A}_{\omega l}(a|\rho) - 2 \sum_{p=1}^{a} \frac{\delta^{(2p-2)}(\omega)}{\rho^{2a-2p+2}} \mathcal{B}_l(a, p) \right\}, \tag{2.15}$$

where

$$\mathcal{A}_{\omega l}(a|\rho) = \int_{-1}^{1} P_l(\mathfrak{u}) e^{-|\omega|\sqrt{1-\mathfrak{u}}/\rho} (1-\mathfrak{u})^{a-1/2} d\mathfrak{u}, \tag{2.16}$$

$$\mathcal{B}_l(a, p) = \int_{-1}^{1} P_l(\mathfrak{u}) (1-\mathfrak{u})^{a-p} d\mathfrak{u}. \tag{2.17}$$

The second integral here is a standard one. The result is that the integral vanishes whenever $l \geq a - p + 1$ and otherwise gives

$$\mathcal{B}_l(a, p) = \frac{(-1)^l 2^{a-p+1} \Gamma(a-p+1)^2}{\Gamma(a-p+l+2)\Gamma(a-p+1-l)}. \tag{2.18}$$

The $\mathcal{A}_{\omega l}(a|\rho)$ integral can also be easily performed and there are several different equivalent representations. The tidiest form involves derivatives of the modified Bessel functions

$$\mathcal{A}_{\omega l}(a|\rho) = 2^{a+3/2} \frac{\partial^{2a}}{\partial z^{2a}} I_{l+1/2}(z) K_{l+1/2}(z), \tag{2.19}$$

where

$$z = \frac{|\omega|}{\sqrt{2}\,\rho} = \frac{|\omega|\, r}{\sqrt{f}}. \tag{2.20}$$

However, this is not the best representation for numerically computing this object. For numerical purposes, except when $z \gg 1$, we find the following representation

much more efficient

$$\mathcal{A}_{\omega l}(a|\rho) = 2^a\sqrt{2\pi}(-1)^l\Bigg\{\Gamma(a+\tfrac{1}{2})^2\,{}_2\hat{F}_3\left(\begin{array}{c}\{a+\frac{1}{2},a+\frac{1}{2}\}\\ \{a+l+\frac{3}{2},a-l+\frac{1}{2},\frac{1}{2}\}\end{array}\middle|\,\frac{\omega^2}{2\rho^2}\right) \\ -\Gamma(a+1)^2\frac{|\omega|}{\sqrt{2}\,\rho}\,{}_2\hat{F}_3\left(\begin{array}{c}\{a+1,a+1\}\\ \{\frac{3}{2},a+l+2,a-l+1\}\end{array}\middle|\,\frac{\omega^2}{2\rho^2}\right)\Bigg\}. \tag{2.21}$$

In the previous expression, ${}_2\hat{F}_3$ is the regularized generalized hypergeometric function defined as

$${}_2\hat{F}_3\left(\begin{array}{c}\{a_1,a_2\}\\ \{b_1,b_2,b_3\}\end{array}\middle|\,z\right) = \frac{{}_2F_3\left(\begin{array}{c}\{a_1,a_2\}\\ \{b_1,b_2,b_3\}\end{array}\middle|\,z\right)}{\Gamma(b_1)\Gamma(b_2)\Gamma(b_3)}, \tag{2.22}$$

where ${}_2F_3$ is the generalized hypergeometric function [60]. Now using the fact that,

$$\left(\frac{1}{\rho}\frac{\partial}{\partial\rho}\right)^b\rho^{-c} = (-1)^b 2^b\frac{\Gamma(c/2+b)}{\Gamma(c/2)}\rho^{-c-2b}, \tag{2.23}$$

we can easily express the derivatives in terms of hypergeometric functions. Putting all of the above together, and after some simplification, we obtain the following expression for the regularization parameters

$$\Psi_{\omega l}(a,b|r) = \mathcal{I}_{\omega l}(a,b|r) \\ -\frac{(2r^2)^a}{f^{a+b+1}}\frac{(-1)^{a+l}}{b!}\sum_{p=1}^{a}\frac{2^{a-p}(a-p)!(a-p+b)!}{(a-p+l+1)!(a-p-l)!}\left(\frac{f}{2r^2}\right)^p\delta^{(2p-2)}(\omega), \tag{2.24}$$

where, for later convenience, we have defined

$$\mathcal{I}_{\omega l}(a,b|r) = \frac{(2r^2)^{a-1/2}}{f^{a+b+1/2}}\frac{2^{a-2}\sqrt{2\pi}(-1)^{a+l}}{\Gamma(b+1)} \\ \times\Bigg\{\Gamma(a+\tfrac{1}{2})\Gamma(a+b+\tfrac{1}{2})\,{}_2\hat{F}_3\left(\begin{array}{c}\{a+\frac{1}{2},a+b+\frac{1}{2}\}\\ \{a+l+\frac{3}{2},a-l+\frac{1}{2},\frac{1}{2}\}\end{array}\middle|\,\frac{\omega^2r^2}{f}\right) \\ -\Gamma(a+1)\Gamma(a+b+1)\frac{|\omega|r}{\sqrt{f}}\,{}_2\hat{F}_3\left(\begin{array}{c}\{a+1,a+b+1\}\\ \{\frac{3}{2},a+l+2,a-l+1\}\end{array}\middle|\,\frac{\omega^2r^2}{f}\right)\Bigg\}. \tag{2.25}$$

Substituting this back into Eq. (2.9) and performing the ω integration in the terms

involving delta distributions gives

$$\frac{\Delta\tau^{2a+2b}}{s^{2+2b}} = \sum_{l=0}^{\infty}(2l+1)P_l(\cos\gamma)\int_{-\infty}^{\infty}d\omega\, e^{i\omega\Delta\tau}\mathcal{I}_{\omega l}(a,b|r) + \frac{1}{f^{b+1}}\sum_{p=1}^{a}\frac{(a-p+b)!}{b!(a-p)!}\left(\frac{2r^2}{f}\right)^{a-p}\Delta\tau^{2p-2}(\cos\gamma-1)^{a-p}. \tag{2.26}$$

In arriving at the last line of this expression, we made use of the identity

$$\sum_{l=0}^{k}\frac{(-1)^l(2l+1)P_l(\cos\gamma)}{(k+l+1)!(k-l)!} = \frac{(1-\cos\gamma)^k}{2^k(k!)^2}, \tag{2.27}$$

which can be proved by induction. In the coincidence limit, the last line of Eq. (2.26) is nonzero only when $p = a = 1$.

2.3.2 Regularization Parameters for the Logarithmic Terms in the Tail

In this subsection, we derive a mode-sum representation for the terms in the tail part of the Hadamard parametrix which in the partial coincidence limit $\Delta r = 0$ involves terms of the form $\Delta\tau^{2b}s^{2a-2b}\log(s^2/\ell^2)$. For later convenience, we will write the logarithmic terms as

$$\Delta\tau^{2b}s^{2a-2b}\log(s^2/\ell^2) = \Delta\tau^{2b}s^{2a-2b}\log(\rho^2\Delta\tau^2+1-\mathfrak{u}) + \Delta\tau^{2b}s^{2a-2b}\log(2r^2/\ell^2). \tag{2.28}$$

The second term here is polynomial in $\Delta\tau^2$ and s^2 and requires no mode-sum representation. This term contains the arbitrary lengthscale ℓ which encodes part of the renormalization ambiguity (see, for example, Refs. [14, 25, 61]). For the first term above, we assume the mode-sum representation

$$\Delta\tau^{2b}s^{2a-2b}\log(\rho^2\Delta\tau^2+1-\cos\gamma) = \sum_{l=0}^{\infty}(2l+1)P_l(\cos\gamma)\int_{-\infty}^{\infty}d\omega\, e^{i\omega\,\Delta\tau}\,\chi_{\omega l}(a,b\,|r) \tag{2.29}$$

and as before, we can invert to obtain a formal double integral expression for the regularization parameters

$$\chi_{\omega l}(a,b|r) = \frac{(2r^2)^{a-b}}{4\pi}\int_{-1}^{1}d\mathfrak{u}P_l(\mathfrak{u})\lim_{\bar\alpha\to a}\frac{\partial}{\partial\bar\alpha}\int_{-\infty}^{\infty}e^{-i\omega t}t^{2b}(\rho^2t^2+1-\mathfrak{u})^{\bar\alpha-b}dt, \tag{2.30}$$

where we have expressed the log terms as the limit of a derivative with respect to an exponent $\bar{\alpha}$, not to be confused with a spacetime index α, and where t and $\mathfrak{u}$ are defined as before. The time integral above is a complicated generalized function but we can express it in terms of the derivative of a simpler integral as

$$\begin{aligned}\chi_{\omega l}(a,b\,|r) =&\frac{(2r^2)^{a-b}}{4\pi}\frac{1}{2^b}\left(\frac{1}{\rho}\frac{\partial}{\partial\rho}\right)^b\int_{-1}^{1}d\mathfrak{u}P_l(\mathfrak{u})\\ &\times\lim_{\bar{\alpha}\to a}\frac{\partial}{\partial\bar{\alpha}}\frac{\Gamma(\bar{\alpha}-b+1)}{\Gamma(\bar{\alpha}+1)}\int_{-\infty}^{\infty}e^{-i\omega t}(\rho^2t^2+1-\mathfrak{u})^{\bar{\alpha}}dt.\end{aligned}\tag{2.31}$$

The advantage of this form is that the time integral can now be performed explicitly yielding,

$$\chi_{\omega l}(a,b\,|r)=\frac{(2r^2)^{a-b}}{\sqrt{2\pi}}\frac{1}{2^b}\left(\frac{1}{\rho}\frac{\partial}{\partial\rho}\right)^b\int_{-1}^{1}d\mathfrak{u}P_l(\mathfrak{u})\mathcal{F}_{\omega l}(a,b\,|\mathfrak{u},r)\tag{2.32}$$

where

$$\begin{aligned}&\mathcal{F}_{\omega l}(a,b\,|\mathfrak{u},r)=\\ &\quad\lim_{\bar{\alpha}\to a}\frac{\partial}{\partial\bar{\alpha}}\left\{\frac{2^{\bar{\alpha}}\rho^{\bar{\alpha}-1/2}\Gamma(\bar{\alpha}-b+1)}{|\omega|^{\bar{\alpha}+1/2}\Gamma(-\bar{\alpha})\Gamma(\bar{\alpha}+1)}(1-\mathfrak{u})^{\bar{\alpha}/2+1/4}K_{\bar{\alpha}+1/2}\left(\frac{|\omega|\sqrt{1-\mathfrak{u}}}{\rho}\right)\right\},\end{aligned}\tag{2.33}$$

and $K_{\bar{\alpha}+1/2}(z)$ is the modified Bessel function of the second kind. From the series representation of the Bessel function, we obtain

$$\begin{aligned}&\mathcal{F}_{\omega l}(a,b\,|\mathfrak{u},r)=\\ &\quad\frac{\pi}{\sqrt{2}}\lim_{\bar{\alpha}\to a}\frac{\partial}{\partial\bar{\alpha}}\left\{\frac{\Gamma(\bar{\alpha}-b+1)}{\Gamma(\bar{\alpha}+1)}\frac{\sec\pi\bar{\alpha}\,(2\rho)^{2\bar{\alpha}}}{\Gamma(-\bar{\alpha})|\omega|^{2\bar{\alpha}+1}}\sum_{k=0}^{\infty}\frac{1}{k!\Gamma(-\bar{\alpha}+k+\frac{1}{2})}\frac{\omega^{2k}(1-\mathfrak{u})^k}{(2\rho)^{2k}}\right.\\ &\quad\left.-\frac{\Gamma(\bar{\alpha}-b+1)}{\Gamma(\bar{\alpha}+1)}\frac{\sec\pi\bar{\alpha}\,(1-\mathfrak{u})^{\bar{\alpha}+1/2}}{\Gamma(-\bar{\alpha})2\rho}\sum_{k=0}^{\infty}\frac{1}{k!\Gamma(\bar{\alpha}+k+\frac{3}{2})}\frac{\omega^{2k}(1-\mathfrak{u})^k}{(2\rho)^{2k}}\right\}.\end{aligned}\tag{2.34}$$

The second term here is straightforward to deal with in the limit as $\bar{\alpha}\to a$. In particular, it is evidently an entire function of $\bar{\alpha}$. In fact, if we consider the Taylor series for $1/\Gamma(-\bar{\alpha})$ about a positive integer a, we have

$$\frac{1}{\Gamma(-\bar{\alpha})}=(-1)^{a+1}a!(\bar{\alpha}-a)+(-1)^{a+1}a!\psi(a+1)(\bar{\alpha}-a)^2+\mathcal{O}(\bar{\alpha}-a)^3,\tag{2.35}$$

where $\psi(z)=\Gamma'(z)/\Gamma(z)$ is the polygamma function, and so it is clear that the only term in the last line of Eq. (2.34) that survives the limit $\bar{\alpha}\to a$ is when the $\bar{\alpha}$-derivative acts on $1/\Gamma(-\bar{\alpha})$.

The first term in Eq. (2.34) is more subtle owing to the presence of the $|\omega|^{-2\bar{\alpha}-1}$ term. Clearly this is not an ordinary function since it is singular at $\omega=0$. It is a

generalized function whose definition involves a regularization at $\omega = 0$ (not to be confused with the renormalization prescription required to regularize the coincidence limit of the point-split two-point function). One way to treat this is to simply introduce an infra-red cutoff in the ω-integral in Eq. (2.28), but this is not the rigorous approach. We will see that, if we treat $|\omega|^{-2\bar{\alpha}-1}$ rigorously as a generalized function, a cutoff will emerge naturally and indeed it will be clear that the overall result will be independent of this choice. The salient point is that, as a function of the exponent $\bar{\alpha}$, the definition (which involves its regularization as a distribution) of $|\omega|^{-2\bar{\alpha}-1}$ has a simple pole at integer values of $\bar{\alpha}$. However, this pole is canceled by the zero in $1/\Gamma(-\bar{\alpha})$ at integer values (see Eq. (2.35)) so that the combination $1/(\Gamma(-\bar{\alpha})|\omega|^{2\bar{\alpha}+1})$ is actually an entire function. We require an expansion of this combination about the integer $\bar{\alpha} = a$ up to order $(\bar{\alpha} - a)^2$ if we are to compute the limit appearing in Eq. (2.34). We already have a series for $1/\Gamma(-\bar{\alpha})$. Next, we note the Laurent series for $|\omega|^{-2\bar{\alpha}-1}$ which can be found in Ref. [62],

$$|\omega|^{-2\bar{\alpha}-1} = -\frac{\delta^{(2a)}(\omega)}{(2a)!(\bar{\alpha}-a)} + |\omega|^{-2a-1} + \frac{\delta^{(2a)}(\omega)}{(2a)!}2\log\lambda + \mathcal{O}(\bar{\alpha}-a), \tag{2.36}$$

where the λ appearing here is an arbitrary inverse lengthscale required because ω has dimensions of inverse length. This inverse lengthscale will be shown later to be related to an infra-red cutoff in certain integrals over the frequency. The corresponding result for Eq. (2.36) in Ref. [62] is actually for a dimensionless generalized function and so doesn't contain the additional $\log\lambda$ term, but applying the result from [62] to $\hat{\omega} = \omega/\lambda$ gives Eq. (2.36). It is essential to understand that $|\omega|^{-2a-1}$ appearing on the right-hand side is to be understood in terms of its regularization as a generalized function. For example, for $\varphi(\omega)$ a test function of compact support, we have

$$\begin{aligned}(|\omega|^{-2a-1}, \varphi(\omega)) = \int_0^\infty d\omega\, \omega^{-2a-1}\Big[&\varphi(\omega) + \varphi(-\omega) \\ &- 2\sum_{m=0}^{a-1}\frac{\varphi^{(2m)}(0)}{(2m)!}\omega^{2m} - 2\frac{\varphi^{(2a)}(0)}{(2a)!}\omega^{2a}\theta(\lambda-\omega)\Big],\end{aligned} \tag{2.37}$$

where $\theta(z)$ is the step function. The last term in the regularization requires this step function since otherwise the integral would not converge at infinity.

Now combining Eqs. (2.35) and (2.36) gives us the desired expansion

$$\begin{aligned}\frac{1}{\Gamma(-\bar{\alpha})|\omega|^{2\bar{\alpha}+1}} =& \frac{(-1)^a a!}{(2a)!}\delta^{(2a)}(\omega) \\ &+ (\bar{\alpha}-a)(-1)^a a!\Big[\frac{(\psi(a+1)-2\log\lambda)}{(2a)!}\delta^{(2a)}(\omega) - \frac{1}{|\omega|^{2a+1}}\Big] \\ &+ \mathcal{O}(\bar{\alpha}-a)^2. \end{aligned} \tag{2.38}$$

Employing these limits in Eq. (2.34) gives, after some tedious simplifications,

$$\begin{aligned}\mathcal{F}_{\omega l}(a,b\,|\mathfrak{u},r) = \frac{\pi}{\sqrt{2}}(a-b)!\Bigg\{&((\psi(a-b+1)+\psi(\tfrac{1}{2}-a+k)+2\ln(2\rho/\lambda)) \\ &\times\sum_{k=0}^{a}\frac{\delta^{(2a-2k)}(\omega)(1-\mathfrak{u})^k(2\rho)^{2a-2k}}{k!(2a-2k)!\Gamma(k-a+\frac{1}{2})} \\ -\sum_{k=0}^{\infty}\frac{|\omega|^{2k-2a-1}(1-\mathfrak{u})^k(2\rho)^{2a-2k}}{k!\Gamma(k-a+\frac{1}{2})} &+\sum_{k=0}^{\infty}\frac{\omega^{2k}(1-\mathfrak{u})^{k+a+1/2}}{k!\Gamma(k+a+\frac{3}{2})(2\rho)^{2k+1}}\Bigg\}, \end{aligned} \tag{2.39}$$

where we also made use of the distributional identity

$$\omega^{2k}\delta^{(2a)}(\omega) = \begin{cases}\frac{(2a)!}{(2a-2k)!}\delta^{(2a-2k)}(\omega) & k\le a \\ 0 & k>a\end{cases} \tag{2.40}$$

to truncate the infinite sums involving delta distributions. Substituting this expression back into Eq. (2.32) and performing the integration yields

$$\begin{aligned}\chi_{\omega l}(a,b\,|r) = \sqrt{\pi}(2r^2)^{a-b}(a-b)!\frac{(-1)^l}{2^b}\left(\frac{1}{\rho}\frac{\partial}{\partial\rho}\right)^b \\ \times\Bigg\{\sum_{k=0}^{\infty}\frac{\Gamma(k+a+\frac{3}{2})2^{k+a+3/2}\omega^{2k}}{k!\,\Gamma(k+a+l+\frac{5}{2})\,\Gamma(k+a-l+\frac{3}{2})(2\rho)^{2k+1}} \\ -\sum_{k=0}^{\infty}\frac{k!2^k(2\rho)^{2a-2k}|\omega|^{2k-2a-1}}{(k+l+1)!(k-l)!\Gamma(k-a+\frac{1}{2})} \\ +[\psi(a-b+1)+\psi(k-a+\tfrac{1}{2})+2\log(2\rho/\lambda)] \\ \times\sum_{k=0}^{a}\frac{k!2^k(2\rho)^{2a-2k}\delta^{(2a-2k)}(\omega)}{(2a-2k)!(k+l+1)!(k-l)!\Gamma(k-a+\frac{1}{2})}\Bigg\}. \end{aligned} \tag{2.41}$$

The second term is a generalized function of ω whenever $k \le a$ and an ordinary function otherwise. In the former case, it is understood in the sense of Eq. (2.37). It would be better if we could express the definition in Eq. (2.37) in a way that is independent of the test function. It can be shown that the regularization in

Eq. (2.37) is equivalent to defining the generalized function as

$$\frac{1}{|\omega|^{2j+1}} = \frac{\theta(\omega^2-\lambda^2)}{|\omega|^{2j+1}} + 2\sum_{k\neq j}^{\infty} \frac{\lambda^{2k-2j}\delta^{(2k)}(\omega)}{(2k)!(2k-2j)}, \qquad j>0\in\mathbb{Z} \tag{2.42}$$

where $\lambda > 0$ is the arbitrary cut-off. This can be straightforwardly proven by splitting the integral in Eq. (2.37) into intervals $(0,\lambda)$ and (λ,∞), and then employing a Taylor series about $\omega = 0$ for the test function on the interval $(0,\lambda)$ (we report the derivation of Eq. (2.42) in Appendix A.5). Employing definition (2.42) in the second term of Eq. (2.41) for $k \leq a$ gives

$$\begin{aligned}
\chi_{\omega l}(a,b\,|r) = {}& \sqrt{\pi}(2r^2)^{a-b}(a-b)!\frac{(-1)^l}{2^b}\left(\frac{1}{\rho}\frac{\partial}{\partial\rho}\right)^b \\
&\times\Bigg\{\sum_{k=0}^{\infty}\frac{\Gamma(k+a+\frac{3}{2})2^{k+a+3/2}\omega^{2k}}{k!\,\Gamma(k+a+l+\frac{5}{2})\,\Gamma(k+a-l+\frac{3}{2})(2\rho)^{2k+1}} \\
&-\theta(\omega^2-\lambda^2)\sum_{k=0}^{a}\frac{k!2^k(2\rho)^{2a-2k}|\omega|^{2k-2a-1}}{(k+l+1)!(k-l)!\Gamma(k-a+\frac{1}{2})} \\
&-\sum_{k=0}^{\infty}\frac{(k+a+1)!2^{k+a+1}|\omega|^{2k+1}}{(k+a+l+2)!(k+a+1-l)!\Gamma(k+\frac{3}{2})(2\rho)^{2k+2}} \\
&-2\sum_{k=0}^{a}\frac{k!2^k(2\rho)^{2a-2k}}{(k+l+1)!(k-l)!\Gamma(k-a+\frac{1}{2})}\sum_{p\neq a-k}^{\infty}\frac{\lambda^{2p+2k-2a}\delta^{(2p)}(\omega)}{(2p)!(2p+2k-2a)} \\
&+[\psi(a-b+1)+\psi(k-a+\tfrac{1}{2})+2\log(2\rho/\lambda)] \\
&\times\sum_{k=0}^{a}\frac{k!2^k(2\rho)^{2a-2k}\delta^{(2a-2k)}(\omega)}{(2a-2k)!(k+l+1)!(k-l)!\Gamma(k-a+\frac{1}{2})}\Bigg\}.
\end{aligned} \tag{2.43}$$

Finally computing the derivatives and simplifying gives

$$\begin{aligned}
\chi_{\omega l}(a,b\,|r) = {}& \mathcal{J}_{\omega l}(a,b\,|r) + \sqrt{\pi}(2r^2\rho^2)^{a-b}(a-b)!\,2^{2a}(-1)^l \\
&\times\Bigg\{\sum_{k=0}^{a}\frac{k!(a-k)!\delta^{(2a-2k)}(\omega)}{(a-k-b)!(2a-2k)!\Gamma(k-a+\frac{1}{2})(k+l+1)!(k-l)!(2\rho^2)^k} \\
&\times\left[\psi(a-b+1)-\psi(a-b-k+1)+\psi(a-k+1)+\psi(k-a+\tfrac{1}{2})+2\log(\tfrac{2\rho}{\lambda})\right] \\
&-2\sum_{k=0}^{a}\frac{(a-k)!k!}{(a-k-b)!\Gamma(k-a+\frac{1}{2})(k+l+1)!(k-l)!(2\rho^2)^k} \\
&\times\sum_{\substack{p=0\\p\neq a-k}}^{\infty}\frac{\delta^{(2p)}(\omega)\lambda^{2p-2a+2k}}{(2p)!(2p-2a+2k)}\Bigg\},
\end{aligned} \tag{2.44}$$

where

$$\begin{aligned}\mathcal{J}_{\omega l}(a,b\,|r) &= \sqrt{\pi}(2r^2\rho^2)^{a-b}(a-b)!2^{2a}(-1)^l \\ &\times\Bigg\{-\sum_{k=0}^{a-b}\frac{\theta\left(\omega^2-\lambda^2\right)(a-k)!k!|\omega|^{2k-2a-1}}{(a-k-b)!\Gamma(k-a+\frac{1}{2})(k+l+1)!(k-l)!(2\rho^2)^k} \\ &-\frac{(-1)^b}{(2\rho^2)^{a+1}}|\omega|(a+1)!b!\,{}_2\hat{F}_3\left(\begin{array}{c|c}\{a+2,b+1\} & \\ \{\frac{3}{2},a-l+2,a+l+3\} & \frac{\omega^2}{2\rho^2}\end{array}\right) \\ &+\frac{(-1)^b}{2^{a+1/2}\rho^{2a+1}}\Gamma(a+\tfrac{3}{2})\Gamma(b+\tfrac{1}{2})\,{}_2\hat{F}_3\left(\begin{array}{c|c}\{a+\frac{3}{2},b+\frac{1}{2}\} & \\ \{\frac{1}{2},a-l+\frac{3}{2},a+l+\frac{5}{2}\} & \frac{\omega^2}{2\rho^2}\end{array}\right)\Bigg\}.\end{aligned} \tag{2.45}$$

Putting this together gives

$$\begin{aligned}&\Delta\tau^{2b}s^{2a-2b}\log(\rho^2\Delta\tau^2+1-\cos\gamma) = \int_{-\infty}^{\infty}d\omega\,e^{i\omega\Delta\tau}\sum_{l=0}^{\infty}(2l+1)P_l(\cos\gamma)\chi_{\omega l}(a,b|r) \\ &=\int_{-\infty}^{\infty}d\omega\,e^{i\omega\Delta\tau}\sum_{l=0}^{\infty}(2l+1)P_l(\cos\gamma)\mathcal{J}_{\omega l}(a,b\,|r) \\ &+\sqrt{\pi}(2r^2\rho^2)^{a-b}(a-b)!2^{2a}\Bigg\{\sum_{k=0}^{a-b}\frac{(-1)^{a-k}(a-k)!\Delta\tau^{2a-2k}(1-\cos\gamma)^k}{2^k k!(a-k-b)!(2a-2k)!\Gamma(k-a+\frac{1}{2})(2\rho^2)^k} \\ &\times\Big[\psi(a-b+1)-\psi(a-b-k+1)+\psi(a-k+1)+\psi(k-a+\tfrac{1}{2})+2\log(2\rho/\lambda)\Big] \\ &-\sum_{k=1}^{b}\frac{(-1)^b(b-k)!(k-1)!\Delta\tau^{2b-2k}(1-\cos\gamma)^{k+a-b}}{2^{k+a-b}(k+a-b)!(2b-2k)!\Gamma(k-b+\frac{1}{2})(2\rho^2)^{k+a-b}} \\ &-2\sum_{k=0}^{a-b}\frac{(a-k)!(1-\cos\gamma)^k}{2^k k!(a-k-b)!\Gamma(k-a+\frac{1}{2})(2\rho^2)^k}\sum_{\substack{p=0\\p\neq a-k}}^{n-k}\frac{(-1)^p\Delta\tau^{2p}\lambda^{2p-2a+2k}}{(2p)!(2p-2a+2k)}\Bigg\}.\end{aligned} \tag{2.46}$$

Even though the sum over p in equation (2.46) is technically up to ∞, we actually only need terms up to order Δx^{2n} in the Hadamard parametrix. In that expression, the order of the expansion is given by $(1-\cos\gamma)^k\Delta\tau^{2p}$ and is Δx^{2k+2p}. Hence, we have truncated the sum at $p=n-k$. In arriving at the expression above, we have also made use of the identity (2.27).

2.3.3 Mode-sum expression for the parametrix

We now have mode-sum representations of all the relevant terms in Eq. (2.8) yielding the following mode-sum representation of the Hadamard parametrix

$$
\begin{aligned}
K(x,x') = {} & \frac{1}{8\pi^2}\int_{-\infty}^{\infty} d\omega\, e^{i\omega\Delta\tau}\sum_{l=0}^{\infty}(2l+1)P_l(\cos\gamma)k^{(n)}_{\omega l}(r) \\
& + \frac{1}{8\pi^2}\Bigg\{\sum_{a=1}^{n}\sum_{b=1}^{a}\mathcal{D}^{(\mathrm{p})}_{ab}(r)\Delta\tau^{2a-2b}s^{2b-2} + \sum_{a=1}^{n-1}\sum_{b=0}^{a}\mathcal{T}^{(\mathrm{p})}_{ab}(r)\Delta\tau^{2b}s^{2a-2b} \\
& + \sum_{a=0}^{n-1}\sum_{b=0}^{a}\mathcal{T}^{(\mathrm{l})}_{ab}(r)\Delta\tau^{2b}s^{2a-2b}\log(4f/(\ell^2\lambda^2)) \\
& + \sum_{a=1}^{n}\sum_{b=0}^{a}\frac{\mathcal{D}^{(\mathrm{r})}_{ab}(r)\,(2r^2)^{-b-1}}{b!\,(\rho^2)^{a+b+1}}\sum_{p=1}^{a}\frac{(-1)^{a+p}(a-p+b)!\rho^{2p}}{(a-p)!}\Delta\tau^{2p-2}(1-\cos\gamma)^{a-p} \\
& + \sum_{a=1}^{n-1}\sum_{b=0}^{a-1}\frac{\mathcal{T}^{(\mathrm{r})}_{ab}(r)\,(2r^2)^{-b-1}}{b!\,(\rho^2)^{a+b+2}}\sum_{p=1}^{a+1}\frac{(-1)^{a+1+p}(a+1-p+b)!\rho^{2p}}{(a+1-p)!}\Delta\tau^{2p-2}(1-\cos\gamma)^{a+1-p} \\
& + \sum_{a=0}^{n-1}\sum_{b=0}^{a}\mathcal{T}^{(\mathrm{l})}_{ab}(r)\sqrt{\pi}(2r^2\rho^2)^{a-b}(a-b)!2^{2a} \\
& \times\Bigg[\sum_{k=0}^{a-b}\frac{(-1)^{a-k}(a-k)!\Delta\tau^{2a-2k}(1-\cos\gamma)^k}{2^k k!(a-k-b)!(2a-2k)!\Gamma(k-a+\frac{1}{2})(2\rho^2)^k}\Big[\psi(a-b+1) \\
& - \psi(a-b-k+1)+\psi(a-k+1)+\psi(k-a+\tfrac{1}{2})\Big] \\
& - \sum_{k=1}^{b}\frac{(-1)^b(b-k)!(k-1)!\Delta\tau^{2b-2k}(1-\cos\gamma)^{k+a-b}}{2^{k+a-b}(k+a-b)!(2b-2k)!\Gamma(k-b+\frac{1}{2})(2\rho^2)^{k+a-b}} \\
& - 2\sum_{k=0}^{a-b}\frac{(a-k)!(1-\cos\gamma)^k}{2^k k!(a-k-b)!\Gamma(k-a+\frac{1}{2})(2\rho^2)^k}\sum_{\substack{p=0\\p\neq a-k}}^{n-k}\frac{(-1)^p\Delta\tau^{2p}\lambda^{2p-2a+2k}}{(2p)!(2p-2a+2k)}\Bigg]\Bigg\} \\
& + \mathcal{O}(\Delta x^{2n}\log\Delta x),
\end{aligned}
\tag{2.47}
$$

where we have defined for compactness

$$
\begin{aligned}
k^{(n)}_{\omega l}(r) = {} & \sum_{a=0}^{n}\sum_{b=0}^{a}\mathcal{D}^{(\mathrm{r})}_{ab}(r)\mathcal{I}_{\omega l}(a,b|r) + \sum_{a=1}^{n-1}\sum_{b=0}^{a-1}\mathcal{T}^{(\mathrm{r})}_{ab}(r)\mathcal{I}_{\omega l}(a+1,b|r) \\
& + \sum_{a=0}^{n-1}\sum_{b=0}^{a}\mathcal{T}^{(\mathrm{l})}_{ab}(r)\mathcal{J}_{\omega l}(a,b\,|r).
\end{aligned}
\tag{2.48}
$$

While the expression (2.47) looks very complicated, we note that many of the terms vanish in the coincidence limit.

2.4 Vacuum polarization and components of the RSET

When computing vacuum polarization, the coincidence limit removes almost all of the finite terms in the Hadamard parametrix above. We obtain

$$\begin{aligned}\langle\hat{\Phi}^2\rangle_{\rm ren} = \frac{1}{8\pi^2}\Bigg\{ &\int_{-\infty}^{\infty}\sum_{l=0}^{\infty}(2l+1)\left(g_{\omega l}(r) - k^{(n)}_{\omega l}(r)\right)d\omega \\ &- \sqrt{\pi}\sum_{a=1}^{n-1}\sum_{b=0}^{a}\mathcal{T}^{(\rm l)}_{ab}(r)\,\frac{(a-1)!2^{2a}f^{a-b}}{\Gamma(-a+\frac{1}{2})\lambda^{2a}}\Bigg\} \\ &- \frac{1}{8\pi^2}\left[\mathcal{D}^{(\rm p)}_{11}(r) + \frac{\mathcal{D}^{(\rm r)}_{10}(r)}{f} + \frac{\mathcal{D}^{(\rm r)}_{11}(r)}{f^2} + \mathcal{T}^{(\rm l)}_{00}(r)(\log(f/(\ell^2\lambda^2)) - 2\gamma_{\rm E})\right], \quad (2.49)\end{aligned}$$

where $\gamma_{\rm E}$ is Euler's constant. The mode-sum terms above can be made to converge as fast as we like by choosing n appropriately large. It can be shown that the renormalized vacuum polarization is completely independent on the choice of the cutoff (we report the calculations in appendix A.1 for clarity). This property can also be proven for the regularization terms for the stress energy tensor. For a massless scalar field, and either conformally-coupled or in spacetimes where the Ricci scalar vanishes[1], the ℓ-dependent term vanishes since $\mathcal{T}^{(\rm l)}_{00} = 0$. Hence, the renormalized vacuum polarization is uniquely determined, as the renormalization ambiguity vanishes in the expression.

The components of the RSET may be written in the form [53]:

$$\langle\hat{T}^{\alpha}{}_{\beta}\rangle_{\rm ren} = -\mathsf{w}^{\alpha}{}_{\beta} - (\xi-\tfrac{1}{2})\mathsf{w}^{;\alpha}{}_{;\beta} + (\xi-\tfrac{1}{4})\Box\mathsf{w}\,\delta^{\alpha}{}_{\beta} + \xi R^{\alpha}{}_{\beta}\mathsf{w} - \frac{1}{8\pi^2}v_1\delta^{\alpha}{}_{\beta}. \quad (2.50)$$

where v_1 is defined as in Eq. (1.70d) and

$$\begin{aligned}&\mathsf{w}(r) = \langle\hat{\Phi}^2\rangle_{\rm ren}, \\ &\mathsf{w}_{\alpha\beta}(x) \equiv \lim_{x\to x'}\left[W(x,x')_{;\alpha\beta}\right], \\ &W(x,x') = G(x,x') - K(x,x'). \end{aligned} \quad (2.51)$$

Due to the symmetry of the background spacetime w is a function of r only, therefore once it has been calculated numerically to high accuracy on a suitably dense grid, the derivatives of w appearing in Eq. (2.50) are now easily and accurately obtained by differentiating an interpolation function for w. Considering the

[1] Note that from App. A.3, $\mathcal{T}^{(\rm l)}_{00} = \frac{6\mu^2r^2-(6\xi-1)\left(r^2f''+4rf'+2f-2\right)}{12r^2}$, and the Ricci scalar for a spacetime with metric (2.1) is $R = -\frac{\left(r^2f''+4rf'+2f-2\right)}{r^2}$.

components of $\mathsf{w}^{\alpha}{}_{\beta}$, we have, by virtue of the wave equation satisified by $W(x,x')$, that [23]:

$$\mathsf{w}^{r}{}_{r} = -\mathsf{w}^{\tau}{}_{\tau} - \mathsf{w}^{\theta}{}_{\theta} - \mathsf{w}^{\phi}{}_{\phi} + \xi R\mathsf{w} + \mu^2\mathsf{w} - \frac{3}{4\pi^2}v_1. \tag{2.52}$$

For the remaining non-zero components, $\mathsf{w}^{\tau}{}_{\tau}$ and $\mathsf{w}^{\theta}{}_{\theta} = \mathsf{w}^{\phi}{}_{\phi}$, it is advantageous to express these in terms of mixed derivatives at x and x' of $W(x,x')$, since this avoids introducing additional connection terms associated with covariant derivatives, and derivatives of $\mathsf{w}(r) = \langle\hat{\Phi}^2\rangle_{\rm ren}$, using Synge's Rule [53]:

$$\mathsf{w}_{\alpha\beta}(x) = \tfrac{1}{2}\mathsf{w}_{;\alpha\beta}(x) - \lim_{x\to x'}\left[W(x,x')_{;\alpha'\beta}\right]. \tag{2.53}$$

The required mixed time derivatives and mixed angular derivatives may be obtained by taking appropriate derivatives of Eq. (2.8). Therefore, the RSET is determined by the calculation of three mode sums Eq. (2.49) along with the following two mode sums:

$$\begin{aligned}
[g^{\tau\tau'}W_{,\tau\tau'}] =& \frac{1}{8\pi^2 f}\Bigg\{\int_{-\infty}^{\infty}\sum_{l=0}^{\infty}(2l+1)\omega^2\left(g_{\omega l} - k^{(n)}_{\omega l}\right)d\omega \\
&- \sqrt{\pi}\sum_{\substack{a=0\\a\neq 1}}^{n-1}\sum_{b=0}^{a}\mathcal{T}^{(\rm l)}_{ab}(r)\,\frac{a!2^{2a}f^{a-b}}{\Gamma(\frac{1}{2}-a)(a-1)\lambda^{2a-2}}\Bigg\} \\
&+ \frac{1}{4\pi^2}\Bigg[\mathcal{T}^{(\rm p)}_{10} + \mathcal{D}^{(\rm p)}_{22} + \frac{1}{f}(\mathcal{T}^{(\rm p)}_{11} + \mathcal{D}^{(\rm p)}_{21}) + \frac{\mathcal{D}^{(\rm r)}_{20}}{f^2} + \frac{\mathcal{D}^{(\rm r)}_{21}}{f^3} + \frac{\mathcal{D}^{(\rm r)}_{22}}{f^4} + \frac{\mathcal{T}^{(\rm r)}_{10}}{f^2} \\
&+ (\mathcal{T}^{(\rm l)}_{10} + \frac{\mathcal{T}^{(\rm l)}_{11}}{f})(\log(f/(\ell^2\lambda^2)) - 2\gamma_{\rm E} + 3)\Bigg],
\end{aligned} \tag{2.54}$$

$$\begin{aligned}
[g^{\phi\phi'}W_{,\phi\phi'}] =& \frac{1}{16\pi^2 r^2}\Bigg\{\int_{-\infty}^{\infty}\sum_{l=0}^{\infty}(2l+1)l(l+1)\left(g_{\omega l} - k^{(n)}_{\omega l}\right)d\omega \\
&+ \sqrt{\pi}\sum_{a=2}^{n-1}\sum_{b=0}^{a}\mathcal{T}^{(\rm l)}_{ab}\,\frac{r^2(a-b)(a-2)!2^{2a}f^{a-b-1}}{\Gamma(\frac{3}{2}-a)\lambda^{2a-2}}\Bigg\} \\
&+ \frac{1}{4\pi^2}\Bigg[\mathcal{D}^{(\rm p)}_{22} + \mathcal{T}^{(\rm p)}_{10} - \frac{\mathcal{D}^{(\rm r)}_{20}}{f^2} - 2\frac{\mathcal{D}^{(\rm r)}_{21}}{f^3} - 3\frac{\mathcal{D}^{(\rm r)}_{22}}{f^4} \\
&- \frac{\mathcal{T}^{(\rm r)}_{10}}{f^2} + \frac{\mathcal{T}^{(\rm l)}_{11}}{f} + \mathcal{T}^{(\rm l)}_{10}(\log(f/(\ell^2\lambda^2)) - 2\gamma_{\rm E} + 1)\Bigg].
\end{aligned} \tag{2.55}$$

In the extended coordinate prescription, the rate of convergence of the mode-sums is directly related to the order n of the expansion of the Hadamard parametrix. The convergence of the mode-sums can be improved by subtracting higher-order terms of the Hadamard parametrix. The large frequency and large l behavior of

$g_{\omega l}(r) - k^{(n)}_{\omega l}(r)$ is dependent on the order of the expansion n of the Hadamard parametrix. Specifically, we find numerically that the large-ω expansion of $g_{\omega l}(r)$ takes, in general, the form

$$g_{\omega l}(r) \sim \sum_{j=0}^{\infty} a_j(l,r)\omega^{-2j-1}, \tag{2.56}$$

where $a_j(l,r)$ are functions of l and r. By construction, the renormalization counterterms $k^{(n)}_{\omega l}(r)$ contain exactly the terms with $j = 0, 1, .., n$

$$k^{(n)}_{\omega l}(r) \sim \sum_{j=0}^{n} a_j(l,r)\omega^{-2j-1}. \tag{2.57}$$

Hence, for large ω, we find $g_{\omega l}(r) - k^{(n)}_{\omega l}(r) = \mathcal{O}(\omega^{-2n-3})$. An analogous expansion can be done in the large l limit. Thus, the behavior of the renormalized integrand $g_{\omega l}(r) - k^{(n)}_{\omega l}(r)$ at large ω and large l is found numerically to depend on the order of the expansion n as follows:

$$g_{\omega l}(r) - k^{(n)}_{\omega l}(r) = \begin{cases} \sim \omega^{-2n-3}, & \text{large } \omega, \text{ fixed } l, \\ \sim l^{-2n-3}, & \text{large } l, \text{ fixed } \omega. \end{cases} \tag{2.58}$$

In Figures 2.1 and 2.2, we numerically illustrate this convergence behavior for the case of a Schwarzschild black hole. In Figure 2.1, the upper blue line shows the large-(ωM) behavior of the unrenormalized quantity $g_{\omega l}$ evaluated at fixed l and r. This plot is interpreted as follows: since $\log_{10}|(\omega M)Mg_{\omega l}|$ approaches a constant value in the large frequency limit (it is a line of slope 0), then one can infer that $(\omega M)Mg_{\omega l} \sim \mathcal{O}(1)$ at large ωM and hence $Mg_{\omega l} \sim (\omega M)^{-1}$ at large ωM. The remaining curves in Fig. 2.1 report the large-(ωM) behavior, at fixed l and r, of the renormalized quantity $g_{\omega l} - k^{(n)}_{\omega l}$ for progressively higher expansion order n of the parametrix. By inspecting the different curves, one can verify that the large frequency behavior reflects the one reported in Eq. (2.58), showing that indeed the rate of convergence of the renormalized mode-sums can be increased by including higher expansion orders of the Hadamard parametrix. In the Figure, factors of M are introduced to make all the quantities dimensionless, and a logarithmic scale is employed to make the different curves clearly visible in a single plot.

Similarly, Figure 2.2 reports the behavior of the unrenormalized and renormalized radial Green's function at large l for fixed ω and r. Once again, the numerical results are in agreement with the analytical prediction in Eq. (2.58), confirming the efficacy of the method.

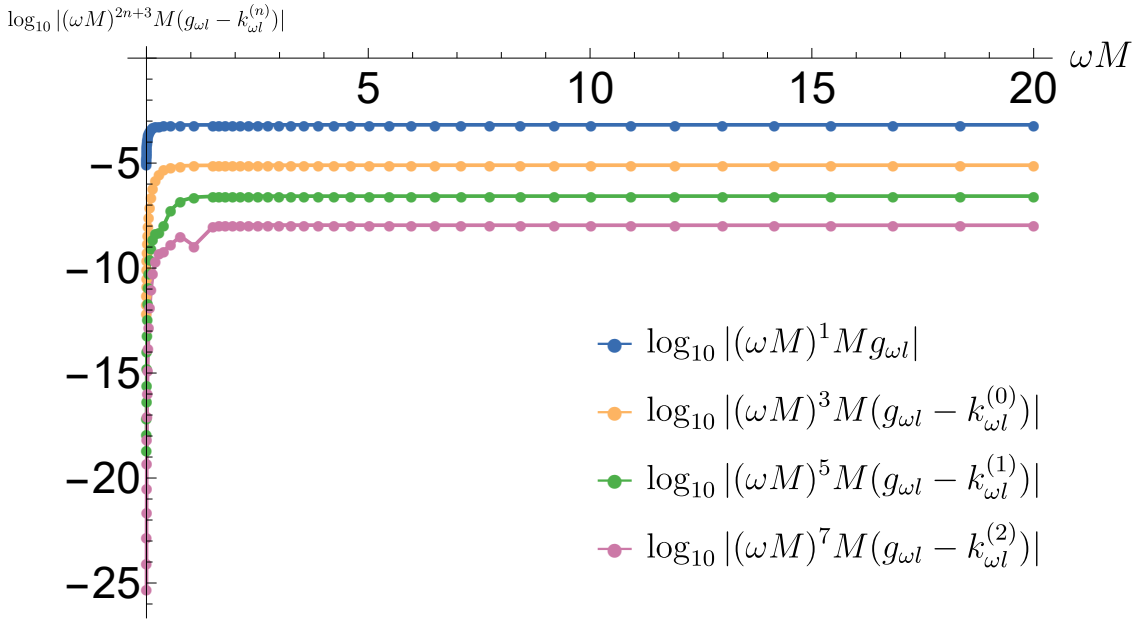


Figure 2.1: *Analysis of the convergence of $g_{\omega l}(r)-k^{(n)}_{\omega l}(r)$ for a massless scalar field on the exterior of a Schwarzschild black hole at different orders of expansion n for fixed l and large ω. Results obtained with the set of parameters: $M=1$, $r=3M$, and $l=0$.*

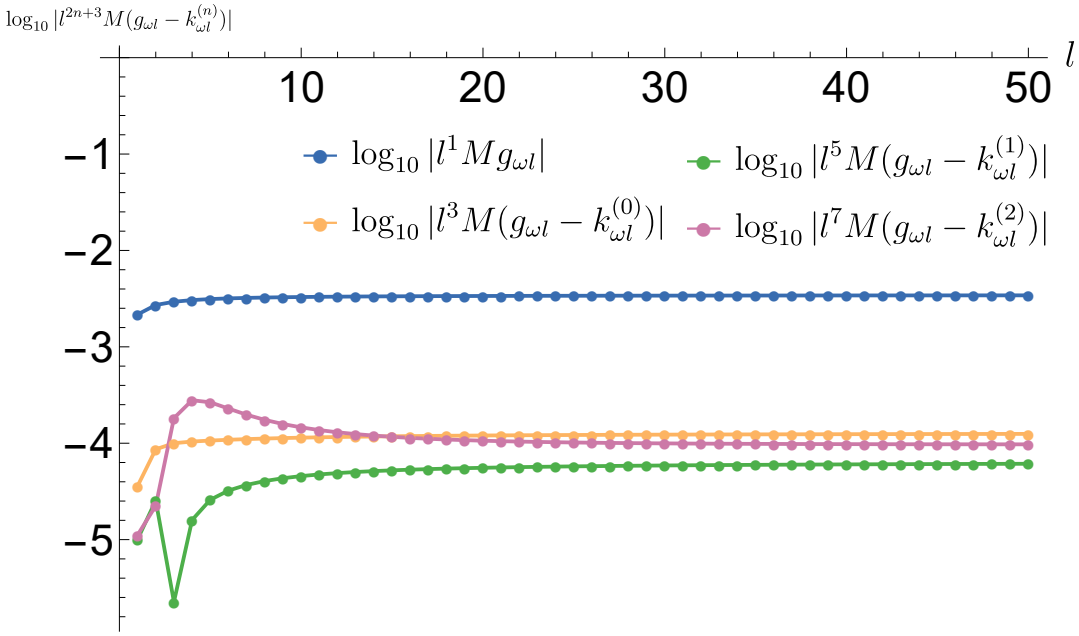


Figure 2.2: *Analysis of the convergence of $g_{\omega l}(r)-k^{(n)}_{\omega l}(r)$ for a massless scalar field on the exterior of a Schwarzschild black hole at different orders of expansion n for fixed ω and large l. Results obtained with the set of parameters: $M=1$, $r=3M$, and $\omega M=0.1$.*

2.5 Conclusions

In this Chapter, we have provided a generalisation of the extended coordinate prescription to directly compute the renormalized stress-energy tensor (RSET) of scalar fields in the Boulware vacuum state. While the extended coordinate approach was first developed for the calculation of expectation values for a scalar field in the Hartle-Hawking state, it can be used to obtain results for other quantum states using a state subtraction approach [3]. However, for spacetimes where one does not have a Hartle-Hawking state to leverage as a reference state, such as an extremal black hole or the spacetime of a star then a direct approach to compute the RSET is required.

We treated the Boulware state as a zero temperature state, defined on the Wick-rotated Riemannian manifold. Such treatment is convenient because the Euclidean Green's function possesses a simpler singularity structure, which is only singular in the coincident limit, thereby simplifying the development of a renormalization procedure for computing the RVP and the RSET. Nonetheless, unlike in the treatment of the Hartle-Hawking state, in which one usually imposes a periodicity condition in Euclidean time that discretizes the frequency spectrum, such identification is not viable in the treatment of the Boulware state; the frequency spectrum remains continuous, making the analytical and numerical treatments more challenging.

In the extended coordinate approach, the Hadamard parametrix, which encodes the short-distance behaviour of the two-point function, is expanded in a set of extended coordinates. The terms in this expansion are then rewritten as mode-sums of the same form as those appearing in the unrenormalized Euclidean Green's function, thereby enabling a mode-by-mode renormalization. The main technical challenge in applying this approach to a scalar field at zero temperature arises from having a continuous frequency spectrum, and hence the mode sums involve improper integrals over ω (as opposed to the Hartle-Hawking case where we sum over discrete values of ω). As a result, when we express terms in the Hadamard parametrix as mode-sums, we find that the integrands are not ordinary functions of ω and we must treat these mode-sums rigorously as generalized functions. When we do this, we see that an infra-red cutoff naturally appears in the integrals over ω in such a way so that the final results are independent of this cutoff.

Having developed this new direct renormalization technique, in the next Chapter, we apply the method to compute the renormalized stress-energy tensor on the exterior of a subextremal Reissner-Nordström black hole and comparing the results against those obtained through the state subtraction approach in [3]. We then apply the direct renormalization approach to compute the RSET for both massless and massive scalar fields propagating in an extremal Reissner-Nordström spacetime.

Chapter 3

Computing the RSET in non-extremal and extremal Reissner-Nordström black holes

The material in this chapter is based on the following article:

1. J. Arrechea, C. Breen, A. Ottewill, L. Pisani, P. Taylor, Renormalized stress-energy tensor for scalar fields in the Boulware state with applications to extremal black holes, *Phys. Rev. D*, 111, 085009 (2025) [1].

3.1 Introduction

In this Chapter, we apply the renormalization scheme presented in Chapter 2 to the case of scalar fields in the Boulware state in the Reissner-Nordström black hole spacetime. As a consistency check, we first verify this new method by reproducing results for the non-extremal case, which were obtained via the state subtraction method in [3]. We then apply the method to the case of an extremal black hole, where we investigate the regularity of the Boulware state on the event horizon for both massless and massive scalar fields. The regularity of the renormalized-stress energy tensor for massless fields has previously been examined by Anderson et al. [63] using a WKB approximation (see [64–67] for discussions about backreaction effects). Our results reinforce the existing numerical evidence of the regularity of the RSET for massless fields in extremal black holes. Additionally, we provide the first (to the best of our knowledge) extension of those results to massive fields.

An overview of the Chapter is given below. In Section 3.2, we discuss the numerical implementation of the method for both cases and the numerical challenges. In Sec. 3.3, we apply the new method to compute the RSET for a scalar field on the Reissner-Nordstrom spacetime, including the extremal case where a direct cal-

culation is necessary. In Sec. 3.4, we employ our accurate RSET results to solve the first-order semiclassical equations to compute the backreaction on the extremal Reissner-Nordstrom black hole spacetime. Finally, in Sec. 3.5, we conclude with a discussion.

3.2 Numerical Implementation

3.2.1 Non-Extremal Modes

To obtain the non-extremal Reissner-Nordström Euclidean line element, we take the general static, spherically symmetric line element defined in Eq. (2.1) and set the radial function to

$$f(r) = \frac{(r - r_+)(r - r_-)}{r^2}. \tag{3.1}$$

where $r_\pm = M \pm \sqrt{M^2 - Q^2}$. M and Q are the mass and the charge of the black hole, respectively, while r_+ and r_- are the event and inner horizons.

As seen from Eqs. (2.49),(2.54) and (2.55), the mode sums required to obtain the RSET involve the computation of the radial Green function $g_{\omega l}$ in Eq. (2.3), defined as the normalized product of solutions to the radial equation (2.4).

For the non-extremal case the computation of the $p_{\omega l}(r)$ modes is simplified by recasting the radial equation (2.4) into a confluent Heun form. This is achieved by expressing the dependent variable $\Upsilon_{\omega l}(r)$ as:

$$\Upsilon_{\omega l}(r) = e^{-(\omega - \bar{\omega})r} e^{\omega r_*} Y_{\omega l}(r)$$

and introducing a new independent variable:

$$\eta = \frac{r_+ - r}{r_+ - r_-}.$$

The radial equation then takes the form of the confluent Heun equation:

$$\eta(\eta - 1)Y''_{\omega l}(\eta) + (\bar{c}_3(\eta - 1) + \bar{c}_4\eta + \eta(\eta - 1)\bar{c}_5)Y'_{\omega l}(\eta) + (\bar{c}_2\eta - \bar{c}_1)Y_{\omega l}(\eta) = 0 \tag{3.2}$$

where $'$ represents differentiation with respect to η and

$$\begin{aligned}
\bar{c}_1 &= l(l+1) + r_+^2(\omega-\bar{\omega})^2 - (r_+ + r_-)(\omega-\bar{\omega}) - 2\,r_+\bar{\omega} \\
\bar{c}_2 &= (r_+^2 - r_-^2)(\omega-\bar{\omega})^2 - 2(r_+ - r_-)\bar{\omega} \\
\bar{c}_3 &= 1 + \frac{2\omega\, r_+^2}{r_+ - r_-} \\
\bar{c}_4 &= 1 - \frac{2\omega\, r_-^2}{r_+ - r_-} \\
\bar{c}_5 &= -2\bar{\omega}(r_+ - r_-) \\
\eta &= \frac{r_+ - r}{r_+ - r_-}
\end{aligned} \tag{3.3}$$

and with

$$\bar{\omega} = \sqrt{\omega^2 + \mu^2}. \tag{3.4}$$

If we let $\mathsf{H}(\bar{c}_1, \bar{c}_2, \bar{c}_3, \bar{c}_4, \bar{c}_5; \eta)$ denote the solution to Eq. (3.2) that is analytic in the vicinity of $\eta = 0$, i.e. $r = r_+$, and normalized to unity there, then we may express the $p_{\omega l}$ solution as:

$$p_{\omega l}(r) = e^{-(\omega-\bar{\omega})r} e^{\omega\, r_*} \mathsf{H}(\bar{c}_1, \bar{c}_2, \bar{c}_3, \bar{c}_4, \bar{c}_5; \eta), \tag{3.5}$$

where it is assumed that $\omega > 0$. We have implemented the $\omega \to -\omega$ symmetry in Eq. (2.4) to rewrite the frequency integral in the mode-expansion in Eq. (2.3) so that it only involves positive frequencies. Consequently, all the solutions can be defined for $\omega > 0$. The other linearly independent solution to Eq. (3.2) is discarded for the construction of the $p_{\omega l}$ modes, since it is irregular at $\eta = 0$.

Computing the $q_{\omega l}(r)$ modes is computationally harder. While these modes can still be written in confluent Heun form, the Heun functions with the appropriate boundary conditions for $q_{\omega l}(r)$ are not built into *Mathematica*. There are several options one can consider for computing $q_{\omega l}(r)$ but we found it most efficient to simply numerically integrate the radial equation inwards from a large r value using an asymptotic expansion for the initial conditions (see for example [45] for details of the asymptotic expansion). The initial conditions were optimized so that the asymptotic expansion solved the wave equation to our working precision with the least number of terms in the asymptotic expansion and for the smallest reasonable r value at which this precision could be achieved. Using this approach, the mode solutions and their derivatives that were generated were accurate to at least 30 significant digits. We tested this accuracy by checking the constancy of the Wronskian over the radial grid for the solution pairs $\{p_{\omega l}(r), q_{\omega l}(r)\}$.

3.2.2 Extremal Modes

The extremal black hole metric can be obtained by setting the radial function in Eq. (2.1) to

$$f(r) = \left(1 - \frac{M}{r}\right)^2 . \tag{3.6}$$

The resulting mode equation (2.4) amounts to

$$\Upsilon''_{\omega l} + \frac{2\Upsilon'_{\omega l}}{r-M} - \left[\frac{r^4\omega^2}{(r-M)^4} + \frac{\mu^2 r^2 + l\,(l+1)}{(r-M)^2}\right]\Upsilon_{\omega l} = 0. \tag{3.7}$$

Here, $'$ means differentiation with respect to r. For convenience, we follow [68] and adopt the dimensionless coordinate $\tilde{\eta} = r/M - 1$, for which the wave equation is

$$\tilde{\eta}^4 \frac{d^2}{d\tilde{\eta}^2}\Upsilon_{\omega l} + 2\tilde{\eta}^3 \frac{d}{d\tilde{\eta}}\Upsilon_{\omega l} - \left[\omega^2 M^2 (\tilde{\eta}+1)^4 + l\,(l+1)\,\tilde{\eta}^2 + \mu^2 M^2 \tilde{\eta}^2 (\tilde{\eta}+1)^2\right]\Upsilon_{\omega l} = 0. \tag{3.8}$$

The radial solutions regular at the horizon and at radial infinity obey, respectively, the asymptotic expansions

$$p_{\omega l} = \tilde{\eta}^{2\omega M} e^{-\omega M/\tilde{\eta}} \sum_{k=0}^{\infty} a_k \tilde{\eta}^k, \;\; \tilde{\eta} \to 0 \tag{3.9}$$

and

$$q_{\omega l} = \tilde{\eta}^{-2\omega M} e^{\omega M/\tilde{\eta}} e^{-\sqrt{\omega^2+\mu^2} M \tilde{\eta}} \sum_{k=0}^{\infty} b_k \tilde{\eta}^{-k-\nu_0}, \;\; \tilde{\eta} \to \infty. \tag{3.10}$$

In obtaining these solutions we assumed, once again, that $\omega > 0$. We note that near $\tilde{\eta} = 0$ we have an asymptotic expansion instead of a Frobenius expansion, since $\tilde{\eta} = 0$ is an irregular singular point of the ODE (3.8). Replacing these relations in Eq. (3.8) we find the following recursion relations for the a_k, b_k coefficients,

$$\begin{aligned}
a_0 =& 1, \\
a_1 =& \left[\tilde{\mu}^2 + l\,(l+1) + 2\tilde{\omega}\,(\tilde{\omega}-1)\right]\frac{a_0}{2\tilde{\omega}}, \\
a_2 =& \left[\tilde{\mu}^2 + 2\tilde{\omega}^2\right]\frac{a_0}{2\tilde{\omega}} + \left[\tilde{\mu}^2 + l\,(l+1) + 2\tilde{\omega}\,(\tilde{\omega}-3) - 2\right]\frac{a_1}{4\tilde{\omega}}, \\
a_k =& \left(\tilde{\mu}^2 + \tilde{\omega}^2\right)\frac{a_{k-3}}{2\tilde{\omega}k} + \left(\tilde{\mu}^2 + 2\tilde{\omega}^2\right)\frac{a_{k-2}}{\tilde{\omega}k} \\
&+ \left[k\,(1-k) + \tilde{\mu}^2 + l\,(l+1) - 4\tilde{\omega}k + 2\tilde{\omega}\,(1+\tilde{\omega})\right]\frac{a_{k-1}}{2\tilde{\omega}k},
\end{aligned} \tag{3.11}$$

for the $p_{\omega l}$ mode, where $\tilde{\omega} = \omega M$, $\tilde{\mu} = \mu M$. For the $q_{\omega l}$ mode we have, instead,

$$\begin{aligned}
\nu_0 =& 1 - 2\tilde{\omega} + \sqrt{\tilde{\omega}^2 + \tilde{\mu}^2} + \frac{\tilde{\omega}^2}{\sqrt{\tilde{\omega}^2 + \tilde{\mu}^2}}, \\
b_0 =& 1, \\
b_1 =& \left[\tilde{\mu}^2 + l\,(l+1) + \nu_0\,(1 - \nu_0 - 4\tilde{\omega}) + 2\tilde{\omega}\left(1 + \tilde{\omega} - \sqrt{\tilde{\omega}^2 + \tilde{\mu}^2}\right)\right] b_0 \\
& \times \left[2\tilde{\mu}^2 - 2\nu_0\sqrt{\tilde{\omega}^2 + \tilde{\mu}^2} + 4\tilde{\omega}\left(\tilde{\omega} - \sqrt{\tilde{\omega}^2 + \tilde{\mu}^2}\right)\right]^{-1}, \\
b_k =& \frac{(\nu_0 + k - 2)\,\tilde{\omega} b_{k-2}}{(\nu_0 + k - 1)\sqrt{\tilde{\omega}^2 + \tilde{\mu}^2} - 2\tilde{\omega}\left(\tilde{\omega} - \sqrt{\tilde{\omega}^2 + \tilde{\mu}^2}\right) - \tilde{\mu}^2} \\
& \left[-k^2 + k\,(3 - 2\nu_0 - 4\tilde{\omega}) + l\,(l+1) + \tilde{\mu}^2 - \nu_0^2\right. \\
& \left. + \nu_0\,(3 - 4\tilde{\omega}) + 2\tilde{\omega}\left(3 + \tilde{\omega} - \sqrt{\tilde{\omega}^2 + \tilde{\mu}^2}\right) - 2\right] b_{k-1} \\
& \times \left[2\,(\nu_0 + k - 1)\sqrt{\tilde{\omega}^2 + \tilde{\mu}^2} - 4\tilde{\omega}\left(\tilde{\omega} - \sqrt{\tilde{\omega}^2 + \tilde{\mu}^2}\right) - 2\tilde{\mu}^2\right]^{-1}.
\end{aligned} \tag{3.12}$$

3.2.3 Accuracy Issues

The numerical implementation of the direct method is more challenging than the extended coordinate method developed for thermal states. Most of the issues are related to the sampling of the continuous frequency spectrum. To numerically perform the integral in ω, one needs to interpolate the integrand over a predefined ω-grid. This grid must be fine enough so that the interpolation function works well, ensuring the result is independent of the grid choice. This becomes challenging when the integrand is very large and rapidly decaying. As a result, one needs a very dense grid to properly interpolate a rapidly varying function. The appropriate density of the ω-grid is obtained by comparing the results of the integral obtained with different grid choices and interpolation orders. The grid is considered sufficiently dense when varying these parameters does not affect the result up to a desired number of significant digits.

Another issue is related to the cancellation of the cutoff-dependent terms. We have shown analytically that the renormalized vacuum polarization does not depend on the choice of the cutoff, as the cutoff-dependent terms ultimately cancel each other. However, achieving this outcome numerically is more challenging and can significantly impact the accuracy of the results. For the case of a thermal state [51–53], where cutoff terms are not present, one can increase the accuracy of the results by increasing the expansion order of the singular field (n in Eq. (2.8)). Moreover, this is extremely efficient numerically as only a very modest number of modes are required. However, for the direct approach, the magnitude of the cutoff-dependent terms increases with increasing expansion order, and so does the potential

error introduced by the numerical cancellation of these terms. To counteract this, as the expansion order increases, one has to also increase the density in the grid in ω immediately after the cutoff. In effect if one increases the expansion order, one has to also significantly increase the number of numerical modes required, making the process increasingly inefficient. Hence, there is a balance to be struck between the accuracy of the results and the efficiency of the method. For the results contained in this Chapter, we have found that a third-order expansion ($n = 3$) and summing/integrating up to $l = 40/\omega = 5$ with an ω-grid that is denser near $\omega = 0$ and in the ω-range immediately above the cutoff gives sufficiently accurate results, with the conservation equation satisfied to approximately 9-10 decimal places.

There is an important exception to this choice, and that is in the vicinity of the event horizon. All the cutoff-dependent terms vanish on the event horizon, and therefore, as we approach the horizon, the error introduced by these terms also decreases. This is particularly true in the extremal case, where the metric function $f(r)$ has a double root. Therefore, for points close to the horizon (up at a distance of approximately $M/10$), we employ a sixth-order expansion to obtain our results and find that the conservation equation is satisfied to approximately 13-15 decimal places for a massless field and 10-11 decimal places for the massive case. In addition, particularly near the horizon, the integral is dominated by the low-ω behavior. Hence, it is crucial to select the smallest point in the ω-grid accordingly to avoid losing important contributions. The integrand is then extrapolated to $\omega = 0$. Specifically, the first point in the ω-grid is chosen to be small enough that the extrapolation process introduces a negligible error.

Conveniently, we found different representations for $\mathcal{I}_{\omega l}(a, b\,|r)$ and $\mathcal{J}_{\omega l}(a, b\,|r)$. The most amenable to numerical implementation are the ones reported in the derivations above, namely in Eqs. (2.25) and (2.45), which involve differences of two hypergeometric functions. However, these representations fail whenever $\frac{|\omega|\,r}{\sqrt{f}} \gg 1$, due to catastrophic cancellation. In this context, the catastrophic cancellation arises from subtracting two nearly equal very large terms, namely, each term with a hypergeometric function in Eq. (2.25), in the case of $\mathcal{I}_{\omega l}(a, b, |r)$, and each term with a hypergeometric function in Eq. (2.45), in the case of $\mathcal{J}_{\omega l}(a, b, |r)$. Performing this subtraction with sufficient accuracy would require numerical computations with several hundred digits of precision, which is impractical. Therefore, for the region of the domain where $\frac{|\omega|\,r}{\sqrt{f}} \gg 1$, we found the representations in terms of derivatives of modified Bessel functions and generalized incomplete gamma functions more efficient and not subject to the numerical errors arising from the catastrophic cancellations. These expressions will turn particularly useful in Chapters 5 and 6. We include them in appendix A.2 for convenience.

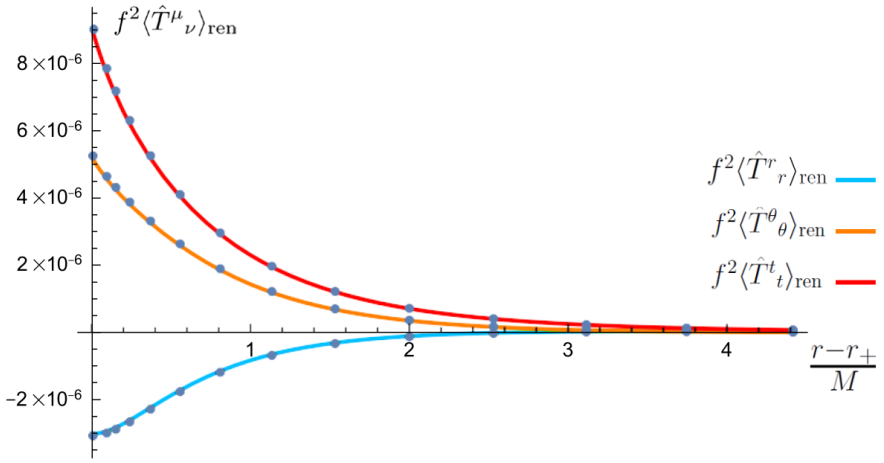


Figure 3.1: *RSET components in the Boulware state for a massless, minimally coupled scalar field calculated via the direct method (line) and the state subtraction method (dots). The background spacetime is the non-extremal Reissner-Nordström spacetime with $Q = M/5$.*

3.3 Results

3.3.1 Non-Extremal Results

In Fig. 3.1 we compare the results of the direct method outlined in this thesis to the corresponding results obtained via a state-subtraction approach in [3], for the calculation of the RSET for a massless, minimally coupled scalar field in the Boulware state. The background spacetime on which this calculation is performed is the non-extremal Reissner-Nordström spacetime with $Q = M/5$. As is evident from the plot in Fig. 3.1, in which the RSET components $f^2\langle\hat{T}^{\alpha}_{\beta}\rangle$ calculated via the direct method are depicted with colored lines while those obtained in [3] via the state-subtraction approach are represented by dots, there is good agreement between the two approaches, verifying the new method presented in this thesis. However, the state-subtraction method appears to be more accurate, as measured by the conservation equation, in the vicinity of the event horizon. This suggests that for space-times where there exists a Hartle-Hawking state to use as a reference state, taking the state-subtraction approach outlined in [3] is the appropriate choice. However, for other space-times, such as the extremal Reissner-Nordström spacetime considered in the next section, where we do not have a Hartle-Hawking state to exploit, the direct approach is required.

Inserting the expressions in Eqs. (2.49), (2.54), (2.55) into Eq. (2.50) results in a natural splitting of the RSET components into a numeric and an analytic part:

$$\langle\hat{T}^{\alpha}{}_{\beta}\rangle_{\rm ren} = \langle\hat{T}^{\alpha}{}_{\beta}\rangle_{\rm numeric} + \langle\hat{T}^{\alpha}{}_{\beta}\rangle_{\rm analytic}, \tag{3.13}$$

where $\langle\hat{T}^{\alpha}{}_{\beta}\rangle_{\text{numeric}}$ contains the terms in Eqs. (2.49), (2.54), (2.55) that are in curly brackets, while $\langle\hat{T}^{\alpha}{}_{\beta}\rangle_{\text{analytic}}$ is comprised of those terms in square brackets. We give explicitly the expressions for both $\langle\hat{T}^{\alpha}{}_{\beta}\rangle_{\text{numeric}}$ and $\langle\hat{T}^{\alpha}{}_{\beta}\rangle_{\text{analytic}}$ in Appendix A.4. Interestingly, with these definitions, both $\langle\hat{T}^{\alpha}{}_{\beta}\rangle_{\text{numeric}}$ and $\langle\hat{T}^{\alpha}{}_{\beta}\rangle_{\text{analytic}}$ are independently conserved. In fact $\langle\hat{T}^{\alpha}{}_{\beta}\rangle_{\text{analytic}}$ is equal, up to the addition of a conserved tensor, to the equivalent analytic component obtained by the AHS method [45], which in turn reproduces Page's approximation for a massless field [69]. The fact that our direct method reproduces the AHS results, whose derivation depended on the use of the WKB approximation to the radial Green function, is surprising, particularly when contrasted with the results of the extended coordinates approach for a thermal state [53]. In that case the equivalent analytic component does not reproduce the AHS equivalent and neither the analytic nor numerical components are independently conserved, rather only their combination is conserved.

We observe that the leading-order divergence of the RSET at the horizon is determined entirely by $\langle\hat{T}^{\alpha}{}_{\beta}\rangle_{\text{analytic}} \propto f^{-2}$, with $\langle\hat{T}^{\alpha}{}_{\beta}\rangle_{\text{numeric}} \propto f^{-1}$ amounting to a sub-leading correction. This indicates that $\langle\hat{T}^{\alpha}{}_{\beta}\rangle_{\text{analytic}}$ indeed captures exactly the singular behaviour of the Boulware state at event horizons, and further justifies its use in backreaction analyses as an analytic approximation to the exact RSET [70].

3.3.2 Extremal Results

In this section, we present the results of the extended coordinate approach to the calculation of the RSET for a scalar field in the Boulware quantum state on an extremal Reissner-Nordström spacetime.

In Figs. 3.2 and 3.3 we present the components of the RSET in the exterior region of the black hole for a massless and massive field ($\mu M = 1/10$) respectively. For the massless case, on the horizon $\langle\hat{T}^{\alpha}{}_{\beta}\rangle_{\text{numeric}}$ vanishes and the RSET is given precisely by $\langle\hat{T}^{\alpha}{}_{\beta}\rangle_{\text{analytic}}$ with

$$\langle\hat{T}^{\alpha}{}_{\beta}\rangle|_{r=M} = \langle\hat{T}^{\alpha}{}_{\beta}\rangle_{\text{analytic}}|_{r=M} = \frac{1}{2880\pi^2 M^4}\delta^{\alpha}{}_{\beta}, \tag{3.14}$$

which is equal to the corresponding RSET in the Bertotti-Robinson spacetime. A result that may be expected since the near-extremal horizon geometry is asymptotically congruent to that of the Bertotti-Robinson spacetime [63]. The fact that $\langle\hat{T}^{\alpha}{}_{\beta}\rangle_{\text{analytic}}$ is exact on the horizon, suggests that it might serve as a good approximation for the full RSET in a reasonable domain of the exterior, at least in the massless case. However this is not the case, with $\langle\hat{T}^{\alpha}{}_{\beta}\rangle_{\text{analytic}}$ failing to capture the main features of the full results, except in the immediate vicinity of the horizon. Finally, as r increases we see that all RSET components tend to 0, as would be expected for the Boulware state, which is truly vacuum for static observers at

infinity.

For the massive case, the situation is quite different. Here both $\langle \hat{T}^{\alpha}{}_{\beta} \rangle_{\text{analytic}}$ and $\langle \hat{T}^{\alpha}{}_{\beta} \rangle_{\text{numeric}}$ diverge logarithmically on the horizon, however these divergences cancel to render each of the components of $\langle \hat{T}^{\alpha}{}_{\beta} \rangle$ finite there. Specifically, the analytic terms become, in the near-horizon limit,

$$\langle \hat{T}^{\alpha}{}_{\beta} \rangle_{\text{analytic}}|_{r=M} = \frac{\mu^2}{8\pi^2} \left[\frac{\left(\xi - \frac{1}{6}\right)}{M^2} \text{diag}\,(1,1,-1,-1) + \frac{\mu^2}{4} \delta^{\alpha}{}_{\beta} \right] \log\left(\frac{r}{M} - 1\right). \quad (3.15)$$

In contrast to the massless case, only the $\langle \hat{T}^{r}{}_{r} \rangle$ and $\langle \hat{T}^{t}{}_{t} \rangle$ components agree on the horizon with $\langle \hat{T}^{\theta}{}_{\theta} \rangle$ taking on a distinct value. For massive fields, the $r \to \infty$ behaviour of the RSET components depends on the renormalisation lengthscale ℓ. In fact, from the numerical results we find that the RSET approaches the following value:

$$\langle \hat{T}^{\alpha}{}_{\beta} \rangle_{\infty} = \frac{\delta^{\alpha}{}_{\beta} \mu^4}{128\pi^2} \left[3 + 4 \log\left(\frac{2e^{-\gamma_{\text{E}}}}{\mu\, \ell} \right) \right]. \quad (3.16)$$

Therefore, there is a natural choice of the lengthscale for massive fields for which the RSET tends to 0 as $r \to \infty$. This choice is given by:

$$\ell = \frac{2}{\mu} \exp\{3/4 - \gamma_{\text{E}}\}, \quad (3.17)$$

and is the value chosen for the results presented in Figs. 3.3 and 3.5. For the massless case we simply set $\ell = M$.

The coordinate system of Eq. (2.1), with the radial function (3.6), is singular at $r = M$. To assess the regularity of the stress-energy tensor at the horizon, we instead work in the orthonormal frame of a freely falling observer. The energy density and radial pressure measured by such an observer at the horizon are equal to each other and proportional to the quantity

$$\langle \hat{\mathcal{E}} \rangle = \frac{\langle \hat{T}^{r}{}_{r} \rangle - \langle \hat{T}^{t}{}_{t} \rangle}{f}. \quad (3.18)$$

Note that the energy density measured by a freely falling observer is not given by the $\langle \hat{T}^{t}{}_{t} \rangle$ component only, but is instead obtained by contracting the stress-energy tensor with the four-velocity u^{α} of the infalling observer, $\langle \hat{T}_{\alpha\beta} \rangle u^{\alpha} u^{\beta}$. Hence, one obtains Eq. (3.18). The renormalized stress-energy tensor is regular at the horizon if and only if the components $\langle \hat{T}^{t}{}_{t} \rangle$, $\langle \hat{T}^{r}{}_{r} \rangle$, $\langle \hat{T}^{\theta}{}_{\theta} \rangle = \langle \hat{T}^{\phi}{}_{\phi} \rangle$ and the quantity $\langle \hat{\mathcal{E}} \rangle$ remain finite in the limit $r \to M$ [63]. We have already discussed the regularity of the components of the RSET for both massless and massive fields. We now turn our attention to $\langle \hat{\mathcal{E}} \rangle$.

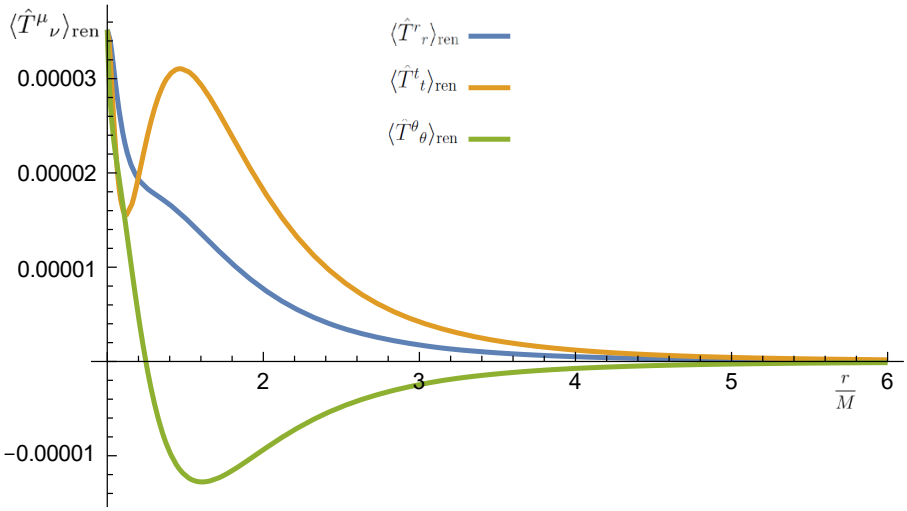


Figure 3.2: *Plot of the components $\langle\hat{T}^{\alpha}{}_{\beta}\rangle_{ren}$ for a conformally coupled massless field in the Boulware state, on an extremal Reissner-Nordström spacetime.*

The analytic contribution $\langle\hat{\mathcal{E}}\rangle_{\rm analytic}$ is not regular on the event horizon

$$\begin{aligned}\langle\hat{\mathcal{E}}\rangle_{\rm analytic} &= \frac{\langle\hat{T}^{r}{}_{r}\rangle_{\rm analytic} - \langle\hat{T}^{t}{}_{t}\rangle_{\rm analytic}}{f} \\ &= -\frac{\mu^2\left[3M^2\mu^2 + 12\left(\xi - \frac{1}{6}\right)\right]}{96\pi^2M^2}\left(\frac{r}{M}-1\right)^{-2} + \frac{15M^4\mu^4+2}{240\pi^2M^4}\left(\frac{r}{M}-1\right)^{-1} \\ &\quad - \frac{1}{60\pi^2M^4}\log\left(\frac{r}{M}-1\right) + \mathcal{O}\left(\frac{r}{M}-1\right)^{0}. \end{aligned} \tag{3.19}$$

This quantity possesses a $(r-M)^{-1}$ leading order divergence for a massless field and a $(r-M)^{-2}$ for a massive field. However, in Figures 3.4 and 3.5, we show, for a massless and massive field ($\mu M = 1/10$) respectively, that this divergence appears to be precisely canceled by a corresponding divergence from $\langle\hat{\mathcal{E}}\rangle_{\rm numeric}$, leaving a total $\langle\hat{\mathcal{E}}\rangle$ that is finite on the event horizon. The subleading logarithmic divergence also cancels. In the massless case, this agrees with previous results [63]. Of course, to prove this definitively would require a closed form expression for the quantity $\langle\hat{\mathcal{E}}\rangle$ on the horizon (or equivalently a near horizon expression for $\langle\hat{T}^{\alpha}{}_{\beta}\rangle_{\rm ren}$ to $\mathcal{O}(r-M)^2$). However, we feel the numerical results presented here provide compelling evidence for the regularity of the Boulware state for both massless and massive fields.

We have therefore used the novel method presented in the paper to confirm the results of [63] for a massless field and provide, to the best of our knowledge, the first exact results for the RSET of a massive scalar field in the extremal Reissner-Nordström spacetime.

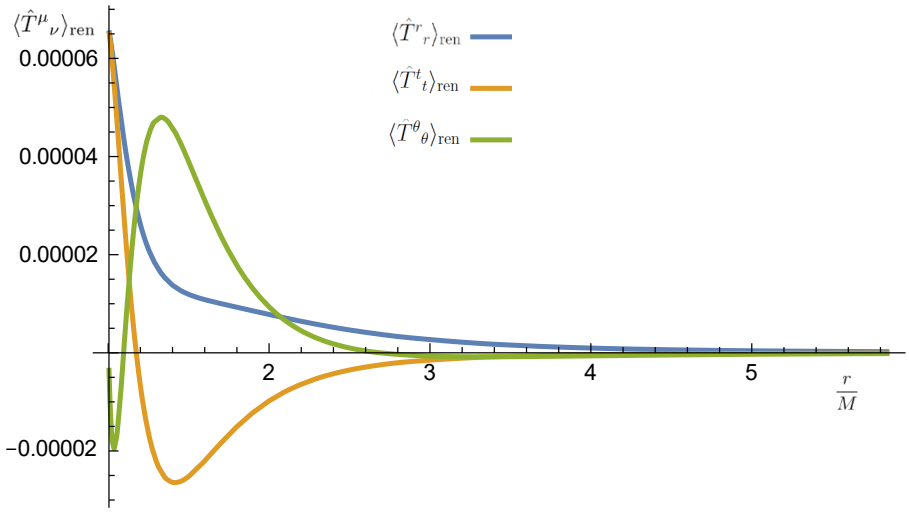


Figure 3.3: *Plot of the components $\langle\hat{T}^{\alpha}{}_{\beta}\rangle_{ren}$ for a minimally coupled field with mass $\mu M = 1/10$ in the Boulware state, on an extremal Reissner-Nordström spacetime.*

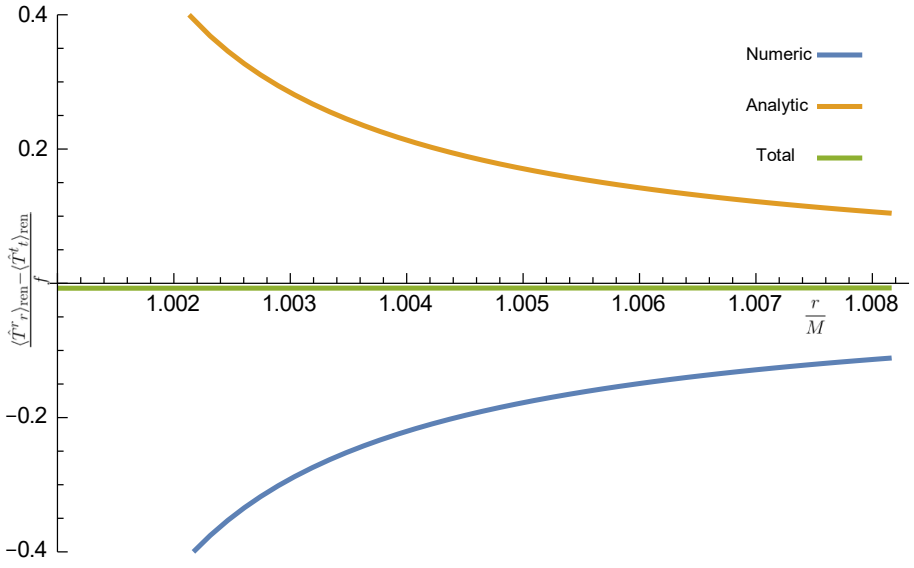


Figure 3.4: *Plot of the cancellation of the divergence in the numerical and analytical contributions to the quantity $\langle\hat{\mathcal{E}}\rangle$ for a minimally coupled massless field, leaving a total result that appears to be finite on the event horizon of the extremal Reissner-Nordström spacetime*

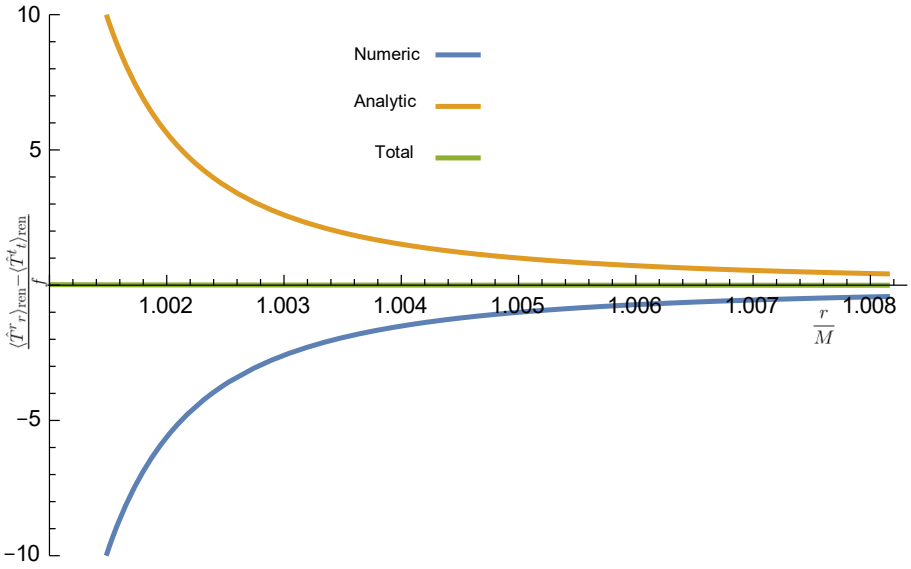


Figure 3.5: *Plot of the cancellation of the divergence in the numerical and analytical contributions to the quantity $\langle \hat{\mathcal{E}} \rangle$ for a minimally coupled field with mass $\mu = M/10$, leaving a total result that appears to be finite on the event horizon of the extremal Reissner-Nordström spacetime*

3.4 Backreaction in extremal black holes

Computing the RSET in the background of an extremal black hole naturally begs the question of whether extremal horizons are stable under quantum corrections. For the static, spherically symmetric extremal black holes under consideration, despite the field being in a static zero-temperature vacuum state and thus not inducing any evaporation process at lowest order in the semiclassical approximation, the quantum fields generate a RSET which is (generically) non-vanishing at the horizon and will backreact on the background metric.

We wish to solve the semiclassical equations (1.87) perturbatively. To do so, we follow the procedure outlined in Sec. 1.6. We first assume the RSET ambiguity is fixed so that all the freedom is contained in the constants on the left-hand side. In particular, we take the arbitrary renormalization lengthscale ℓ as in Eq. (3.17).

Since we wish to expand perturbatively about the extremal Reissner-Nordström solution, we further assume in Eq. (1.89) that $\Lambda = 0$ such that the zeroth order equation simplifies to

$$G_{\alpha\beta} = 8\pi\, T^{(\mathrm{cl})}_{\alpha\beta}\,, \tag{3.20}$$

where we reiterate that both sides of this equation are evaluated on the background spacetime. Taking the classical stress-energy tensor to be that derived from the Faraday tensor and assuming spherical symmetry yields the Reissner-Nordström

solution at the zeroth order. Then at first order in ϵ, we have from (1.90)

$$\delta G_{\alpha\beta} + \delta G^{-1}\, G_{\alpha\beta} + \delta\Lambda\, g_{\alpha\beta} + \delta\mathfrak{a}_1\, H^{(1)}_{\alpha\beta} = 8\pi\, \left(\langle \hat{T}_{\alpha\beta}\rangle_{\rm ren} + \delta T^{(\rm cl)}_{\alpha\beta}\right), \tag{3.21}$$

where now the $H^{(2)}_{\alpha\beta}$ tensor vanishes on the background spacetime, the perturbation of the Einstein tensor $\delta G_{\alpha\beta}$ is given in Eq. (1.91) in terms of the trace-reversed metric perturbation (1.92) and

$$\delta T^{(\rm cl)}_{\alpha\beta} = \frac{1}{4\pi}\left(-\frac{1}{4}h_{\alpha\beta}F_{\rho\sigma}F^{\rho\sigma} - \frac{1}{2}g_{\alpha\beta}F_{\rho\sigma}\delta F^{\rho\sigma} + F_{\alpha\sigma}\delta F^{\sigma}_{\ \beta} + \delta F_{\alpha\sigma}F^{\sigma}_{\ \beta}\right), \tag{3.22}$$

where we have introduced the following expansion for the electromagnetic field tensor

$$\mathsf{F}_{\alpha\beta} = F_{\alpha\beta} + \epsilon\delta F_{\alpha\beta}. \tag{3.23}$$

The solution space to Eq. (3.21) is very large so we focus on the simplest case for which the constants $\delta\Lambda$, $\delta\mathfrak{a}_1$ and δG^{-1} either vanish or are higher order in the perturbative expansion so that they do not contribute in Eq. (3.21). We can weaken the assumption that δG^{-1} vanishes and instead consider that this term can be absorbed into a redefinition of the charge of the background solution, a fact which can be easily seen from the zeroth order equation.

Following [71], we assume the full metric coefficients have the form

$$\mathsf{g}_{tt} = -e^{2\psi(r)}\,(1-2m(r)/r)\,, \quad \mathsf{g}_{rr} = (1-2m(r)/r)^{-1}\,, \tag{3.24}$$

where $m(r)$ denotes the Misner-Sharp mass, and then we expand these metric functions as

$$\psi(r) \simeq \log\left[1+\epsilon\mathcal{R}(r)\right], \quad m(r) \simeq M\left(1-\frac{M}{2r}\right)\left[1+\epsilon\mathcal{M}(r)\right]. \tag{3.25}$$

Note that $\delta T^{(\rm cl)}_{\alpha\beta}$ is in general nonzero. It is, however, convenient to consider the linear-order in ϵ semiclassical equation with up and down indices

$$\delta G^{\alpha}_{\ \beta} = 8\pi\left(\delta T^{\alpha\ (\rm cl)}_{\ \beta} + \langle \hat{T}^{\alpha}_{\ \beta}\rangle_{\rm ren}\right), \tag{3.26}$$

with

$$\delta T^{\alpha\ (\rm cl)}_{\ \beta} = g^{\alpha\gamma}\delta T^{(\rm cl)}_{\gamma\beta} + \delta g^{\alpha\gamma}T^{(\rm cl)}_{\gamma\beta}, \tag{3.27a}$$

$$\delta G^{\alpha}_{\ \beta} = g^{\alpha\gamma}\delta G_{\gamma\beta} + \delta g^{\alpha\gamma}G_{\gamma\beta}, \tag{3.27b}$$

$$\langle \hat{T}^{\alpha}_{\ \beta}\rangle_{\rm ren} = g^{\alpha\gamma}\langle \hat{T}_{\gamma\beta}\rangle_{\rm ren}, \tag{3.27c}$$

where we have introduced the inverse metric

$$\mathsf{g}^{\alpha\beta} = g^{\alpha\beta} + \epsilon\delta g^{\alpha\beta} + \mathcal{O}(\epsilon^2), \tag{3.28}$$

with

$$\delta g^{\alpha\beta} = -h^{\alpha\beta}, \tag{3.29}$$

and

$$h^{\alpha\beta} = g^{\alpha\gamma}g^{\beta\delta}h_{\gamma\delta}. \tag{3.30}$$

Introducing Eqs. (3.27) into Eq. (3.26) yields

$$g^{\alpha\gamma}\delta G_{\gamma\beta} + \delta g^{\alpha\gamma}G_{\gamma\beta} = 8\pi\left(g^{\alpha\gamma}\delta T^{(\mathrm{cl})}_{\gamma\beta} + \delta g^{\alpha\gamma}T^{(\mathrm{cl})}_{\gamma\beta}\right) + 8\pi g^{\alpha\gamma}\langle\hat{T}_{\gamma\beta}\rangle_{\mathrm{ren}}. \tag{3.31}$$

Since we are considering a neutral quantum scalar field, we can assume that the total charge is not affected by the presence of the field, meaning that the linear-order (in ϵ) contribution to $\mathsf{Q} = Q + \epsilon\delta Q$, with $Q = M$, vanishes: $\delta Q = 0$ [63]. Under this assumption, one can show that

$$\delta T^{\alpha\ (\mathrm{cl})}_{\ \beta} = g^{\alpha\gamma}\delta T^{(\mathrm{cl})}_{\gamma\beta} + \delta g^{\alpha\gamma}T^{(\mathrm{cl})}_{\gamma\beta} = 0, \tag{3.32}$$

resulting in the following simpler form for the semiclassical equations

$$g^{\alpha\gamma}\delta G_{\gamma\beta} + \delta g^{\alpha\gamma}G_{\gamma\beta} = 8\pi g^{\alpha\gamma}\langle\hat{T}_{\gamma\beta}\rangle_{\mathrm{ren}}. \tag{3.33}$$

Hence, using Eq. (3.33) we finally obtain

$$\begin{aligned} \frac{2\,(z-1)^2\,\mathcal{R}'(z)}{M^2 z^3} &= 8\pi M^2\left(\langle\hat{T}^r_{\ r}\rangle - \langle\hat{T}^t_{\ t}\rangle\right), \\ -\frac{\mathcal{M}(z)}{M^2 z^4} - \frac{(2z-1)\,\mathcal{M}'(z)}{M^2 z^3} &= 8\pi M^2\langle\hat{T}^t_{\ t}\rangle, \end{aligned} \tag{3.34}$$

where we have used the dimensionless coordinate $z = r/M$, and we have dropped the subscript "ren" on the RSET components for typographical convenience. The first equation is clearly the difference between the radial and temporal equations, and the angular equations are such that the Bianchi identities are satisfied. Once the RSET is specified (here we replace it by the numerical values for massless and massive fields shown in the previous section), we can integrate Eqs. (3.34) for $\mathcal{M}$ and $\mathcal{R}$. The full solutions for the perturbations are numerical, and we can only calculate them within the region for which we have numerical RSET values at our disposal.

For massless fields in the near-horizon limit $z \to z_{\mathrm{e}}$, with $z_{\mathrm{e}} = 1$ being the position of the extremal horizon, we can make use of the fact that the energy density and

pressures of the exact RSET are given, to leading order in $z - z_{\rm e}$, by Eq. (3.14) to obtain the following analytic solutions for the perturbations

$$\mathcal{M} = -\frac{C_0}{1080\pi} + \mathcal{O}\left(z - z_{\rm e}\right), \quad \mathcal{R} = \frac{K_0}{1080\pi} + \mathcal{O}\left(z - z_{\rm e}\right), \tag{3.35}$$

where $\{C_0, K_0\}$ are arbitrary integration constants. For massive fields, however, we cannot follow a similar argument since we ignore the exact values the RSET must reach at the extremal horizon, and extrapolating our numerical results introduces spurious errors. However, backreaction analyses have been done in the limit of large field mass [67]. Written in ingoing Eddington-Finkelstein coordinates, the metric components become

$$\begin{aligned} g_{vv} =& g_{tt} = -\frac{\epsilon C_0}{1080\pi} + \mathcal{O}\left(z - z_{\rm e}\right), \\ g_{vr} =& e^{\psi} = 1 + \frac{\epsilon K_0}{1080\pi} + \mathcal{O}\left(z - z_{\rm e}\right). \end{aligned} \tag{3.36}$$

In light of these expressions, we observe that the metric receives a correction so that g_{tt} is no longer vanishing at $z = z_{\rm e}$. For negative ϵC_0 we have $g_{tt} > 0$, hence the surface $z = z_{\rm e}$ appears to lie inside a trapped region. In this case perturbative corrections have shifted the position of the horizon from its classical value $z_{\rm e} = 1$ to a new position $z_{\rm H} > z_{\rm e}$ which must be found numerically. The surface gravity associated to this quantum-corrected horizon is equal to

$$\kappa_{\rm H} = \frac{e^{\psi}}{2M}\frac{\partial}{\partial z}\left(1 - \frac{2Mm}{z}\right) + \frac{e^{\psi}}{M}\left(1 - \frac{2Mm}{z}\right)\frac{\partial \psi}{\partial z}\bigg|_{z_{\rm H}}. \tag{3.37}$$

Extremal horizons are characterized by a vanishing surface gravity, i.e., a quadratic root in g_{vv}. In the Reissner-Nordström metric, this comes from the fact that $Q = M$. The RSET makes the Misner-Sharp mass acquire a radial dependence, but does not affect the charge, allowing for the possibility of breaking the delicate balance of scales required by extremal horizons. In practice what we observe is that the backreacted spacetime, locally around $z = z_{\rm e}$, becomes like the sub-extremal or super-extremal Reissner-Nordström spacetimes depending on which sign we choose for the mass perturbations. Since we do not have exact results for $z < z_{\rm e}$, we cannot obtain the quantum-corrected metric in the region $z \ll z_{\rm H}$.

Together with shifting the position of the horizon outwards, taking $\epsilon C_0 < 0$ makes it acquire a positive surface gravity. The relative position and surface gravity of the quantum-corrected horizon are shown in Fig. 3.6. For massless fields, we see this non-extremal horizon smoothly tends to a horizon of the extremal kind in the $\epsilon C_0 \to 0$ limit. In the massive case, since we lack RSET values arbitrarily close to $z_{\rm e}$, we have not been able to generate reliable results in the $\epsilon C_0 \to 0$ limit. Nonetheless,

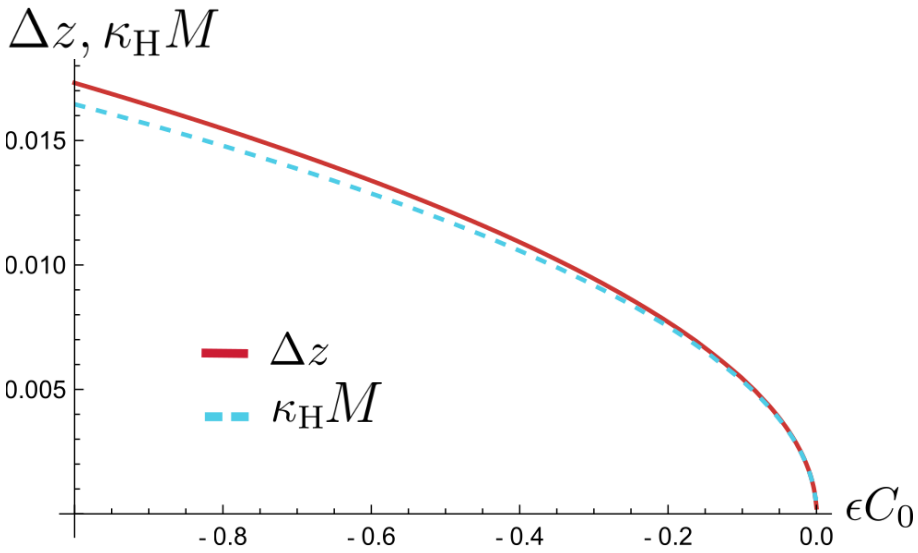


Figure 3.6: *Position of the perturbed horizon $\Delta z = z_{\rm H} - z_e$ and its surface gravity $\kappa_{\rm H}$ for a semiclassically corrected extremal black hole. Corrections from minimally coupled massive and massless fields shift the Misner-Sharp mass by a constant value, which either breaks the extremal horizon into a pair of inner and outer horizons (if $C_0 < 0$), or eliminates any horizon entirely (if $C_0 > 0$). Our results do not change qualitatively as long as $\epsilon K_0 \ll 1$, so we set $K_0 = 0$ here.*

for large and negative ϵC_0 values, the curves for the massless and massive cases are indistinguishable.

We can integrate Eqs. (3.34) away from the black hole to obtain the behaviour of perturbations at large z. The $\mathcal{R}$ function can be absorbed in a redefinition of the t coordinate, while the $\mathcal{M}$ function shifts the Arnowitt–Deser–Misner (ADM) mass by a constant factor. Under the choice of renormalized constants $\delta\Lambda = \delta G^{-1} = 0$, the RSET decays at large z as $\langle \hat{T}^{\alpha}_{\ \beta} \rangle \propto \mathcal{O}(z^{-4})$ for massive fields and as $\langle \hat{T}^{\alpha}_{\ \beta} \rangle \propto \mathcal{O}(z^{-6})$ for massless fields. In both cases, it can be shown from Eq. (3.34) that, for $z \gg z_e$, $\mathcal{M} = C_\infty + \mathcal{O}(z^{-1})$.

Figure 3.7 shows the $\mathcal{R}$ and $\mathcal{M}$ functions for the minimally coupled massless field (continuous lines) and the minimally coupled $\mu M = 1/10$ field. We have integrated the equations in the radial domain for which we have reliable results for the RSET. These are $z \in [M, 5.75M]$ and $z \in [1.005M, 5.75M]$ in the massless and massive cases, respectively. For the massless case, preserving the extremal horizon ($C_0 = 0$) translates into a negative correction to the ADM mass of $C_\infty \approx -2.5 \times 10^{-3}$, so that $M_{\rm ADM} = M + C_\infty < Q$. In this case, in order to preserve an extremal horizon, we would need to start with a sub-extremal black hole and perturb it semiclassically. For the massive case, integrating outwards with $C_0 = 0$ we obtain $C_\infty \approx 9.7 \times 10^{-4}$, so that $M_{\rm ADM} > Q$. In this case extremality would be preserved if we started with a super-extremal black hole and corrected it semiclassically. This discrepancy in $\mathcal{M}$ at large distances can be traced back to the differing signs of the $\langle \hat{T}^{t}_{\ t} \rangle$ component in

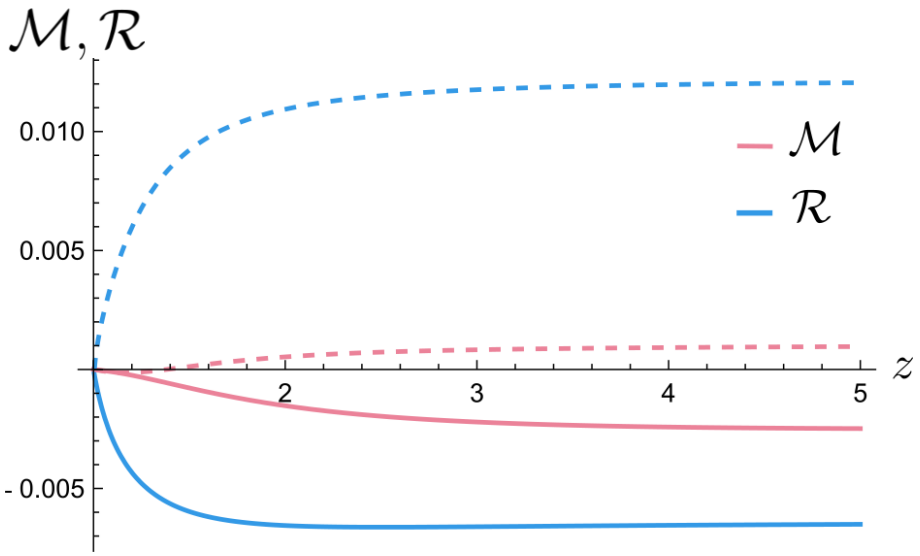


Figure 3.7: *Solutions for the perturbations $\mathcal{R}(r)$ of the redshift function (in blue) $\mathcal{M}(r)$ and the Misner-Sharp mass (in pink) in terms of the radial coordinate z. The continuous lines correspond to the $\mu M = 0$ case and the dashed lines to the $\mu M = 1/10$ case. Taking $C_0 = K_0 = 0$, we have integrated within the domain of z values in which we have reliable numerical results for the RSET.*

each case (see Figs. 3.2 and 3.3). For massless fields, the ξ-dependent contributions to the RSET vanish at the horizon and as $r \to \infty$. Regions in which $\langle \hat{T}^t{}_t \rangle$ changes sign only appear for $\xi \gtrsim 1/4$, hence these results are expected to hold qualitatively for a broad range of curvature couplings.

So far we have considered $\delta\mathfrak{a}_1 = 0$. For non-vanishing $\delta\mathfrak{a}_1$ in Eq. (3.21), we observe that the $H^{(1)}_{\alpha\beta}$ tensor is sub-leading with respect to the RSET contribution in the tt equation of Eq. (3.34) as the event horizon of the classical solution is approached, hence allowing $\delta\mathfrak{a}_1 \neq 0$ does not affect the analysis. In the $rr - tt$ equation of Eq. (3.34), both $(H_r^{r\ (1)} - H_t^{t\ (1)})(z-1)^{-2}$ and $(\langle \hat{T}^r{}_r \rangle - \langle \hat{T}^t{}_t \rangle)(z-1)^{-2}$ are finite as $z \to 1$. Nevertheless, it can be shown that the near-horizon analysis presented above still holds if $\delta\mathfrak{a}_1 \neq 0$. Thus, allowing $\delta\mathfrak{a}_1 \neq 0$ does not modify the position of the perturbed horizon nor its surface gravity. For large z, the tensor $H^{(1)}_{\alpha\beta}$ decays $\propto z^{-6}$, hence the perturbations $\mathcal{M}$ and $\mathcal{R}$ still approach constant values at infinity. However, the contribution from $H^{(1)}_{\alpha\beta}$ for intermediate z values can change the sign of the perturbations $\mathcal{M}$ and $\mathcal{R}$ at infinity. For example, a sufficiently large and negative $\delta\mathfrak{a}_1$ leads to a positive C_∞ in the massless minimally coupled case.

The loss of extremality is expected to occur due to a breakdown of the delicate balance between charge and mass contributions that extremal horizons require. Since we are only incorporating the vacuum polarization effects from an uncharged massless scalar field, this balance is broken at first order in perturbation theory. However, it is still plausible that the vacuum polarization effects from the electromagnetic field only displace the position of the horizon without changing its extremal

nature.

On the one hand, for negative ϵC_0, it is clear (since the corrections are perturbative) that we are observing a splitting of the extremal horizon into a pair of outer and inner horizons. By solving Eq. (1.87) perturbatively to higher order in ϵ, we would find: i) that the quantum state in which this RSET is evaluated is no longer a zero-temperature vacuum state, but a mixed state instead (as expected from the event horizon acquiring a temperature) and ii) that this state is singular at the newly formed inner horizon [54]. On the other hand, for positive ϵC_0 the function g_{vv} has zero roots, hence the extremal horizon disappears entirely and the perturbed metric describes a horizonless (and singular) object, whose associated vacuum state has zero temperature. Finally, between both regimes there is a separatrix solution with $C_0 = 0$ that preserves both the position and the surface gravity of the extremal horizon. This solution could potentially exist for all orders in ϵ only if we fine-tune the perturbations so that their contribution to the Misner-Sharp mass vanishes at every order in ϵ. Of course, the treatment adopted in this section only deals with static solutions from the start, hence we remain agnostic in regard to the stability of extremal horizons under time-dependent perturbations.

3.5 Conclusions

Having developed a direct approach for computing the renormalized stress-energy tensor of quantum scalar fields in the Boulware vacuum state in Chapter 2, in this Chapter we first applied it to the non-extremal Reissner-Nordström spacetime. In this case we reproduced the results obtained via the state subtraction approach in [3], thereby verifying the new direct approach. We then applied the direct approach the the calculation of the RSET in an extremal Reissner-Nordström spacetime, for both a massless and massive scalar field. The massless case had previously been considered in [63], however, the results presented in [1] and in this Chapter are the first results obtained for a massive field.

Once we have calculated the RSET components we used these results to investigate the regularity of the Boulware state by calculating the energy density on the horizon as perceived by a freely falling observer. Here we find strong numerical evidence that the Boulware state is regular for both the massless and massive case. However, we stress that these results are indicative only and to say anything conclusive requires exact results on the horizon.

Despite lacking a definite proof of the RSET regularity at extremal horizons, we can nonetheless assume that it is indeed regular to give a hint on the backreaction effects it would entail. By solving the static semiclassical equations perturbatively [71] we have seen that, unless perturbations are fine-tuned to every order in the expan-

sion, extremal horizons are unstable. If these perturbations contribute positively to the Misner-Sharp mass, the extremal horizon splits into a pair of outer and inner horizons, while in the opposite scenario the horizon disappears completely, leaving no marginally trapped surfaces in the spacetime. We also analyzed how extremality at the horizon results in a change in the ratio between the ADM mass and the charge, which depends on the overall sign of the semiclassical energy density.

Chapter 4

Application of the extended coordinate method to thin shells

The material in this chapter is based on the following article:

1. J. Arrechea, C. Breen, A. Ottewill, L. Pisani, P. Taylor, Vacuum polarization and renormalized stress-energy tensor of spherical thin shells, *arXiv*:2607.07583 (2026) [2].

4.1 Introduction

As discussed in the previous Chapters, one of the primary motivations for developing a direct renormalization technique for the Boulware state is the absence, in some spacetimes of interest, of a Hartle-Hawking state that could serve as a reference state for renormalization. In Chapter 3, we demonstrated the efficacy of the direct renormalization prescription developed in this thesis in the context of one such spacetime: the extremal Reissner-Nordström black hole. However, the method is general, and its applicability is not limited to black holes but to any static spherically symmetric spacetime that admits the Boulware state.

Of particular interest are the horizonless equilibrium configurations like compact stars [72–74] and thin shells [75], for which the Boulware state constitutes the natural vacuum state. Notably, little work has been carried out in these settings owing to the complications introduced by classical matter sources and to the fact that semiclassical effects are potentially but not obviously relevant in these contexts. The direct renormalization method developed in Chapter 2 opens new avenues of investigation in this direction and provides us with a powerful tool for analyzing the properties of the Boulware vacuum in the context of horizonless compact objects.

Specifically, the work we present in this Chapter is part of a broader program aimed at investigating the semiclassical effects in horizonless compact objects. In

general relativity, Buchdahl's theorem [76] defines an upper bound on the compactness of a static, spherically symmetric equilibrium star composed of standard matter. In the semiclassical context, however, the renormalized stress-energy tensor can violate some of the assumptions underlying Buchdahl's theorem. Including semiclassical backreaction effects may then allow for the existence of more compact horizonless objects than in the classical framework, possibly beyond the Buchdahl limit. To explore this possibility, it is useful to study configurations that can approach the black hole limit, where semiclassical effects may become particularly important.

In this Chapter, we examine the simplest scenario in which matter can be placed arbitrarily close to the black hole limit: a spherical thin shell in equilibrium with an empty Minkowski interior. We show that the values of the renormalized vacuum polarization and of the renormalized stress-energy tensor components remain bounded at the centre of the shell in the black hole limit. Additionally, we investigate the emergence of the Boulware divergence in the RSET components in the black hole limit. We will see that this effect is difficult to isolate, since a Casimir-type divergence associated with the presence of the shell dominates near the surface.

Although this setting is more idealized than a constant density star, it presents similar technical difficulties, in particular, the presence of matching conditions across a matter boundary. Future work will focus on extending this analysis to semiclassical compact stars.

The contents of this Chapter are organised as follows. In Section 4.2, we discuss how the extended coordinate method presented in Chapter 2 can be applied in the context of a spherically symmetric spacetime with a thin shell. In Section 4.3, we set the framework of the study: we outline Israel's thin-shell formalism and define a spherical thin shell joining a Minkowski interior to a Schwarzschild exterior. In Section 4.4, we discuss the details of the numerical computation of the Euclidean modes in this framework and study the numerical convergence of the renormalized mode-sums both inside and outside the shell. Next, in Sec. 4.5, we analyze the divergent behavior of the renormalized vacuum polarization and of the RSET near the shell analytically by means of a WKB and a weak-field approximation. The full numerical results are then presented in Sec. 4.6 for a wide range of parameters. Finally, we conclude in Sec. 4.8.

4.2 The extended coordinate method

In the context of spherical thin shells, the Euclidean line-element defined in (2.1) shall be generalized to

$$ds^2 = f(r)d\tau^2 + h(r)dr^2 + r^2(d\theta^2 + \sin^2\theta\, d\phi^2), \tag{4.1}$$

where $h(r)$ is another arbitrary function of r. Now, we have two free functions $f(r)$ and $h(r)$, whereas in the case of a black hole, we just have one free function $f(r)$, since, by Birkhoff's theorem, the metric in Eq. (4.1) with $h(r) = 1/f(r)$ is the unique spherically symmetric solution of the vacuum (or electro-vacuum) Einstein equations. Therefore, the extended coordinate prescription presented in Chapter 2 shall then be generalized to a metric of the form (4.1).

We consider, once again, a scalar field satisfying the Klein-Gordon equation (2.2), and define the renormalized vacuum polarization as the coincident limit of the difference between the point-split Euclidean Green's function $G_{\rm B}(x, x')$ (satisfying Eq. (1.55)) and the Hadamard parametrix for the Euclidean propagator $K(x, x')$ (as defined in Eq. (1.73))

$$\langle {\rm B}|\hat{\Phi}^2|{\rm B}\rangle_{\rm ren} := \lim_{x'\to x}\left\{G_{\rm B}(x, x') - K(x, x')\right\}. \tag{4.2}$$

At the thin shell radius $r = r_0$, $G_{\rm B}(x, x')$ is not smooth resulting in a $\langle {\rm B}|\hat{\Phi}^2|{\rm B}\rangle_{\rm ren}$ that is not smooth. The Euclidean Green's function for the Boulware state is most easily expressed as a mode-sum of the form

$$G_{\rm B}(x, x') = \frac{1}{8\pi^2}\sum_{l=0}^{\infty}(2l+1)P_l(\cos\gamma)\int_{-\infty}^{\infty} d\omega\, e^{i\omega\Delta\tau} g_{\omega l}(r, r'), \tag{4.3}$$

where, with the metric in Eq. (4.1), the bi-distribution $g_{\omega l}(r, r')$ satisfies the equation

$$\left\{\frac{d}{dr}\left(\frac{r^2\sqrt{f}}{\sqrt{h}}\frac{d}{dr}\right) - \sqrt{h\, f}\left[\frac{\omega^2 r^2}{f} + l(l+1) + r^2(\mu^2 + \xi\, R)\right]\right\} g_{\omega l}(r, r') = -\delta(r - r'). \tag{4.4}$$

The radial Green's function $g_{\omega l}(r, r')$ is contructed as in Eq. (1.98), with the normalization constant defined now as

$$N_{\omega l} = -\frac{r^2\sqrt{f}}{\sqrt{h}}\mathcal{W}\{p_{\omega l}, q_{\omega l}\} = -\frac{r^2\sqrt{f}}{\sqrt{h}}\left(\frac{d\, q_{\omega l}}{dr}p_{\omega l} - \frac{d\, p_{\omega l}}{dr}q_{\omega l}\right). \tag{4.5}$$

We discuss the details of the computation of the radial modes $p_{\omega l}(r)$ and $q_{\omega l}(r)$ and of their normalization constant $N_{\omega l}$ in the context of thin shells in Sec. 4.4.

The treatment of the Hadamard parametrix is analogous to that presented in Chapter 2. We once again choose the set of extended coordinates $\{s^2, \Delta\tau^2, \Delta r\}$, where

$$s^2 = f(r)\,\Delta\tau^2 + 2r^2(1-\cos\gamma). \tag{4.6}$$

Then if we expand the Hadamard parametrix in these extended coordinates and take the partial coincidence limit $r' = r$ (or $\Delta r = 0$) for simplicity, we get an expansion of the form:

$$\begin{aligned} K(x,x') = \frac{1}{8\pi^2}\Bigg(&\sum_{a=0}^{n}\sum_{b=0}^{a}\mathcal{D}^{(\mathrm{r})}_{ab}(r)\frac{\Delta\tau^{2a+2b}}{s^{2b+2}} + \sum_{a=1}^{n}\sum_{b=1}^{a}\mathcal{D}^{(\mathrm{p})}_{ab}(r)\Delta\tau^{2a-2b}s^{2b-2} \\ &+ \sum_{a=1}^{n-1}\sum_{b=0}^{a-1}\mathcal{T}^{(\mathrm{r})}_{ab}(r)\frac{\Delta\tau^{2a+2b+2}}{s^{2b+2}} + \sum_{a=0}^{n-1}\sum_{b=0}^{a}\mathcal{T}^{(\mathrm{l})}_{ab}(r)s^{2a-2b}\Delta\tau^{2b}\log\left(\frac{s^2}{\ell^2}\right) \\ &+ \sum_{a=1}^{n-1}\sum_{b=0}^{a}\mathcal{T}^{(\mathrm{p})}_{ab}(r)s^{2a-2b}\Delta\tau^{2b}\Bigg) + \mathcal{O}(\Delta x^{2n}\log\Delta x), \end{aligned} \tag{4.7}$$

where the Hadamard coefficients $\mathcal{D}^{(\mathrm{r/p})}_{ab}$ and $\mathcal{T}^{(\mathrm{r/l/p})}_{ab}$ must be computed for a metric of the form (4.1). The corresponding coefficients are reported in Appendix B.1. As discussed in Sec. 2.3, the only terms that need to be written as mode-sums are the terms that are rational and logarithmic in $\Delta\tau$ and s. To achieve this, we adopt the mode-sum representations

$$\frac{\Delta\tau^{2a+2b}}{s^{2+2b}} = \sum_{l=0}^{\infty}(2l+1)P_l(\cos\gamma)\int_{-\infty}^{\infty}d\omega\, e^{i\omega\Delta\tau}\Psi_{\omega l}(a,b|r), \tag{4.8}$$

$$\Delta\tau^{2b}s^{2a-2b}\log(s^2) = \sum_{l=0}^{\infty}(2l+1)P_l(\cos\gamma)\int_{-\infty}^{\infty}d\omega\, e^{i\omega\Delta\tau}\chi_{\omega l}(a,b|r), \tag{4.9}$$

for some yet to be determined functions $\Psi_{\omega l}(a,b|r)$ and $\chi_{\omega l}(a,b|r)$ which we call regularization parameters. Conveniently, since we are taking the radial points at coincidence ($\Delta r = 0$), s^2 is defined as in Eq. (2.6). As a result, the regularization parameters are independent of the function $h(r)$ and identical to those derived in Chapter 2. Specifically, the regularization parameters $\Psi_{\omega l}(a,b|r)$ and $\chi_{\omega l}(a,b|r)$ take the same form as in Eqs. (2.24) and (2.44), respectively.

Therefore, the expressions derived in Sec. 2.4, together with the Hadamard coefficients given in App. B.1, can be directly employed for the computation of the renormalized vacuum polarization and renormalized stress-energy tensor. For in-

stance, the renormalized vacuum polarization is

$$\langle \mathrm{B}|\hat{\Phi}^2|\mathrm{B}\rangle_{\mathrm{ren}} = \frac{1}{8\pi^2}\Bigg\{ \int_{-\infty}^{\infty} \sum_{l=0}^{\infty} (2l+1)\left(g_{\omega l}(r) - k_{\omega l}^{(n)}(r)\right) d\omega \\ - \sqrt{\pi} \sum_{a=1}^{n-1} \sum_{b=0}^{a} \mathcal{T}_{ab}^{(\mathrm{l})}(r)\, \frac{(a-1)!\, 2^{2a} f^{a-b}}{\Gamma(-a+\frac{1}{2})\lambda^{2a}} \Bigg\} \\ - \frac{1}{8\pi^2}\left[\mathcal{D}_{11}^{(\mathrm{p})}(r) + \frac{\mathcal{D}_{10}^{(\mathrm{r})}(r)}{f} + \frac{\mathcal{D}_{11}^{(\mathrm{r})}(r)}{f^2} + \mathcal{T}_{00}^{(\mathrm{l})}(r)(\log(f/(\ell^2\lambda^2)) - 2\gamma_{\mathrm{E}}) \right]. \tag{4.10}$$

As discussed in Sec. 2.4, the computation of the renormalized stress-energy tensor according to Eq. (2.50) requires the computation of the two additional mode-sums in Eqs. (2.54) and (2.55).

4.3 Thin shells in equilibrium

4.3.1 General Formalism

The spacetime we will consider is that of a spherical and static thin shell that connects a Minkowski interior with a Schwarzschild exterior, though much of the essential details can also be applied to non-vacuum interior spacetimes such as stars. The Minkowski interior is of particular interest as any curvature-dependent terms in the RSET will vanish, isolating the purely non-local nature of the contribution coming from the boundary conditions defining the quantum state and contributions coming from the matching across the shell.

To make this Chapter as self-contained as possible, we briefly review here the thin shell formalism presented in [75, 77] (and Appendix B in [78]) assuming a generic interior of the form (4.1). We will specialize for the case under consideration at the end of this section. We start by considering two spherically symmetric spacetimes

$$\begin{aligned} ds_-^2 &= -f_-(r)dt_-^2 + h_-(r)dr^2 + r^2 d\Omega^2, \quad r < r_0 \\ ds_+^2 &= -f_+(r)dt_+^2 + h_+(r)dr^2 + r^2 d\Omega^2, \quad r > r_0 \end{aligned} \tag{4.11}$$

matched at the spherical timelike boundary $r = r_0$. In order for this layer to be a solution to the Einstein equations, it must satisfy Israel-Darmois junction conditions [75, 79]. We introduce the geometrical quantities that allow us to characterize the junction conditions. We define coordinates intrinsic to our hypersurface, $\zeta^A = \{\tau, \theta, \phi\}$ where τ here is a proper time coordinate (not to be confused with Euclidean time τ). The basis vectors tangent to the hypersurface of the boundary

are thus

$$e_A^{\alpha(\pm)} = \frac{\partial x_\pm^\alpha}{\partial \zeta^A}. \tag{4.12}$$

Explicitly, we have

$$\begin{aligned} e_A^{t(\pm)} &= \left(\frac{\partial t_\pm}{\partial \tau}, 0, 0\right) = \left(\frac{1}{\sqrt{f_\pm(r)}}, 0, 0\right) \\ e_A^{r(\pm)} &= (0,0,0)\,, \quad e_A^{\theta(\pm)} = (0,1,0)\,, \quad e_A^{\phi(\pm)} = (0,0,1)\,. \end{aligned} \tag{4.13}$$

The unit spacelike vectors normal to this surface are

$$n_\alpha^{(\pm)} = \left(0, \sqrt{h_\pm(r)}, 0, 0\right). \tag{4.14}$$

Now the first Israel-Darmois junction condition demands continuity of the induced metric $h_{AB}^{(\pm)} = g_{\alpha\beta} e_A^{(\pm)\alpha} e_B^{(\pm)\beta}$ across the boundary, i.e.,

$$[\![h_{AB}]\!] = h_{AB}^{(+)} - h_{AB}^{(-)} = 0 \tag{4.15}$$

were here and throughout we have adopted the notation

$$[\![\mathcal{O}]\!] \equiv \mathcal{O}^{(+)} - \mathcal{O}^{(-)}. \tag{4.16}$$

This condition translates into the following relation between the interior and exterior time coordinates

$$\left(\frac{dt_-}{d\tau}\right)^2 = \frac{f_+(r_0)}{f_-(r_0)} \left(\frac{dt_+}{d\tau}\right)^2, \tag{4.17}$$

making g_{tt} continuous at $r = r_0$. The line-element on the hypersurface is then

$$ds^2 = h_{AB} d\zeta^A d\zeta^B = -d\tau^2 + r_0^2 d\Omega^2. \tag{4.18}$$

Since the first junction condition is a constraint on the induced metric, the function $h(r)$ can still exhibit jumps. Constraints on the jump in $h(r)$ is specified by the second junction condition. First we define the extrinsic curvature of the hypersurface as

$$K_{AB}^{(\pm)} = n_{\alpha;\beta} e_A^{(\pm)\alpha} e_B^{(\pm)\beta}, \quad K^{(\pm)} = K_{AB}^{(\pm)} h^{AB}. \tag{4.19}$$

Explicitly, we have

$$\begin{aligned}
K^{(\pm)}_{\tau\tau} =& -\frac{1}{2}\frac{f'_{\pm}(r_0)}{f_{\pm}(r_0)\sqrt{h_{\pm}(r_0)}},\\
K^{(\pm)}_{\theta\theta} =& \frac{r_0}{\sqrt{h_{\pm}(r_0)}},\\
K^{(\pm)}_{\phi\phi} =& \frac{r_0\sin^2\theta}{\sqrt{h_{\pm}(r_0)}},\\
K^{(\pm)} =& \frac{1}{2}\frac{f'_{\pm}(r_0)}{f_{\pm}(r_0)\sqrt{h_{\pm}(r_0)}} + \frac{2}{r_0}\frac{1}{\sqrt{h_{\pm}(r_0)}}.
\end{aligned} \tag{4.20}$$

The discontinuity of the extrinsic curvature across the boundary is

$$[\![K^{\tau}{}_{\tau}]\!] = \frac{1}{2}\frac{f'_{+}(r_0)}{f_{+}(r_0)\sqrt{h_{+}(r_0)}} - \frac{1}{2}\frac{f'_{-}(r_0)}{f_{-}(r_0)\sqrt{h_{-}(r_0)}}, \tag{4.21}$$

$$[\![K^{\theta}{}_{\theta}]\!] = [\![K^{\phi}{}_{\phi}]\!] = \frac{1}{r_0\sqrt{h_{+}(r_0)}} - \frac{1}{r_0\sqrt{h_{-}(r_0)}}, \tag{4.22}$$

$$\begin{aligned}
[\![K]\!] =& \frac{1}{2}\left(\frac{f'_{+}(r_0)}{f_{+}(r_0)\sqrt{h_{+}(r_0)}} - \frac{f'_{-}(r_0)}{f_{-}(r_0)\sqrt{h_{-}(r_0)}}\right)\\
&+ \frac{2}{r_0}\left[\frac{1}{\sqrt{h_{+}(r_0)}} - \frac{1}{\sqrt{h_{-}(r_0)}}\right].
\end{aligned} \tag{4.23}$$

The second Israel-Darmois junction condition identifies the behaviour in the extrinsic curvature across the boundary with the stress-energy associated to the boundary itself. In particular, discontinuity of the extrinsic curvature across the boundary indicates a thin shell with intrinsic stress-energy S_{AB} given by the Lanczos equation [80, 81]

$$8\pi S_{AB} = -\left([\![K_{AB}]\!] - [\![K]\!]h_{AB}\right). \tag{4.24}$$

To express the Ricci scalar in the four-dimensional spacetime in terms of the distributional stress-energy tensor on the hypersurface, we work in coordinates where the continuity of the metric is explicit across the shell $r = r_0$, i.e., as well as the new time coordinate τ introduced earlier, we would also introduce a proper radial coordinate z by $dz/dr = \sqrt{h_{\pm}(r)}$ for $r \gtrless r_0$ whence the metric is

$$ds^2 = -d\tau^2 + dz^2 + r^2(z)d\Omega^2 \tag{4.25}$$

where r here is given implicitly as a function of z. Then, it is straightforwardly

shown that

$$R = -8\pi S\,\delta(z - z_0), \tag{4.26}$$

where $S = h^{AB}S_{AB}$ and $z_0 = z(r_0)$. If we wish to write this in terms of the r coordinate, then, since the metric is not continuous in r, we need to define

$$R = \begin{cases} \bar{R}^-\,\delta(r - r_0), & r < r_0, \\ \bar{R}^+\,\delta(r - r_0), & r > r_0, \end{cases} \tag{4.27}$$

where we have introduced the relation

$$\bar{R}^\pm = -\frac{8\pi S}{\sqrt{h_\pm(r_0)}}. \tag{4.28}$$

On the other hand, if $f(r)$ is C^1 and $h(r)$ is C^0 at the boundary, as occurs, for example, at the surfaces of many fluid stars [82, 83], the jump in extrinsic curvature vanishes and hence there is no stress-energy associated with the boundary itself. Nevertheless, such boundaries are sharp enough as to cause a jump in Ricci scalar across the surface, which leaves an imprint in the propagation of field modes.

It is interesting to express the stress-energy tensor S_{AB} as that of a perfect fluid to obtain the surface energy density ρ and the surface tangential pressure P, where

$$S_{AB} = \rho\,u_A u_B + P\,(h_{AB} + u_A u_B)\,. \tag{4.29}$$

Specifically, we have $S^\tau{}_\tau = -\rho$ and $S^\theta{}_\theta = S^\phi{}_\phi = P$ where

$$\rho = \frac{1}{4\pi r_0}\left(\frac{1}{\sqrt{h_-(r_0)}} - \frac{1}{\sqrt{h_+(r_0)}}\right), \tag{4.30}$$

$$P = \frac{1}{8\pi r_0}\left[\frac{1}{\sqrt{h_+(r_0)}} - \frac{1}{\sqrt{h_-(r_0)}}\right] + \frac{1}{16\pi}\left(\frac{f'_+(r_0)}{f_+(r_0)\sqrt{h_+(r_0)}} - \frac{f'_-(r_0)}{f_-(r_0)\sqrt{h_-(r_0)}}\right). \tag{4.31}$$

The complete stress-energy tensor of the surface layer is then [75, 77]

$$T^{\alpha\beta} = S^{AB}e^\alpha{}_A e^\beta{}_B\,\frac{\delta(r - r_0)}{\sqrt{h_\pm(r_0)}} = S^{\alpha\beta}\,\frac{\delta(r - r_0)}{\sqrt{h_\pm(r_0)}}. \tag{4.32}$$

4.3.2 Matching Minkowski to Schwarzschild Spacetimes

Now we specialize to the case where the interior spacetime is Minkowski with line element

$$ds_-^2 = -dt_-^2 + dr^2 + r^2 d\Omega^2 \tag{4.33}$$

and the exterior spacetime is Schwarzschild with line element

$$ds_+^2 = -\left(1 - \frac{2M}{r}\right) dt_+^2 + \left(1 - \frac{2M}{r}\right)^{-1} dr^2 + r^2 d\Omega^2. \tag{4.34}$$

Now the continuity condition (4.17) implies $dt_-^2 = (1 - 2M/r_0)dt_+^2$ so we express both metrics in terms of the Schwarzschild time and drop the subscript + for typographical convenience,

$$\begin{aligned} ds_-^2 &= -\left(1 - \frac{2M}{r_0}\right) dt^2 + dr^2 + r^2 d\Omega^2, \\ ds_+^2 &= -\left(1 - \frac{2M}{r}\right) dt^2 + \left(1 - \frac{2M}{r}\right)^{-1} dr^2 + r^2 d\Omega^2. \end{aligned} \tag{4.35}$$

The Ricci scalar of the shell is (4.26) with

$$S = S^{AB} h_{AB} = \frac{1}{4\pi r_0} \left[\frac{2 - 3M/r_0}{\sqrt{1 - \frac{2M}{r_0}}} - 2 \right]. \tag{4.36}$$

In terms of the surface energy density and tangential pressure, we have

$$\begin{aligned} \rho =& \frac{1}{4\pi r_0} \left(1 - \sqrt{1 - \frac{2M}{r_0}}\right) \\ P =& -\frac{1}{8\pi r_0} \left(1 - \sqrt{1 - \frac{2M}{r_0}}\right)^{-1} - \frac{1}{8\pi r_0^2} \frac{M}{\sqrt{1 - \frac{2M}{r_0}}}. \end{aligned} \tag{4.37}$$

It is worth noting that the trace S has the following asymptotic limits

$$\begin{aligned} S \sim& \frac{1}{8\pi \sqrt{2M r_0 \left(1 - \frac{2M}{r_0}\right)}} && r_0 \to 2M \\ S \sim& -\frac{M}{4\pi r_0^2} && r_0 \to \infty, \end{aligned} \tag{4.38}$$

i.e., it is positive in the black hole limit and negative in the large-shell limit, respec-

tively. Finally, we note that the trace S can also be written as

$$S = \frac{\left(1 - 3\sqrt{1 - \frac{2M}{r_0}}\right)\rho}{2\sqrt{1 - \frac{2M}{r_0}}}, \tag{4.39}$$

showing that it vanishes exactly at the Buchdahl compactness limit $2M/r_0 = 8/9$ [76], the maximum compactness for constant-density stars in general relativity.

4.4 Numerical Approach

4.4.1 Euclidean Modes

One of the advantages of the extended coordinate prescription described in Chapter 2 is that it makes use of Euclidean techniques which simplify the calculation of the field's radial modes. In particular, the radial modes on the Lorentzian spacetime are generally oscillatory solutions (except for possible bound state modes) whereas on the Euclidean geometry, the radial modes are generally exponentially growing or decaying functions of r. Computing the Euclidean modes is computationally easier.

The coincidence limit of the one-dimensional radial Green's function appearing in the calculation of the vacuum polarization and the RSET is

$$g_{\omega l}(r) = \frac{p_{\omega l}(r)\, q_{\omega l}(r)}{N_{\omega l}}, \tag{4.40}$$

where $p_{\omega l}(r)$ and $q_{\omega l}(r)$ are linearly independent solutions to the Sturm-Liouville homogeneous second-order linear differential equation

$$\frac{d}{dr}\left(\frac{r^2\sqrt{f}}{\sqrt{h}}\frac{d\,\Upsilon_{\omega l}}{dr}\right) - \sqrt{h\,f}\left(\frac{\omega^2 r^2}{f} + l\,(l+1) + r^2(\mu^2 + \xi R)\right)\Upsilon_{\omega l} = 0 \tag{4.41}$$

and the normalization constant $N_{\omega l}$ is given by Eq. (4.5). The Boulware quantum state can be defined as a zero temperature Euclidean state and can be specified by imposing appropriate boundary conditions on these modes. The modes $p_{\omega l}(r)$ are obtained by imposing boundary conditions on the left boundary of the region of interest and integrating outward in r while $q_{\omega l}(r)$ are obtained by imposing boundary conditions on the right boundary of the region of interest and integrating inwards in r.

In our thin shell model, the spacetime is separated into two different patches, hence the solutions to Eq. (4.41) will have to be suitably connected through the shell. We denote by $\{p^{\rm M}_{\omega l}, q^{\rm M}_{\omega l}\}$ a basis of Minkowski modes, i.e., linearly independent

solutions of Eq. (4.41) with $h(r) = 1$ and $f(r) = (1-2M/r_0)$. Similarly, we denote by $\{p^{\rm S}_{\omega l}, q^{\rm S}_{\omega l}\}$ a basis of Schwarzschild modes, i.e., linearly independent solutions of with $f(r) = [h(r)]^{-1} = (1-2M/r)$. Once these bases of modes are obtained independently in each region, the Euclidean modes associated to the thin shell spacetime correspond to

$$p^{\rm shell}_{\omega l} = \begin{cases} p^{\rm M}_{\omega l}, & r < r_0 \\ a_{\omega l} p^{\rm S}_{\omega l} + b_{\omega l} q^{\rm S}_{\omega l}, & r > r_0 \end{cases} \tag{4.42}$$

and

$$q^{\rm shell}_{\omega l} = \begin{cases} c_{\omega l} p^{\rm M}_{\omega l} + d_{\omega l} q^{\rm M}_{\omega l}, & r < r_0 \\ q^{\rm S}_{\omega l}, & r > r_0 \end{cases} \tag{4.43}$$

and equivalently for their radial derivatives. The coefficients $\{a_{\omega l}, b_{\omega l}, c_{\omega l}, d_{\omega l}\}$ are found numerically by matching the Schwarzschild and Minkowski modes bases at $r = r_0$. Finally, the Wronskian constant can be related to the respective one in these mode bases via

$$N^{\rm shell}_{\omega l} = \begin{cases} d_{\omega l} N^{\rm M}_{\omega l}, & r < r_0 \\ a_{\omega l} N^{\rm S}_{\omega l}, & r > r_0. \end{cases} \tag{4.44}$$

The next two subsections contain details about how these two mode bases are calculated including the boundary conditions and the matching conditions. As we will see, the matching results in discontinuous radial derivatives for the modes at $r = r_0$.

4.4.2 Schwarzschild modes

Outside the shell, the spacetime is Schwarzschild and the homogeneous radial equation is

$$\left\{ \frac{d}{dr}\left(r^2 - 2Mr\right)\frac{d}{dr} - l\left(l+1\right) - \mu^2 r^2 - \frac{\omega^2 r^2}{1-\frac{2M}{r}} \right\} \Upsilon_{\omega l} = 0. \tag{4.45}$$

This equation has a regular singular point at $r = 2M$ and an irregular singular point at $r = \infty$. We take $p^{\rm S}_{\omega l}(r)$ to be the modes regular at $r = 2M$. This solution can be expressed in terms of the regular confluent Heun function as, assuming once again that $\omega > 0$,

$$p^{\rm S}_{\omega l}(r) = \frac{e^{-2M\omega+\Omega r}}{(2M)^{2M\omega}} \left(\frac{r}{2M} - 1\right)^{2M\omega} \mathsf{H}\left(c_1, c_2, c_3, c_4, c_5; \mathfrak{z}\right), \tag{4.46}$$

where we have labelled

$$\begin{aligned} c_1 =& l(l+1) - 2M\left\{\omega + \Omega - 2M\left[\mu^2 + 2\omega\left(\omega - \Omega\right)\right]\right\}, \\ c_2 =& 4M\left[M\left(\omega - \Omega\right)^2 - \Omega\right], \\ c_3 =& 1 + 4M\omega, \\ c_4 =& 1, \\ c_5 =& -4M\Omega, \\ \Omega =& \sqrt{\mu^2 + \omega^2}, \\ \mathfrak{z} =& 1 - \frac{r}{2M}. \end{aligned} \tag{4.47}$$

In our notation, the confluent Heun function $\mathsf{H}(c_1, c_2, c_3, c_4, c_5; \mathfrak{z})$ is the function which satisfies

$$\mathfrak{z}(\mathfrak{z}-1)\mathsf{H}''(\mathfrak{z}) + (c_3(\mathfrak{z}-1) + c_4\mathfrak{z} + \mathfrak{z}(\mathfrak{z}-1)c_5)\mathsf{H}'(\mathfrak{z}) + (c_2\mathfrak{z} - c_1)\mathsf{H}(\mathfrak{z}) = 0 \tag{4.48}$$

and is normalized to unity at $\mathfrak{z} = 0$. The advantage of expressing our solution in terms of confluent Heun functions is that an efficient routine for computing this function is built into the software package *Mathematica*.

We take as our $q^{\mathrm{S}}_{\omega l}(r)$ modes the solutions to Eq. (4.45) that are regular at $r = \infty$. While these solutions can still be expressed in terms of confluent Heun functions, they correspond to Heun functions of the logarithmic kind which are not yet implemented in *Mathematica*. We instead proceed by obtaining the $q^{\mathrm{S}}_{\omega l}(r)$ mode through direct integration of Eq. (4.45). To obtain these modes, most of the difficulty lies in reliably generating the boundary conditions at $r = \infty$. Since this is an irregular singular point, the solution for large r is an asymptotic series solution and therefore non-converging. So care is needed in truncating this series to obtain a sufficiently accurate starting value for the numerical integration. We obtain this asymptotic series solution by first factoring out the leading-order exponential behaviour from the $q^{S}_{\omega l}(r)$ modes. We write

$$q^{\mathrm{S}}_{\omega l}(r) = e^{-\Omega r}\tilde{q}_{\omega l}(r), \tag{4.49}$$

where $\tilde{q}_{\omega l}$ satisfies

$$\begin{aligned} r\left(r-2M\right)^2 \frac{d^2\tilde{q}_{\omega l}}{dr^2} + 2\left(r-2M\right)\left[2\Omega M r - M - \left(1-\Omega r\right)r\right]\frac{d\tilde{q}_{\omega l}}{dr} \\ + \Big[2\mu^2 M r^2 - l\left(l+1\right)\left(r-2M\right) \\ -2\Omega\left(2M^2 - 3Mr + r^2\right) - 4\Omega^2 M\left(r-M\right)r\Big]\tilde{q}_{\omega l} = 0. \end{aligned} \tag{4.50}$$

Assuming the series expansion

$$\tilde{q}_{\omega l} = r^{-v_0} \sum_{j=0}^{\infty} \frac{b_j}{r^j}, \tag{4.51}$$

we obtain

$$v_0 = 1 + \frac{\mu^2 M}{\Omega} + \frac{2M\omega^2}{\Omega}, \tag{4.52}$$

and the following three-term recurrence relation for the b_j coefficients

$$\begin{aligned} b_j = &\left\{4M^2 \left(v_0 + j - 3\right)^2 b_{j-3}\right. \\ &+2M \left[l\left(l+1\right) - \left(2v_0 + 2j - 5\right)\left(v_0 + j - 2 - 2\Omega M\right)\right] b_{j-2} \\ &+ \left[\left(v_0 - l + j - 2\right)\left(v_0 + l + j - 1\right)\right. \\ &\left.\left.+4\Omega^2 M^2 - 2\Omega M \left(4v_0 + 4j - 7\right)\right] b_{j-1}\right\} \\ &\times \left\{2\left[2\Omega^2 M - \mu^2 M - \Omega v_0 - 2\Omega\left(j-1\right)\right]\right\}^{-1}, \end{aligned} \tag{4.53}$$

assuming the initial conditions $b_{-2} = b_{-1} = 0$ and $b_0 = 1$.

We found it necessary to adapt the radial position of the outer boundary of our integration domain for each mode according to the specific values of l and ω to ensure that the wave equation is satisfied to our desired tolerance. Specifically, the radius at which the outer boundary conditions are imposed must be increased with both ω and l. Once this outer boundary is selected, we integrate Eq. (4.51) towards the horizon and obtain the $q^{\mathrm{S}}_{\omega l}$ mode from Eq. (4.49).

With this setup, we proceed with our mode calculation ensuring that the Wronskian condition (4.5) is satisfied everywhere up to 30 decimal places. Maintaining this degree of precision makes it very inefficient to obtain modes in the frequency range $\omega \gtrsim 20/M$. In most cases, the contribution of such high-ω modes to the RSET is negligible, with the exception of the very near-shell region.

4.4.3 Minkowski modes

The mode equation in the shell interior becomes

$$\left\{\frac{d}{dr}\left(r^2 \frac{d}{dr}\right) - \left[l\left(l+1\right) + \tilde{\Omega}^2 r^2\right]\right\} \Upsilon_{\omega l} = 0, \tag{4.54}$$

where $\tilde{\Omega}^2 = \mu^2 + \omega^2/\left(1 - 2M/r_0\right)$. Note that the frequency appearing here is different to that appearing in the usual treatment of a quantum field in Minkowski spacetime since our time coordinate on the Minkowski interior is scaled so that the metric is continuous across the shell. Apart from this trivial rescaling of the time

coordinate (and hence the frequency), the linearly independent solutions are the usual modified spherical Bessel functions. We take $p^{\rm M}_{\omega l}(r)$ to be the solution regular at the origin $r=0$ and $q^{\rm M}_{\omega l}(r)$ to be the solution regular at infinity. Hence we have

$$\begin{aligned} p^{\rm M}_{\omega l}(r) =& \sqrt{2}\left(\frac{\tilde{\Omega}}{2}\right)^{-l}\Gamma\left(l+\frac{3}{2}\right)\frac{I_{l+\frac{1}{2}}\left(\tilde{\Omega}r\right)}{\sqrt{\tilde{\Omega}r}}, \\ q^{\rm M}_{\omega l}(r) =& \frac{1}{\sqrt{2\left(1-\frac{2M}{r_0}\right)}}\left(\frac{\tilde{\Omega}}{2}\right)^{l}\sqrt{\frac{\tilde{\Omega}}{r}}\frac{K_{l+\frac{1}{2}}\left(\tilde{\Omega}r\right)}{\Gamma\left(l+\frac{3}{2}\right)}, \end{aligned} \tag{4.55}$$

where $I_{l+\frac{1}{2}}$ and $K_{l+\frac{1}{2}}$ are the modified Bessel functions [60] and we have normalized the solutions so that $N^{\rm M}_{\omega l}=1$.

4.4.4 Matching conditions at the surface

Let $\Upsilon^{\rm shell}_{\omega l}(r)$ represent either $p^{\rm shell}_{\omega l}(r)$ or $q^{\rm shell}_{\omega l}(r)$. Now we impose that our modes are continuous across the boundary which means

$$[\![\Upsilon^{\rm shell}_{\omega l}]\!]=0. \tag{4.56}$$

In terms of the Minkowski and Schwarzschild modes, this implies

$$\begin{aligned} p^{\rm M}_{\omega l}(r_0) &= a_{\omega l}\, p^{\rm S}(r_0)+b_{\omega l}\, q^{\rm S}_{\omega l}(r_0), \\ q^{\rm S}_{\omega l}(r_0) &= c_{\omega l}\, p^{\rm M}_{\omega l}(r_0)+d_{\omega l}\, q^{\rm M}_{\omega l}(r_0). \end{aligned} \tag{4.57}$$

Notice that condition (4.56) implies the shell is transparent for the scalar field, i.e., that we do not force the field itself, its radial derivative, or a combination both, to vanish at the surface. Conducting shells can be modelled by imposing Dirichlet, Neumann, or Robin boundary conditions to the field, which affect the near-shell divergences of the RVP and RSET [84]. We leave aside such situations here, focusing on the purely gravitational effect of the shell on the modes.

Now the derivatives of the modes across the shell are more complicated because of the Ricci scalar term appearing in Eq. (4.41). Integrating this equation over the interval $(r_0-\epsilon, r_0+\epsilon)$ and then taking the limit $\epsilon\to 0$ gives

$$\left[\!\!\left[\frac{1}{\sqrt{h(r)}}\frac{d\Upsilon^{\rm shell}_{\omega l}(r)}{dr}\right]\!\!\right]=-8\pi\,\xi\,S\,\Upsilon^{\rm shell}_{\omega l}(r_0). \tag{4.58}$$

So we see that the derivatives of the modes are not continuous across the shell. In fact, even for the case of minimal coupling $\xi=0$, it is $(h(r))^{-1/2}\frac{d\Upsilon^{\rm shell}_{\omega l}(r)}{dr}$ that

is continuous and not the derivative of the modes themselves. In terms of the Schwarzschild and Minkowski modes, this condition implies

$$\sqrt{1-\frac{2M}{r_0}}\left(a_{\omega l}\, p^{\mathrm{S}}_{\omega l}{}'(r_0)+b_{\omega l}\, q^{\mathrm{S}}_{\omega l}{}'(r_0)\right)-p^{\mathrm{M}\prime}_{\omega l}(r_0)=-8\pi\,\xi\,S\,p^{\mathrm{M}}_{\omega l}(r_0),$$
$$\sqrt{1-\frac{2M}{r_0}}q^{\mathrm{S}}_{\omega l}{}'(r_0)-\left(c_{\omega l}\, p^{\mathrm{M}\prime}_{\omega l}(r_0)+d_{\omega l}\, q^{\mathrm{M}\prime}_{\omega l}(r_0)\right)=-8\pi\,\xi\,S\,q^{\mathrm{S}}_{\omega l}(r_0). \tag{4.59}$$

Now solving Eq. (4.57) and (4.59) gives

$$a_{\omega l}=\frac{1}{N^{\mathrm{S}}_{\omega l}}\left[r^2\sqrt{f}\left(q^{\mathrm{S}}_{\omega l}\frac{dp^{\mathrm{M}}_{\omega l}}{dr}-8\pi\xi S p^{\mathrm{M}}_{\omega l}q^{\mathrm{S}}_{\omega l}\right)-r^2 f\, p^{\mathrm{M}}_{\omega l}\frac{dq^{\mathrm{S}}_{\omega l}}{dr}\right]_{r=r_0}$$
$$b_{\omega l}=-\frac{1}{N^{\mathrm{S}}_{\omega l}}\left[r^2\sqrt{f}\left(p^{\mathrm{S}}_{\omega l}\frac{dp^{\mathrm{M}}_{\omega l}}{dr}-8\pi\xi S p^{\mathrm{M}}_{\omega l}p^{\mathrm{S}}_{\omega l}\right)-r^2 f\, p^{\mathrm{M}}_{\omega l}\frac{dp^{\mathrm{S}}_{\omega l}}{dr}\right]_{r=r_0}$$
$$c_{\omega l}=\frac{1}{N^{\mathrm{M}}_{\omega l}}\left[r^2\sqrt{f}q^{\mathrm{M}}_{\omega l}\frac{dq^{\mathrm{S}}_{\omega l}}{dr}+8\pi\xi S r^2 q^{\mathrm{M}}_{\omega l}q^{\mathrm{S}}_{\omega l}-r^2\, q^{\mathrm{S}}_{\omega l}\frac{dq^{\mathrm{M}}_{\omega l}}{dr}\right]_{r=r_0}$$
$$d_{\omega l}=-\frac{1}{N^{\mathrm{M}}_{\omega l}}\left[r^2\sqrt{f}p^{\mathrm{M}}_{\omega l}\frac{dq^{\mathrm{S}}_{\omega l}}{dr}+8\pi\xi S r^2 p^{\mathrm{M}}_{\omega l}q^{\mathrm{S}}_{\omega l}-r^2\, q^{\mathrm{S}}_{\omega l}\frac{dp^{\mathrm{M}}_{\omega l}}{dr}\right]_{r=r_0}. \tag{4.60}$$

The above coefficients are then obtained numerically from the Schwarzschild and Minkowski modes for a large range of ω and l values.

For fixed l and large ω, each of these coefficients is an exponentially growing function of ω. This, of course, presents a numerical issue, especially when computing ratios of these coefficients for large ω. This problem can be circumvented by using a WKB approximation, which is very accurate in the large frequency regime. Although the WKB is not a uniform approximation in r and typically suffers near the black hole event horizon, this non-uniformity does not pose a problem in the context of spherical thin shells, as no event horizon is present. This way, we can obtain analytical large-frequency approximations for these matching coefficients.

4.4.5 Tests of convergence

We now have all the ingredients required to calculate the renormalized vacuum polarization and the renormalized stress-energy tensor of thin shell spacetimes. As we will see in this Subsection, only approximate numerical results can be attained as $r \to r_0$ due to a loss of convergence in the integrals and mode sums appearing in the extended-coordinate prescription. In this section, we numerically analyze the rate of convergence of the renormalized mode-sums inside and outside the thin shell and in the limit in which the surface of the shell is approached.

The renormalized integrand $g_{\omega l}-k^{(n)}_{\omega l}(r)$ can be expressed in terms of the pure

Minkowski and Schwarzschild modes using expressions (4.43) and (4.42), respectively, and the Wronskian constant relation (4.44). We find

$$g^{\rm shell}_{\omega l} = \frac{p^{\rm shell}_{\omega l} q^{\rm shell}_{\omega l}}{N^{\rm shell}_{\omega l}} = \begin{cases} \frac{p^{\rm M}_{\omega l} q^{\rm M}_{\omega l}}{N^{\rm M}_{\omega l}} + \frac{c_{\omega l}}{d_{\omega l}} \frac{\left(p^{\rm M}_{\omega l}\right)^2}{N^{\rm M}_{\omega l}}, & r < r_0 \\ \\ \frac{p^{\rm S}_{\omega l} q^{\rm S}_{\omega l}}{N^{\rm S}_{\omega l}} + \frac{b_{\omega l}}{a_{\omega l}} \frac{\left(q^{\rm S}_{\omega l}\right)^2}{N^{\rm S}_{\omega l}}, & r > r_0. \end{cases} \tag{4.61}$$

The first terms on the right-hand side of these expressions are the Green's functions in Minkowski and Schwarzschild spacetime $g^{\rm M}_{\omega l}$ and $g^{\rm S}_{\omega l}$, respectively, whose large-ω and l behaviour is exactly cancelled by the regularization parameters $k^{(n)}_{\omega l}$. The second terms, however, are a consequence of the discontinuity in the derivative of the modes induced by the shell. These boundary terms are exponentially convergent in both ω and l everywhere for $r \neq r_0$. However, the rate of convergence is not uniform in r, and indeed becomes very slow as $r \to r_0$, so that an unreasonable amount of modes could be required to compute the renormalized quantities. Exactly at $r = r_0$, these terms do not converge. In the following, we show numerical evidence for this statement.

As discussed in Sec. 2.4, in the extended coordinate prescription, the rate of convergence of the mode-sums is directly related to the order n of the expansion of the Hadamard parametrix. In general, the convergence of the mode-sums can be improved by subtracting higher-order terms of the Hadamard parametrix. The behavior of the renormalized integrand $g_{\omega l}(r) - k^{(n)}_{\omega l}(r)$ at large ω and large l depends on the order of the expansion n according to Eq. (2.58).

Let us consider, at first, a radial point on the exterior region and far enough from the shell. Fig. 4.1 reports the large-frequency trend of $g_{\omega l}(r) - k^{(n)}_{\omega l}(r)$ for a fixed l-mode, while Fig. 4.2 presents its large-l trend at fixed ω. These Figures are produced in the same fashion as those presented for the Schwarzschild case in Sec. 2.4. The logarithmic scale in the Figures is introduced for visualization purposes. Since the quantities $\log_{10}|(\omega M)^{2n+3} M(g_{\omega l} - k^{(n)}_{\omega l})|$ in Fig. 4.1 asymptote to horizontal lines in the large frequency regime, it follows that $M(g_{\omega l} - k^{(n)}_{\omega l}) \sim (\omega M)^{-2n-3}$ at large frequency, where the M factors are introduced to render all the quantities dimensionless. To simplify the notation, we omit them in the remainder of the discussion. Similarly, by inspecting the curves in Fig. 4.2, one can verify that the behavior at large l for fixed ω is $M(g_{\omega l} - k^{(n)}_{\omega l}) \sim l^{-2n-3}$. These convergence rates are in agreement with those expected from Eq. (2.58).

The interior of the shell (in case of a massless field) represents an exception to the convergence pattern in Eq. (2.58). In particular, the higher-order terms in the expansion of the Hadamard parametrix, which involve derivatives of the radial

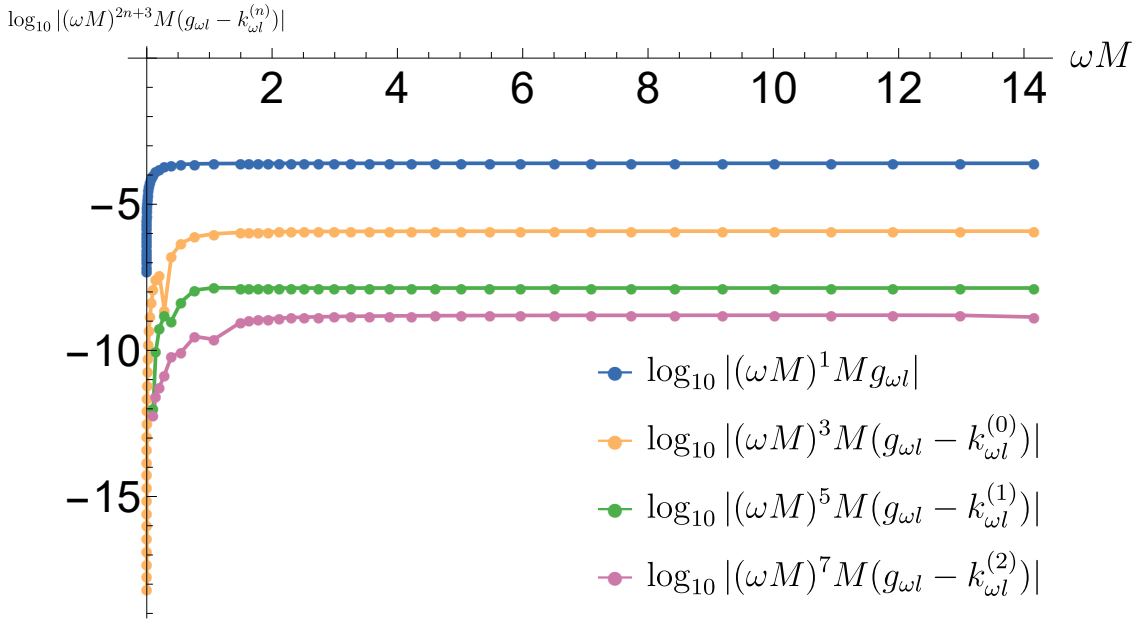


Figure 4.1: *Analysis of the convergence of $g_{\omega l}(r)-k^{(n)}_{\omega l}(r)$ for a massless scalar field on the exterior of the thin shell for $r \gg r_0$ at different orders of expansion n for fixed l and large ω. Results obtained with the set of parameters: $r_0 = 2.001M$, $r = 5M$ and $l = 1$.*

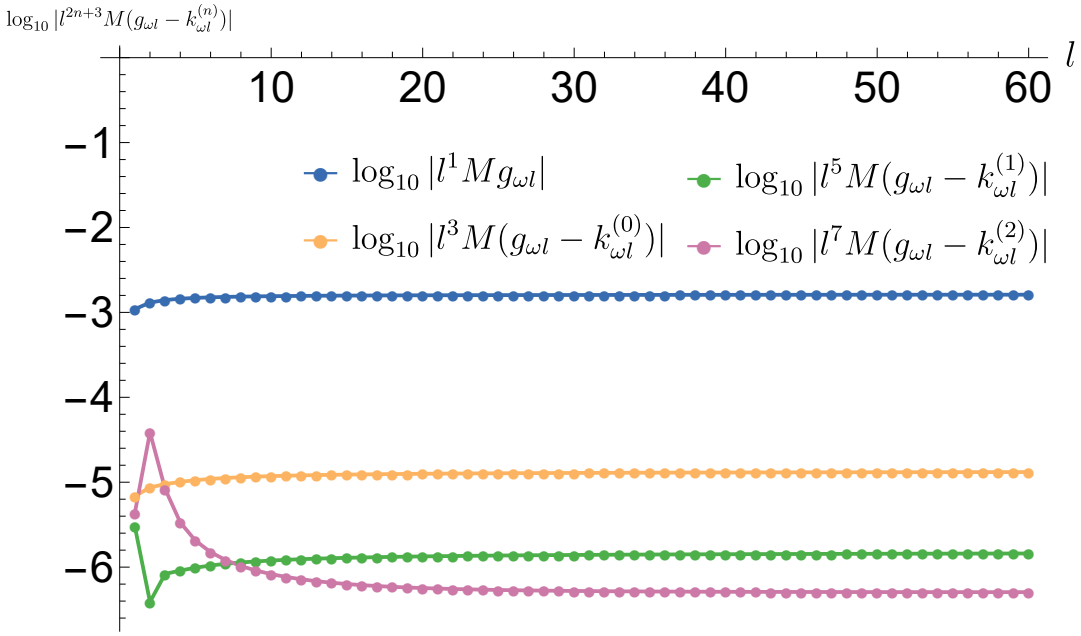


Figure 4.2: *Analysis of the convergence of $g_{\omega l}(r)-k^{(n)}_{\omega l}(r)$ for a massless scalar field on the exterior of the thin shell for $r \gg r_0$ at different orders of expansion n for fixed ω and large l. Results obtained with the set of parameters: $r_0 = 2.001M$, $r = 5M$ and $\omega M = 0.01$.*

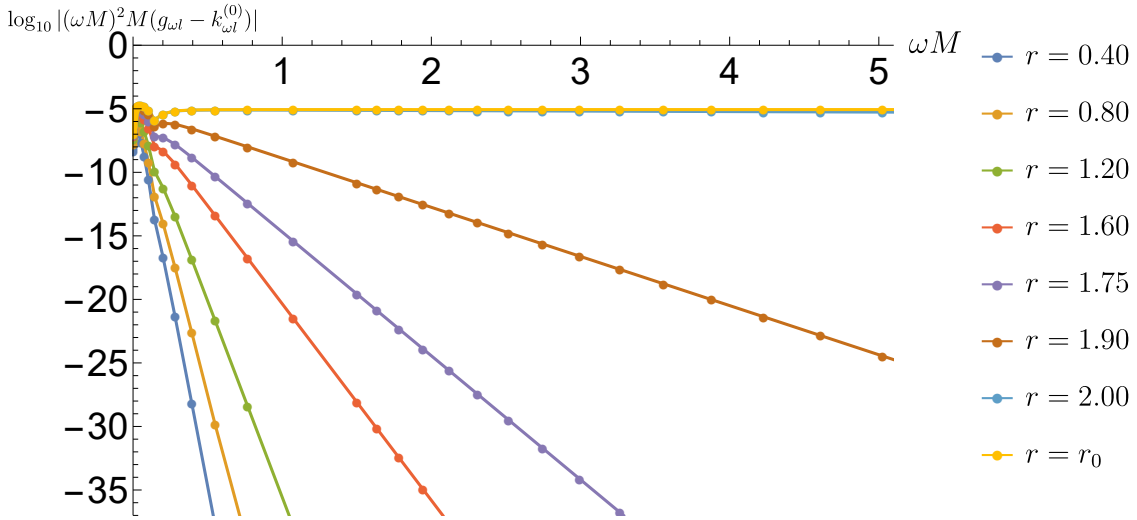


Figure 4.3: *Analysis of the convergence of $g_{\omega l}(r) - k^{(0)}_{\omega l}(r)$ for a massless scalar field on the Minkowski interior of the thin shell at different radial points for fixed l and large ω. Results obtained with the set of parameters: $r_0 = 2.001M$ and $l = 1$. The figure shows how the rate of convergence decreases as $r \to r_0$. On the surface, the function $g_{\omega l}(r_0) - k^{(0)}_{\omega l}(r_0)$ scales as ω^{-2} at large ω*

functions $f(r)$ and $h(r)$, vanish in Minkowski spacetime for a massless field. Thus, in this particular case, the Hadamard parametrix is fully encoded in the expansion up to order $n = 0$. Therefore, the Minkowski interior with a massless field provides a useful scenario for studying the convergence as the surface is approached, allowing us to isolate any loss of convergence due to the boundary.

To this end, Figures 4.3 and 4.4 show that the behavior of the renormalized integrand in the interior region for a massless scalar field at large frequency and large l strongly depends on the radial distance from the shell. As $r \to r_0$, the decay rate in ω and l of the renormalized integrand decreases rapidly as the shell surface is approached. In Figures 4.3 and 4.4, lines with a negative slope indicate a convergence rate that is faster than ω^{-2} and l^{-1}, respectively. Clearly, as $r \to r_0$, the convergence rate decreases. On the surface, $g_{\omega l}(r_0) - k^{(0)}_{\omega l}(r_0)$ scales as ω^{-2} for fixed l at large ω (as shown in Fig. 4.3), but as l^{-1} for fixed ω at large l (see Fig. 4.4). As a result, the ω-integral converges, but the l-sum diverges on the shell surface, thus making the mode-sum divergent there. Furthermore, radial points near the surface require truncating the ω-integral and the l-sum at increasingly large ω and l values to obtain accurate results, making the numerical method challenging to apply.

Now, before we discuss further the numerical results, we take a brief detour in order to better understand the expected results near the thin shell. We develop two independent approximate analytic expressions for the RVP and RSET employing a WKB approximation for the Euclidean modes and a weak field approximation.

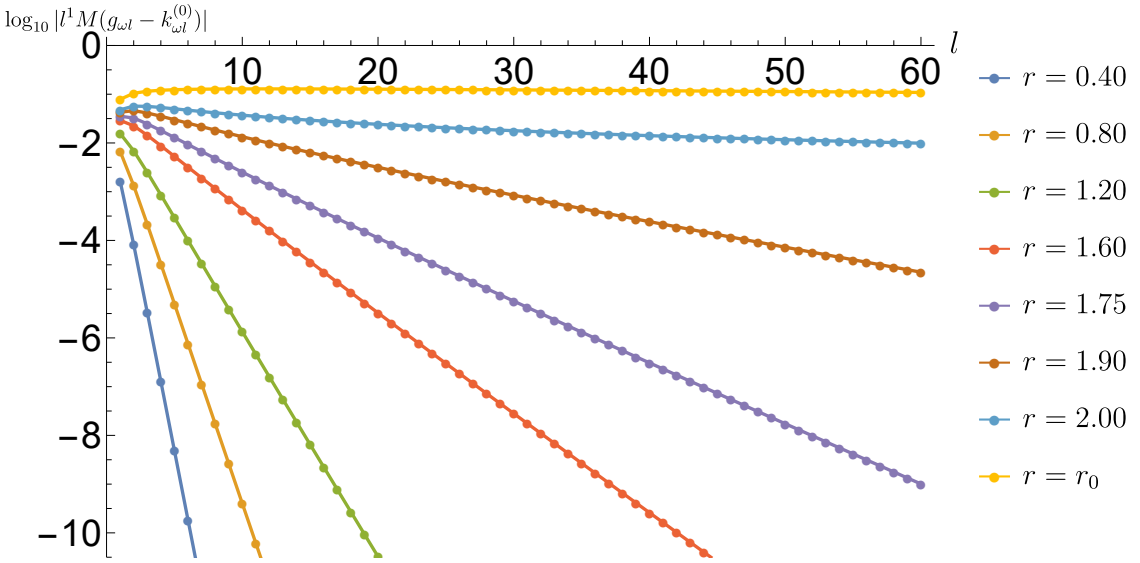


Figure 4.4: *Analysis of the convergence of $g_{\omega l}(r) - k^{(0)}_{\omega l}(r)$ for a massless scalar field on the Minkowski interior of the thin shell at different radial points for fixed ω and large l. Results obtained with the set of parameters: $r_0 = 2.001M$ and $\omega M = 0.01$. The figure shows how the rate of convergence decreases as $r \to r_0$. On the surface, the function $g_{\omega l}(r_0) - k^{(0)}_{\omega l}(r_0)$ scales as l^{-1} at large l.*

4.5 Analytical near-shell approximations

4.5.1 WKB approximation

In this Section, we will employ the WKB approximation in order to calculate the leading order divergence in the RSET components as the surface is approached.

From inspection of $g^{\text{shell}}_{\omega l}$ in Eq. (4.61) we see that the presence of the shell is encoded in the terms:

$$\frac{c_{\omega l}}{d_{\omega l}} \frac{(p^M_{\omega l}(r))^2}{N^M_{\omega l}}, \qquad \frac{b_{\omega l}}{a_{\omega l}} \frac{(q^S_{\omega l}(r))^2}{N^S_{\omega l}}. \tag{4.62}$$

Therefore, these terms must be the source of the near-shell divergence that is evident in our numerical calculations. As discussed in Subsections 4.4.4 and 4.4.5, as $r \to r_0$, the mode-sums involving the terms above are dominated by their large-ω and large-l contributions. These terms may therefore be approximated using a WKB expansion, which provides accurate results in the large ω and l regime.

We take the following WKB approximation to the mode functions in the interior

and exterior:

$$p^M_{\omega l}(r) \approx \frac{1}{\sqrt{2r^2 W_M(r)}} \exp\left[\int_{r_0}^{r} \frac{W_M(r')}{\sqrt{f(r_0)}} dr'\right] \tag{4.63}$$

$$q^M_{\omega l}(r) \approx \frac{1}{\sqrt{2r^2 W_M(r)}} \exp\left[-\int_{r_0}^{r} \frac{W_M(r)}{\sqrt{f(r_0)}} dr\right] \tag{4.64}$$

$$q^S_{\omega l}(r) \approx \frac{1}{\sqrt{2r^2 W_S(r)}} \exp\left[-\int_{r_0}^{r} \frac{W_S(r)}{f(r)} dr\right] \tag{4.65}$$

$$p^S_{\omega l}(r) \approx \frac{1}{\sqrt{2r^2 W_S(r)}} \exp\left[\int_{r_0}^{r} \frac{W_S(r)}{f(r)} dr\right] \tag{4.66}$$

where we have taken:

$$W_M^2(r) = \lambda^2 f(r_0)/r^2 + \omega^2, \quad W_S^2(r) = \lambda^2 f(r)/r^2 + \omega^2,$$

with $\lambda = l + 1/2$.

We will outline the calculation in the interior and simply present the exterior results, as the method is very similar for both. Inserting the WKB approximation and introducing a new variable $x = \lambda^2 f(r_0)/r_0^2 + \omega^2$, we obtain:

$$\frac{c_{\omega l}}{d_{\omega l}} \frac{(p^M_{\omega l}(r))^2}{N^M_{\omega l}} \approx \frac{r_0\left(x+\omega^2\right) - r_0\sqrt{f(r_0)}\left(16\pi\xi r_0 S x + x + \omega^2\right) - M\left(x+3\omega^2\right)}{r_0\sqrt{f(r_0)}\left(16\pi\xi r_0 S x + x + \omega^2\right) + M\left(x+3\omega^2\right) - r_0\left(x+\omega^2\right) - 4r_0^2 x^{3/2}} \times \frac{1}{2r^2 W_M(r)} \exp\left[\frac{2}{\sqrt{f(r_0)}} \int_{r_0}^{r} W_M(r') dr'\right]. \tag{4.67}$$

The final term in the denominator will dominate for both large ω and λ (large x), so we ignore the other terms in the denominator. We then expand the r dependent terms in the near-surface limit to obtain:

$$\frac{c_{\omega l}}{d_{\omega l}} \frac{(p^M_{\omega l}(r))^2}{N^M_{\omega l}} \approx \frac{r_0\sqrt{f(r_0)}\left(16\pi\xi r_0 S x + x + \omega^2\right) + M\left(x+3\omega^2\right) - r_0\left(x+\omega^2\right)}{4r_0^2 x^{3/2}} \times \left(\frac{1}{2r_0^2\sqrt{x}} + \frac{\varepsilon\left(x+\omega^2\right)}{2r_0^3 x^{3/2}}\right) \exp\left[-\frac{2\sqrt{x}}{\sqrt{f(r_0)}}\varepsilon\right] \left(1 + \sqrt{\frac{x}{r_0^2 f(r)}}\left(\frac{\omega^2}{x} - 1\right)\varepsilon^2\right), \tag{4.68}$$

where ε is the proper radial distance from the shell ($r_0 - r$ in interior). The leading order terms in ε are sufficient to calculate the leading order divergence in the RVP, however we require the higher order terms to correctly capture the divergence in the RSET. In order to calculate these divergences we must evaluate the following

double mode sums:

$$\begin{aligned}
&\int_0^\infty \sum_{l=0}^\infty (2l+1)\frac{c_{\omega l}}{d_{\omega l}}\frac{(p^M_{\omega l}(r))^2}{N^M_{\omega l}}d\omega,\\
&\int_0^\infty \sum_{l=0}^\infty (2l+1)\omega^2\frac{c_{\omega l}}{d_{\omega l}}\frac{(p^M_{\omega l}(r))^2}{N^M_{\omega l}}d\omega,\\
&\int_0^\infty \sum_{l=0}^\infty (2l+1)\frac{l(l+1)}{2}\frac{c_{\omega l}}{d_{\omega l}}\frac{(p^M_{\omega l}(r))^2}{N^M_{\omega l}}d\omega,
\end{aligned} \tag{4.69}$$

which is achieved by employing our approximate expression in Eq. (4.68). We will focus on the first mode sum; the procedure for the others is very similar. To evaluate the sum over l, we use the Watson-Sommerfeld formula to convert the sum into an integral, with the leading order behavior coming from:

$$\begin{aligned}
&\int_0^\infty \sum_{l=0}^\infty (2l+1)\frac{c_{\omega l}}{d_{\omega l}}\frac{(p^M_{\omega l}(r))^2}{N^M_{\omega l}}d\omega\\
&\approx \int_0^\infty \int_0^\infty 2\lambda\frac{c_{\omega\lambda}}{d_{\omega\lambda}}\frac{(p^M_{\omega\lambda}(r))^2}{N^M_{\omega\lambda}}d\lambda d\omega.
\end{aligned} \tag{4.70}$$

Using the approximate expression in Eq. (4.68), this integral can be computed in closed form in terms of the exponential integral function. Hence, we can write down the leading order divergence for the RVP in the interior:

$$\langle\hat{\Phi}^2\rangle^- = \frac{\left(\xi-\frac{1}{6}\right)S}{2\pi\varepsilon} + O(\log(\varepsilon)). \tag{4.71}$$

Similarly, we are able to calculate the leading order behavior to the other modes sums in Eq. (4.69), yielding the following expressions for the leading order divergence for the RSET components in the interior:

$$\begin{aligned}
\langle\hat{T}^t{}_t\rangle^- &= \frac{3[\![K^\tau_\tau]\!]-4\pi S}{1440\pi^2\varepsilon^3} + \frac{\left(\xi-\frac{1}{6}\right)^2 S}{\pi\varepsilon^3} + \mathcal{O}(\varepsilon^{-2})\\
\langle\hat{T}^\theta{}_\theta\rangle^- &= \frac{3[\![K^\theta_\theta]\!]-4\pi S}{1440\pi^2\varepsilon^3} + \frac{\left(\xi-\frac{1}{6}\right)^2 S}{\pi\varepsilon^3} + \mathcal{O}(\varepsilon^{-2})\\
\langle\hat{T}^r{}_r\rangle^- &= \frac{3[\![K^\theta_\theta]\!]-4\pi S}{1440\pi^2 r_0\varepsilon^2} + \frac{\left(\xi-\frac{1}{6}\right)^2 S}{r_0\pi\varepsilon^2} + O(\varepsilon^{-1}),
\end{aligned} \tag{4.72}$$

where $[\![K^\tau_\tau]\!]$ and $[\![K^\theta_\theta]\!]$ are defined in Eq. (4.21). We note that $\langle\hat{T}^\alpha{}_\beta\rangle^-$ is a conserved quantity, relative to the interior metric, to leading order in ε.

The analysis for the exterior proceeds in a similar manner and yields the following

expressions:

$$\begin{aligned}
\langle\hat{\Phi}^2\rangle^+ &= \frac{\left(\xi-\frac{1}{6}\right)S}{2\pi\varepsilon}+O(\log(\varepsilon)),\\
\langle\hat{T}^t{}_t\rangle^+ &= \frac{3[\![K^\tau_\tau]\!]-4\pi S}{1440\pi^2\varepsilon^3}+\frac{\left(\xi-\frac{1}{6}\right)^2 S}{\pi\varepsilon^3}+\mathcal{O}(\varepsilon^{-2})\\
\langle\hat{T}^\theta{}_\theta\rangle^+ &= \frac{3[\![K^\theta_\theta]\!]-4\pi S}{1440\pi^2\varepsilon^3}+\frac{\left(\xi-\frac{1}{6}\right)^2 S}{\pi\varepsilon^3}+\mathcal{O}(\varepsilon^{-2})\\
\langle\hat{T}^r{}_r\rangle^+ &= \frac{(3r_0f'(r_0)-4)(360\left(\xi-\frac{1}{6}\right)^2-1)S}{1440\pi r_0\sqrt{f(r_0)}\varepsilon^2}\\
&\quad-\frac{(3r_0f'(r_0)[\![K^\tau_\tau]\!]+f(r_0)[\![K^\theta_\theta]\!])}{1920\pi^2 r_0\sqrt{f(r_0)}\varepsilon^2}+O(\varepsilon^{-1}),
\end{aligned}\tag{4.73}$$

where ε is now the proper spatial distance outside the surface defined as

$$\varepsilon=\int_{r_0}^{r} f(r')^{-1/2}=f(r_0)^{-1/2}(r-r_0)+O\big((r-r_0)^2\big).\tag{4.74}$$

Once more $\langle\hat{T}^\alpha{}_\beta\rangle^+$ is a conserved quantity to leading order in ε, relative to the exterior Schwarzchild metric.

Interestingly, the renormalized vacuum polarization both inside (see Eq. (4.71)) and outside (see Eq. (4.73)) the shell is finite at the shell surface in the conformal case when $\xi=1/6$.

Finally, comparing the expressions in Eq. (4.73) with Eq. (4.72) and Eq. (4.71) we observe the following relationships between the leading order interior and exterior near shell divergences

$$\langle\hat{\Phi}^2\rangle^+_1=\langle\hat{\Phi}^2\rangle^-_1,\quad \langle\hat{T}^t{}_t\rangle^+_3=\langle\hat{T}^t{}_t\rangle^-_3,\quad \langle\hat{T}^\theta{}_\theta\rangle^+_3=\langle\hat{T}^\theta{}_\theta\rangle^-_3\tag{4.75}$$

where, for example, $\langle\hat{\Phi}^2\rangle^\pm_1$ denotes the coefficient of ε^{-1} in $\langle\hat{\Phi}^2\rangle^\pm$. We also note that the RSET has the correct trace in both the interior and exterior, however this is guaranteed from the construction of the RSET in Eq. (2.50).

As a check, when expressed in terms of the extrinsic curvature of the thin shell, as in Eqs. (4.72) and (4.73), the divergence structure of the RSET is found to be in agreement with the divergence obtained for a spacetime with a boundary, as studied by Deutsch and Candelas in Ref. [84], where they derived the leading-order divergences of the components of the RSET and their coefficients as the boundary is approached using a Green's function approach and conservation arguments. In principle, a stronger divergence proportional to ε^{-4} could be present, as is found in [84]. Such a term appears if the shell enforces Dirichlet, Neumann, or Robin boundary conditions on the field. The situation is even more complicated if one

assumes that there is propagation along the shell [85]. In our case, the shell is transparent, so the only scattering is due to the curvature of the spacetime. Hence the singularities appearing in the RSET are weaker and due to gravitational effects only.

4.5.2 Weak field approximation

In this section, under the assumption of small shell compactness ($M/r_0 \ll 1$), we employ a weak field approximation to analyze the behavior of the renormalized vacuum polarization and RSET in the near-shell limit. Indeed, there exist closed-form analytical expressions for renormalized expectation values on the weak-field approximated spacetime [86–88]. So, in what follows, we start simply deriving the weak-field approximation before considering a quantum field on the spacetime.

In the weak field approximation, one assumes that the metric $g_{\alpha\beta}$, which in this context satisfies the Einstein equations sourced by the stress-energy tensor of a static, spherical thin shell

$$R_{\alpha\beta} - \frac{1}{2} g_{\alpha\beta} R = 8\pi\, T^{(\text{shell})}_{\alpha\beta}, \tag{4.76}$$

can be expressed as a linear perturbation around Minkowski spacetime (see, for instance, [87]) $g_{\alpha\beta} \sim \eta_{\alpha\beta} + \epsilon\, g^{(1)}_{\alpha\beta}$, where $\eta_{\alpha\beta}$ is the Minkowski metric and ϵ is simply a bookkeeping parameter. This approximation is valid under the assumption that $|g^{(1)}_{\alpha\beta}| \ll 1$, which holds for small values of shell compactness: $M/r_0 \ll 1$. We employ similar expansions for

$$\begin{aligned} R_{\alpha\beta} &\sim R^{(0)}_{\alpha\beta} + \epsilon R^{(1)}_{\alpha\beta}, \\ R &\sim R^{(0)} + \epsilon R^{(1)}, \\ T_{\alpha\beta} &\sim T^{(0)}_{\alpha\beta} + \epsilon\, T^{(1)}_{\alpha\beta}, \end{aligned} \tag{4.77}$$

where $R^{(0)}_{\alpha\beta} = 0$ and $R^{(0)} = 0$, $T^{(0)}_{\alpha\beta} = 0$. We employ an expansion in ϵ to formally derive the zeroth and linear order Einstein equations. In addition, whenever explicit expressions for the quantities at first order in the ϵ expansion are required, namely $g^{(1)}_{\alpha\beta}$, $T^{(1)}_{\alpha\beta}$, $R^{(1)}_{\alpha\beta}$ and $R^{(1)}$, a further expansion in the compactness M/r_0 is performed for consistency. Hence, the first-order terms in the ϵ expansion are linear in M/r_0 [88]. For instance, $T^{(1)}_{\alpha\beta}$ is obtained as a linear order expansion in M/r_0 of the distributional stress-energy tensor of the shell in Eq. (4.32)

$$\begin{aligned} T^{\tau}_{\ \tau}{}^{(1)} &= -\frac{M}{4\pi r_0^2}\delta(r - r_0), \\ T^{r}_{\ r}{}^{(1)} &= T^{\theta}_{\ \theta}{}^{(1)} = T^{\phi}_{\ \phi}{}^{(1)} = 0. \end{aligned} \tag{4.78}$$

At linear order in ϵ we obtain for the Einstein equations

$$G^{(1)}_{\alpha\beta} = R^{(1)}_{\alpha\beta} - \frac{1}{2}\eta_{\alpha\beta}R^{(1)} = 8\pi\, T^{(1)}_{\alpha\beta} \tag{4.79}$$

where the Einstein tensor at linear order in ϵ is

$$G^{(1)}_{\alpha\beta} = \frac{1}{2}\Big[-\bar{\Box}\, g^{(1)}_{\alpha\beta} + 2\bar{\nabla}_\gamma\bar{\nabla}_{(\alpha}\, g^{\gamma\ (1)}_{\beta)} - \bar{\nabla}_\alpha\bar{\nabla}_\beta g^{(1)} - \eta_{\alpha\beta}(\bar{\nabla}_\gamma\bar{\nabla}_\delta g^{\gamma\delta\ (1)} - \bar{\Box} g^{(1)})\Big], \tag{4.80}$$

and $g^{(1)} = \eta^{\alpha\beta}g^{(1)}_{\alpha\beta}$ is the trace of the linear order metric. Within this section, we adopt the notation $\bar{\Box}$ and $\bar{\nabla}$ to highlight that the covariant derivatives are with respect to the flat background spacetime. To compute the perturbation to the metric at linear order $g^{(1)}_{\alpha\beta}$, we assume

$$g^{(1)}_{\alpha\beta} = \mathrm{diag}(\mathcal{A}(r), \mathcal{B}(r), 0, 0), \tag{4.81}$$

which is justified by staticity and spherical symmetry. Introducing this ansätz and the stress-energy tensor of the shell at linear order (see Eq. (4.78)) into Eqs. (4.79) and (4.80) yields for the $\tau\tau$ and rr components of the Einstein equations

$$\frac{\partial_r(r\mathcal{B}(r))}{r^2} = \frac{2M}{r_0^2}\delta(r-r_0), \tag{4.82}$$

$$-\frac{\mathcal{B}(r)}{r^2} + \frac{\mathcal{A}'(r)}{r} = 0. \tag{4.83}$$

Integrating the first equation gives

$$g^{(1)}_{rr} = \mathcal{B}(r) = \frac{2M}{r}\Theta(r-r_0) + \frac{C_1}{r} = \frac{2M}{r}\Theta(r-r_0), \tag{4.84}$$

where we have set the integration constant $C_1 = 0$, such that the interior spacetime remains Minkowski and the exterior metric retrieves the expected Schwarzschild metric at linear order. We note that, while an expression of the form $\Theta(r)/r$ is ill-defined at $r = 0$, the expression $\Theta(r-r_0)/r$ in Eq. (4.84) is instead locally integrable and well-defined as a distribution everywhere as long as $r_0 > 0$. Similarly, integrating the second equation, we obtain

$$\begin{aligned} g^{(1)}_{\tau\tau} = \mathcal{A}(r) &= \left(-\frac{2M}{r} + \frac{2M}{r_0}\right)\Theta(r-r_0) + C_2 \\ &= \left(-\frac{2M}{r} + \frac{2M}{r_0}\right)\Theta(r-r_0) - \frac{2M}{r_0}. \end{aligned} \tag{4.85}$$

We have set the integration constant $C_2 = -2M/r_0$ to reflect asymptotic flatness as

$r \to \infty$. Note also that the $\tau\tau$ component of the metric receives a shift of $-2M/r_0$ (as expected from Eq. (4.35)) in the interior, ensuring that $g^{(1)}_{\tau\tau}$ is continuous across the shell. Effectively, the perturbation on the metric generates a spacetime that is Schwarzschild (at linear order in M/r) for $r > r_0$ and that remains Minkowksi in the interior $r < r_0$. Note that integrating the linearized Einstein equations yields a metric that indeed satisfies the assumption $g^{(1)}_{\alpha\beta} \ll 1$ (if $M/r_0 \ll 1$), thereby making the perturbation theory consistent despite the presence of delta distributions in the shell's stress-energy tensor.

Introducing the metric components (4.84) and (4.85) into the equation for the Ricci tensor at linear order

$$R^{(1)}_{\alpha\beta} = \frac{1}{2}\Big[-\bar{\Box}\, g^{(1)}_{\alpha\beta} + 2\bar{\nabla}_\gamma \bar{\nabla}_{(\alpha}\, g^{\gamma\ (1)}_{\beta)} - \bar{\nabla}_\alpha \bar{\nabla}_\beta g^{(1)} \Big], \tag{4.86}$$

we find

$$\begin{aligned} R^{\tau\ (1)}_{\ \tau} &= -\frac{M}{r_0^2}\delta(r-r_0) = \bar{R}^{\tau\ (1)}_{\ \tau}\delta(r-r_0), \\ R^{r\ (1)}_{\ r} &= \frac{M}{r_0^2}\delta(r-r_0) = \bar{R}^{r\ (1)}_{\ r}\delta(r-r_0), \\ R^{\theta\ (1)}_{\ \theta} &= \frac{M}{r_0^2}\delta(r-r_0) = \bar{R}^{\theta\ (1)}_{\ \theta}\delta(r-r_0), \end{aligned} \tag{4.87}$$

and

$$R^{(1)} = R^{\alpha\ (1)}_{\ \alpha} = \frac{2M}{r_0^2}\delta(r-r_0) = \bar{R}^{(1)}\,\delta(r-r_0) = -8\pi S^{(1)}\,\delta(r-r_0), \tag{4.88}$$

where we have defined for later convenience

$$\begin{aligned} \bar{R}^{r\ (1)}_{\ r} = \bar{R}^{\theta\ (1)}_{\ \theta} = -\bar{R}^{\tau\ (1)}_{\ \tau} = \frac{M}{r_0^2}, \\ \bar{R}^{(1)} = -8\pi S^{(1)} = \frac{2M}{r_0^2}. \end{aligned} \tag{4.89}$$

Note that, at linear order, there is no need to define $\bar{R}^{(1)\ \pm}$, since $\bar{R}^{(1)\ -} = \bar{R}^{(1)\ +}$. The linearized expressions for the Ricci scalar and tensor satisfy the contracted Bianchi identities with respect to a flat background.

The renormalized vacuum polarization and the RSET of a massless scalar field in the Boulware state can be obtained from the one-loop effective action computed using covariant perturbation theory [89–91]. In the weak field regime and at linear order in $R^{(1)}$, these quantities can be expressed as [86–88]

$$\langle \hat{\Phi}^2 \rangle_{\rm ren} = \frac{1}{16\pi^2}\left(\xi - \frac{1}{6}\right)\log\left(\frac{-\bar{\Box}}{\nu^2}\right) R^{(1)}(x) \tag{4.90}$$

and

$$\langle \hat{T}^{\alpha}_{\ \beta} \rangle_{\rm ren} = -\frac{\left(\xi - \frac{1}{6}\right)^2}{16\pi^2} (\bar{\nabla}^{\alpha}\bar{\nabla}_{\beta} - \delta^{\alpha}_{\ \beta}\bar{\Box}) \log\left(\frac{-\bar{\Box}}{\nu^2}\right) R^{(1)}(x) \\ - \frac{1}{5760\pi^2}\left[(2\bar{\nabla}^{\alpha}\bar{\nabla}_{\beta} + \delta^{\alpha}_{\ \beta}\bar{\Box}) \log\left(\frac{-\bar{\Box}}{\nu^2}\right) R^{(1)}(x) - 6\bar{\Box} \log\left(\frac{-\bar{\Box}}{\nu^2}\right) R^{\alpha\ (1)}_{\ \beta}(x)\right], \tag{4.91}$$

where the nonlocal operator $\log(-\bar{\Box}/\nu^2)$ is defined through its action on $R^{(1)}(x)$ (or $R^{\alpha\ (1)}_{\ \beta}(x)$) as [87]

$$\log\left(\frac{-\bar{\Box}}{\nu^2}\right) R^{(1)}(x) = \int_{\mathbb{R}^4} d^4k\, \widetilde{R}^{(1)}(k) e^{ik\cdot x} \log\left(\frac{k^2}{\nu^2}\right), \tag{4.92}$$

where $\widetilde{R}^{(1)}(k)$ denotes the Fourier transform of $R^{(1)}(x)$, x denotes coordinates in Minkowski spacetime, ν is an arbitrary parameter, k is the four-momentum and $k^2 = \eta^{\alpha\beta}k_\alpha k_\beta$. Additionally, when the nonlocal operator in Eq. (4.92) acts on a time-independent scalar function, then its action can be simplified to [88]

$$\log\left(\frac{-\bar{\Box}}{\nu^2}\right) \varphi(\vec{x}) = -\frac{1}{2\pi} \int \mathrm{d}^3\vec{x}'\, \frac{\varphi(\vec{x}')}{|\vec{x} - \vec{x}'|^3}, \tag{4.93}$$

with φ denoting either $R^{(1)}$ or $R^{\alpha\ (1)}_{\ \beta}$ and assumed to vanish at infinity. Here, $\vec{x}$ denotes Cartesian spatial coordinates on flat spacetime. Note that the local terms dependent on $\log(\nu^2)$ have been dropped since $R^{(1)}(x) = 0$ and $R^{\alpha\ (1)}_{\ \beta}(x) = 0$ at any spacetime point outside or inside the shell. The integral in Eq. (4.93) requires regularization in the sense of distributions due to the singularity at $\vec{x}' = \vec{x}$ whenever $\varphi(\vec{x}) \neq 0$. However, in the case under consideration, where $\varphi(\vec{x}') \propto \delta(r' - r_0)$, we show in Appendix B.2 that the integral is convergent for any $r \neq r_0$ without requiring regularization.

What we need for deriving the RVP and the RSET is to compute the terms of the form $\log\left(\frac{-\bar{\Box}}{\nu^2}\right) R^{(1)}(x)$ and $\log\left(\frac{-\bar{\Box}}{\nu^2}\right) R^{\alpha\ (1)}_{\ \beta}(x)$. We leave the details of this computation in Appendix B.2, and report here the results.

Introducing the expression (B.11) into (4.90) yields the expression for the renormalized vacuum polarization

$$\langle \hat{\Phi}^2 \rangle_{\rm ren} = \begin{cases} -\frac{1}{8\pi^2}\left(\xi - \frac{1}{6}\right) \frac{\bar{R}^{(1)} r_0}{(r_0 - r)(r + r_0)}, & r < r_0, \\ -\frac{1}{8\pi^2}\left(\xi - \frac{1}{6}\right) \frac{\bar{R}^{(1)} r_0^2}{r(r - r_0)(r + r_0)}, & r > r_0, \end{cases} \tag{4.94}$$

where $\bar{R}^{(1)}$ is defined as in Eq. (4.89). Thus, taking the near-surface limit gives on

the interior

$$\langle\hat{\Phi}^2\rangle^{-}_{\rm ren} = -\frac{\left(\xi-\frac{1}{6}\right)\bar{R}^{(1)}}{16\pi^2\varepsilon} + O(\log(\varepsilon)), \tag{4.95}$$

and on the exterior

$$\langle\hat{\Phi}^2\rangle^{+}_{\rm ren} = -\frac{\left(\xi-\frac{1}{6}\right)\bar{R}^{(1)}}{16\pi^2\varepsilon} + O(\log(\varepsilon)), \tag{4.96}$$

where we adopt a notation consistent with Sec. 4.5.1.

Finally, taking the relevant derivatives of the expressions for $\log\left(\frac{-\bar{\Box}}{\nu^2}\right)R^{(1)}(x)$ and $\log\left(\frac{-\bar{\Box}}{\nu^2}\right)R^{\alpha}{}_{\beta}{}^{(1)}(x)$ derived in Appendix B.2 and substituting in Eq. (4.91) yields the components of the RSET. In the near-surface limit, the weak field approximation gives the following predictions for the leading order divergences. On the interior,

$$\begin{aligned}
\langle\hat{T}^t{}_t\rangle^{-}_{\rm ren} &= \frac{-3\bar{R}^{\tau}{}_{\tau}{}^{(1)} + \frac{\bar{R}^{(1)}}{2}}{1440\pi^2\varepsilon^3} - \frac{\left(\xi-\frac{1}{6}\right)^2\bar{R}^{(1)}}{8\pi^2\varepsilon^3} + \mathcal{O}(\varepsilon^{-2}),\\
\langle\hat{T}^\theta{}_\theta\rangle^{-}_{\rm ren} &= \frac{-3\bar{R}^{\theta}{}_{\theta}{}^{(1)} + \frac{\bar{R}^{(1)}}{2}}{1440\pi^2\varepsilon^3} - \frac{\left(\xi-\frac{1}{6}\right)^2\bar{R}^{(1)}}{8\pi^2\varepsilon^3} + \mathcal{O}(\varepsilon^{-2}),\\
\langle\hat{T}^r{}_r\rangle^{-}_{\rm ren} &= \frac{-3\bar{R}^{r}{}_{r}{}^{(1)} + \frac{\bar{R}^{(1)}}{2}}{1440\pi^2\, r_0\,\varepsilon^2} - \frac{\left(\xi-\frac{1}{6}\right)^2\bar{R}^{(1)}}{8\pi^2\, r_0\,\varepsilon^2} + \mathcal{O}(\varepsilon^{-1}),
\end{aligned} \tag{4.97}$$

and on the exterior

$$\begin{aligned}
\langle\hat{T}^t{}_t\rangle^{+}_{\rm ren} &= \frac{-3\bar{R}^{\tau}{}_{\tau}{}^{(1)} + \frac{\bar{R}^{(1)}}{2}}{1440\pi^2\varepsilon^3} - \frac{\left(\xi-\frac{1}{6}\right)^2\bar{R}^{(1)}}{8\pi^2\varepsilon^3} + \mathcal{O}(\varepsilon^{-2}),\\
\langle\hat{T}^\theta{}_\theta\rangle^{+}_{\rm ren} &= \frac{-3\bar{R}^{\theta}{}_{\theta}{}^{(1)} + \frac{\bar{R}^{(1)}}{2}}{1440\pi^2\varepsilon^3} - \frac{\left(\xi-\frac{1}{6}\right)^2\bar{R}^{(1)}}{8\pi^2\varepsilon^3} + \mathcal{O}(\varepsilon^{-2}),\\
\langle\hat{T}^r{}_r\rangle^{+}_{\rm ren} &= \frac{3\bar{R}^{r}{}_{r}{}^{(1)} - \frac{\bar{R}^{(1)}}{2}}{1440\pi^2\, r_0\,\varepsilon^2} + \frac{\left(\xi-\frac{1}{6}\right)^2\bar{R}^{(1)}}{8\pi^2\, r_0\,\varepsilon^2} + \mathcal{O}(\varepsilon^{-1}),
\end{aligned} \tag{4.98}$$

where the quantities $\bar{R}^{(1)}$, $\bar{R}^{\tau}{}_{\tau}{}^{(1)}$, $\bar{R}^{r}{}_{r}{}^{(1)}$ and $\bar{R}^{\theta}{}_{\theta}{}^{(1)}$ are defined in Eq. (4.89). Both the interior and exterior components satisfy, at leading order in ε, the conservation equation with respect to flat spacetime.

To compare these weak-field approximations to the WKB approximations of the previous section, we must expand the WKB expressions in Eqs. (4.71)-(4.73) in the small compactness parameter M/r_0, assuming this to be small. This ensures we are evaluating the WKB approximation in the same domain of validity as the weak-field approximation. When we do this, we find agreement between the two approximations for both the RVP and the RSET components.

4.6 Numerical results

Having developed analytical approximations valid in the near-shell region, where, as outlined in Section 4.4.5, obtaining accurate numerical results would require an increasingly large number of ω and l modes, thus making the numerical approach impractical, we can now proceed to compute full numerical results in the rest of the spacetime.

In all the numerical results shown in what follows, we have obtained the Euclidean modes guaranteeing a constant Wronskian up to 25 decimal places. This accuracy is enough to obtain reliable numerical results. We considered the wide range of ω values $\omega M \in [10^{-10}, 20]$, and summed up to $l = 30$ unless specified otherwise. The ω-grid was set to be denser near $\omega = 0$ and in the ω-range immediately above the cutoff. The accuracy of the obtained renormalized stress-energy tensor was assessed by verifying whether the components satisfy the conservation equation. The residual of the conservation equation was found to be approximately $3-6$ orders of magnitude smaller than the individual RSET components, except in the region near the thin shell, where the numerical results fail to capture the large-l contributions.

We first provide numerical validation of the analytical results obtained for the near-shell divergences via the WKB (and weak-field) approximations. In Figures 4.5 and 4.6, we present the renormalized vacuum polarization and stress-energy tensor near the shell surface from the inside and outside rescaled by their corresponding divergent factors to isolate the coefficients and compare them with those reported in Eqs. (4.71),(4.72), and (4.73). Specifically, we report these quantities as computed for an increasing number of l-modes. The frequency integral converges at the shell, and so it is only necessary to look at the behavior as $l_{\max}$ is increased. As expected, providing a definitive numerical validation of the analytical results proves challenging, as this would require computing an extremely large number of modes. Nonetheless, the plots indicate that, as more l-modes are included in the sum, the numerical results gradually approach the analytical predictions, thus providing numerical evidence supporting their validity. We chose to show results for a shell of $r_0 = 3M$ because bigger shells require fewer l modes to observe the surface divergences approximated clearly. We have checked that more compact shells show a similar agreement between numerical results and analytic expressions.

Next, we study the properties of the RVP and RSET for a massless minimally coupled scalar field in the bulk of the spacetime in the black hole limit, by analyzing shells of increasing compactness. Focusing first on the interior region, Fig. 4.7 shows that, near the central point $r = 0$, the values of the RVP and of the RSET components increase in magnitude as $r_0 \to 2M$, but retain finite values. The RVP

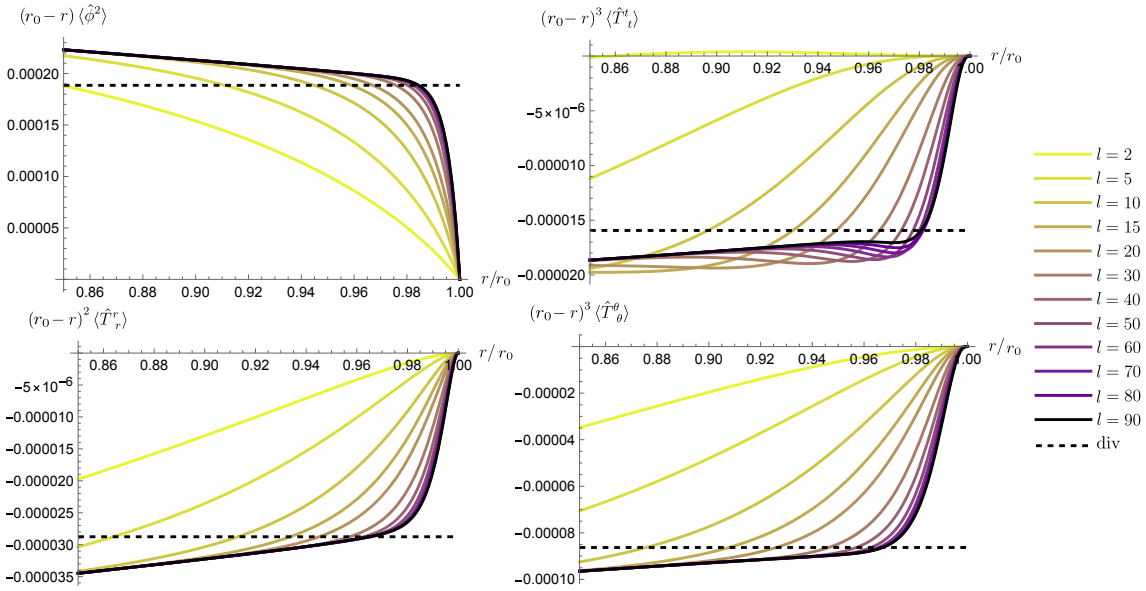


Figure 4.5: *Vacuum polarization and renormalized stress-energy tensor of a massless, minimally coupled scalar field near the surface of a spherical thin shell of radius $r_0 = 3M$ from the interior. The colored curves are purely numerical results obtained by summing up to increasing l values and integrating up to $\omega M = 20$. The black dashed lines correspond to the coefficient of the leading-order analytic divergence estimated through the WKB approximation. A tendency to approximate these values is visible for the vacuum polarization and all RSET components.*

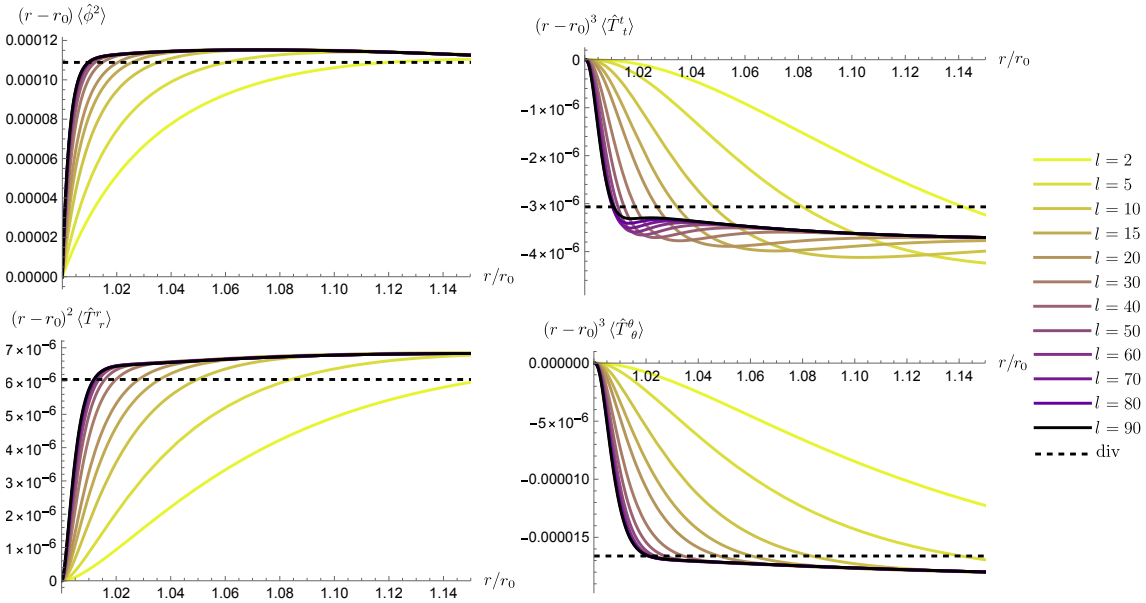


Figure 4.6: *Vacuum polarization and renormalized stress-energy tensor of a massless, minimally coupled scalar field near the surface of a spherical thin shell of radius $r_0 = 3M$ from the exterior. The colored curves are purely numerical results obtained by summing up to increasing l values and integrating up to $\omega M = 20$. The black dashed lines correspond to the coefficient of the leading-order analytic divergence estimated through the WKB approximation. A tendency to approximate these values is visible for the vacuum polarization and all RSET components.*

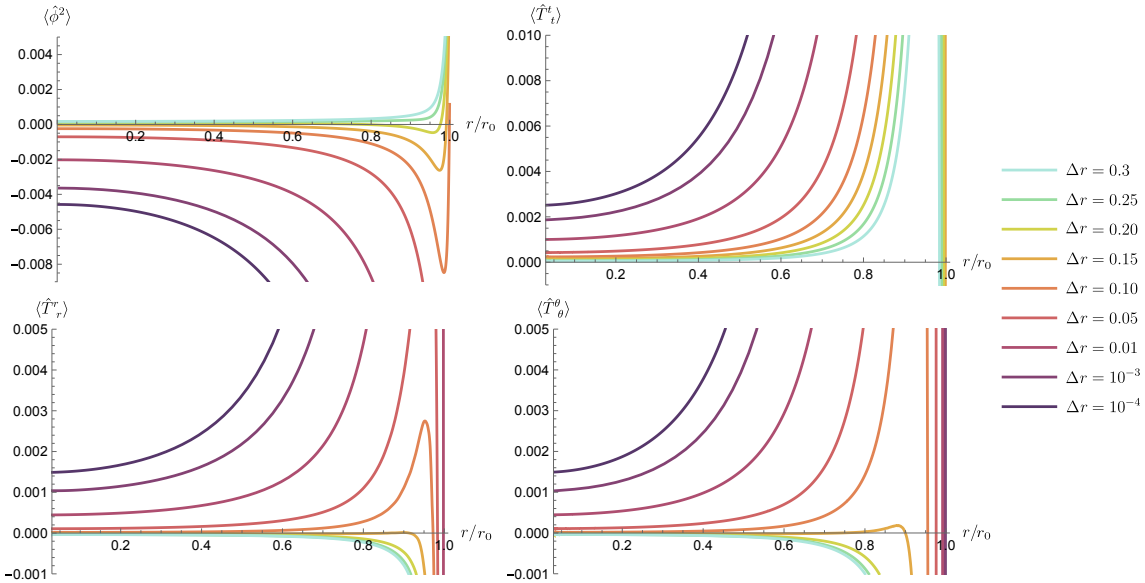


Figure 4.7: *Renormalized vacuum polarization and renormalized stress-energy tensor of a massless, minimally coupled scalar field inside spherical thin shells of different radii r_0. These are purely numerical results obtained by summing up to $l = 30$ and integrating up to $\omega M = 20$. Results near the surface of the shell are missing large-l contributions that would make them agree with our analytic results. For the computation of this plot, we have fixed $M = 1$ and considered shells of decreasing radii $r_0/M = \{2.30, 2.25, 2.20, 2.15, 2.10, 2.05, 2.01, 2.001, 2.0001\}$. We defined $\Delta r = r_0 - 2M$.*

and the radial and angular components of the RSET change sign as the shell radius reduces to around $r_0 \sim 2.15M$, while the energy density remains always negative. We note that, as discussed earlier in the Chapter, near the shell, our numerical results are not accurate, as they miss important large frequency and large l contributions. Figure 4.8 reports the corresponding results on the exterior. In the exterior region, the vacuum polarization and the energy density are negative for any compactness value, while the pressures change sign as r_0 decreases. In this Figure, we also compare the RVP and RSET results for a minimally coupled, massless scalar field in the Boulware state propagating in a Schwarzschild black hole spacetime. As the compactness is increased, both the RVP and all the RSET components approach those corresponding to the Boulware vacuum of a Schwarzschild black hole for radial points far enough from the shell.

4.7 Backreaction effects at the surface of the shell

In this Section, we will compute the backreaction effects produced by the RSET in the interior region of the shell. The analysis can be straightforwardly extended to the exterior, but the simplicity of the interior region allows us to calculate the backreacted metric analytically near the surface of the shell. Said metric is computed

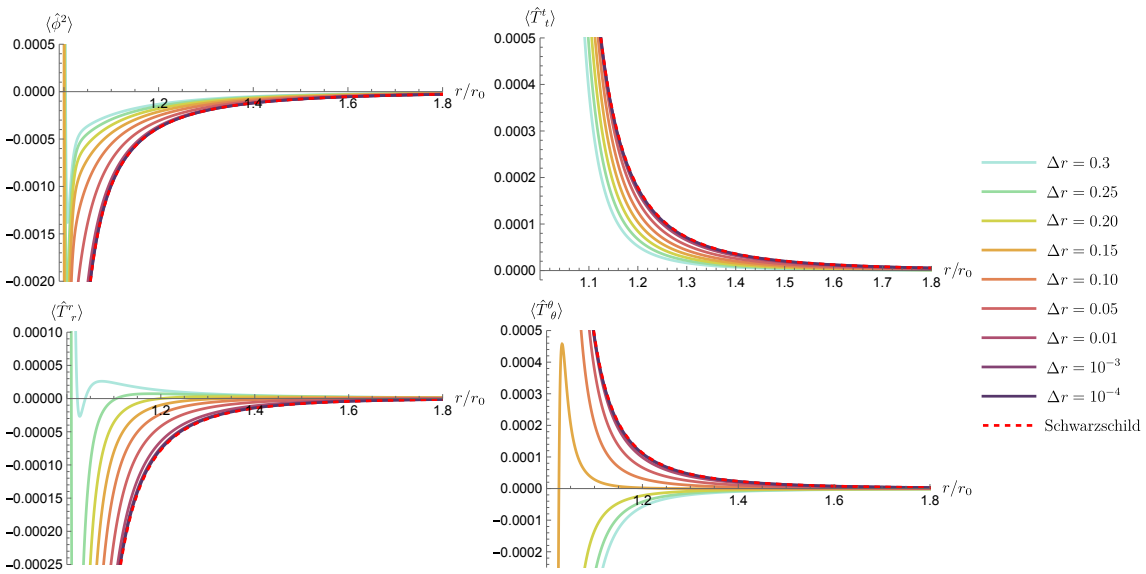


Figure 4.8: *Renormalized vacuum polarization and renormalized stress-energy tensor of a massless, minimally coupled scalar field outside spherical thin shells of different radii. These are purely numerical results obtained by summing up to $l = 30$ and integrating up to $\omega M = 20$. Results near the surface of the shell are missing large-l contributions that would make them agree with our analytic results. For the computation of this plot, we have fixed $M = 1$ and considered shells of decreasing radii $r_0/M = \{2.30, 2.25, 2.20, 2.15, 2.10, 2.05, 2.01, 2.001, 2.0001\}$. We defined $\Delta r = r_0 - 2M$.*

by linearizing the semiclassical Einstein equations (1.87).

We expand the metric as $\mathsf{g}_{\alpha\beta} = g_{\alpha\beta} + \epsilon h_{\alpha\beta}$. It is clear that $H^{(1)}_{\alpha\beta} = H^{(2)}_{\alpha\beta} = 0$ everywhere except on the shell, since in Ricci-flat spacetimes ($R_{\alpha\beta} = R = 0$). Hence, they do not contribute to the equations at linear order in ϵ both inside and outside the shell, notably simplifying the analysis. At first order in ϵ, we have

$$\delta G_{\alpha\beta} + \delta G^{-1}\, G_{\alpha\beta} + \delta\Lambda\, g_{\alpha\beta} = 8\pi\, \langle \hat{T}_{\alpha\beta} \rangle_{\rm ren}, \tag{4.99}$$

where we have written the renormalized constants in the form $\Lambda + \epsilon\delta\Lambda$ (with the background value $\Lambda = 0$) and $G + \epsilon\delta G$. There is an additional ambiguity in the form of a renormalization lengthscale entering the RSET [45], but it can also be checked to vanish in the case under consideration. The perturbation of the Einstein tensor is given explicitly in Eq. (1.91).

Inside the shell, where the metric $g_{\alpha\beta}$ is Minkowski, we have $G_{\alpha\beta} = 0$, hence the second term in Eq. (4.99) is absent. We further assume $\delta\Lambda = 0$ for simplicity. The resulting $\mathcal{O}(\epsilon)$ equations inside the shell are

$$\delta G_{\alpha\beta} = 8\pi \langle \hat{T}_{\alpha\beta} \rangle_{\rm ren}. \tag{4.100}$$

Adopting the same procedure as in Sec. 3.4, we write the full metric coefficients as

$$\mathsf{g}_{tt} = -e^{2\psi(r)}\left(1-2m(r)/r\right), \quad \mathsf{g}_{rr} = \left(1-2m(r)/r\right)^{-1}, \tag{4.101}$$

where $m(r)$ denotes the Misner-Sharp mass, and then we expand these metric functions as

$$\psi(r) = \frac{1}{2}\log\left(1-\frac{2M}{r_0}\right)\left(1+\epsilon\mathcal{R}(r)\right), \quad m(r) = \epsilon\mathcal{M}(r). \tag{4.102}$$

We obtain the following tt and rr components of the linearized semiclassical Einstein equations

$$\begin{aligned} -\frac{2\epsilon\mathcal{M}'}{r^2} =& 8\pi\epsilon\langle\hat{T}^t{}_t\rangle + \mathcal{O}\left(\epsilon^2\right), \\ \frac{\epsilon\left(-2\mathcal{M}'+r\mathcal{R}'\right)}{r^2} =& 8\pi\epsilon\langle\hat{T}^r{}_r\rangle + \mathcal{O}\left(\epsilon^2\right), \end{aligned} \tag{4.103}$$

where we have dropped the subscript 'ren' for typographical convenience. These can be combined to produce a differential equation for $\mathcal{R}$

$$\frac{\epsilon\mathcal{R}'}{r} = 8\pi\epsilon\left(\langle\hat{T}^r{}_r\rangle - \langle\hat{T}^t{}_t\rangle\right) + \mathcal{O}\left(\epsilon^2\right) \tag{4.104}$$

We are going to solve these equations near the surface of the shell $r \to r_0$.

The tt component of the RSET obeys the near-shell expansion

$$\langle\hat{T}^t{}_t\rangle = \frac{\langle\hat{T}^t{}_t\rangle_3^-}{(r_0-r)^3} + \mathcal{O}\left(r_0-r\right)^{-2}, \tag{4.105}$$

where $\langle\hat{T}^t{}_t\rangle_3^-$ is the coefficient of the leading-order divergence in Eq. (4.72). Recall the divergence in the $\langle\hat{T}^r{}_r\rangle$ component is subleading. Replacing (4.105) in Eq. (4.103), we find

$$\begin{aligned} \mathcal{R}(r) =& -\frac{4\pi r_0}{(r_0-r)^2}\langle\hat{T}^t{}_t\rangle_3^- + \mathcal{O}\left(r_0-r\right)^{-1}, \\ \mathcal{M}(r) =& -\frac{2\pi r_0^2}{(r_0-r)^2}\langle\hat{T}^t{}_t\rangle_3^- + \mathcal{O}\left(r_0-r\right)^{-1}. \end{aligned} \tag{4.106}$$

When inserted in the Ricci scalar, these functions yield $R \propto (r_0-r)^{-4}$, indicating the presence of a curvature singularity at $r = r_0$ generated by the backreaction of the RSET. Of course, since the RSET is infinite, the validity of truncating the semiclassical equations to linear order in ϵ is put into question. Hence, the metric functions (4.106) should be interpreted as the proof that static idealized infinitesimally thin shells break down the perturbative character of the semiclassical expansion.

4.8 Conclusions

In this Chapter, we presented a detailed analysis of the features of the renormalized vacuum polarization and stress-energy tensor for a quantum scalar field in the Boulware vacuum, propagating in a spacetime with a static, spherical thin shell matching a Minkowski interior to a Schwarzschild exterior. In line with the previous Chapters, we once again treated the Boulware state as a zero temperature state, defined on the Wick-rotated Riemannian manifold. This allowed us to employ the renormalization prescription outlined in Ch. 2, requiring only a modification of the Hadamard coefficients to adapt them to a general static, spherically symmetric metric of the form (4.1).

Having outlined the renormalization approach, we have then presented Israel's thin shell formalism and applied it to a spherical thin shell joining Minkowski and Schwarzschild spacetimes. Then, we showed how the Euclidean modes, necessary for the computation of the Euclidean Green's function for the wave equation on the thin-shell spacetime of the shell, are most efficiently obtained as a linear combination of the Minkowski and Schwarzschild modes, with the coefficients computed by matching conditions at the shell. This formulation also explicitly isolates the boundary terms, which encode the presence of the shell and associated Casimir-type non-Hadamard divergences, in the Green's function. The methodology we have introduced in this work can be generalized, in a straightforward way, to other static material configurations with Schwarzschild exteriors.

To estimate how renormalized expectation values diverge at the shell, we adopted a WKB approximation for the Euclidean modes. We found the power and sign of these divergences to be in agreement with results in flat spacetime with a boundary [84]. As an independent consistency check, we also implemented a weak-field approximation [87] valid in the regime of small shell compactness, $M/r_0 \ll 1$. We showed that a thin shell can arise from perturbations of a Minkowski background, and we computed the RVP and RSET at leading order in M/r_0. The obtained results were in agreement with the WKB ones at leading order in M/r_0. We also performed a backreaction calculation near $r = r_0$ to estimate the quantum corrections to the background metric.

Having determined the analytical properties of the Boulware vacuum at the boundaries of the spacetime, we then carried out an extensive numerical analysis, evaluating the RVP and RSET throughout the spacetime over a wide range of parameters. We first provided a numerical verification of the divergent behavior obtained with the analytic methods, by computing the RVP and the RSET near the shell for an increasing number of l-modes and showing that the coefficients of the leading-order divergences for each component seem to approach their analytical

predictions in the limit as $l \to l_{\max}$, both inside and outside the shell. Additionally, we evaluated the RVP and RSET for thin shells of different compactness. In this setting, near the central point $r = 0$, the values of the RVP and of the RSET components increase with the compactness, but remain finite in the black hole limit.

The work presented in this Chapter represents the first step in a broader program of computing renormalized quantities in a variety of spacetimes describing compact objects. A natural and straightforward extension of this study would be to consider shells with finite thickness. These models would make it possible to disentangle the Boulware divergence of the RSET in the black hole limit from the additional divergences associated with the sharp boundary in the thin-shell idealization. Unfortunately, deriving smooth thick shell models having the right distributional stress-energy tensor in the thin shell limit is a sophisticated problem.

Furthermore, the generality of our treatment makes it simple to consider different shell interiors. For example, spherical shells enclosing a static de Sitter (gravastars [92]) or anti de Sitter (AdS-stars [78]) interior have been proposed as black hole mimickers supported by vacuum polarization effects. It would therefore be interesting to investigate the properties of the Boulware vacuum in these scenarios as well.

Finally, another interesting scenario in which the renormalization method described in this Chapter can be employed is that of spacetimes describing compact stars in equilibrium. In general relativity, Buchdahl's theorem establishes an upper limit on the compactness of a spherically symmetric object composed of isotropic matter [76]. Beyond this compactness, the object would collapse into a black hole. The Buchdahl limit is reached when the pressures of the fluid diverge at their center. We expect the vicinity of this situation to generate strong vacuum polarization effects that will backreact on the background [93–95], either taming this growth of the pressure (relaxing the compactness bound), or stimulating it (making the bound more stringent). This direction is currently being explored.

Chapter 5

Vacuum polarization and renormalized stress-energy tensor on the interior of a Reissner-Nordström black hole

5.1 Introduction

In this Chapter, we leave behind the treatment of compact objects and return to the subextremal Reissner-Nordström black hole, focusing on its interior region. Like the Kerr black hole, the Reissner-Nordström spacetime is of particular interest for the study of quantum fields because of the presence of an inner Cauchy horizon. The existence of a Cauchy horizon poses a challenge to determinism in general relativity, since it marks the boundary of the region of spacetime uniquely determined from a suitable set of initial data on a Cauchy surface [17]. This motivated the formulation of the strong cosmic censorship conjecture [96], which suggests that for generic initial data, the solution spacetime determined by the data should not be extendible as a suitably regular Lorentzian manifold [97].

When classical matter perturbations are introduced into the spacetime, the blue-shift instability can lead to the formation of a null curvature singularity along the Cauchy horizon of both charged black holes [98–103] and spinning black holes [104–106]. However, this singularity is known to be weak in Tipler's sense [107], both in the charged [100] and rotating case [104, 108], meaning that an infalling observer is not necessarily destroyed by tidal deformations before the $r = 0$ singularity becomes visible.

Quantum effects have long been expected to have a stronger influence on the stability of the Cauchy horizon [109, 110]. Recent semiclassical studies have rein-

forced this picture in both the Reissner-Nordström-de Sitter (RNdS) [111–114] and Reissner-Nordström spacetimes [115, 116].

In Reissner-Nordström spacetime, recent works based on the pragmatic mode-sum regularization method have initially focused on the computation of the renormalized vacuum polarization for massless, minimally coupled, scalar fields on the black hole interior [117–119]. These studies showed that the computation of the RVP near the Cauchy horizon is already a nontrivial task. In [119], it was shown that RVP is finite at the Cauchy horizon for massless, minimally coupled fields in both the Hartle-Hawking and Unruh states. Establishing this result required obtaining numerical results at extraordinarily small distances from the Cauchy horizon, together with analytical approximations for the dominant inverse-power tails in the tortoise coordinate r_*^{-k} that describe the approach of the renormalized vacuum polarization to its Cauchy horizon value.

In subsequent studies, the PMR method was then employed to obtain the semi-classical stress-energy fluxes for a minimally coupled massless scalar field near the Cauchy horizon of a Reissner-Nordström black hole. The fluxes are found to be nonzero for both the Hartle-Hawking and Unruh states in sub-extremal Reissner-Nordström black holes [115] and to vanish in the extremal limit [116].

This Chapter presents a renormalization method for studying the effects of massive quantum fields in the interior region of a Reissner-Nordström black hole, allowing for arbitrary coupling to the gravitational background. To this end, we generalize the extended coordinate prescription to black hole interiors, working directly in the Lorentzian manifold for the first time.

This Chapter is organized as follows. In Sec. 5.2, we first construct the Wightman propagator for massive fields in the Hartle-Hawking and Unruh states in the interior of a Reissner-Nordström black hole. In Sec. 5.3 we discuss a renormalization prescription for computing quantum expectation values in the interior of static, spherically symmetric black holes. We show that renormalization parameters derived for zero-temperature states on the Euclidean exterior are precisely those required for the Hartle-Hawking and Unruh states on the Lorentzian interior. We discuss the numerical approach in Sec. 5.4, while Sec. 5.5 provides a detailed discussion on the convergence of the mode-sums. In Sections 5.6 and 5.7, we apply the new method to compute the renormalized vacuum polarization and the renormalized stress-energy tensor for massless and massive quantum scalar fields in the interior region of a Reissner-Nordström black hole. Finally, in Sec. 5.8, we conclude with a discussion.

5.2 The two-point function for a massive field inside a Reissner-Nordström black hole

5.2.1 A Basis of Separable Modes

We want to express the Wightman propagator for a massive neutral scalar field in the Unruh [11] and Hartle-Hawking [37, 120] states on the interior of a Reissner-Nordström black hole in terms of the modes in static Schwarzschild coordinates. The metric in these coordinates is

$$ds^2 = -f(r)dt^2 + \frac{dr^2}{f(r)} + r^2\left(d\theta^2 + \sin^2\theta\, d\phi^2\right), \tag{5.1}$$

where

$$f(r) = 1 - \frac{2M}{r} + \frac{Q^2}{r^2}, \tag{5.2}$$

with M and Q the mass and charge of the black hole, respectively, where we assume $Q < M$. Even though the Unruh and Hartle-Hawking states are defined in terms of null coordinates, not static coordinates, the advantage of working in these coordinates is that the wave equation is separable, and it is possible to re-express the Unruh and Hartle-Hawking propagators on the exterior in terms of the resultant separable modes. The goal of this section is to show how to analytically continue the Wightman functions in the Unruh and Hartle-Hawking states across the event horizon and express them in terms of separable modes in the (t, r, θ, ϕ) coordinates. This latter part is non-trivial since the boundary conditions for the Unruh and Hartle-Hawking states are not defined in terms of the modes in Schwarzschild coordinates, even though the Wightman propagators themselves are most easily computed in terms of these modes.

Let us start by obtaining a basis of the separable mode solutions to the Klein-Gordon equation in the massive case in Schwarzschild coordinates. The Klein-Gordon equation for a scalar field Φ is

$$(\Box - \mu^2 - \xi R)\Phi = 0, \tag{5.3}$$

where $\Box$ is the d'Alambertian operator, μ is the mass of the scalar field, ξ is its coupling to the gravitational background, and R is the Ricci scalar. Although $R = 0$ in the case of Reissner-Nordström spacetime, we have included ξR in Eq. (5.3) for generality. Specifically, while the present Chapter and Chapter 6 focus on the Reissner-Nordström spacetime, the renormalization prescription we present in Sec. 5.3 is valid for a generic spherically symmetric spacetime, including spacetimes with a nonva-

nishing Ricci scalar, for example, Reissner-Nordström-de Sitter. In addition, the renormalized stress-energy tensor still depends on the coupling ξ, even when $R = 0$. We take as a basis

$$u_{\omega lm} = \mathcal{N}_\omega e^{-i\omega t} Y_{lm}(\theta, \phi) \Phi_{\omega l}(r), \tag{5.4}$$

where the indices are $\omega \in \mathbb{R}$, $l \in \mathbb{N}$ and $m = -l, ..., l$, $\mathcal{N}_\omega$ is a normalization constant, $Y_{lm}(\theta, \phi)$ are the spherical harmonics normalized by

$$\int_0^{2\pi} d\phi \int_0^{\pi} \sin\theta \, d\theta \, Y_{lm}(\theta, \phi) \, Y^*_{l'm'}(\theta, \phi) = \delta_{ll'} \delta_{mm'}, \tag{5.5}$$

and $\Phi_{\omega l}(r)$ is a solution of the radial equation

$$\left[\frac{d}{dr} \left(r^2 f(r) \frac{d}{dr} \right) + \frac{\omega^2 r^2}{f(r)} - \mu^2 r^2 - l(l+1) \right] \Phi_{\omega l}(r) = 0. \tag{5.6}$$

It is helpful to recast this equation in Schrödinger form by writing $\Phi_{\omega l}(r) = \psi_{\omega l}(r)/r$, where $\psi_{\omega l}(r)$ satisfies

$$\left\{ \frac{d^2}{dr_*^2} + V_{\omega l}(r) \right\} \psi_{\omega l}(r) = 0, \tag{5.7}$$

where we have employed the radial tortoise coordinate

$$r_* = r + \frac{1}{2\kappa_+} \ln \left(\frac{|r - r_+|}{r_+ - r_-} \right) + \frac{1}{2\kappa_-} \ln \left(\frac{|r - r_-|}{r_+ - r_-} \right), \tag{5.8}$$

with $r_\pm = M \pm \sqrt{M^2 - Q^2}$ the two Killing horizons corresponding to the event horizon (upper sign) and Cauchy horizon (lower sign), and $\kappa_\pm = \frac{1}{2} f'(r_\pm)$ the respective surface gravity of these Killing horizons. We note that with this definition, $\kappa_- < 0$. The potential in the radial equation is

$$V_{\omega l}(r) = \omega^2 - f(r) \left(\mu^2 + \frac{l(l+1)}{r^2} + \frac{f'(r)}{r} \right). \tag{5.9}$$

Note that the potential asymptotes to

$$V_{\omega l}(r) \sim \begin{cases} \omega^2, & r \to r_\pm, \\ \omega^2 - \mu^2, & r \to \infty. \end{cases} \tag{5.10}$$

For a massive field, we see that the nature of the boundary conditions as $r \to \infty$ will depend on the sign of $\omega^2 - \mu^2$. Regardless of this sign, there is also a choice to

be made for the branch of the square root. We define

$$\begin{aligned} \tilde{\omega} &:= \mathrm{sgn}(\omega)\sqrt{\omega^2-\mu^2}, & \omega^2 &> \mu^2, \\ \Omega &:= \sqrt{\mu^2-\omega^2}, & \omega^2 &< \mu^2. \end{aligned} \tag{5.11}$$

First considering the regime $\omega^2 > \mu^2$, we define a useful pair of linearly independent solutions to the radial equation. We illustrate these solutions in Fig. 5.1. We label the solution $\psi^{\mathrm{in}}_{\omega l}(r)$ as the one with boundary condition

$$\psi^{\mathrm{in}}_{\omega l}(r) \sim \begin{cases} B^{\mathrm{in}}_{\omega l} e^{-i\omega r_*}, & r \to r_+, \\ \\ e^{-i\tilde{\omega} r_*} + A^{\mathrm{in}}_{\omega l} e^{i\tilde{\omega} r_*}, & r \to \infty, \end{cases} \tag{5.12}$$

where $B^{\mathrm{in}}_{\omega l}$ and $A^{\mathrm{in}}_{\omega l}$ are respectively the dimensionsless transmission and reflection coefficients for the "in" mode. If we were to consider also the harmonic time dependence, we can interpret the "in" mode as a unit-amplitude wave originating at past null infinity $\mathscr{I}^-$ which scatters off the background curvature, partially reflecting back to future null infinity $\mathscr{I}^+$ and partially transmitting to the future event horizon $\mathcal{H}_R$. These modes are shown in Figure 5.1.

For the other independent solution, we label $\psi^{\mathrm{up}}_{\omega l}(r)$ as the one with boundary conditions

$$\psi^{\mathrm{up}}_{\omega l}(r) \sim \begin{cases} e^{i\omega r_*} + A^{\mathrm{up}}_{\omega l} e^{-i\omega r_*}, & r \to r_+ \\ \\ B^{\mathrm{up}}_{\omega l} e^{i\tilde{\omega} r_*}, & r \to \infty, \end{cases} \tag{5.13}$$

where $B^{\mathrm{up}}_{\omega l}$ and $A^{\mathrm{up}}_{\omega l}$ are the transmission and reflection coefficients for the "up" mode, respectively. Again, if we were to factor in the harmonic time dependence, the "up" mode would correspond to a unit-amplitude wave propagating out of the past event horizon $\mathcal{H}_{\mathrm{past}}$ partially reflecting back to the future event horizon and partially transmitting to future null infinity. This is plotted in Fig. 5.1.

When $\omega^2 < \mu^2$, the corresponding "in" mode is exponentially growing at infinity

$$\psi^{\mathrm{in}}_{\omega l}(r) \sim e^{\Omega r_*}, \ (\omega^2 < \mu^2) \qquad r \to \infty. \tag{5.14}$$

The exponential growth of the modes for $\omega^2 < \mu^2$ means that within this regime there are no normalizable eigenfunctions for the eigenvalue problem defined by Eq. (5.3); i.e., the interval $\omega^2 < \mu^2$ is not in the spectrum of the differential operator in Eq. (5.3) with the "in" boundary conditions. Hence, although it is mathematically possible

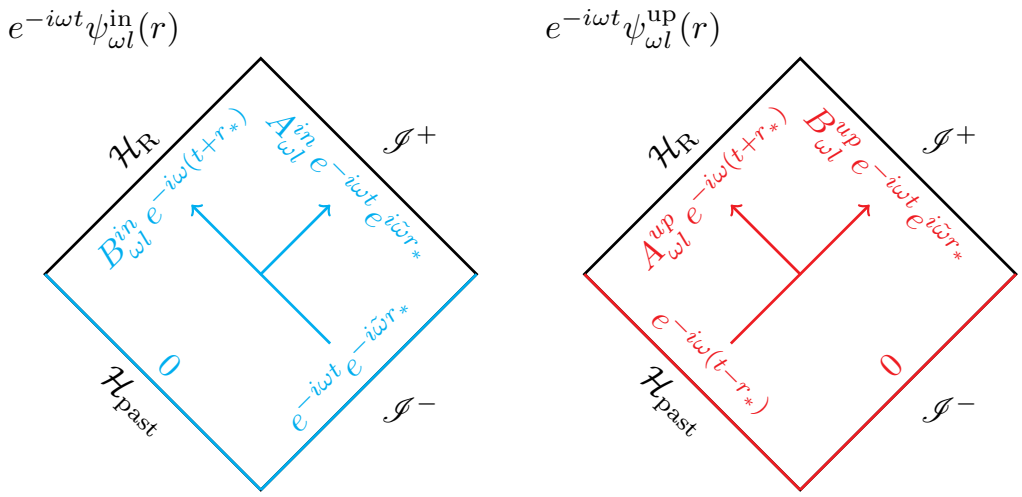


Figure 5.1: *Exterior separable "in" and "up" modes illustrated on the right wedge of the Penrose diagram of the Reissner-Nordström black hole.*

to define the "in" modes in the regime $\omega^2 < \mu^2$, these modes must be excluded from the construction of the Wightman function. On the other hand, the "up" modes, when $\omega^2 < \mu^2$, are defined by the asymptotic form

$$\psi^{\rm up}_{\omega l}(r) \sim \begin{cases} e^{i\omega r_*} + A^{\rm up}_{\omega l} e^{-i\omega r_*}, & r \to r_+, \\ \\ B^{\rm up}_{\omega l} e^{-\Omega r_*}, & r \to \infty, \end{cases} \tag{5.15}$$

and are hence exponentially damped at infinity. The "up" modes with $\omega^2 < \mu^2$ are known as the bound state modes, since they are localized near the event horizon, and are to be included in the classical phase space of normalizable (see below) solutions. The "up" modes for $\omega^2 < \mu^2$ are also represented in Fig. 5.1.

With these independent radial solutions defined, we have $\Phi^{\rm in/up}_{\omega l}(r) := \psi^{\rm in/up}_{\omega l}(r)/r$. Hence, our basis modes to the wave operator consist of

$$u^{\rm in/up}_{\omega lm}(x) = \mathcal{N}^{\rm in/up}_{\omega} e^{-i\omega t} Y_{lm}(\theta,\phi) \Phi^{\rm in/up}_{\omega l}(r), \tag{5.16}$$

where $\mathcal{N}^{\rm in/up}_{\omega}$ are normalization constants. The "in" modes are defined for $\omega^2 > \mu^2$ and satisfy the boundary conditions in Eq. (5.12). The "up" modes are defined for all $\omega \in \mathbb{R}$ and satisfy the boundary conditions in Eqs. (5.13) and (5.15). We refer to these modes as the "Boulware modes". If we endow the phase space of classical solutions with the Klein-Gordon inner product

$$\langle u_J, u_{J'} \rangle = -i \int_\Sigma \left(u_J \nabla_\alpha u^*_{J'} - u^*_{J'} \nabla_\alpha u_J \right) n^\alpha d\Sigma, \tag{5.17}$$

where J runs over the indices $\{\omega, l, m\}$ and the integral here is over a Cauchy

surface Σ with unit future-directed normal n^α. We move the Cauchy surface onto $\mathcal{H}_{\rm past} \cup \mathscr{I}^-$, where we can take advantage of the fact that we have simple boundary conditions $u^{\rm in}_J = 0$ on $\mathcal{H}_{\rm past}$ and $u^{\rm up}_J = 0$ on $\mathscr{I}^-$. Hence, it can be shown that

$$\begin{aligned} \langle u^{\rm in}_J, u^{\rm in}_{J'} \rangle &= 4\pi\, \tilde{\omega} |\mathcal{N}^{\rm in}_\omega|^2 \delta_{JJ'}, \quad (\omega^2 > \mu^2), \\ \langle u^{\rm up}_J, u^{\rm up}_{J'} \rangle &= 4\pi\, \omega |\mathcal{N}^{\rm up}_\omega|^2 \delta_{JJ'}, \end{aligned} \tag{5.18}$$

where $\delta_{JJ'} := \delta(\omega - \omega')\delta_{ll'}\delta_{mm'}$. These conditions imply that the "in" modes have positive norm only for $\tilde{\omega} > 0$ while the "up" modes have positive norm only for $\omega > 0$. We see clearly now that the appropriate normalized solutions have normalization factors

$$\begin{aligned} \mathcal{N}^{\rm in}_\omega &= \frac{1}{\sqrt{4\pi|\tilde{\omega}|}}, \quad (\omega^2 > \mu^2), \\ \mathcal{N}^{\rm up}_\omega &= \frac{1}{\sqrt{4\pi|\omega|}}. \end{aligned} \tag{5.19}$$

Moreover, the constancy of the Wronskian of linearly independent solutions of the radial equation implies for $\omega^2 > \mu^2$

$$\begin{aligned} \tilde{\omega}\left[1 - |A^{\rm in}_{\omega l}|^2\right] &= \omega |B^{\rm in}_{\omega l}|^2, \\ \omega\left[1 - |A^{\rm up}_{\omega l}|^2\right] &= \tilde{\omega} |B^{\rm up}_{\omega l}|^2, \\ \tilde{\omega} B^{\rm up}_{\omega l} &= \omega B^{\rm in}_{\omega l}, \end{aligned} \tag{5.20}$$

while, for the bound state modes,

$$|A^{\rm up}_{\omega l}|^2 = 1, \qquad \omega^2 < \mu^2. \tag{5.21}$$

5.2.2 The Boulware State

To define the field in the Boulware vacuum state [38], we note the modes $u^{\rm in/up}_{\omega lm}$ are positive frequency with respect to Schwarzschild time t along $\mathscr{I}^-$ and $\mathcal{H}_{\rm past}$ respectively. Positive norm "in" modes have $\tilde{\omega} > 0$, while positive norm "up" modes have $\omega > 0$. We can then expand the quantum field in these modes as

$$\begin{aligned} \hat{\Phi}(x) = &\sum_{l=0}^{\infty} \sum_{m=-l}^{l} \int_\mu^\infty d\omega \left(\hat{a}^{\rm in}_{\omega lm} u^{\rm in}_{\omega lm}(x) + \hat{a}^{\rm in\,\dagger}_{\omega lm} u^{\rm in\,*}_{\omega lm}(x) \right) \\ &+ \sum_{l=0}^{\infty} \sum_{m=-l}^{l} \int_0^\infty d\omega \left(\hat{a}^{\rm up}_{\omega lm} u^{\rm up}_{\omega lm}(x) + \hat{a}^{\rm up\,\dagger}_{\omega lm} u^{\rm up\,*}_{\omega lm}(x) \right) \end{aligned} \tag{5.22}$$

where $\hat{a}^{\text{in/up}}_{\omega lm}$ are some operator coefficients and we have used the fact that the transformation $\omega \to -\omega$ in the basis corresponds to complex conjugation, given that $B^{\text{in/up}}_{\omega l}$ are chosen to satisfy this symmetry. The operator coefficients in this expansion satisfy the commutation relations

$$[\hat{a}^{\text{in}}_J, \hat{a}^{\text{in}\,\dagger}_{J'}] = \delta_{JJ'}, \qquad [\hat{a}^{\text{up}}_J, \hat{a}^{\text{up}\,\dagger}_{J'}] = \delta_{JJ'}, \tag{5.23}$$

with all other commutators vanishing. The Boulware vacuum is then defined by

$$\begin{aligned} \hat{a}^{\text{in}}_{\omega lm}|\text{B}\rangle &= 0, \qquad \tilde{\omega} > 0, \\ \hat{a}^{\text{up}}_{\omega lm}|\text{B}\rangle &= 0, \qquad \omega > 0. \end{aligned} \tag{5.24}$$

Finally, the Wightman function for a massive scalar field in the Boulware vacuum is given by

$$\begin{aligned} G_{\text{B}}(x,x') =& \langle \text{B}|\hat{\Phi}(x)\,\hat{\Phi}(x')|\text{B}\rangle \\ =& \sum_{l=0}^{\infty}\sum_{m=-l}^{l}\left[\int_{\mu}^{\infty} d\omega\, u^{\text{in}}_{\omega lm}(x) u^{\text{in}\,*}_{\omega lm}(x') + \int_{0}^{\infty} d\omega\, u^{\text{up}}_{\omega lm}(x) u^{\text{up}\,*}_{\omega lm}(x')\right]. \end{aligned} \tag{5.25}$$

It is well-known that this vacuum state is not a Hadamard state on the event horizon [39] (see also the results presented in Chapter 3) and hence cannot be extended into the interior. We have defined the Boulware state for completeness, even though it will not be used explicitly in this Chapter.

5.2.3 The Unruh state on the interior

In this section, we derive the Wightman two-point function in terms of *separables* modes on the black hole interior for a massive scalar field in the Unruh state. This is accomplished by introducing a set of non-separable modes defined across both the exterior and interior regions of the black hole, which we call "Unruh modes" and encode the boundary conditions for the Unruh state. We then introduce a new set of separable modes defined only on the interior and establish a mapping between these two sets of modes, expressing the Wightman function in terms of the separable modes, which can be conveniently computed numerically.

To define the Unruh modes, it is necessary to introduce two additional sets of coordinates: the Eddington–Finkelstein coordinates and the Kruskal coordinates. The Eddington-Finkelstein coordinates are

$$u = \pm(t - r_*), \qquad v = t + r_*, \tag{5.26}$$

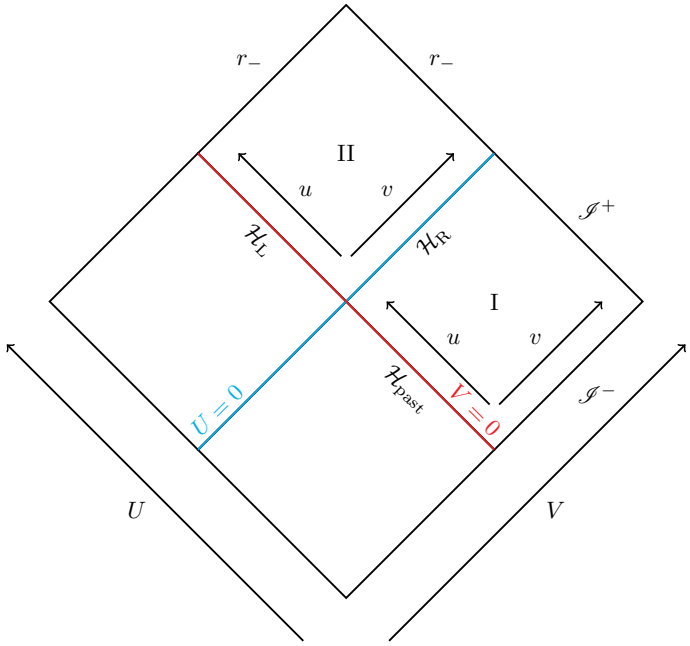


Figure 5.2: *Penrose diagram of the Reissner-Nordström black hole. Highlighted are the surfaces $U = 0$ and $V = 0$.*

where the upper $(+)$ sign in the definition of u corresponds to the exterior while the lower $(-)$ sign corresponds to the interior. The Kruskal coordinates are defined as follows

$$U = \mp \frac{1}{\kappa_+} e^{\mp \kappa_+ u}, \quad V = \frac{1}{\kappa_+} e^{\kappa_+ v}, \tag{5.27}$$

where again the upper sign is for the exterior and the lower sign for the interior. These additional sets of coordinates are reported in Fig. 5.2, which depicts the Penrose diagram of the Reissner-Nordström spacetime. The Unruh state is defined by treating the modes originating from the past horizon on a different footing to those originating at past null infinity. We write the Unruh mode solutions of the scalar field equation (5.3) as

$$\begin{aligned} g^{\mathrm{in}}_{\omega lm} &= \frac{1}{\sqrt{4\pi|\tilde{\omega}|}} Y_{lm}(\theta,\phi) \frac{1}{r} \chi^{\mathrm{in}}_{\omega l}(U,V), \quad (\omega^2 > \mu^2), \\ g^{\mathrm{up}}_{\omega lm} &= \frac{1}{\sqrt{4\pi|\omega|}} Y_{lm}(\theta,\phi) \frac{1}{r} \chi^{\mathrm{up}}_{\omega l}(U,V), \quad (\omega \in \mathbb{R}). \end{aligned} \tag{5.28}$$

where $r = r(U,V)$ and $\chi^{\mathrm{in/up}}_{\omega l}$ are obtained by inserting this ansätz into the wave equation (5.3) expressed in Kruskal coordinates. We will refer to the modes $g^{\mathrm{in/up}}_{\omega lm}$ as the "Unruh modes". Note that these modes are not separable. The appropriate

boundary condition on the "up" modes is

$$\chi^{\rm up}_{\omega l} \sim \begin{cases} e^{-i\omega U}, & V = 0, \\ 0, & \mathscr{I}^-. \end{cases} \tag{5.29}$$

The surface $V = 0$ covers both the past event horizon $\mathcal{H}_{\rm past}$ and the left event horizon (or the future event horizon of the other external universe) $\mathcal{H}_{\rm L}$ (See Fig. 5.3). We see that the $g^{\rm up}_{\omega lm}(x)$ modes are positive frequency with respect to U along $V = 0$. Employing the inner product (5.17) it is also readily shown that the modes satisfy the correct normalization condition

$$\langle g^{\rm up}_J, g^{\rm up}_{J'} \rangle = \delta_{JJ'}, \quad \omega > 0, \tag{5.30}$$

and have positive norm when $\omega > 0$.

For the "in" modes, when $\omega^2 > \mu^2$, the Unruh boundary conditions are

$$\chi^{\rm in}_{\omega l} \sim \begin{cases} 0, & V = 0, \\ e^{-i\omega t} e^{-i\tilde{\omega} r_*}, & \mathscr{I}^-, \end{cases} \tag{5.31}$$

so that the modes originating at past null infinity are positive frequency with respect to Schwarzschild time along $\mathscr{I}^-$. Note that $g^{\rm in}_{\omega lm} \equiv u^{\rm in}_{\omega lm}$ in the exterior. When $\omega^2 < \mu^2$, the radial dependence for the Unruh "in" modes will be analogous to that of the Boulware $u^{\rm in}_{\omega lm}$ modes and therefore will be exponentially growing at infinity. Hence, the $g^{\rm in}_{\omega lm}$ with $\omega^2 < \mu^2$ are excluded from the construction of the Wightman function. As in the Boulware case, the Unruh "in" modes with $\tilde{\omega} > 0$ have positive unit norm with respect to the inner product:

$$\langle g^{\rm in}_J, g^{\rm in}_{J'} \rangle = \delta_{JJ'}, \quad \tilde{\omega} > 0. \tag{5.32}$$

We can perform an analogous quantization procedure to the one adopted above by expanding the quantum field in terms of the Unruh modes as

$$\begin{aligned} \hat{\Phi}(x) = &\sum_{l=0}^{\infty} \sum_{m=-l}^{l} \int_{\mu}^{\infty} d\omega \, \left(\hat{b}^{\rm in}_{\omega lm} g^{\rm in}_{\omega lm}(x) + \hat{b}^{\rm in\,\dagger}_{\omega lm} g^{\rm in\,*}_{\omega lm}(x) \right) \\ &+ \sum_{l=0}^{\infty} \sum_{m=-l}^{l} \int_{0}^{\infty} d\omega \, \left(\hat{b}^{\rm up}_{\omega lm} g^{\rm up}_{\omega lm}(x) + \hat{b}^{\rm up\,\dagger}_{\omega lm} g^{\rm up\,*}_{\omega lm}(x) \right) \end{aligned} \tag{5.33}$$

where $\hat{b}^{\rm in/up}_{\omega lm}$ and $\hat{b}^{\rm in/up\ \dagger}_{\omega lm}$ are annihilation and creation operators respectively and we have used the fact that the transformation $\omega \to -\omega$ corresponds to complex

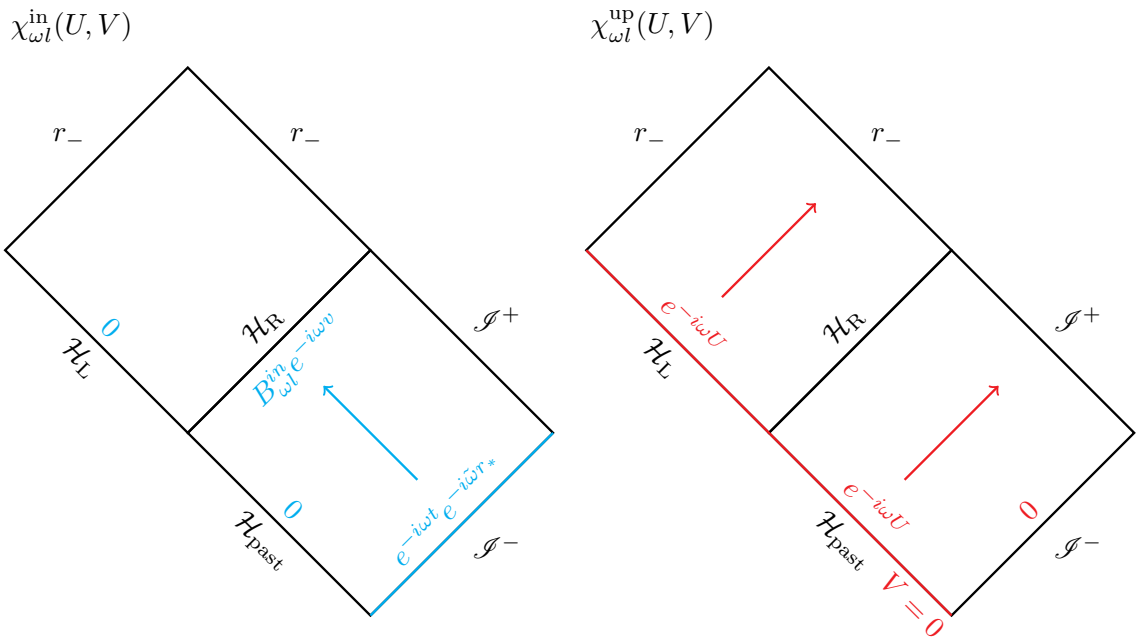


Figure 5.3: *Unruh "in" and "up" modes represented on the exterior and interior regions of the Penrose diagram of the Reissner-Nordström black hole.*

conjugation. The operators satisfy the commutation relations

$$[\hat{b}^{\rm in}_J, \hat{b}^{\rm in\,\dagger}_{J'}] = \delta_{JJ'}, \qquad [\hat{b}^{\rm up}_J, \hat{b}^{\rm up\,\dagger}_{J'}] = \delta_{JJ'}, \tag{5.34}$$

with all other commutators vanishing. The Unruh vacuum is defined by

$$\begin{aligned} \hat{b}^{\rm in}_{\omega lm}|{\rm U}\rangle &= 0, \qquad \tilde{\omega} > 0, \\ \hat{b}^{\rm up}_{\omega lm}|{\rm U}\rangle &= 0, \qquad \omega > 0. \end{aligned} \tag{5.35}$$

This yields the following Wightman two-point function for a massive scalar field in the Unruh state

$$\begin{aligned} G_{\rm U}(x,x') &= \langle {\rm U}|\hat{\Phi}(x)\,\hat{\Phi}(x')|{\rm U}\rangle \\ &= \sum_{l=0}^{\infty}\sum_{m=-l}^{l}\left[\int_{\mu}^{\infty} d\omega\, g^{\rm in}_{\omega lm}(x) g^{\rm in\,*}_{\omega lm}(x') + \int_{0}^{\infty} d\omega\, g^{\rm up}_{\omega lm}(x) g^{\rm up\,*}_{\omega lm}(x')\right]. \end{aligned} \tag{5.36}$$

Note that the previous expression is valid both in the interior and in the exterior of the black hole. As already mentioned, the problem is that the modes are not separable in (U,V) coordinates. However, on the exterior spacetime, it is known

how to express the Unruh modes in terms of the Boulware modes above [3, 39, 121]:

$$G^{\rm ext}_{\rm U}(x,x') = \sum_{l=0}^{\infty}\sum_{m=-l}^{l}\left[\int_{\mu}^{\infty} d\omega\, u^{\rm in}_{\omega lm}(x)u^{\rm in\,*}_{\omega lm}(x') + \int_{0}^{\infty} d\omega \coth\left(\frac{\omega\pi}{\kappa_+}\right) u^{\rm up}_{\omega lm}(x)u^{\rm up\,*}_{\omega lm}(x')\right]. \tag{5.37}$$

The question is whether we can express the Unruh modes in terms of separable modes on the interior. This was achieved for massless fields in Ref. [117] and we modify and extend their analysis here. We start with an independent set of basis modes on the interior, defined $\forall\omega \in \mathbb{R}$ and only in region II of the diagram in Fig. 5.2,

$$\begin{aligned}\varpi^{\rm L}_{\omega lm} &= \frac{1}{\sqrt{4\pi|\omega|}} Y_{lm}(\theta,\phi)\frac{1}{r}\zeta^{\rm L}_{\omega l}(u,v),\\ \varpi^{\rm R}_{\omega lm} &= \frac{1}{\sqrt{4\pi|\omega|}} Y_{lm}(\theta,\phi)\frac{1}{r}\zeta^{\rm R}_{\omega l}(u,v),\end{aligned} \tag{5.38}$$

with boundary conditions

$$\zeta^{\rm L}_{\omega l}(u,v) \sim \begin{cases} e^{-i\omega u} & \mathcal{H}_{\rm L}\\ 0 & \mathcal{H}_{\rm R}\end{cases} \tag{5.39}$$

and

$$\zeta^{\rm R}_{\omega l}(u,v) \sim \begin{cases} 0 & \mathcal{H}_{\rm L}\\ e^{-i\omega v} & \mathcal{H}_{\rm R}.\end{cases} \tag{5.40}$$

These modes are now easily expressed in separable (t,r) coordinates as

$$\zeta^{\rm L}_{\omega l}(t,r) = e^{i\omega t}\Psi^{\rm II}_{\omega l}(r), \qquad \zeta^{\rm R}_{\omega l}(t,r) = e^{-i\omega t}\Psi^{\rm II}_{\omega l}(r), \tag{5.41}$$

where $\Psi^{\rm II}_{\omega l}(r)$ is a solution to the radial equation (5.7) satisfying the boundary condition

$$\Psi^{\rm II}_{\omega l}(r) \sim e^{-i\omega r_*}, \quad r \to r_+. \tag{5.42}$$

We illustrate the interior modes in Fig. 5.4.

Starting with the "in" modes, we wish to obtain the map between the $g^{\rm in}_{\omega lm}$ modes and the $\varpi^{\rm R}_{\omega lm}$ modes. Noting that $\chi^{\rm in}_{\omega l} \sim e^{-i\omega t}e^{-i\tilde{\omega}r_*}$ on $\mathscr{I}^-$ as well as $\chi^{\rm in}_{\omega l} \sim 0$ on

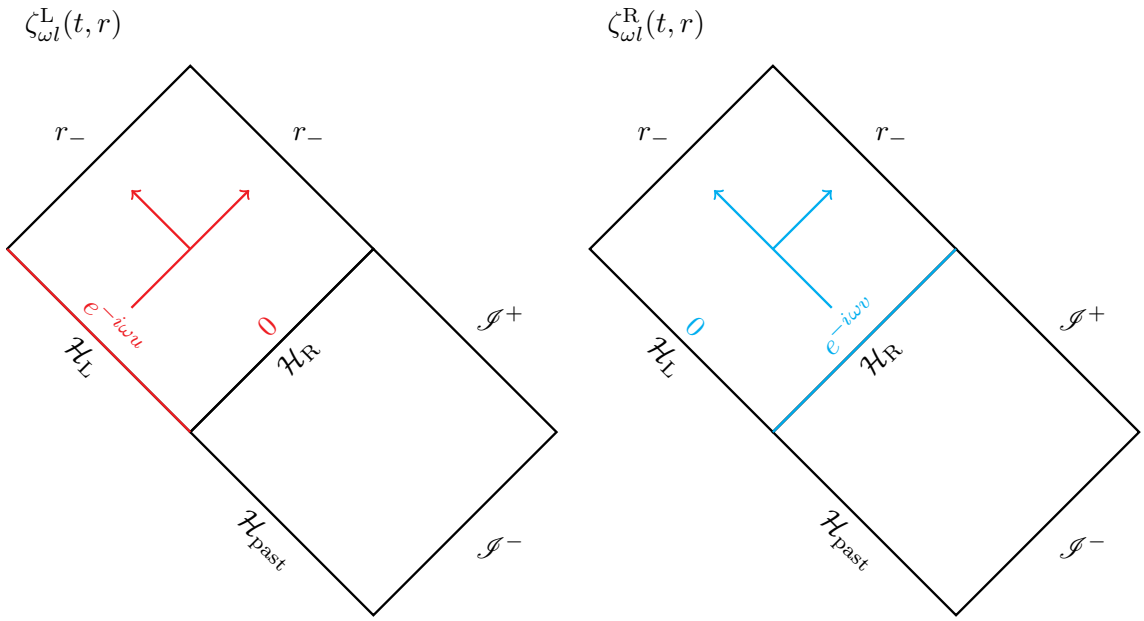


Figure 5.4: *Interior separable "L" and "R" modes represented on the interior region of the Penrose diagram of the Reissner-Nordström black hole.*

$\mathcal{H}_{\mathrm{past}}$, we can propagate this mode to $\mathcal{H}_R$ to obtain

$$g^{\mathrm{in}}_{\omega lm}\Big|_{\mathcal{H}_R} \sim \frac{1}{\sqrt{4\pi|\tilde{\omega}|}} Y_{lm}(\theta,\phi) B^{\mathrm{in}}_{\omega l} \frac{e^{-i\omega v}}{r_+}. \tag{5.43}$$

We also have that

$$\varpi^{\mathrm{R}}_{\omega lm}\Big|_{\mathcal{H}_R} \sim \frac{1}{\sqrt{4\pi|\omega|}} Y_{lm}(\theta,\phi) \frac{e^{-i\omega v}}{r_+}. \tag{5.44}$$

In general, a positive frequency Unruh mode $g^{\mathrm{in}}_{\omega lm}$ may have a mix of positive and negative frequency $\varpi^{\mathrm{R}}_{\omega lm}$ modes so that on $\mathcal{H}_R$ we have

$$\frac{1}{\sqrt{4\pi|\tilde{\omega}|}} B^{\mathrm{in}}_{\omega l} e^{-i\omega v} = \frac{1}{2\pi} \int_{-\infty}^{\infty} C_{\omega\omega'} \frac{1}{\sqrt{4\pi|\omega'|}} e^{-i\omega' v} d\omega' \tag{5.45}$$

for some coefficients $C_{\omega\omega'}$, which gives

$$C_{\omega\omega'} = 2\pi \sqrt{\frac{|\omega'|}{|\tilde{\omega}'|}} B^{\mathrm{in}}_{\omega l}\, \delta(\omega-\omega'). \tag{5.46}$$

We also have that both $g^{\mathrm{in}}_{\omega lm}$ and $\varpi^{\mathrm{R}}_{\omega lm}$ vanish on $\mathcal{H}_{\mathrm{L}}$. The linearity of the wave equation makes the relation between $g^{\mathrm{in}}_{\omega lm}$ and $\varpi^{\mathrm{R}}_{\omega lm}$ valid not only on $\mathcal{H}_{\mathrm{L}} \cup \mathcal{H}_{\mathrm{R}}$ but also at any spacetime point in the interior [117]. So, from Eqs. (5.43), (5.44), (5.45) and (5.46) we must have that on the interior, the "in" mode in (t, r, θ, ϕ) coordinates

is

$$g^{\rm in}_{\omega lm}(t,r,\theta,\phi) = \frac{1}{2\pi}\int_{-\infty}^{\infty} \frac{C_{\omega\omega'}}{\sqrt{4\pi|\omega'|}} Y_{lm}(\theta,\phi)\frac{1}{r}\zeta^{\rm R}_{\omega' l}(t,r)\, d\omega'$$
$$= \frac{1}{\sqrt{4\pi|\tilde{\omega}|}} Y_{lm}(\theta,\phi) B^{\rm in}_{\omega l}\frac{1}{r}\zeta^{\rm R}_{\omega l}(t,r) = B^{\rm in}_{\omega l}\sqrt{\frac{|\omega|}{|\tilde{\omega}|}}\varpi^{\rm R}_{\omega lm}. \tag{5.47}$$

Turning now to the "up" modes. We wish to express the $g^{\rm up}_{\omega lm}$ modes in terms of the interior modes $\varpi^{\rm L/R}_{\omega lm}$. On $\mathcal{H}_L$, we have

$$g^{\rm up}_{\omega lm}\Big|_{\mathcal{H}_L} \sim \frac{1}{\sqrt{4\pi|\omega|}} Y_{lm}(\theta,\phi)\,\frac{e^{-i\omega U}}{r_+},$$
$$\varpi^{\rm L}_{\omega lm}\Big|_{\mathcal{H}_L} \sim \frac{1}{\sqrt{4\pi|\omega|}} Y_{lm}(\theta,\phi)\,\frac{e^{-i\omega u}}{r_+}. \tag{5.48}$$

The frequencies in each case are with respect to different null coordinates so that a positive frequency mode with respect to U contains positive and negative frequency u modes. Hence relating the boundary conditions gives on $\mathcal{H}_{\rm L}$

$$\frac{1}{\sqrt{4\pi|\omega|}} e^{-i\omega U} = \frac{1}{2\pi}\int_{-\infty}^{\infty} D_{\omega\omega'}\frac{1}{\sqrt{4\pi|\omega'|}} e^{-i\omega' u} d\omega', \tag{5.49}$$

for some coefficients $D_{\omega\omega'}$. Inverting this, gives

$$\frac{D_{\omega\omega'}}{\sqrt{4\pi|\omega'|}} = \frac{1}{\sqrt{4\pi|\omega|}}\int_{-\infty}^{\infty} e^{-i\omega U} e^{i\omega' u} du. \tag{5.50}$$

Note that this integral is being evaluated on the interior and so we have, using the lower sign in Eq. (5.27),

$$\int_{-\infty}^{\infty} e^{-i\omega U} e^{i\omega' u} du = \int_{-\infty}^{\infty} \exp\{-i(\omega/\kappa_+)e^{\kappa_+ u} + i\omega' u\} du$$
$$= \frac{1}{\kappa_+}\int_0^{\infty} e^{ibt} t^{z-1} dt, \qquad \text{with } b = -\omega/\kappa_+, \quad z = i\omega'/\kappa_+. \tag{5.51}$$

If $\Im\{b\} > 0$ and $\Re\{z\} > 0$, then this integral would converge in the ordinary sense. If we take $\omega \to \omega - i\epsilon$ and $\omega' \to \omega' - i\epsilon$ with $\epsilon > 0$, then we obtain

$$\int_{-\infty}^{\infty} e^{-i\omega U} e^{i\omega' u} du = \frac{1}{\kappa_+}\lim_{\epsilon\to 0^+}\left(\frac{i\,(\omega - i\epsilon)}{\kappa_+}\right)^{-i(\omega' - i\epsilon)/\kappa_+}\Gamma\left(\frac{i(\omega' - i\epsilon)}{\kappa_+}\right) \tag{5.52}$$

where the right-hand side is to be understood in the sense of generalized functions. When ω and ω' are nonzero, we can take this limit explicitly in a straightforward way. If ω or ω' is zero, then the right-hand side is strictly only understood in terms of generalized functions and the $\epsilon \to 0^+$ limit can only be computed after integra-

tion against a test function of compact support. Nevertheless, for typographical convenience, we shall simply write the result as

$$\frac{D_{\omega\omega'}}{\sqrt{4\pi|\omega'|}} = \frac{1}{\kappa_+\sqrt{4\pi|\omega|}}\left(\frac{i\,\omega}{\kappa_+}\right)^{-i\omega'/\kappa_+}\Gamma\left(\frac{i\omega'}{\kappa_+}\right). \tag{5.53}$$

Similarly, if we consider the boundary conditions on $\mathcal{H}_{\text{past}}$, the $\zeta^{\text{L}}_{\omega l}(t,r)$ mode vanishes there, as it is only defined in region II of the Penrose diagram in Fig. 5.2 and cannot be back-propagated into the region I. By contrast, the $\zeta^{R}_{\omega l}(t,r)$ mode, which is $e^{-i\omega v}$ on $\mathcal{H}^R$, can be back-propagated assuming $\zeta^{R}_{\omega l}(t,r) \sim B^{\text{up}}_{\omega l}/A^{\text{up}}_{\omega l}e^{i\tilde{\omega}r_*-i\omega t}$ at $\mathscr{I}^+$ and using Eq. (5.13) when $\omega^2 > \mu^2$ and assuming $\zeta^{R}_{\omega l}(t,r) \sim B^{\text{up}}_{\omega l}/A^{\text{up}}_{\omega l}e^{-\Omega r_*-i\omega t}$ at $\mathscr{I}^+$ and using Eq. (5.15) when $\omega^2 < \mu^2$. Hence we have

$$\begin{aligned} g^{\text{up}}_{\omega lm}\Big|_{\mathcal{H}_{\text{past}}} &\sim \frac{1}{\sqrt{4\pi|\omega|}}Y_{lm}(\theta,\phi)\,\frac{e^{-i\omega\,U}}{r_+}, \\ \varpi^{\text{R}}_{\omega lm}\Big|_{\mathcal{H}_{\text{past}}} &\sim \frac{1}{\sqrt{4\pi|\omega|}}\,\frac{Y_{lm}(\theta,\phi)}{A^{\text{up}}_{\omega l}}\,\frac{e^{-i\omega u}}{r_+}. \end{aligned} \tag{5.54}$$

As before, the frequencies here are with respect to different null coordinates and in general a frequency with respect to one coordinate will have a mixture of frequencies with respect to the other. We write on $\mathcal{H}_{\text{past}}$

$$\frac{1}{\sqrt{4\pi|\omega|}}e^{-i\omega\,U} = \frac{1}{2\pi}\int_{-\infty}^{\infty}\frac{E_{\omega\omega'}}{\sqrt{4\pi|\omega'|}A^{\text{up}}_{\omega' l}}e^{-i\omega' u}d\omega', \tag{5.55}$$

for some coefficients $E_{\omega\omega'}$, and so, inverting the Fourier transform gives

$$\frac{E_{\omega\omega'}}{\sqrt{4\pi|\omega'|}} = \frac{A^{\text{up}}_{\omega' l}}{\sqrt{4\pi|\omega|}}\int_{-\infty}^{\infty}e^{-i\omega\,U}e^{i\omega' u}du. \tag{5.56}$$

This is being evaluated on the black hole exterior and so U and u are given by the upper sign in Eqs. (5.26)-(5.27). Apart from this, the details are almost identical to the calculation outlined above so we omit the details, stating only the result that

$$\frac{E_{\omega\omega'}}{\sqrt{4\pi|\omega'|}} = \frac{A^{\text{up}}_{\omega' l}}{\kappa_+\sqrt{4\pi|\omega|}}\left(\frac{-i\,\omega}{\kappa_+}\right)^{i\omega'/\kappa_+}\Gamma\left(\frac{-i\omega'}{\kappa_+}\right), \tag{5.57}$$

where here we understand ω and ω' to mean $\omega+i\epsilon$ and $\omega'+i\epsilon$ as $\epsilon\to 0^+$, respectively.

Additionally, from Eqs. (5.29), (5.39) and (5.40) together with (5.13) and (5.15), that have been used to back-propagate $\varpi^{\text{R}}_{\omega lm}$ on the exterior, it is clear that both $g^{\text{up}}_{\omega l}$, $\varpi^{\text{L}}_{\omega lm}$ and $\varpi^{\text{R}}_{\omega lm}$ vanish on $\mathscr{I}^-$.

Thus, we have specified data on $\mathcal{H}_{\text{L}}\cup\mathcal{H}_{\text{past}}\cup\mathscr{I}^-$. Putting together Eqs. (5.48), (5.54), (5.49), (5.55), (5.53) and (5.57) and using the fact that the wave equation is

linear, the "up" solution in terms of (t, r, θ, ϕ) coordinates must be

$$\begin{aligned} g^{\rm up}_{\omega lm}(t,r,\theta,\phi) &= \frac{Y_{lm}(\theta,\phi)}{2\pi\, r}\left\{\int_{-\infty}^{\infty}\frac{D_{\omega\omega'}}{\sqrt{4\pi|\omega'|}}\zeta^{\rm L}_{\omega' l}(t,r)d\omega' + \int_{-\infty}^{\infty}\frac{E_{\omega\omega'}}{\sqrt{4\pi|\omega'|}}\zeta^{\rm R}_{\omega' l}(t,r)d\omega'\right\} \\ &= \frac{Y_{lm}(\theta,\phi)}{2\pi\, r\,\kappa_+\sqrt{4\pi|\omega|}}\left\{\int_{-\infty}^{\infty}\left(\frac{i\,\omega}{\kappa_+}\right)^{-i\omega'/\kappa_+}\Gamma\left(\frac{i\omega'}{\kappa_+}\right)\zeta^{\rm L}_{\omega' l}(t,r)d\omega'\right. \\ &\qquad \left. + \int_{-\infty}^{\infty}A^{\rm up}_{\omega' l}\left(\frac{-i\,\omega}{\kappa_+}\right)^{i\omega'/\kappa_+}\Gamma\left(\frac{-i\omega'}{\kappa_+}\right)\zeta^{\rm R}_{\omega' l}(t,r)d\omega'\right\}. \end{aligned} \tag{5.58}$$

Introducing Eq. (5.58) into Eq. (5.36) requires the computation of integrals involving combinations of products of $D_{\omega\omega'}$, $E_{\omega\omega'}$ and their complex conjugates, such as

$$\begin{aligned} \int_0^\infty D_{\omega\omega'}D^*_{\omega\omega''}\,d\omega &= \frac{\sqrt{|\omega'|}\sqrt{|\omega''|}}{\kappa_+^2}\Gamma\left(\frac{i\omega'}{\kappa_+}\right)\Gamma\left(-\frac{i\omega''}{\kappa_+}\right)\int_0^\infty\frac{d\omega}{\omega}\left(\frac{i\omega}{\kappa_+}\right)^{-\frac{i\omega'}{\kappa_+}}\left(-\frac{i\omega}{\kappa_+}\right)^{\frac{i\omega''}{\kappa_+}} \\ &= \frac{\sqrt{|\omega'|}\sqrt{|\omega''|}}{\kappa_+^2}\Gamma\left(\frac{i\omega'}{\kappa_+}\right)\Gamma\left(-\frac{i\omega''}{\kappa_+}\right)e^{\frac{\pi}{2\kappa_+}(\omega'+\omega'')}\int_0^\infty\frac{d\omega}{\omega}e^{i\frac{(\omega''-\omega')}{\kappa_+}\log\left(\frac{\omega}{\kappa_+}\right)}. \end{aligned} \tag{5.59}$$

In the last line we expressed this integral in a form which can be conveniently solved by substitution, using $y = \frac{1}{\kappa_+}\log(\frac{\omega}{\kappa_+})$, to yield after some simplifications

$$\int_0^\infty D_{\omega\omega'}D^*_{\omega\omega''}\,d\omega = (2\pi)^2\frac{\mathrm{sgn}(\omega')}{1-e^{-2\pi\omega'/\kappa_+}}\delta(\omega'-\omega''). \tag{5.60}$$

With a similar procedure, we can compute the remaining necessary integrals

$$\begin{aligned} &\int_0^\infty D_{\omega\omega'}E^*_{\omega\omega''}\,d\omega = \int_0^\infty E_{\omega\omega'}D^*_{\omega\omega''}\,d\omega = 2\pi^2 A^{\rm up}_{\omega' l}\,\mathrm{sgn}(\omega')\,\mathrm{csch}\left(\frac{\pi\omega'}{\kappa_+}\right)\delta(\omega'+\omega''), \\ &\int_0^\infty E_{\omega\omega'}E^*_{\omega\omega''}\,d\omega = (2\pi)^2|A^{\rm up}_{\omega' l}|^2\mathrm{sgn}(\omega')\frac{1}{1-e^{-2\pi\omega'/\kappa_+}}\delta(\omega'-\omega''). \end{aligned} \tag{5.61}$$

Finally, introducing the interior separable modes (defined by Eqs. (5.38) and (5.41)) into the mode-sum expression for the Unruh Wightman function (5.36), which is originally expressed in terms of the Unruh modes (5.28), and using the mode map-

ping relations (5.47) and (5.58) together with Eqs. (5.60) and (5.61), we obtain

$$\begin{aligned} G_{\rm U}(x,x') =& \frac{1}{(4\pi)^2 r\, r'} \sum_{l=0}^{\infty} (2l+1) P_l(\cos\gamma) \Bigg\{ \int_{\mu}^{\infty} \frac{d\omega}{\tilde{\omega}} |B^{\rm in}_{\omega l}|^2 e^{i\omega\Delta t} \Psi^{\rm II}_{\omega l}(r) \Psi^{\rm II}_{\omega l}{}^{*}(r') \\ &+ \int_0^{\infty} \frac{d\omega}{\omega} \Bigg[\frac{(e^{-i\omega\Delta t} + e^{i\omega\Delta t} |A^{\rm up}_{\omega l}|^2)}{1 - e^{-2\pi\omega/\kappa_+}} \Psi^{\rm II}_{\omega l}(r) \Psi^{\rm II}_{\omega l}{}^{*}(r') \\ &- \frac{(e^{i\omega\Delta t} + e^{-i\omega\Delta t} |A^{\rm up}_{\omega l}|^2)}{1 - e^{2\pi\omega/\kappa_+}} \Psi^{\rm II}_{\omega l}{}^{*}(r) \Psi^{\rm II}_{\omega l}(r') \\ &+ 2\cos(\omega\Delta t)\, \mathrm{csch}\left(\frac{\pi\omega}{\kappa_+}\right) \Re\{ A^{\rm up}_{\omega l} \Psi^{\rm II}_{\omega l}(r) \Psi^{\rm II}_{\omega l}(r') \} \Bigg] \Bigg\}, \end{aligned} \tag{5.62}$$

where $\Delta t \equiv t' - t$. Here, we have used the addition theorem

$$\sum_{m=-l}^{l} Y_{lm}(\theta,\phi) Y_{lm}(\theta',\phi') = \frac{2l+1}{4\pi} P_l(\cos\gamma), \tag{5.63}$$

where γ is the angular separation between the two points. Note that in the massless limit, Eq. (5.62) agrees with the expression in Eq. (3.13) in Ref. [117] up to a factor of 2, which comes from the fact that they consider the Hadamard function rather than the Wightman propagator. We define $\Phi^{\rm II}_{\omega l}(r) = \Psi^{\rm II}_{\omega l}(r)/r$ to be the solution to Eq. (5.6) in region II with asymptotics

$$\Phi^{\rm II}_{\omega l}(r) \sim \begin{cases} \dfrac{1}{r_-} A_{\omega l} e^{i\omega r_*} + \dfrac{1}{r_-} B_{\omega l} e^{-i\omega r_*}, & r \to r_-, \\ \dfrac{e^{-i\omega r_*}}{r_+}, & r \to r_+, \end{cases} \tag{5.64}$$

where the constants $A_{\omega l}$ and $B_{\omega l}$ are the interior scattering coefficients. Then, in the coincidence limit, the mode-sum representation of the Wightman function for the field in the Unruh state on the interior is formally given by

$$G_{\rm U}(x,x) = \frac{1}{4\pi^2} \sum_{l=0}^{\infty} (2l+1) \int_0^{\infty} g^{\rm U}_{\omega l}(r) d\omega, \tag{5.65}$$

where we have defined for later convenience

$$\begin{aligned} g^{\rm U}_{\omega l}(r) :=& \frac{1}{4\omega} \Bigg[(1 - |A^{\rm up}_{\omega l}|^2) |\Phi^{\rm II}_{\omega l}(r)|^2 \theta(\omega - \mu) + \coth\left(\frac{\pi\omega}{\kappa_+}\right) (1 + |A^{\rm up}_{\omega l}|^2) |\Phi^{\rm II}_{\omega l}(r)|^2 \\ &+ 2\mathrm{csch}\left(\frac{\pi\omega}{\kappa_+}\right) \Re\{ A^{\rm up}_{\omega l} \left(\Phi^{\rm II}_{\omega l}(r)\right)^2 \} \Bigg], \end{aligned} \tag{5.66}$$

and where $\theta(\omega-\mu)$ is the Heaviside step function. In arriving to Eq. (5.66), we made use of Eq. (5.20) to express $|B^{\rm in}_{\omega l}|^2$ in terms of $|A^{\rm up}_{\omega l}|^2$. Of course, we note that the expression in the coincident limit in Eq. (5.65) with Eq. (5.66) is not well defined, since neither the sum nor the integral converges. Nonetheless, the expression for each individual l and ω mode is well defined.

5.2.4 The Hartle-Hawking state on the interior

In this section, we derive the Wightman two-point function in terms of *separable* modes on the black hole interior for a massive scalar field in the Hartle-Hawking state. Following the procedure outlined in Ref. [117], exploiting the regularity of both the Hartle-Hawking and Unruh propagators across the horizon, we derive the expression in the following manner. Having obtained an expression for the Unruh propagator in the interior in terms of separable modes, and knowing expressions (from the literature) valid in the black hole exterior for both the Unruh and Hartle-Hawking propagators, the difference between the latter can be trivially extended across the event horizon in separable coordinates.

Using the expressions for the Unruh propagator on the exterior (5.37), together with the exterior propagator for the Hartle-Hawking state [3]

$$G^{\rm ext}_{\rm H}(x,x') = \sum_{l=0}^{\infty}\sum_{m=-l}^{l}\left[\int_{\mu}^{\infty} d\omega \coth\left(\frac{\omega\pi}{\kappa_+}\right) u^{\rm in}_{\omega lm}(x)u^{\rm in\,*}_{\omega lm}(x') + \int_{0}^{\infty} d\omega \coth\left(\frac{\omega\pi}{\kappa_+}\right) u^{\rm up}_{\omega lm}(x)u^{\rm up\,*}_{\omega lm}(x')\right], \tag{5.67}$$

we obtain the difference between the exterior propagators

$$G^{\rm ext}_{\rm H}(x,x') - G^{\rm ext}_{\rm U}(x,x') = \sum_{l=0}^{\infty}\sum_{m=-l}^{l}\int_{\mu}^{\infty} d\omega \left(\coth\left(\frac{\omega\pi}{\kappa_+}\right) - 1\right) u^{\rm in}_{\omega lm}(x)u^{\rm in\,*}_{\omega lm}(x'). \tag{5.68}$$

Note that this difference is regular at the event horizon and only involves the "in" modes, which can be analytically continued into the interior by replacing $u^{\rm in}_{\omega lm}$ by $g^{\rm in}_{\omega lm}$. Therefore, the Wightman function for the Hartle-Hawking state on the interior can then be obtained by analytic continuation across the event horizon as

$$G_{\rm H}(x,x') = G_{\rm U}(x,x') + \left(G^{\rm ext}_{\rm H}(x,x') - G^{\rm ext}_{\rm U}(x,x')\right), \tag{5.69}$$

where $G_{\rm U}(x,x')$ is the interior Wightman function in the Unruh state in Eq. (5.62). Substituting into Eq. (5.69) the mode-sum expressions (5.62) and (5.68), replacing

$u^{\rm in}_{\omega lm}$ by $g^{\rm in}_{\omega lm}$, using Eq. (5.47) and simplifying yields

$$
\begin{aligned}
&G_{\rm H}(x,x') = \\
&= \frac{1}{(4\pi)^2 r\, r'} \sum_{l=0}^{\infty} (2l+1) P_l(\cos\gamma) \Bigg\{ \int_{\mu}^{\infty} \frac{d\omega}{\tilde{\omega}} \coth\left(\frac{\pi\omega}{\kappa_+}\right) |B^{\rm in}_{\omega l}|^2 e^{i\omega\Delta t} \Psi^{\rm II}_{\omega l}(r) \Psi^{\rm II}_{\omega l}{}^*(r') \\
&\quad + \int_0^{\infty} \frac{d\omega}{\omega} \Bigg[\frac{(e^{-i\omega\Delta t} + e^{i\omega\Delta t}|A^{\rm up}_{\omega l}|^2)}{1 - e^{-2\pi\omega/\kappa_+}} \Psi^{\rm II}_{\omega l}(r) \Psi^{\rm II}_{\omega l}{}^*(r') \\
&\quad - \frac{(e^{i\omega\Delta t} + e^{-i\omega\Delta t}|A^{\rm up}_{\omega l}|^2)}{1 - e^{2\pi\omega/\kappa_+}} \Psi^{\rm II}_{\omega l}{}^*(r) \Psi^{\rm II}_{\omega l}(r') \\
&\quad + 2\cos(\omega\Delta t)\, \mathrm{csch}\left(\frac{\pi\omega}{\kappa_+}\right) \Re\{A^{\rm up}_{\omega l} \Psi^{\rm II}_{\omega l}(r) \Psi^{\rm II}_{\omega l}(r')\} \Bigg] \Bigg\}. \qquad (5.70)
\end{aligned}
$$

The expression for the Wightman function for a massive scalar field in the Hartle-Hawking state in the coincident limit is then formally given by

$$
G_{\rm H}(x,x) = \frac{1}{4\pi^2} \sum_{l=0}^{\infty} (2l+1) \int_0^{\infty} g^{\rm H}_{\omega l}(r) d\omega, \qquad (5.71)
$$

where

$$
\begin{aligned}
g^{\rm H}_{\omega l}(r) =& \frac{1}{4\omega} \Bigg[\coth\left(\frac{\pi\omega}{\kappa_+}\right) (1 - |A^{\rm up}_{\omega l}|^2) |\Phi^{\rm II}_{\omega l}(r)|^2 \theta(\omega - \mu) \\
&+ \coth\left(\frac{\pi\omega}{\kappa_+}\right) (1 + |A^{\rm up}_{\omega l}|^2) |\Phi^{\rm II}_{\omega l}(r)|^2 + 2\mathrm{csch}\left(\frac{\pi\omega}{\kappa_+}\right) \Re\{A^{\rm up}_{\omega l} \left(\Phi^{\rm II}_{\omega l}(r)\right)^2\} \Bigg]. \qquad (5.72)
\end{aligned}
$$

The mode-sum expressions obtained in Eqs. (5.62) and (5.70) are divergent in the coincident limit, hence requiring a renormalization prescription.

5.3 The Extended coordinate method inside a black hole (Lorentzian spacetime)

While in Sec. 5.2 we focused on the specific case of a Reissner-Nordström black hole, in this section, we generalize the analysis and present the extended coordinate renormalization prescription for computing the renormalized vacuum polarization inside an arbitrary spherically symmetric black hole, described by the metric in Eq. (5.1) with generic radial function $f(r)$ (so not necessarily given by Eq. (5.2)). In the following Sections, we then restrict the application of this method to the Reissner-Nordström case.

One possible approach for extending the renormalization procedure to the in-

terior is to perform a double Euclideanization procedure, as outlined in Ref. [122]. Within this procedure, one obtains a Riemannian metric in the interior and considers a quantum field in a thermal state at the temperature associated with the Cauchy horizon of the Lorentzian spacetime. The renormalization prescription in the interior could then be developed by means of Euclidean techniques for a quantum field in this thermal state. A state subtraction would then be necessary in order to obtain the results for a scalar field in the Unruh or Hartle-Hawking state.

An alternative and more direct strategy is to develop the renormalization procedure directly within the Lorentzian framework. The extended coordinate method is particularly well-suited for this purpose, as it involves point splitting in all directions except the radial one. In the interior, the Schwarzschild coordinates t and r exchange their timelike and spacelike roles. Consequently, in the limit $r' \to r$, the spacetime points (t, r, θ, ϕ) and (t', r, θ', ϕ') are spacelike separated. The world function $\sigma(x, x')$ is positive definite when $r = r'$ and the other coordinates are separated. This ensures that bi-distributions like $1/\sigma(x, x')$ and $\log(\sigma(x, x'))$ that appear in the Hadamard parametrix are only ill-defined at coincidence. As a result, we do not need an '$i\epsilon$' prescription to define the bi-distributions in cases where the points may be connected by null geodesics. Conveniently, this allows us to develop an analogous renormalization prescription to that of Euclidean zero-temperature states on the exterior, as presented in Chapter 2.

The work presented in this Chapter takes the second approach and constitutes the first development of the extended coordinate method directly in Lorentzian spacetime. The choice of the extended coordinates shall be adapted in the interior to $\{s, \Delta t, \Delta r\}$, with s^2 defined by

$$s^2 := -f(r)\Delta t^2 + 2r^2(1 - \cos\gamma) = |f|\Delta t^2 + 2r^2(1 - \cos\gamma). \tag{5.73}$$

Note how this definition for s^2 generalizes to the interior Lorentzian sector the one presented in Eq. (2.6) for Euclidean zero-temperature states, with the difference that τ is Wick-rotated back to $\tau \to i\,t$. As outlined in Sec. 2.3, expanding the Hadamard parametrix in Eq. (1.73) in the new set of coordinates, taking $\Delta r = 0$ and simplifying yields

$$\begin{aligned} K(x, x') =& \frac{1}{8\pi^2}\left(\sum_{a=0}^{n}\sum_{b=0}^{a} \mathcal{D}^{(\mathrm{r})}_{ab}(r)\frac{\Delta t^{2a+2b}}{s^{2b+2}} + \sum_{a=1}^{n}\sum_{b=1}^{a} \mathcal{D}^{(\mathrm{p})}_{ab}(r)\Delta t^{2a-2b}s^{2b-2} \right. \\ &+ \sum_{a=1}^{n-1}\sum_{b=0}^{a-1} \mathcal{T}^{(\mathrm{r})}_{ab}(r)\frac{\Delta t^{2a+2b+2}}{s^{2b+2}} + \sum_{a=0}^{n-1}\sum_{b=0}^{a} \mathcal{T}^{(\mathrm{l})}_{ab}(r)s^{2a-2b}\Delta t^{2b}\log\left(\frac{s^2}{\ell^2}\right) \\ &\left. + \sum_{a=1}^{n-1}\sum_{b=0}^{a} \mathcal{T}^{(\mathrm{p})}_{ab}(r)s^{2a-2b}\Delta t^{2b} \right) + \mathcal{O}(\Delta x^{2n}\log\Delta x), \end{aligned} \tag{5.74}$$

where we have used the same notation as Section 2.3 for the Hadamard coefficients $\mathcal{D}_{ab}^{(\mathrm{r/p})}(r)$ and $\mathcal{T}_{ab}^{(\mathrm{r/p/l})}(r)$. We note that these coefficients in the Lorentzian manifold can be readily obtained from the equivalent coefficients in the Riemannian manifold reported in Appendix A.3, by Wick rotating back (setting $\tau \to it$) expression (2.8) and including the remaining powers of i into the definition of the Lorentzian coefficients. For instance, for the direct rational terms $\mathcal{D}_{ab}^{(\mathrm{r}),\,\mathrm{Lor.}} = (-1)^{a+b}\,\mathcal{D}_{ab}^{(\mathrm{r}),\,\mathrm{Rie.}}$. We report the Lorentzian coefficients in Appendix C.1 for convenience.

Similarly to what we explained in Sec. 2.3, we only need to derive mode-sum representations for the rational $\Delta t^{2a+2b}/s^{2b+2}$ and $\Delta t^{2a+2b+2}/s^{2b+2}$ and the logarithmic $s^{2a-2b}\Delta t^{2b}\log(s^2/\ell^2)$ terms of the expansion. This can be accomplished by employing mode-sum representations based on the form of the mode-sum for the Wightman functions in Eqs. (5.62) and (5.70) with the radial points taken together. For the rational terms,

$$\frac{\Delta t^{2a+2b}}{s^{2b+2}} = \sum_{l=0}^{\infty}(2l+1)P_l(\cos\gamma)\int_{-\infty}^{\infty} d\omega e^{-i\omega\Delta t}\Psi_{\omega l}(a,b|r), \tag{5.75}$$

while for the logarithmic terms

$$\Delta t^{2b}s^{2a-2b}\log(\rho^2\Delta t^2+1-\cos\gamma) = \sum_{l=0}^{\infty}(2l+1)P_l(\cos\gamma)\int_{-\infty}^{\infty} d\omega\, e^{-i\omega\,\Delta t}\,\chi_{\omega l}(a,b\,|r), \tag{5.76}$$

with the new definition of

$$\rho^2 = \frac{|f|}{2r^2}. \tag{5.77}$$

Inverting these expressions, we obtain double integral representations for the regularization parameters in the Lorentzian sector

$$\Psi_{\omega l}(a,b|r) = \frac{1}{4\pi}\int_{-1}^{1} d\mathfrak{u}\int_{-\infty}^{\infty} dt\frac{e^{-i\omega t}t^{2a+2b}P_l(\mathfrak{u})}{(|f|\,t^2+2r^2(1-\mathfrak{u}))^{1+b}}, \tag{5.78}$$

$$\chi_{\omega l}(a,b|r) = \frac{(2r^2)^{a-b}}{4\pi}\int_{-1}^{1} d\mathfrak{u}P_l(\mathfrak{u})\lim_{\bar{\alpha}\to a}\frac{\partial}{\partial\bar{\alpha}}\int_{-\infty}^{\infty} e^{-i\omega t}t^{2b}(\rho^2t^2+1-\mathfrak{u})^{\bar{\alpha}-b}dt, \tag{5.79}$$

where we have renamed $\Delta t \to -t$ and $\mathfrak{u} = \cos\gamma$ simply to facilitate comparison. In fact, comparing these expressions with the corresponding ones in the Riemannian case, namely Eqs. (2.10) and (2.30), it becomes clear that the integrals in the new expressions are precisely those already computed in Sections 2.3.1 and 2.3.2. The only difference is that $|f|$ (or $-f$) now appears instead of f. Hence, the renormalization parameters will retain the same form of the ones presented in Section 2.3, with the tweak $f \to |f|$ (or $f \to -f$).

Specifically, we report here for convenience the resulting expressions at coincidence for the renormalized vacuum polarization and the two additional mode-sums for the computation of the RSET

$$\begin{aligned}\mathsf{w}^{\mathrm{A}} :=&\langle\hat{\Phi}^2\rangle^{\mathrm{A}}_{\mathrm{ren}} := \lim_{x'\to x}\left(G_{\mathrm{A}}(x,x') - K(x,x')\right)\\ =&\frac{1}{4\pi^2}\Bigg\{\sum_{l=0}^{\infty}(2l+1)\int_0^{\infty}\left(g^{\mathrm{A}}_{\omega l}(r) - k^{(n)}_{\omega l}(r)\right)d\omega\\ &-\frac{1}{2}\sqrt{\pi}\sum_{a=1}^{n-1}\sum_{b=0}^{a}\mathcal{T}^{(\mathrm{l})}_{ab}(r)\,\frac{(a-1)!2^{2a}|f|^{a-b}}{\Gamma(-a+\frac{1}{2})\lambda^{2a}}\Bigg\}\\ &-\frac{1}{8\pi^2}\left[\mathcal{D}^{(\mathrm{p})}_{11}(r) + \frac{\mathcal{D}^{(\mathrm{r})}_{10}(r)}{|f|} + \frac{\mathcal{D}^{(\mathrm{r})}_{11}(r)}{|f|^2} + \mathcal{T}^{(\mathrm{l})}_{00}(r)(\log(|f|/(\ell^2\lambda^2)) - 2\gamma_{\mathrm{E}})\right],\end{aligned} \tag{5.80}$$

$$\begin{aligned}(\tilde{w}^{\mathrm{A}})^{t}{}_{t} :=&[g^{tt'}W_{,tt'}] = \frac{1}{4\pi^2|f|}\Bigg\{\int_0^{\infty}\sum_{l=0}^{\infty}(2l+1)\omega^2\left(g^{\mathrm{A}}_{\omega l} - k^{(n)}_{\omega l}\right)d\omega\\ &-\frac{1}{2}\sqrt{\pi}\sum_{\substack{a=0\\a\neq 1}}^{n-1}\sum_{b=0}^{a}\mathcal{T}^{(\mathrm{l})}_{ab}(r)\,\frac{a!2^{2a}|f|^{a-b}}{\Gamma(\frac{1}{2}-a)(a-1)\lambda^{2a-2}}\Bigg\}\\ &+\frac{1}{4\pi^2}\Bigg[\mathcal{T}^{(\mathrm{p})}_{10} + \mathcal{D}^{(\mathrm{p})}_{22} + \frac{1}{|f|}(\mathcal{T}^{(\mathrm{p})}_{11} + \mathcal{D}^{(\mathrm{p})}_{21}) + \frac{\mathcal{D}^{(\mathrm{r})}_{20}}{|f|^2} + \frac{\mathcal{D}^{(\mathrm{r})}_{21}}{|f|^3} + \frac{\mathcal{D}^{(\mathrm{r})}_{22}}{|f|^4} + \frac{\mathcal{T}^{(\mathrm{r})}_{10}}{|f|^2}\\ &+\left(\mathcal{T}^{(\mathrm{l})}_{10} + \frac{\mathcal{T}^{(\mathrm{l})}_{11}}{|f|}\right)(\log(|f|/(\ell^2\lambda^2)) - 2\gamma_{\mathrm{E}} + 3)\Bigg],\end{aligned} \tag{5.81}$$

$$\begin{aligned}(\tilde{w}^{\mathrm{A}})^{\phi}{}_{\phi} :=&[g^{\phi\phi'}W_{,\phi\phi'}] = \frac{1}{8\pi^2 r^2}\Bigg\{\int_0^{\infty}\sum_{l=0}^{\infty}(2l+1)l(l+1)\left(g^{\mathrm{A}}_{\omega l} - k^{(n)}_{\omega l}\right)d\omega\\ &+\frac{1}{2}\sqrt{\pi}\sum_{a=2}^{n-1}\sum_{b=0}^{a}\mathcal{T}^{(\mathrm{l})}_{ab}\,\frac{r^2(a-b)(a-2)!2^{2a}|f|^{a-b-1}}{\Gamma(\frac{3}{2}-a)\lambda^{2a-2}}\Bigg\}\\ &+\frac{1}{4\pi^2}\Bigg[\mathcal{D}^{(\mathrm{p})}_{22} + \mathcal{T}^{(\mathrm{p})}_{10} - \frac{\mathcal{D}^{(\mathrm{r})}_{20}}{|f|^2} - 2\frac{\mathcal{D}^{(\mathrm{r})}_{21}}{|f|^3} - 3\frac{\mathcal{D}^{(\mathrm{r})}_{22}}{|f|^4}\\ &-\frac{\mathcal{T}^{(\mathrm{r})}_{10}}{|f|^2} + \frac{\mathcal{T}^{(\mathrm{l})}_{11}}{|f|} + \mathcal{T}^{(\mathrm{l})}_{10}(\log(|f|/(\ell^2\lambda^2)) - 2\gamma_{\mathrm{E}} + 1)\Bigg],\end{aligned} \tag{5.82}$$

where $k^{(n)}_{\omega l}$ is defined as in Eq. (2.48), with the regularization parameters $\mathcal{I}_{\omega l}(a,b|r)$ and $\mathcal{J}_{\omega l}(a,b|r)$ defined as in Eqs. (2.25) and (2.45), with the difference that $f\to|f|$ (or $f\to -f$) on the interior, and with the Hadamard coefficients of App. C.1. In arriving at these expressions, we have exploited the $\omega\to-\omega$ symmetry of $k^{(n)}_{\omega l}$. We

use A to denote, generically, either the Hartle–Hawking or the Unruh state. As shown in Appendix A.1, the expression for the renormalized vacuum polarization (5.80) is independent of λ. In fact, there is a λ dependence in $k^{(n)}_{\omega l}$ contained in the terms $\mathcal{I}_{\omega l}(a,b|r)$ and $\mathcal{J}_{\omega l}(a,b|r)$ that precisely cancels that in the analytic terms in Eq. (5.80). The renormalized vacuum polarization depends on the renormalization ambiguity ℓ, when $\mu \neq 0$.

In the following Sections, we will apply the renormalization method presented hereby to compute the renormalized vacuum polarization and stress-energy tensor on the interior of a Reissner-Nordström black hole. However, before presenting the results for the renormalized vacuum polarization and RSET, we discuss the numerical implementation of the method in the interior of a Reissner-Nordström black hole in Section 5.4 and analyze its convergence in Section 5.5.

5.4 Numerical considerations

To obtain the results that we present in Section 5.6 (which are not very close to the Cauchy horizon), we evaluate the expression for the renormalized vacuum polarization in Eq. (2.49) using a Hadamard parametrix expansion of order $n = 3$. This yields a rapidly convergent mode-sum, scaling at large l as $\mathcal{O}(l^{-8})$ for fixed ω and at large ω as $\mathcal{O}(\omega^{-9})$ for fixed l, at least away from the horizons, in agreement with Eq. (2.58). All that is needed to obtain the modes $g_{\omega l}(r)$ are the radial solutions $\Phi^{\rm II}_{\omega l}(r)$ and the exterior reflection coefficients $A^{\rm up}_{\omega l}$. By introducing,

$$\eta = \frac{r_+ - r}{r_+ - r_-}, \tag{5.83}$$

the solutions $\Phi^{\rm II}_{\omega l}(r)$ to the radial equation (5.6), with the boundary conditions (5.64) can be recast in terms of a confluent Heun function H as

$$\Phi^{\rm II}_{\omega l}(r) = \frac{1}{r_+} e^{i(\omega-\tilde{\omega})(r-r_+)} e^{-i\omega r_*} \mathsf{H}\left(a_1, a_2, a_3, a_4, a_5; \eta\right), \tag{5.84}$$

which is a solution to the equation

$$\begin{aligned} &\eta(\eta-1)\mathsf{H}''\left(a_1, a_2, a_3, a_4, a_5; \eta\right) \\ &+ \left(a_3(\eta-1) + a_4\eta + \eta(\eta-1)a_5\right)\mathsf{H}'\left(a_1, a_2, a_3, a_4, a_5; \eta\right) \\ &\qquad + \left(a_2\eta - a_1\right)\mathsf{H}\left(a_1, a_2, a_3, a_4, a_5; \eta\right) = 0, \end{aligned} \tag{5.85}$$

with boundary condition $\mathsf{H}\,(a_1, a_2, a_3, a_4, a_5; 0) = 1$ (so that the expression (5.84) indeed satisfies the boundary condition (5.64)) and where

$$\begin{aligned}
a_1 &= l(l+1) + 2i\tilde{\omega}r_+ - r_+^2(\omega-\tilde{\omega})^2 + i(\omega-\tilde{\omega})(r_+ + r_-),\\
a_2 &= 2i\tilde{\omega}(r_+ - r_-) - (r_+^2 - r_-^2)(\omega-\tilde{\omega})^2,\\
a_3 &= 1 - \frac{2i\omega r_+^2}{r_+ - r_-},\\
a_4 &= 1 + \frac{2i\omega r_-^2}{r_+ - r_-},\\
a_5 &= 2i\tilde{\omega}(r_+ - r_-).
\end{aligned} \tag{5.86}$$

The advantage of employing the Heun form is that the Heun functions which are regular at $\eta = 0$ are built in *Mathematica* and can be computed very efficiently. The expression in Eq. (5.84) is formally only valid for $\omega^2 > \mu^2$. The equivalent expression for the modes with $\omega^2 < \mu^2$ can be obtained by replacing $\tilde{\omega} \to i\Omega$ in Eqs. (5.84) and (5.86).

The exterior reflection coefficients $A^{\rm up}_{\omega l}$ are obtained from the Wronskian condition

$$A^{\rm up}_{\omega l} = -\frac{\mathcal{W}[\tilde{\Phi}^{{\rm in}\,*}_{\omega l}, \tilde{\Phi}^{\rm up}_{\omega l}]}{\mathcal{W}[\tilde{\Phi}^{\rm in}_{\omega l}, \tilde{\Phi}^{\rm up}_{\omega l}]}, \tag{5.87}$$

where $\mathcal{W}[\phi_1, \phi_2]$ is the Wronskian of two solutions ϕ_1 and ϕ_2. Specifically,

$$\mathcal{W}[\tilde{\Phi}^{\rm in}_{\omega l}, \tilde{\Phi}^{\rm up}_{\omega l}] = r^2 f(r)\left(\tilde{\Phi}^{\rm in}_{\omega l}(r)\frac{d}{dr}\tilde{\Phi}^{\rm up}_{\omega l}(r) - \tilde{\Phi}^{\rm up}_{\omega l}(r)\frac{d}{dr}\tilde{\Phi}^{\rm in}_{\omega l}(r)\right), \tag{5.88}$$

which is the Wronskian of the numerical modes $\tilde{\Phi}^{\rm in}_{\omega l} := \Phi^{\rm in}_{\omega l}/B^{\rm in}_{\omega l}$ and $\tilde{\Phi}^{\rm up}_{\omega l} := \Phi^{\rm up}_{\omega l}/B^{\rm up}_{\omega l}$. Note that the numerical "in" mode $\tilde{\Phi}^{\rm in}_{\omega l} = \Phi^{\rm II}_{\omega l}$ and can be computed via Eq. (5.84) using the built-in confluent Heun function in *Mathematica*. The numerical "up" mode $\tilde{\Phi}^{\rm up}_{\omega l}$ is determined by imposing initial conditions at a suitably large radius using an asymptotic series with leading order [3]

$$\tilde{\Phi}^{\rm up}_{\omega l}(r) \sim \begin{cases} \frac{1}{r}e^{i\tilde{\omega}r_*}, & r\to\infty, \quad \omega^2 > \mu^2,\\ \frac{1}{r}e^{-\Omega r_*}, & r\to\infty, \quad \omega^2 < \mu^2. \end{cases} \tag{5.89}$$

Since the Wronskian is a constant, we need only to compute Eq. (5.88) at one radial point for each l and ω. The most efficient routine is to evaluate it at the outer boundary where the boundary conditions for $\tilde{\Phi}^{\rm up}_{\omega l}(r)$ are evaluated. This avoids numerically integrating the $\tilde{\Phi}^{\rm up}_{\omega l}(r)$ modes.

The numerical calculation of the ω-integral in expression (2.49) requires the

computation of the modes for the Wightman function and for the renormalization counter-terms on a predefined ω-grid. The integral is then computed by generating an interpolating function for the integrand. This interpolation process is a potential source of significant numerical error. Selecting a suitable ω-grid is essential to ensure that the grid selection has no effect on the results. The expressions $k^{(n)}_{\omega l}(r)$ are rapidly changing functions of ω near $\omega = 0$ and $\omega = \lambda$. Therefore, it is crucial to build an adaptive ω-grid that is particularly fine in these frequency regimes.

5.5 Convergence of the mode-sums

The first test that can be done to verify the precision of the numerical computations is the study of convergence. One of the features of the extended coordinates method is that the convergence order of both the ω-integral and the l-sum can be increased by subtracting higher-order terms of the Hadamard parametrix. Focusing on the mode-sum contribution to Eq. (5.80), namely

$$\frac{1}{4\pi^2}\sum_{l=0}^{\infty}(2l+1)\int_0^{\infty} d\omega\ \left(g_{\omega l}(r) - k^{(n)}_{\omega l}(r)\right), \tag{5.90}$$

the large frequency and large l behavior of $g_{\omega l}(r) - k^{(n)}_{\omega l}(r)$ is dependent on the order of the expansion n of the Hadamard parametrix according to Eq. (2.58). In Figures 5.5 and 5.6, we show that the numerical results agree with the theoretical predictions in Eq. (2.58) both for large ω and large l. For instance, $\log_{10}|(\omega M)^3 M(g_{\omega l}(r) - k^{(0)}_{\omega l}(r))|$ is a straight line with slope 0 for large ω, fixed l, and hence this shows that $(\omega M)^3 M(g_{\omega l}(r) - k^{(0)}_{\omega l}(r)) \sim 1$ for large ω, or equivalently, $M(g_{\omega l}(r) - k^{(0)}_{\omega l}(r)) \sim (\omega M)^{-3}$, in agreement with Eq. (2.58). The other curves can be interpreted in an analogous way. These plots show results only for the massless case, but we have verified that this behavior holds in the massive case as well.

In the exterior, the behaviour at large frequency and large l is approximately uniform in r [52]. In contrast, the radial dependence of the convergence in the interior is less straightforward. Specifically, in the vicinity of the horizons, the convergence in l for fixed ω is somewhat slower compared with plots away from the horizons, and it is computationally advantageous to perform the ω-integral first. Indeed, after integrating over $\omega \in [0, 25]$ only 5 l-modes are needed to obtain precision up to the first 4 significant digits. On the other hand, performing the l-sum first would require an increasing number of l-modes as $|f(r)| \to 0$. Furthermore, for both massless and massive scalar fields, we find numerically that, to obtain rapidly convergent mode-sums in the regions very close to the horizons, it is sufficient to expand the Hadamard parametrix up to the order containing the divergent terms.

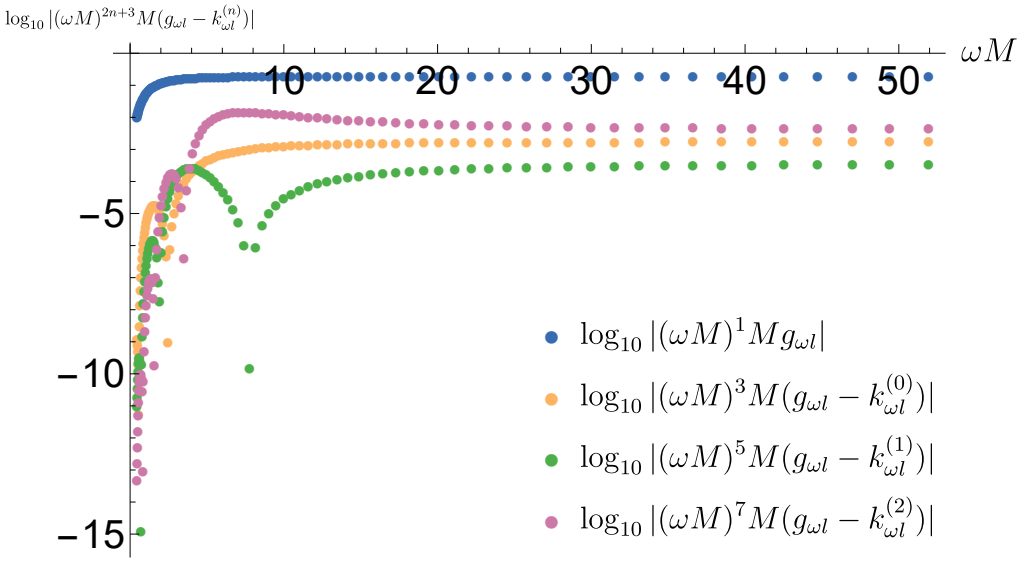


Figure 5.5: *Analysis of the convergence of $g_{\omega l}(r) - k^{(n)}_{\omega l}(r)$ at different orders of expansion n for fixed l and large ω. Results obtained with the set of parameters: $\mu M = 0$, $Q = 0.8M$, $r = M$ and $l = 2$.*

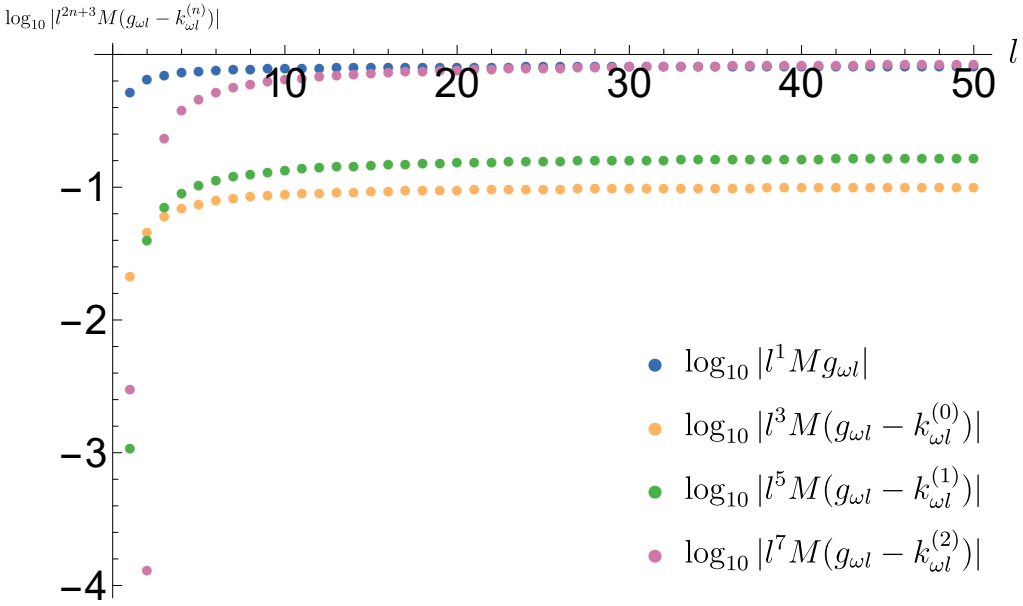


Figure 5.6: *Analysis of the convergence of $g_{\omega l}(r) - k^{(n)}_{\omega l}(r)$ at different orders of expansion n for fixed ω and large l. Results obtained with the set of parameters: $\mu M = 0$, $Q = 0.8M$, $r = M$ and $\omega M = 0.1$.*

In the massless case, this amounts to subtracting the parametrix up to order $n = 0$, whereas for massive fields we expand the parametrix up to order $n = 1$. In fact, although from Eq. (2.58) one should expect, at large frequency, a convergence rate of ω^{-3} in the massless case when using an $n = 0$ expansion, and ω^{-5} in the massive case when using an $n = 1$ expansion, the observed convergence in ω in the regions very close to the horizons is faster than these predictions. Specifically, it is faster than ω^{-3} in the massless case, and faster than ω^{-5} in the massive case, with the convergence rate progressively increasing as the horizon is approached. As stated above, if the ω integral is performed first, only a few l-modes are required to obtain accurate results.

This careful analysis of the convergence of the mode-sums in the region very close to the horizon will play a central role in Chapter 6. In fact, we will see that to understand the behavior of the RVP near the Cauchy horizon, it will be necessary to compute the RVP as close as $\frac{r-r_-}{M} = 10^{-200}$.

5.6 The renormalized vacuum polarization inside a Reissner-Nordström black hole

The method described in Section 5.3 is general and can be applied to computing quantum expectation values inside any spherically symmetric black hole with metric as in Eq. (5.1). In this section, we demonstrate the efficacy of this approach by computing the renormalized vacuum polarization for massless and massive scalar fields, as calculated from Eq. (2.49), in the interior of a Reissner-Nordström black hole. The renormalized vacuum polarization is independent of the coupling ξ in a spacetime where the Ricci scalar $R = 0$, as it is in the Reissner-Nordström case. Therefore, the results presented in this section are valid for any coupling ξ.

In Fig. 5.7, we compare the renormalized vacuum polarization for a massless scalar field in the Hartle-Hawking and Unruh states computed with the method presented in this Chapter against the numerical results obtained in Ref. [119] by using the pragmatic mode-sum renormalization method developed by Levi and Ori in [46]. We find agreement up to 2-3 digits of precision between the two methods, confirming the validity of the methodology we outlined. Additionally, in the Hartle-Hawking case, the results agree with the closed-form expression on the black hole event horizon [123]. An interesting aspect is that the renormalized vacuum polarization appears to have a monotonic behaviour in r and might naively seem to diverge for both states as it approaches the inner horizon. However, it was shown by Lanir et al. in [119] that the renormalized vacuum polarization surprisingly asymptotes to a *finite* negative value for both states after some oscillations in the vicinity of the

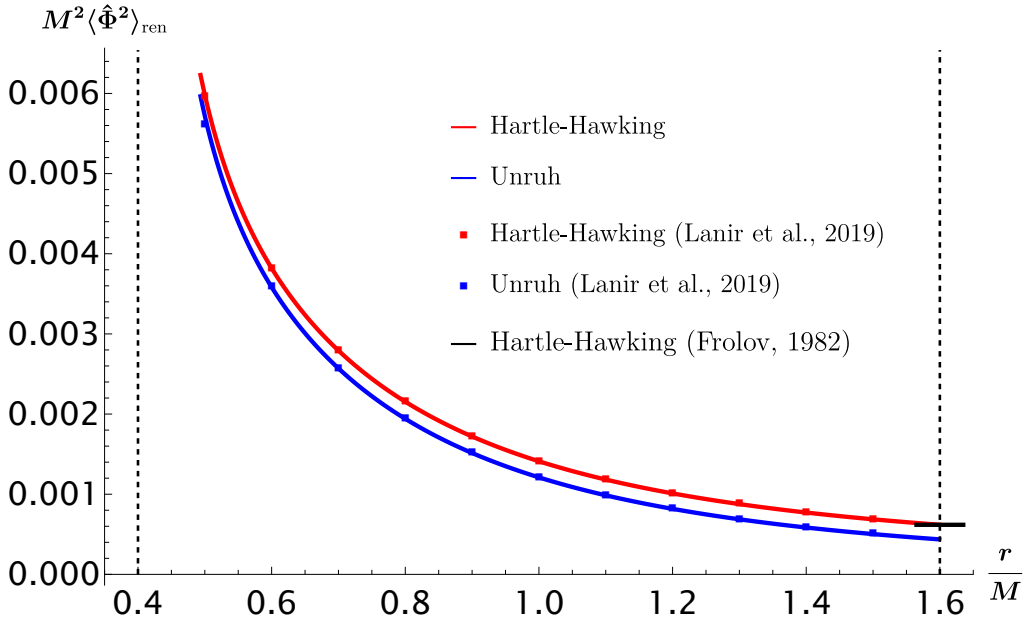


Figure 5.7: *Results for $\langle\hat{\Phi}^2\rangle_{\rm ren}$ obtained with the parameters $Q = 0.8M$, $\mu = 0$. The vertical dashed lines represent the inner (left) and event (right) horizons. The continuous blue and yellow lines are the interpolated numerical results we obtained for the Hartle-Hawking and Unruh states respectively. The squares are the numerical results reported in Ref. [119]. The black solid line refers to the analytical result computed on the black hole horizon as shown in Ref. [123]. This figure is continued near r_- in Fig. 6.1, which presents the results for $\langle\hat{\Phi}^2\rangle_{\rm ren}$ in the vicinity of the inner horizon.*

inner horizon. We verify this behavior in Section 6.3.

Furthermore, having verified the validity of the method, we implemented it to calculate the renormalized vacuum polarization in the case of a massive scalar field. We note that the pragmatic mode-sum scheme has not yet been applied to massive scalar fields. We report the results obtained for a field with mass $\mu M = 1/10$ in the Hartle-Hawking and Unruh states in Fig. 5.8. For a massive field, the renormalized vacuum polarization depends on the choice of the arbitrary lengthscale ℓ. With the choice $\ell = M$, we obtain extrapolated values at the event horizon of $M^2\langle\hat{\Phi}^2\rangle^{\rm H}_{\rm ren} \approx 0.00043$ and $M^2\langle\hat{\Phi}^2\rangle^{\rm U}_{\rm ren} \approx 7.8\times10^{-6}$ for the Hartle-Hawking and Unruh state respectively. We compared these results to the event horizon values computed from the exterior calculation using the methodology detailed in Ref. [3] and found agreement up to two digits of precision. In Fig. 5.8, it is possible to notice that the presence of the mass seems to suppress the state dependence in the renormalized vacuum polarization. Indeed, the two curves corresponding to the Hartle-Hawking and Unruh states are nearly overlapping. Moreover, we performed a near-Cauchy horizon analysis to verify the behavior of the vacuum polarization for a massive field in the limit as $r \to r_-$. We report the outcomes of this analysis in Sec. 6.3.

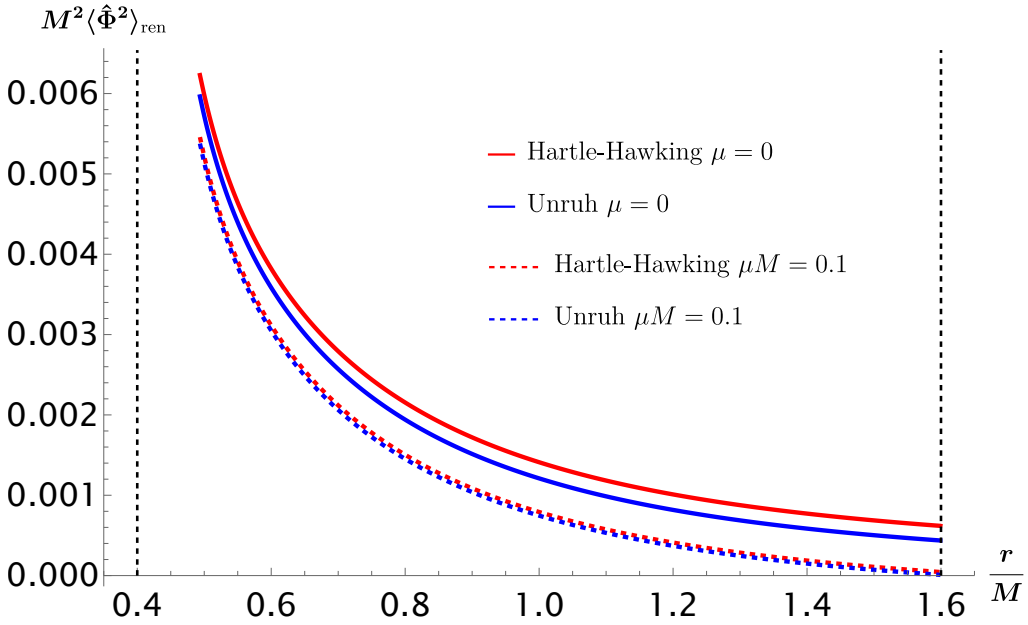


Figure 5.8: *Comparison of results for $\langle\hat{\Phi}^2\rangle_{\rm ren}$ obtained with the parameters $Q = 0.8M$ for a massless and a massive $\mu M = 0.1$ field. The vertical dashed lines represent the inner (left) and event (right) horizons. The results are obtained by setting the arbitrary lengthscale to $\ell = M$.*

5.7 The renormalized stress-energy tensor inside a Reissner-Nordström black hole

With the techniques outlined in section 5.3, we also computed the components of the renormalized stress-energy tensor inside a Reissner-Nordström black hole for massless and massive quantum scalar fields in the Hartle-Hawking and Unruh states. Notwithstanding the fact that computing the RSET on the interior is the first step towards solving the semiclassical equations, the RSET itself encodes important physical information. In this section, we present and discuss the obtained results. We verified our RSET results by checking that the conservation equation is satisfied to some desired accuracy.

In Figures 5.9 and 5.10, we compare the interior and exterior results for massless fields with different couplings for the same RSET components across the event horizon. These figures are obtained by combining the interior results computed in this work with the exterior results from Ref. [3], calculated using the original version of the Extended Coordinate Method. Firstly, we note that the components match smoothly across r_+. As expected, all the components of the RSET in the Hartle-Hawking state are regular on the event horizon. On the other hand, as reported in Figure 5.10, we show that the $\langle\hat{T}^t{}_t\rangle^{\rm U}_{\rm ren}$ and $\langle\hat{T}^r{}_r\rangle^{\rm U}_{\rm ren}$ in the Unruh state diverge like f^{-1} at the event horizon, while the angular components $\langle\hat{T}^\theta{}_\theta\rangle^{\rm U}_{\rm ren} = \langle\hat{T}^\phi{}_\phi\rangle^{\rm U}_{\rm ren}$ are regular.

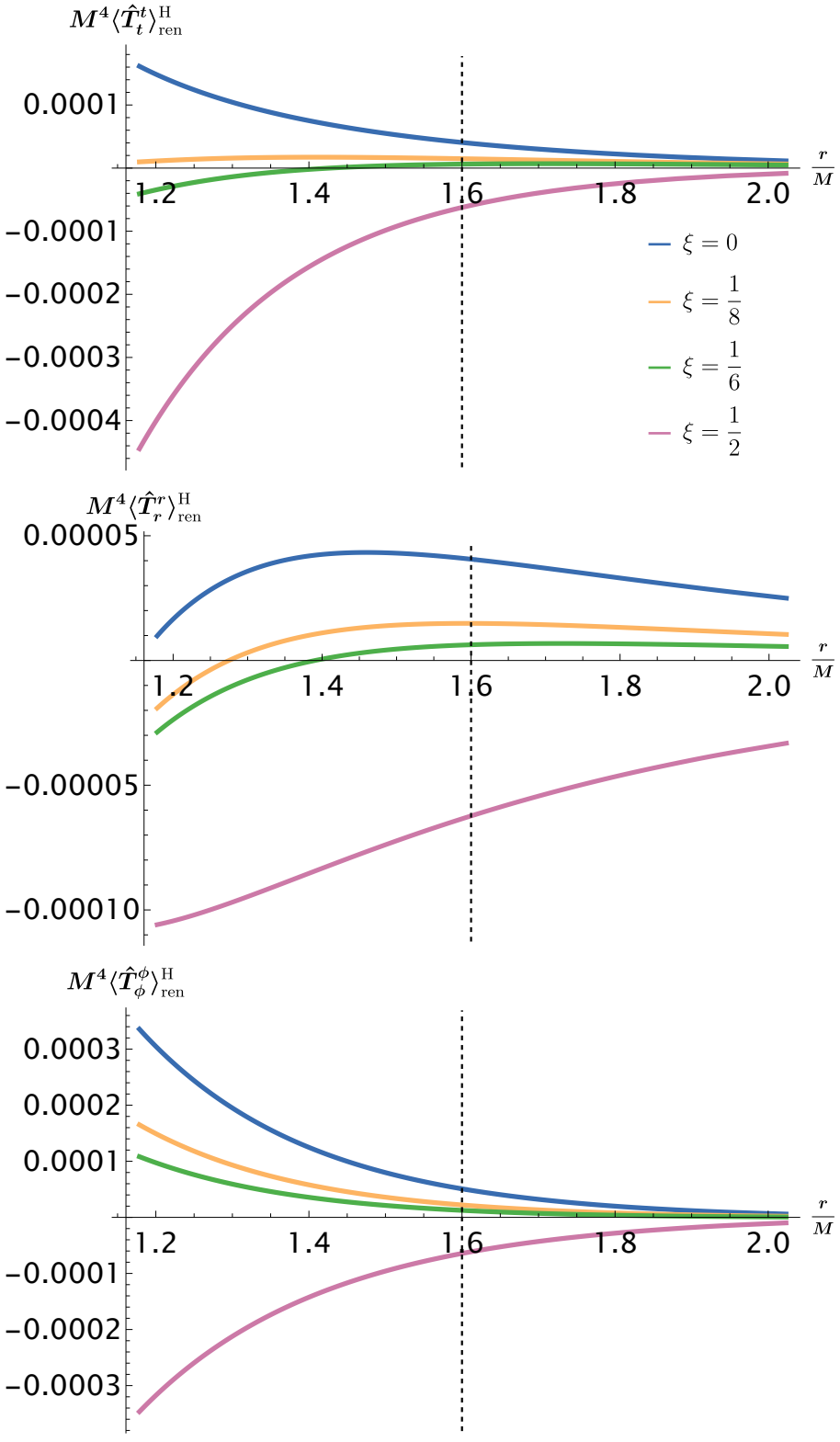


Figure 5.9: *RSET components for a massless field in the Hartle-Hawking state in the region across the event horizon (represented by the vertical black dashed line) of a Reissner-Nordström black hole (with parameters $M = 1$, $Q = 0.8$). The blue, yellow, green and red curves correspond to the different values of the coupling $\xi = \{0, 1/8, 1/6, 1/2\}$. We show from top to bottom $\langle\hat{T}^t{}_t\rangle$, $\langle\hat{T}^r{}_r\rangle$ and $\langle\hat{T}^\phi{}_\phi\rangle$.*

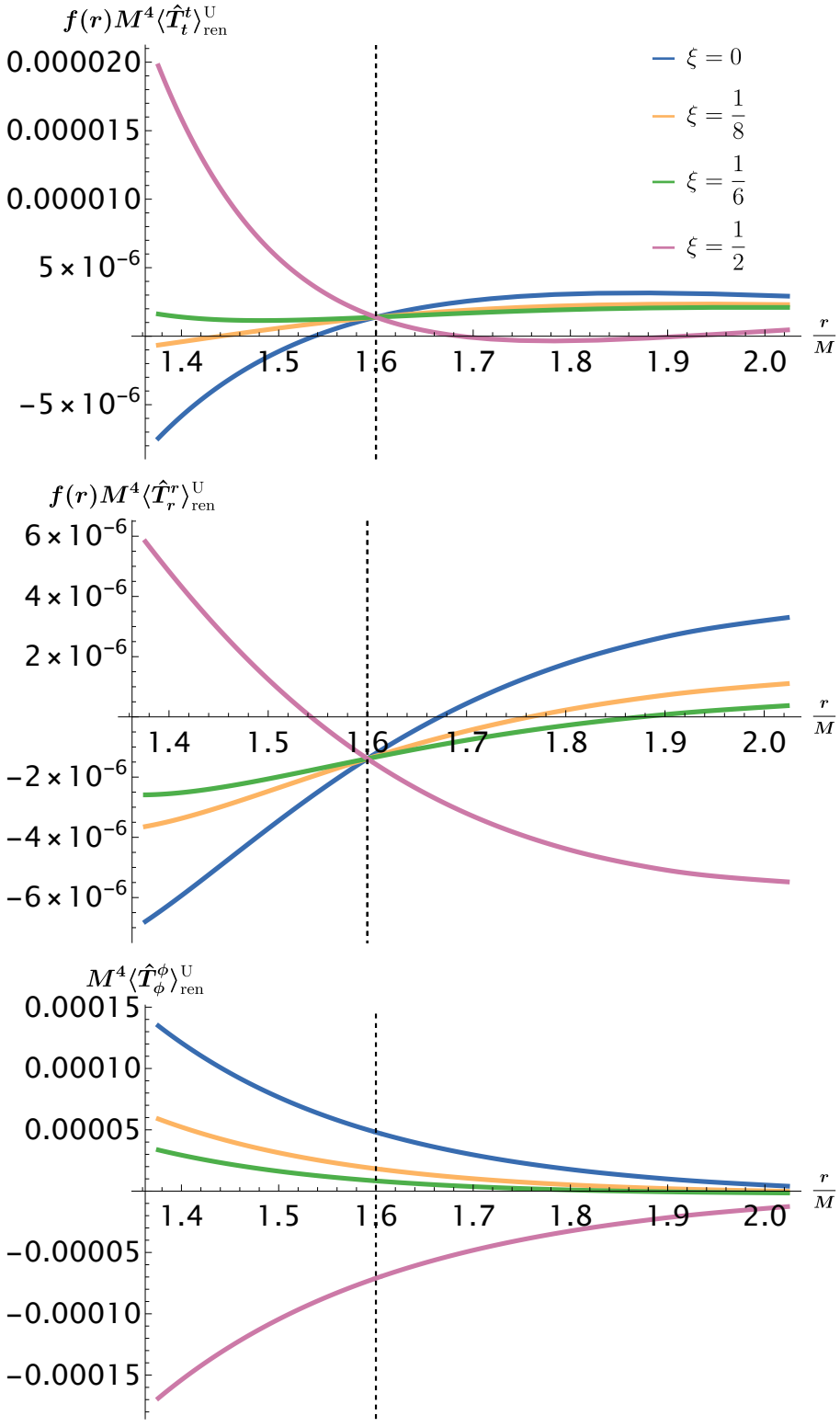


Figure 5.10: *RSET components for a massless field in the Unruh state in the region across the event horizon (represented by the vertical black dashed line) of a Reissner-Nordström black hole (with parameters $M = 1$, $Q = 0.8$). The blue, yellow, green and red curves correspond to the different values of the coupling $\xi = \{0, 1/8, 1/6, 1/2\}$. We show from top to bottom $f\langle\hat{T}^t{}_t\rangle$, $f\langle\hat{T}^r{}_r\rangle$ and $\langle\hat{T}^\phi{}_\phi\rangle$.*

In Figures 5.11 and 5.12 we present the full interior results for the RSET components $\langle \hat{T}^t{}_t \rangle_{\rm ren}$, $\langle \hat{T}^r{}_r \rangle_{\rm ren}$, and $\langle \hat{T}^\phi{}_\phi \rangle_{\rm ren}$, with different values of the coupling ξ, for massless and massive scalar fields in the Hartle-Hawking and Unruh state respectively. The RSET components presented in these figures have been computed by setting the arbitrary constant to $\ell = M$. Unlike the renormalized vacuum polarization, the state dependence appears to be suppressed for both massless and massive fields. When plotted in the same figure, the curves corresponding to the Hartle-Hawking and Unruh states are nearly indistinguishable, except in the region near the event horizon where the $\langle \hat{T}^t{}_t \rangle^{\rm U}_{\rm ren}$ and $\langle \hat{T}^r{}_r \rangle^{\rm U}_{\rm ren}$ components of the RSET diverge as f^{-1}, while the respective components in the Hartle-Hawking state are finite. The components in the massive case present very similar behavior to those in the massless case and indicate a possible divergence at the Cauchy horizon of all the RSET components for both quantum states. However, as we will show in Chapter 6, both the RVP and the RSET exhibit nontrivial behavior as the Cauchy horizon is approached, and the study of their properties in this region requires a different treatment. The coupling ξ plays a significant role in defining the sign of the various components. Specifically, in the leftmost region of the plots, all the components change sign as the coupling increases: $\langle \hat{T}^t{}_t \rangle_{\rm ren}$ and $\langle \hat{T}^\phi{}_\phi \rangle_{\rm ren}$ change from positive to negative, while $\langle \hat{T}^r{}_r \rangle_{\rm ren}$changes from negative to positive. Moreover, the coupling also determines whether the components present sign changes when evaluated at different radial points. For instance, the $\langle \hat{T}^t{}_t \rangle^{\rm H}_{\rm ren}$ component is negative everywhere in the interior for $\xi = 1/2$ and positive everywhere for $\xi = 0$, while exhibits sign changes for the values $\xi = 1/8$ and $\xi = 1/6$.

5.8 Conclusions

In this Chapter, we outlined a methodology for computing the renormalized vacuum polarization of massive scalar fields on the interior of a black hole spacetime with metric (5.1). We then applied this framework for computing the renormalized vacuum polarization and stress-energy tensor for massless and massive scalar fields on the interior region between the two horizons, r_+ and r_-, of a Reissner-Nordström black hole.

In the first part of the Chapter, we presented a derivation for expressing the Wightman function in the interior for a massive scalar field in the Hartle-Hawking and Unruh states as mode-sums over the separable modes of the wave equation. This is a nontrivial task, for which we generalized the method of Lanir et al. [117], which was originally used to obtain the interior propagators for massless fields. The resulting mode-sum expressions diverge in the coincident limit, requiring renormalization. Hence, to renormalize the Wightman function at coincidence in the interior

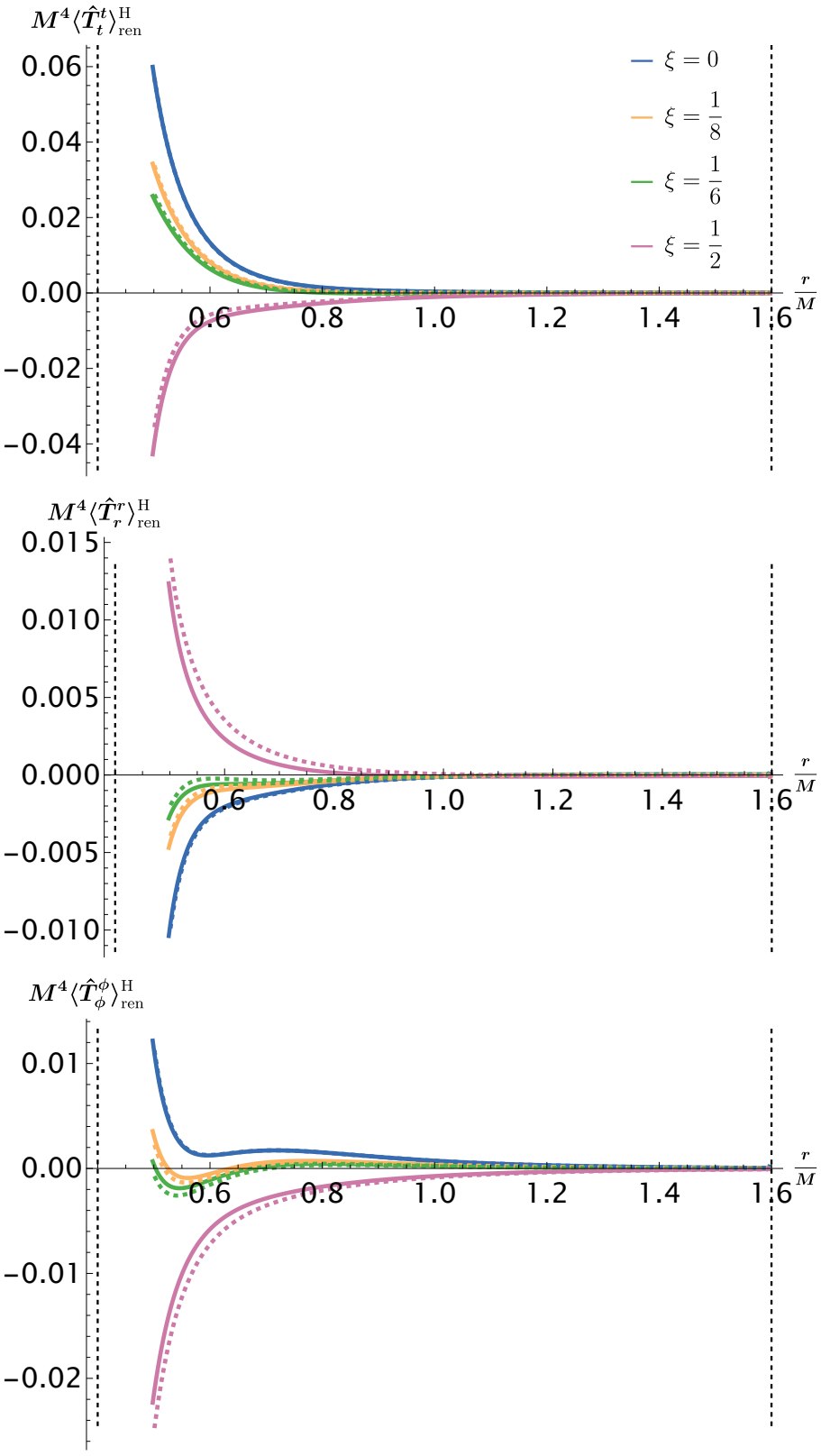


Figure 5.11: *RSET components for massless (solid lines) and massive (dashed lines) fields in the Hartle-Hawking state inside a Reissner-Nordström black hole (with parameters $M = 1$, $Q = 0.8$). The blue, yellow, green and red curves correspond to the different values of the coupling $\xi = \{0, 1/8, 1/6, 1/2\}$. We show from top to bottom $\langle\hat{T}^t{}_t\rangle$, $\langle\hat{T}^r{}_r\rangle$ and $\langle\hat{T}^\phi{}_\phi\rangle$. The RSET for the massive field is computed with the parameter: $\mu M = 0.1$.*

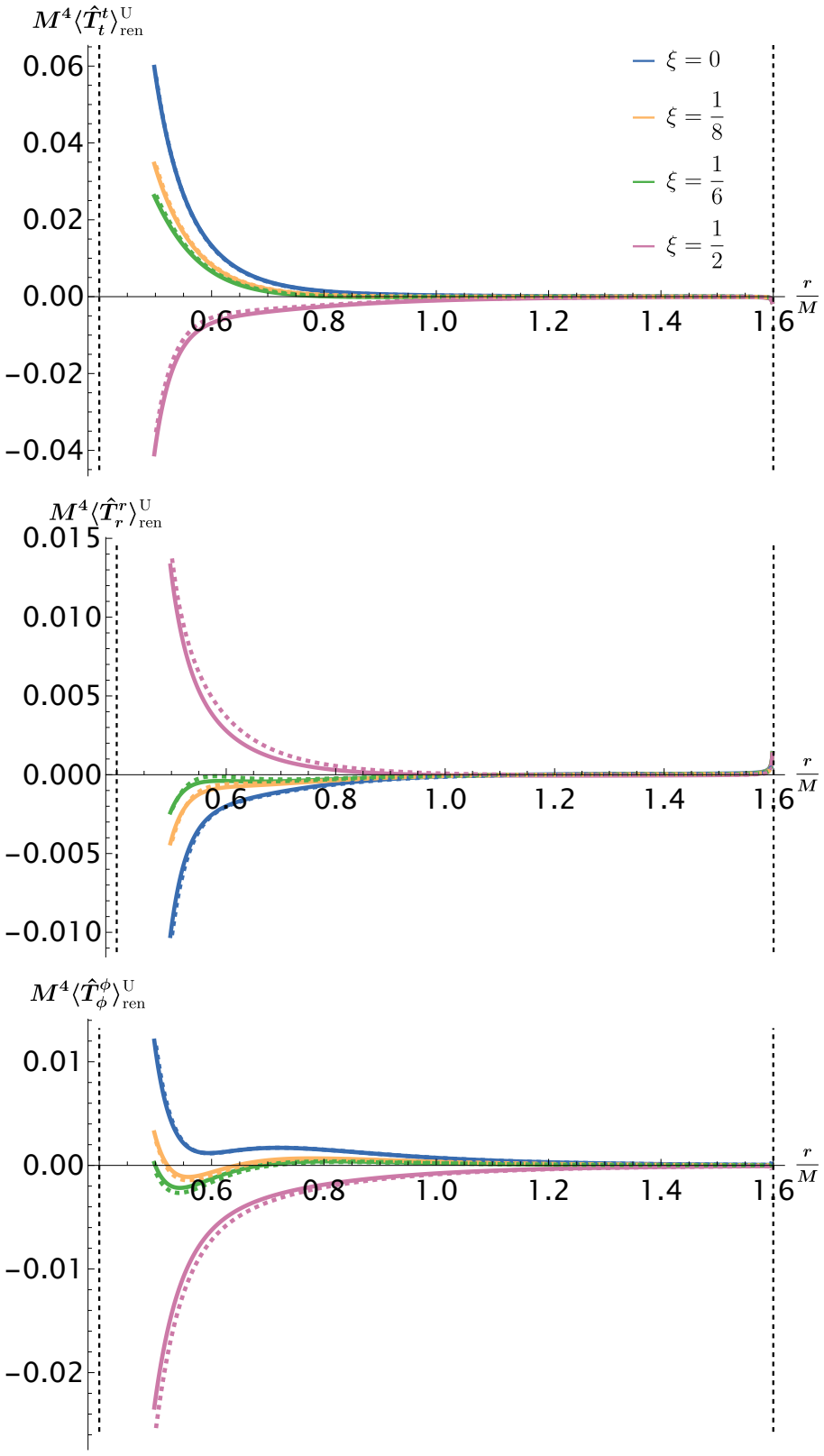


Figure 5.12: *RSET components for massless (solid lines) and massive (dashed lines) fields in the Unruh state inside a Reissner-Nordström black hole (with parameters $M = 1$, $Q = 0.8$). The blue, yellow, green and red curves correspond to the different values of the coupling $\xi = \{0, 1/8, 1/6, 1/2\}$. We show from top to bottom $\langle\hat{T}^t{}_t\rangle$, $\langle\hat{T}^r{}_r\rangle$ and $\langle\hat{T}^\phi{}_\phi\rangle$. The RSET for the massive field is computed with the parameter: $\mu M = 0.1$.*

of the black hole, in the second part of the Chapter, we generalized the extended coordinate method to the black hole interior. We showed that a renormalization prescription valid directly on the Lorentzian manifold can be straightforwardly obtained from the corresponding zero-temperature formalism developed in Chapter 2. The renormalization method described in this Chapter constitutes the first application of the extended coordinate method in Lorentzian spacetime. We emphasise that this methodology is formally valid inside any spherically symmetric black hole, described by the metric in Eq. (5.1), requiring only a modification of the relevant function $f(r)$.

Having solved these challenges, we applied the method for computing the renormalized vacuum polarization in the case of a scalar field propagating on the interior of a Reissner-Nordström black hole. Initially, we focused on obtaining results for massless scalar fields, and we reproduced the results that were obtained in Ref. [119] by means of the pragmatic mode sum renormalization method. Thereafter, having verified the method against existing results, we computed the renormalized vacuum polarization for massive scalar fields inside the black hole. This calculation yielded results in the vicinity of the event horizon that are in agreement with the values obtained by performing the computation on the exterior by means of the original version of the extended coordinate method.

Finally, we obtained the components of the renormalized stress-energy tensor for different values of the coupling ξ on the interior region for both massless and massive scalar fields. To the best of our knowledge, this is the first computation of the RSET for massive fields on the interior of a Reissner-Nordström black hole. We showed that the massless components match smoothly across the event horizon with the exterior ones (as computed in Ref. [93]). The RSET components in the massive case present similar properties to those in the massless case in the region under consideration.

We note that in this chapter, we purposely left the region in the vicinity of the Cauchy horizon out of the analysis. Providing a thorough analysis of the properties of the RVP and the RSET components near the Cauchy horizon will be the purpose of the next Chapter. As discovered in [119], the renormalized vacuum polarization of massless fields exhibits nontrivial behavior when computed extremely close to the Cauchy horizon. Verifying this behavior and extending the analysis to massive fields and the RSET components required consistent numerical and analytical effort that goes beyond the scope of the present Chapter and will be analyzed in depth in the following. For example, we will show that computing the RVP at radial points as close as $\frac{r-r_-}{M} = 10^{-200}$ was found to be necessary.

Chapter 6

Quantum effects near the Cauchy horizon of a Reissner-Nordström black hole

6.1 Introduction

In the previous Chapter, we outlined a methodology for computing the renormalized vacuum polarization and stress-energy tensor inside a Reissner-Nordström black hole, working directly in the Lorentzian manifold. In that Chapter, we presented results in the interior region except very close to the inner horizon, leaving unanswered the question of the asymptotic properties of the various components as the Cauchy horizon is approached. This Chapter addresses this question.

The importance of obtaining results in the vicinity of the inner horizon, both for understanding the implications of quantum effects on the fate of the Cauchy horizon in the context of the Cosmic Censorship hypothesis, together with the surprising behavior of the renormalized vacuum polarization for massless fields near the Cauchy horizon observed in Ref. [119], provides the motivation for the analysis presented in this Chapter. We carry out a detailed investigation of the properties of the renormalized vacuum polarization and of the renormalized stress-energy tensor in this region.

In this Chapter, we compute the renormalized vacuum polarization for both massless and massive scalar fields extraordinarily close to the inner horizon. We complement the numerical results with an analytical treatment that, in agreement with the numerical analysis, reveals the presence of a logarithmic divergence in the RVP at the Cauchy horizon that vanishes in the case of massless fields. In addition, we derive semi-analytical expressions for the RSET components exactly on the Cauchy horizon and discuss their physical implications.

The structure of this Chapter is as follows. In Sec. 6.2, we discuss the numerical difficulties encountered when computing the RVP and RSET near the Cauchy horizon. In Sec. 6.3, we compute the RVP for massless and massive fields and perform an analytical analysis to validate the numerical results. In Section 6.4, we derive semi-analytical expressions for the RSET at the Cauchy horizon, analyze their physical significance, and evaluate them numerically over a wide range of parameters, including the mass of the scalar field, its coupling constant, and the black hole charge. Finally, we conclude the Chapter in Sec. 6.5.

6.2 The numerical challenges for obtaining near-Cauchy horizon results

To study the behavior of the renormalized vacuum polarization in the vicinity of the inner horizon, the use of expression (5.84) is not ideal since the boundary conditions are expressed at the other boundary, namely, at $r = r_+$. Instead we write this solution of Eq. (5.6) in terms of $\Phi^{-}_{\omega l}(r)$ and its complex conjugate, where we define

$$\Phi^{-}_{\omega l}(r) = \frac{1}{r_-} e^{i(\omega-\tilde{\omega})(r-r_-)} e^{-i\omega r_*} \mathsf{H}\left(\bar{a}_1, \bar{a}_2, \bar{a}_3, \bar{a}_4, \bar{a}_5; \bar{\eta}\right), \tag{6.1}$$

with

$$\begin{aligned}
\bar{\eta} &:= \frac{r - r_-}{r_+ - r_-} \\
\bar{a}_1 &:= l(l+1) + 2i\tilde{\omega} r_- - r_-^2(\omega - \tilde{\omega})^2 + i(\omega - \tilde{\omega})(r_+ + r_-), \\
\bar{a}_2 &:= -2i\tilde{\omega}(r_+ - r_-) + (r_+^2 - r_-^2)(\omega - \tilde{\omega})^2, \\
\bar{a}_3 &:= 1 + \frac{2i\omega r_-^2}{r_+ - r_-}, \\
\bar{a}_4 &:= 1 - \frac{2i\omega r_+^2}{r_+ - r_-}, \\
\bar{a}_5 &:= -2i\tilde{\omega}(r_+ - r_-).
\end{aligned} \tag{6.2}$$

The radial function H is a confluent Heun function, normalized to unity as $r \to r_-$, which we compute numerically with the built-in Heun function in *Mathematica*. Equation (6.1) is only valid for the modes with $\omega^2 > \mu^2$. The expression for the $\omega^2 < \mu^2$ modes is found by replacing $\tilde{\omega} \to i\Omega$ in Eqs. (6.1) and (6.2). We can now write the radial solution as a combination of the linearly independent solutions $\Phi^{-}_{\omega l}(r)$ and $\Phi^{-*}_{\omega l}(r)$,

$$\Phi^{\mathrm{II}}_{\omega l}(r) = A_{\omega l}\Phi^{-*}_{\omega l}(r) + B_{\omega l}\Phi^{-}_{\omega l}(r), \tag{6.3}$$

where $A_{\omega l}$ and $B_{\omega l}$ are the same constants as in Eq. (5.64) and are chosen so that the boundary condition (5.64) is satisfied. They can be defined explicitly in terms of Wronskians in the following way:

$$A_{\omega l} = -\frac{r^2 f(r)\, \mathcal{W}[\Phi^{\rm II}_{\omega l}(r), \Phi^{-}_{\omega l}(r)]}{2i\omega}, \tag{6.4}$$

$$B_{\omega l} = \frac{2i\omega - A_{\omega l} r^2 f(r)\, \mathcal{W}[\Phi^{-*}_{\omega l}(r), \Phi^{\rm II}_{\omega l}{}^{*}(r)]}{r^2 f(r)\, \mathcal{W}[\Phi^{-}_{\omega l}(r), \Phi^{\rm II}_{\omega l}{}^{*}(r)]}. \tag{6.5}$$

We will see in Section 6.3.2 that the coefficients $A_{\omega l}$ and $B_{\omega l}$ diverge as $1/\omega$ as $\omega \to 0$ in the case of massive fields, but are finite for massless fields. Since $r^2 f \mathcal{W}[\Phi^{\rm II}_{\omega l}, \Phi^{-}_{\omega l}]$ is constant, we need only to evaluate it at one radial point. We choose to evaluate it at $r = \frac{r_+ + r_-}{2}$ since its evaluation is most efficient when the Heun functions regular at one singular point are not evaluated close to the other singular point. We computed these coefficients, verifying that the Wronskian is constant in r to the working precision, used throughout, of 100 decimal places. We refer to these as the interior scattering coefficients; they satisfy an indefinite conservation relation,

$$|B_{\omega l}|^2 - |A_{\omega l}|^2 = 1. \tag{6.6}$$

When r is sufficiently close to r_-, the solution $\Phi^{\rm II}_{\omega l}(r)$ has the asymptotic behavior in Eq. (5.64).

We have explained how the modes will be computed; let us turn our attention to the renormalization counterterms. For the functions $k^{(n)}_{\omega l}(r)$, the parameter that defines the low and large frequency regimes is not ω itself but the dimensionless quantity

$$z = \frac{|\omega|\, r}{\sqrt{|f|}}, \tag{6.7}$$

which appears as the argument of the hypergeometric functions in

$$\begin{aligned}\mathcal{I}_{\omega l}(a,b|r) = {} & \frac{(2r^2)^{a-1/2}}{|f|^{a+b+1/2}} \frac{2^{a-2}\sqrt{2\pi}(-1)^{a+l}}{\Gamma(b+1)} \\ & \times \left\{ \Gamma(a+\tfrac{1}{2})\Gamma(a+b+\tfrac{1}{2})\, {}_2\hat{F}_3 \left(\begin{matrix} \{a+\frac{1}{2}, a+b+\frac{1}{2}\} \\ \{a+l+\frac{3}{2}, a-l+\frac{1}{2}, \frac{1}{2}\} \end{matrix} \middle| \frac{\omega^2 r^2}{|f|} \right) \right. \\ & \left. - \Gamma(a+1)\Gamma(a+b+1) \frac{|\omega| r}{\sqrt{|f|}}\, {}_2\hat{F}_3 \left(\begin{matrix} \{a+1, a+b+1\} \\ \{\frac{3}{2}, a+l+2, a-l+1\} \end{matrix} \middle| \frac{\omega^2 r^2}{|f|} \right) \right\}. \end{aligned} \tag{6.8}$$

and

$$\mathcal{J}_{\omega l}(a,b\,|r) = \sqrt{\pi}|f|^{a-b}(a-b)!2^{2a}(-1)^l \times \left\{ -\sum_{k=0}^{a-b} \frac{\theta\left(\omega^2-\lambda^2\right)(a-k)!k!|\omega|^{2k-2a-1}r^{2k}}{(a-k-b)!\Gamma(k-a+\frac{1}{2})(k+l+1)!(k-l)!|f|^k} - \frac{(-1)^b r^{2a+2}}{|f|^{a+1}}|\omega|(a+1)!b!\,{}_2\hat{F}_3\left(\begin{matrix}\{a+2,b+1\}\\ \{\frac{3}{2},a-l+2,a+l+3\}\end{matrix}\middle|\frac{\omega^2r^2}{|f|}\right) + \frac{(-1)^b r^{2a+1}}{|f|^{a+1/2}}\Gamma(a+\tfrac{3}{2})\Gamma(b+\tfrac{1}{2})\,{}_2\hat{F}_3\left(\begin{matrix}\{a+\frac{3}{2},b+\frac{1}{2}\}\\ \{\frac{1}{2},a-l+\frac{3}{2},a+l+\frac{5}{2}\}\end{matrix}\middle|\frac{\omega^2r^2}{|f|}\right)\right\}. \tag{6.9}$$

This distinction is particularly relevant near the Cauchy (or event) horizon, where $|f(r)| \to 0$ and competes with ω in defining the different regimes. The low-frequency is the dominant contribution near $r = r_\pm$, and what we mean by low-frequency becomes smaller as we get closer to the horizons. As a result, adapting the first value of the ω-grid is difficult near the horizons, since this value must become extremely small and progressively decrease as $r \to r_\pm$. Moreover, the numerical evaluation of the renormalization counter-terms is challenging at such small frequencies. To address this issue, near the Cauchy horizon, we perform the low-z part of the integral for the regularization counter-terms analytically, using a Taylor expansion about $z = 0$.

Obtaining the renormalization counterterms near the Cauchy horizon is problematic in the large-z regime too. The most efficient (for the numerical computation) representations for computing the regularization parameters $\mathcal{I}_{\omega l}(a,b,|r)$ and $\mathcal{J}_{\omega l}(a,b,|r)$ are given by Eqs. (6.8) and (6.9) and involve hypergeometric functions. However, as previously discussed in Sec. 3.2.3, these expressions encounter problems of catastrophic cancellation when the variable z becomes sufficiently large. The catastrophic cancellation happens from the subtraction of two nearly equal very large terms arising from each term with a hypergeometric function in Eq. (6.8), for $\mathcal{I}_{\omega l}(a,b,|r)$, and each term with a hypergeometric function in Eq. (6.9), for $\mathcal{J}_{\omega l}(a,b,|r)$. Thus, when z is particularly large, using the expressions (6.8) and (6.9) for the numerical computations is impractical. In this regime, we found the alternative expressions in terms of modified Bessel functions reported in Appendix A.2 particularly useful (note, once again, that we need to set $f \to |f|$ in those expressions since we are dealing with the interior). Nonetheless, as we will discuss in Section 6.3, analyzing the behavior of the renormalized vacuum polarization near the inner horizon requires evaluating this quantity at radial points extremely close to the inner horizon. This calculation involves computing the regularization parameters at exceptionally large values of z. For values of $z > 3 \cdot 10^{15}$, even their

representations in terms of Bessel functions break down due to numerical overflow errors. The regularization parameters involve products of Bessel functions of the form $I_\nu(z)K_\nu(z)$, so for very large-z, we employ the asymptotic expansion for large argument for the product of modified Bessel functions [60],

$$I_\nu(z)K_\nu(z) = \frac{1}{2z} + \frac{1}{2z}\sum_{j=0}^{N}\frac{(-1)^{j+1}}{(2z)^{2(j+1)}}\prod_{k=0}^{j}\frac{(2k+1)\left(4\nu^2-(2k+1)^2\right)}{2(k+1)} + \mathcal{O}(z^{-2N-5}), \tag{6.10}$$

expanded up to an appropriate order $\mathcal{O}(z^{-2N-5})$, with $N \geq 0$.

6.3 The renormalized vacuum polarization near the Cauchy horizon

In this Section, we present numerical and analytical results for the renormalized vacuum polarization near the Cauchy horizon.

6.3.1 Numerical results

Fig. 6.1 is the continuation of Fig. 5.7 and depicts the near Cauchy-horizon results for the renormalized vacuum polarization for a massless scalar field in the Hartle-Hawking and Unruh states. These results agree with Fig. 2 in Ref. [119], where it was first shown that the renormalized vacuum polarization for a massless scalar field does not diverge on the Cauchy horizon, but rather approaches a finite negative value. Specifically, we obtain the extrapolated results at the inner horizon $M^2\langle\hat{\Phi}^2\rangle^{\rm H}_{\rm ren} \approx -0.0507$ and $M^2\langle\hat{\Phi}^2\rangle^{\rm U}_{\rm ren} \approx -0.0727$, which agree with those reported in Ref. [119] up to the first two relevant digits of precision. This result for massless fields is extremely surprising. When considering the graph for the renormalized vacuum polarization in Fig. 5.7, one may naively assume it will diverge at the Cauchy horizon since that plot seems to suggest so. Instead, when computed very close to the Cauchy horizon, the RVP has a turning point and, after some oscillations, asymptotes to a finite negative value.

Surprisingly, in the massive case, the outcome is rather different. Indeed, as shown in Fig. 6.2, the vacuum polarization for a massive field in both the Hartle-Hawking and Unruh states diverges logarithmically as the Cauchy horizon is approached, suggesting that quantum effects may be more relevant at the inner horizon in the case of a massive field. In the massive case, all the numerical results presented in this Chapter are obtained by setting the arbitrary lengthscale to $\ell = M$. In Figure 6.3, we report the results obtained in the vicinity of the inner horizon for the

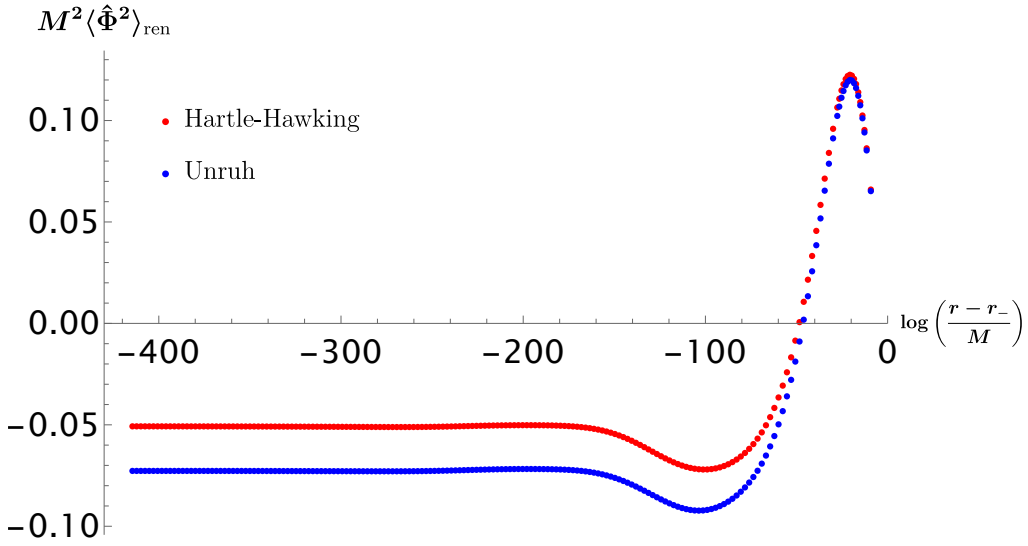


Figure 6.1: *Results for $\langle\hat{\Phi}^2\rangle_{\rm ren}$ in the Hartle-Hawking (red) and Unruh (blue) states obtained with the parameters $Q = 0.8M$, $\mu M = 0$ in the vicinity of the inner horizon. These results range between $10^{-180} \leq \frac{r-r_-}{M} \leq 10^{-4}$.*

Hartle-Hawking and Unruh states for a wide range of masses of the scalar field. In the limit as $\mu \to 0$, the vacuum polarization approaches the massless result. In fact, it can be shown numerically that the divergence is of the form $k(\mu, Q) \log|f|$, with $\lim_{\mu\to 0} k(\mu, Q) = 0$. Again, we see a suppression of the state dependence for larger values of mass.

In Fig. 6.4, we present results for $\langle\hat{\Phi}^2\rangle^{\rm A}_{\rm ren}$ in the Hartle-Hawking and Unruh states for a range of different charges of the black hole. The value of $\langle\hat{\Phi}^2\rangle^{\rm A}_{\rm ren}$ very near the Cauchy horizon is a decreasing function of the charge Q. Moreover, we find numerically $\lim_{Q\to M} k(\mu, Q) = 0$.

As $r \to r_-$, the contribution to $\langle\hat{\Phi}^2\rangle^{\rm A}_{\rm ren}$ is dominated by the low-frequency $l = 0$ mode. These features are illustrated in Fig.s 6.5 and 6.6. Fig. 6.5 provides numerical evidence that the $l = 0$ dominates near the Cauchy horizon. Fig. 6.6 depicts the behavior of $g_{\omega 0}(r)$ as a function of r and ω. This Figure shows the increasing relevance of low-frequency contributions to $g_{\omega 0}(r)$ as r approaches the inner horizon.

In Sec. 6.3.2, we study analytically the behavior of the renormalized vacuum polarization near the Cauchy horizon.

6.3.2 Analytic derivation of the near-Cauchy horizon behaviour

Now, let us consider the behaviour of the renormalized vacuum polarization $\mathsf{w}^{\rm A}(r) = \langle\hat{\Phi}^2\rangle^{\rm A}_{\rm ren}$ (as defined in Eq. (5.80)) near the Cauchy horizon. Using the fact that for $\tilde{\omega} > 0$, we have $\tilde{\omega}\, B^{\rm up}_{\omega l} = \omega\, B^{\rm in}_{\omega l}$ and $\tilde{\omega}(1 - |A^{\rm up}_{\omega l}|^2) = \omega\, |B^{\rm in}_{\omega l}|^2$ (see Eq. (5.20)), we can formally write the renormalized vacuum polarization in the coincidence limit $x' = x$

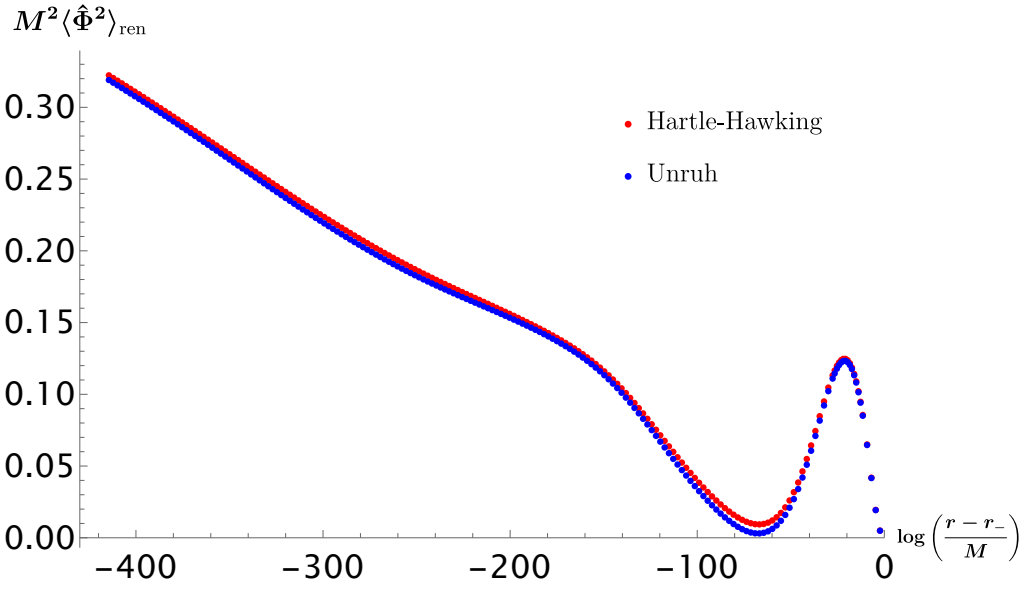


Figure 6.2: *Results for $\langle\hat{\Phi}^2\rangle_{\rm ren}$ in the Hartle-Hawking (red) and Unruh (blue) states obtained with the parameters $Q = 0.8M$, $\mu M = 0.1$ in the vicinity of the inner horizon. These results range between $10^{-180} \leq \frac{r-r_-}{M} \leq 10^{-1}$.*

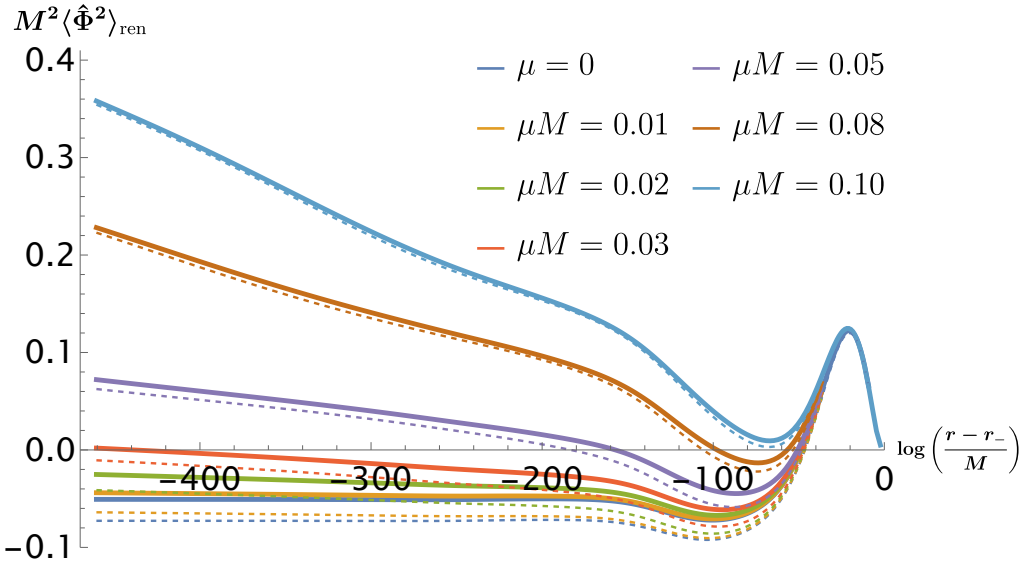


Figure 6.3: *Results for $\langle\hat{\Phi}^2\rangle_{\rm ren}$ in the Hartle-Hawking (solid lines) and Unruh (dashed lines) states obtained with the parameter $Q = 0.8M$ in the vicinity of the inner horizon for different values of the mass of the scalar field μ. These results range between $10^{-200} \leq \frac{r-r_-}{M} \leq 10^{-1}$.*

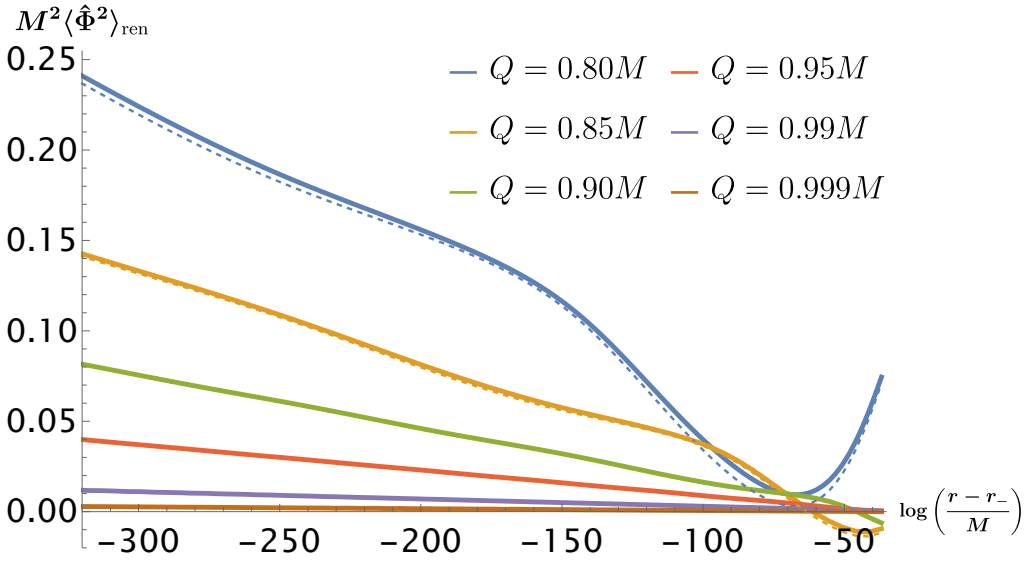


Figure 6.4: *Results for $\langle\hat{\Phi}^2\rangle_{\rm ren}$ in the Hartle-Hawking (solid lines) and Unruh (dashed lines) states obtained with the parameter $\mu M = 0.1$ in the vicinity of the inner horizon for different values of the charge of the black hole Q. These results range between $10^{-140} \leq \frac{r-r_-}{M} \leq 10^{-16}$.*

and with $r \to r_-$ as

$$\mathsf{w}^{\rm A}(r) = \mathsf{w}_<(r) + \mathsf{w}^{\rm A}_>(r) \tag{6.11}$$

where, setting $n = 1$ into Eq. (5.80),

$$\begin{aligned}
\mathsf{w}_<(r) =& \frac{1}{4\pi^2}\sum_{l=0}^{\infty}(2l+1)\int_0^{\mu} d\omega \left\{g^<_{\omega l}(r) - k^{(1)}_{\omega l}(r)\right\} \\
&- \frac{1}{8\pi^2}\left[\mathcal{D}^{(\rm p)}_{11}(r) + \frac{\mathcal{D}^{(\rm r)}_{10}(r)}{|f|} + \frac{\mathcal{D}^{(\rm r)}_{11}(r)}{|f|^2} + \mathcal{T}^{(\rm l)}_{00}(r)(\log(|f|/(\ell^2\lambda^2)) - 2\gamma_{\rm E})\right], \\
\mathsf{w}^{\rm A}_>(r) =& \frac{1}{4\pi^2}\sum_{l=0}^{\infty}(2l+1)\int_{\mu}^{\infty} d\omega \left\{g^{\rm A,>}_{\omega l}(r) - k^{(1)}_{\omega l}(r)\right\},
\end{aligned} \tag{6.12}$$

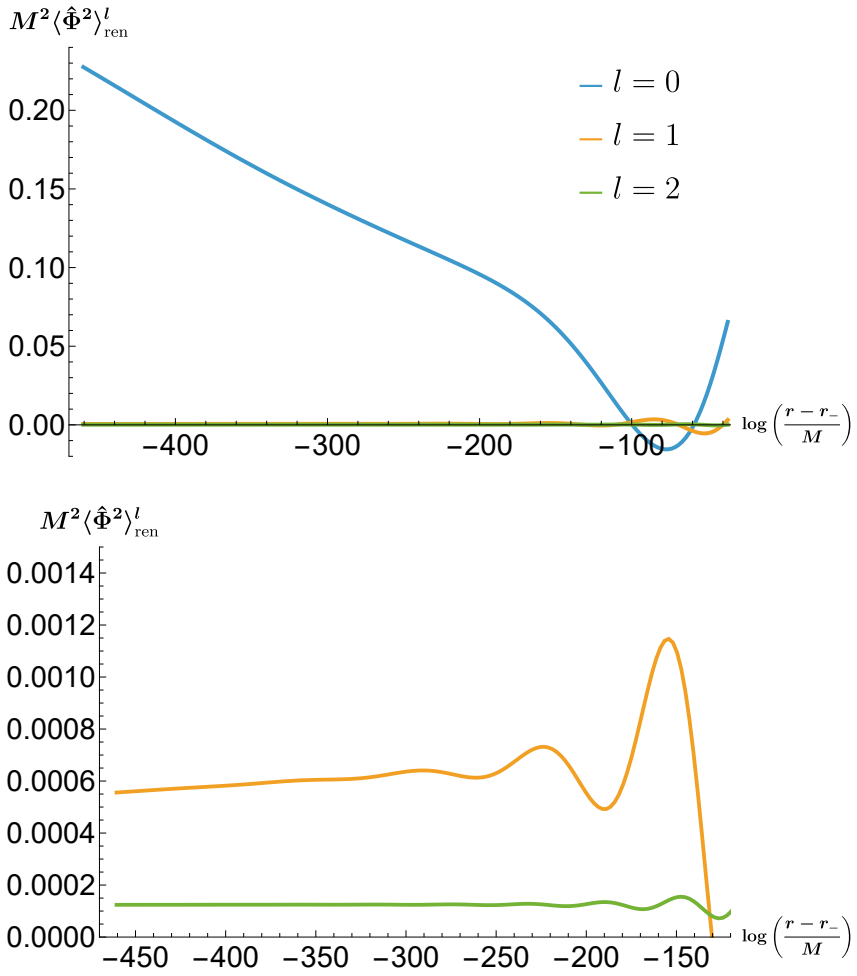


Figure 6.5: *Different l-modes contributions to $\langle\hat{\Phi}^2\rangle_{\text{ren}}$ in the Hartle-Hawking state obtained with the parameter $\mu M = 0.08$ in the vicinity of the inner horizon. These results range between $10^{-200} \leq \frac{r-r_-}{M} \leq 10^{-16}$. This figure shows that the $l = 0$ mode dominates as $r \to r_-$. The bottom plot is a zoom-in that displays the near-inner horizon behavior of the $l = 1$ and $l = 2$ modes.*

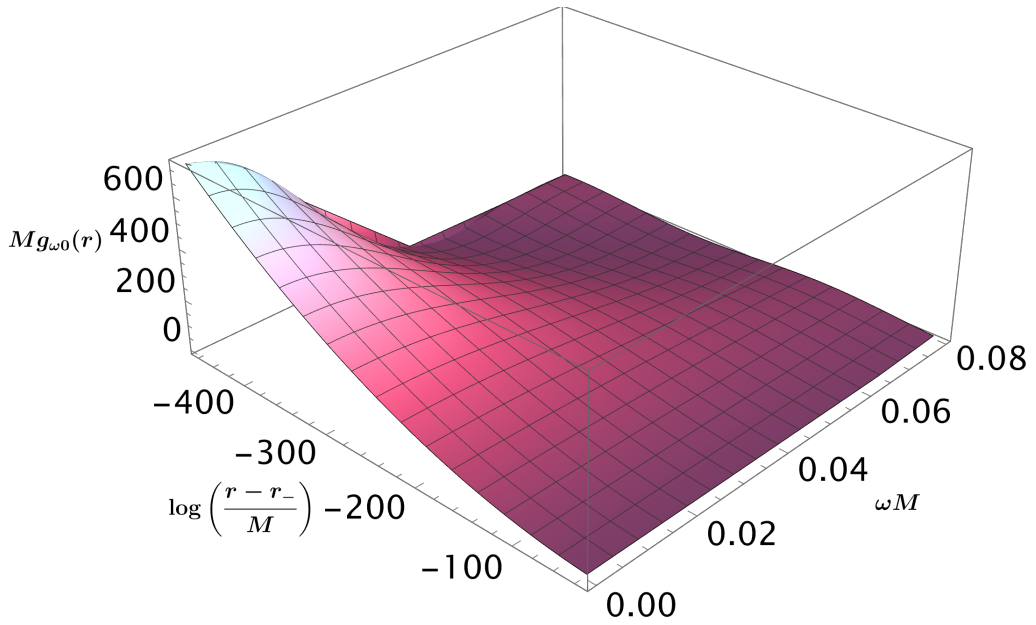


Figure 6.6: *Low frequency behavior of $g_{\omega 0}(r)$ as $r \to r_-$. This graph was obtained for the Hartle-Hawking state with the parameters $Q = 0.8M$ and $\mu M = 0.08$. This figure shows that the low frequency contribution of $g_{\omega 0}(r)$ is increasingly important as $r \to r_-$.*

and

$$
\begin{aligned}
g^{<}_{\omega l}(r) :=& \frac{1}{2\,r_-^2\,\omega}\Big[\Big(|A_{\omega l}|^2 + |B_{\omega l}|^2 + A_{\omega l}\,B^*_{\omega l}e^{2i\omega\, r_*} + A^*_{\omega l}B_{\omega l}e^{-2i\omega\, r_*}\Big)\coth(\tfrac{\pi\,\omega}{\kappa_+}) \\
&+ \Re\Big\{A^{\rm up}_{\omega l}\Big(A^2_{\omega l}e^{2i\omega r_*} + B^2_{\omega l}e^{-2i\omega r_*} + 2A_{\omega l}B_{\omega l}\Big)\Big\}\mathrm{csch}(\tfrac{\pi\omega}{\kappa_+})\Big], \\
g^{{\rm H},>}_{\omega l}(r) =& \frac{1}{2\,r_-^2\,\omega}\Big[\Big(|A_{\omega l}|^2 + |B_{\omega l}|^2 + A_{\omega l}\,B^*_{\omega l}e^{2i\omega\, r_*} + A^*_{\omega l}B_{\omega l}e^{-2i\omega\, r_*}\Big)\coth(\tfrac{\pi\,\omega}{\kappa_+}) \\
&+ \Re\Big\{A^{\rm up}_{\omega l}\Big(A^2_{\omega l}e^{2i\omega r_*} + B^2_{\omega l}e^{-2i\omega r_*} + 2A_{\omega l}B_{\omega l}\Big)\Big\}\mathrm{csch}(\tfrac{\pi\omega}{\kappa_+})\Big], \\
g^{{\rm U},>}_{\omega l}(r) =& \frac{1}{4\,r_-^2\,\omega}\Big[\Big(|A_{\omega l}|^2 + |B_{\omega l}|^2 + A_{\omega l}\,B^*_{\omega l}e^{2i\omega\, r_*} + A^*_{\omega l}B_{\omega l}e^{-2i\omega\, r_*}\Big) \\
&\times\Big(\coth(\tfrac{\pi\,\omega}{\kappa_+}) + 1 + (\coth(\tfrac{\pi\omega}{\kappa_+}) - 1)|A^{\rm up}_{\omega l}|^2\Big) \\
&+ 2\,\Re\Big\{A^{\rm up}_{\omega l}\Big(A^2_{\omega l}e^{2i\omega r_*} + B^2_{\omega l}e^{-2i\omega r_*} + 2A_{\omega l}B_{\omega l}\Big)\Big\}\mathrm{csch}(\tfrac{\pi\omega}{\kappa_+})\Big]. \qquad (6.13)
\end{aligned}
$$

In these expressions, H and U refer to the Hartle-Hawking and Unruh states respectively. In the $\omega < \mu$ regime of the frequency spectrum, $g^{<}_{\omega l}$ is identical for the two states. For massless fields, we can take μ here to be an arbitrary inverse length scale. It is $\mathsf{w}^{\rm A}_{>}(r)$ that is renormalized by the Hadamard counterterms since this contains the high-frequency (or ultra-violet) divergences. Any divergences which might ostensibly emerge from the integral in $\mathsf{w}_<$ are of the low-frequency (or infra-red) type.

Let us start by analysing the asymptotic behavior of $\mathsf{w}_<(r)$. We wish to examine whether there is such an infra-red divergence as $r \to r_-$. This is a particularly subtle limit since the asymptotic form depends on the combination $\omega\, r_*$ which is

indeterminate at $\omega = 0$, $r = r_-$. And yet it is precisely the limit $\omega \to 0$, $r \to r_-$ that we would like to compute since the numerical calculation makes it clear that the dominant contribution to the first integral as $r \to r_-$ is the very low-frequency modes. To obtain a low-frequency approximation that is valid in the limit $r \to r_-$, we avoid taking any low-frequency approximations in terms that involve a radial dependence, in other words, we consider low-frequency approximations only of the scattering coefficients $A_{\omega l}$, $B_{\omega l}$, $A^{\rm up}_{\omega l}$.

Now the scattering theory on the interior is different from that on the exterior in a significant way. On the exterior, conservation of energy implies uniform boundedness of the scattering coefficients $A^{\rm in/up}_{\omega l}$ and $B^{\rm in/up}_{\omega l}$. For example, for a massless field we have $|A^{\rm in}_{\omega l}|^2 + |B^{\rm in}_{\omega l}|^2 = 1$ and, since the left-hand side is the sum of positive definite terms adding to unity, they must be bounded. However, the equivalent energy conservation on the interior is indefinite and is given by Eq. (6.6). The terms on the left hand side now could, in principle, be unbounded and still their difference could be bounded. In fact, this is precisely what happens for a massive field in the limit $\omega \to 0$. The small frequency expansions of the interior scattering coefficients are [124, 125]

$$\begin{aligned} A_{\omega l} &= \frac{i\, q_l}{\omega} + a_l^{(0)} + a_l^{(1)}\, \omega + \mathcal{O}(\omega^2), \\ B_{\omega l} &= -\frac{i\, q_l}{\omega} + b_l^{(0)} + b_l^{(1)}\, \omega + \mathcal{O}(\omega^2) \end{aligned} \tag{6.14}$$

where $q_l \in \mathbb{R}$, $a_l^{(0,1)}, b_l^{(0,1)} \in \mathbb{C}$, $\forall\ l$, and (6.6) implies

$$\begin{aligned} &\Im\{b_l^{(0)}\} = -\Im\{a_l^{(0)}\}, \\ &2q_l\, \Im\{b_l^{(1)}\} = -1 - 2q_l\, \Im\{a_l^{(1)}\} + \Re\{b_l^{(0)}\}^2 - \Re\{a_l^{(0)}\}^2. \end{aligned} \tag{6.15}$$

The real number q_l is related to the Wronskian of zero-frequency solutions of the radial equation (5.6). It has been proven [124] that $q_l = 0$ if and only if the zero-frequency radial equation admits a solution that is bounded on the entire domain $[r_-, r_+]$. For the massless field $\mu = 0$, the zero-frequency radial equation does indeed admit a solution bounded on $[r_-, r_+]$. Specifically, the Legendre polynomial $P_l(1-2\eta)$ with $\eta = (r_+ - r)/(r_+ - r_-)$ is a solution to Eq. (5.6) with $\omega = 0$, $\mu = 0$ and is regular in $r \in [r_-, r_+]$ ($\eta \in [0, 1]$). Hence, for a massless field, $q_l = 0$ and it follows that the interior scattering coefficients are bounded as $\omega \to 0$.

On the other hand, for a massive field $\mu \neq 0$, if a zero-frequency solution to Eq. (5.6) is regular at one of the singular points $r = r_\pm$, then it is necessarily singular at the other [124, 125]. It follows that $q_l \neq 0$ and the scattering coefficients are unbounded as $\omega \to 0$. This presents an additional complication since it is precisely the low-frequency contribution to the Wightman function that we wish to

compute.

We wish to approximate the low-frequency integral

$$G^{<} := \frac{1}{4\pi^2}\sum_{l=0}^{\infty}(2l+1)\int_0^{\mu} d\omega\, g^{<}_{\omega l}(r) \tag{6.16}$$

as $r \to r_-$ using the low-frequency expansions of the form (6.14) along with the low-frequency expansion of the exterior scattering coefficient $A^{\rm up}_{\omega l}$. We are in the regime of bound-state modes $\omega^2 < \mu^2$ whence energy conservation gives $|A^{\rm up}_{\omega l}|^2 = 1$ (see Eq. (5.21)). It can be shown that $A^{\rm up}_{\omega l} \to -1$ as $\omega \to 0$ [116] (see also Appendix C.2) and imposing the conservation condition we obtain the small frequency expansion

$$\begin{aligned} &A^{\rm up}_{\omega l} = -1 + A^{(1)}_l\,\omega + A^{(2)}_l\omega^2 + \mathcal{O}(\omega^3),\\ &\Re\{A^{(1)}_l\} = 0,\\ &\Re\{A^{(2)}_l\} = \tfrac{1}{2}\Im\{A^{(1)}_l\}^2. \end{aligned} \tag{6.17}$$

Now to arrive at an appropriate small-frequency expansion of $g^{<}_{\omega l}(r)$, one that is valid in the asymptotic limit $r_* \to \infty$, we perform a small frequency expansion of the functions $\coth(\pi\omega/\kappa_+)$ and $\mathrm{csch}(\pi\omega/\kappa_+)$ in Eq. (6.13), but not of the $e^{\pm i\omega r_*}$ factors. We keep the $e^{\pm i\omega r_*}$ factors unexpanded since the quantity ωr_* remains not small in the asymptotic limit $r_* \to \infty$, even if $\omega \to 0$. The result is

$$\begin{aligned} g^{<}_{\omega l}(r) = &+ \frac{\left(\pi^2 q_l^2 + \kappa_+^2 (c_l^{(0)})^2\right)}{2\pi\,\kappa_+\, r_-^2}\frac{\left(1-\cos(2\omega\, r_*)\right)}{\omega^2}\\ &+ \frac{\left(\pi^2 q_l\,\Im\{a_l^{(0)}\} + \kappa_+^2 c_l^{(0)}(c_l^{(1)} + \Im\{a_l^{(0)}\}\Im\{A_l^{(1)}\})\right)}{\pi\,\kappa_+\, r_-^2}\frac{\left(1-\cos(2\omega\, r_*)\right)}{\omega}\\ &- \frac{\left((\Re\{a_l^{(0)}\} + \Re\{b_l^{(0)}\})(\pi^2 q_l^2 + \kappa_+^2 (c_l^{(0)})^2) + c_l^{(0)}\kappa_+^2\right)}{2\pi\,\kappa_+\, q_l\, r_-^2}\frac{\sin(2\omega\, r_*)}{\omega}\\ &+ \mathcal{O}(\omega^j)e^{\pm i\omega r_*}, \qquad j \geq 0, \end{aligned} \tag{6.18}$$

where we have defined

$$c_l^{(k)} = \Re\{a_l^{(k)}\} - \Re\{b_l^{(k)}\} + q_l\,\Im\{A_l^{(k+1)}\} \in \mathbb{R}, \qquad k \in \mathbb{N}, \tag{6.19}$$

and where $A_l^{(k)}$ is the coefficient of ω^k in Eq. (6.17). The terms we are ignoring in this expansion are finite after integrating with respect to ω and then taking the limit $r_* \to \infty$. Now performing this integral and afterwards considering a large r_*

expansion, we obtain

$$\begin{aligned}\int_0^\mu d\omega\, g^<_{\omega l}(r) &\sim \frac{1}{2\,\kappa_+\, r_-^2}(\pi^2 q_l^2 + \kappa_+^2 (c_l^{(0)})^2) r_* + \mathcal{O}(\log(r_*)), \quad r_* \to \infty, \\ &\sim -\frac{r_+^2}{(r_+ - r_-)^2}\left(\pi^2 q_l^2 + \kappa_+^2 (c_l^{(0)})^2\right)\log|f| \\ &\quad + \mathcal{O}(\log(\log|f|)), \qquad\qquad r \to r_-. \end{aligned} \tag{6.20}$$

We also need to compute (see the regularization terms in Eq. (2.49) with $n = 1$)

$$\begin{aligned}K^< := \frac{1}{4\pi^2}\sum_{l=0}^{\infty}(2l+1)\int_0^\mu k^{(1)}_{\omega l}(r)d\omega + \frac{1}{8\pi^2}\Bigg[\mathcal{D}^{(\mathrm{p})}_{11}(r) + \frac{\mathcal{D}^{(\mathrm{r})}_{10}(r)}{|f|} + \frac{\mathcal{D}^{(\mathrm{r})}_{11}(r)}{|f|^2} \\ + \mathcal{T}^{(\mathrm{l})}_{00}(r)\left(\log(|f|/(\ell^2\mu^2)) - 2\gamma_{\mathrm{E}}\right)\Bigg]\end{aligned} \tag{6.21}$$

where

$$k^{(1)}_{\omega l}(r) = \sum_{a=0}^{1}\sum_{b=0}^{a}\mathcal{D}^{(\mathrm{r})}_{ab}(r)\mathcal{I}_{\omega l}(a,b|r) + \mathcal{T}^{(\mathrm{l})}_{00}(r)\mathcal{J}_{\omega l}(0,0|r). \tag{6.22}$$

We note that we only need to subtract the minimal terms in the parametrix that guarantee that we have captured the geometric Hadamard divergences. Since we are not interested in accelerating the numerical convergence, but rather in the analytical behavior near the inner horizon, we simply need to guarantee that the renormalization counterterms have been subtracted, which necessitates $n = 1$.

Using the explicit representation of the regularization parameters $\mathcal{I}_{\omega l}(a,b|r)$ and $\mathcal{J}(a,b|r)$ in terms of modified Bessel functions, we can compute analytically the low frequency integrals of the regularization parameters in the limit $r \to r_-$. This is a sensitive limit since the arguments of the Bessel functions involve $\omega\, r/\sqrt{|f|}$ which is indeterminate at $\omega = 0$, $r = r_-$. Nevertheless, it can be shown that

$$\begin{aligned}\int_0^\mu \mathcal{I}_{\omega l}(0,0|r)d\omega &\sim -\frac{1}{8\,r_-^2}\log|f| + \mathcal{O}(1), \quad r \to r_-, \\ \int_0^\mu \mathcal{I}_{\omega l}(1,0|r)d\omega &\sim -\frac{1}{2|f|}\delta_{l,0} + \mathcal{O}(1), \qquad r \to r_-, \\ \int_0^\mu \mathcal{I}_{\omega l}(1,1|r)d\omega &\sim -\frac{1}{2|f|^2}\delta_{l,0} + \mathcal{O}(1), \qquad r \to r_-, \\ \int_0^\mu \mathcal{J}_{\omega l}(0,0|r)d\omega &\sim -\frac{1}{2}\log|f|\,\delta_{l,0} + \mathcal{O}(1), \quad r \to r_-. \end{aligned} \tag{6.23}$$

We note that there is no contribution at $\mathcal{O}(1/f)$ in the integral of $\mathcal{I}_{\omega l}(1,1|r)$. Putting these details together, we have that for both the Hartle-Hawking and the Unruh

states

$$\mathsf{w}_{<}(r) \sim \left(G^{<} - K^{<}\right) \sim \sum_{l=0}^{\infty}(2l+1)\, h_l(\mu) \log|f|, \quad r \to r_-, \tag{6.24}$$

where

$$h_l(\mu) = -\frac{1}{16\pi^2 r_-^2}\left\{\frac{4r_+^2 r_-^2}{(r_+ - r_-)^2}\left(\pi^2 q_l^2 + \kappa_+^2 (c_l^{(0)})^2\right) - \tfrac{1}{2}\mathcal{D}_{00}^{(\mathrm{r})}\right\}. \tag{6.25}$$

We highlight that, by using the integrals in Eq. (C.43), it can be shown that the same results holds when the Hadamard parametrix is expanded to order $n = 2$.

In the $\omega > \mu$ regime, focusing on the Hartle-Hawking state first, we rearrange the expression for $\mathsf{w}^{\mathrm{H}}_{>}(r)$ as

$$\begin{aligned}\mathsf{w}^{\mathrm{H}}_{>}(r) \sim & \frac{1}{4\pi^2}\sum_{l=0}^{\infty}(2l+1)\int_{\mu}^{\infty} d\omega \left[\frac{\coth(\pi\omega/\kappa_+)}{2\omega\, r_-^2}\left(|A_{\omega l}|^2 + |B_{\omega l}|^2\right)\right. \\ & \left. + \frac{\operatorname{csch}(\pi\omega/\kappa_+)}{2\omega\, r_-^2}\Re\{2A^{\mathrm{up}}_{\omega l}(A_{\omega l}B_{\omega l})\} - k^{(1)}_{\omega l}(r_-)\right] \\ & + \frac{1}{4\pi^2}\sum_{l=0}^{\infty}(2l+1)\Re\left\{\int_{\mu}^{\infty} d\omega\, j_l^{+}(\omega)e^{2i\omega r_*} + \int_{\mu}^{\infty} d\omega\, j_l^{-}(\omega)e^{-2i\omega r_*}\right\}, \\ & \qquad\qquad r \to r_-, \end{aligned} \tag{6.26}$$

where we have taken $\Re\{\cdot\}$ outside the last two integrals, and defined for convenience

$$\begin{aligned} j_l^{+}(\omega) &= \frac{1}{2\omega\, r_-^2}\left[\coth(\pi\,\omega/\kappa_+)A_{\omega l}B^*_{\omega l} + \operatorname{csch}(\pi\omega/\kappa_+)A^{\mathrm{up}}_{\omega l}A^2_{\omega l}\right], \\ j_l^{-}(\omega) &= \frac{1}{2\omega\, r_-^2}\left[\coth(\pi\omega/\kappa_+)A^*_{\omega l}B_{\omega l} + \operatorname{csch}(\pi\omega/\kappa_+)A^{\mathrm{up}}_{\omega l}B^2_{\omega l}\right]. \end{aligned} \tag{6.27}$$

The first integral is a rapidly convergent integral (since $k^{(1)}_{\omega l}(r)$ by definition captures the ultraviolet behaviour of $g^{\mathrm{H},>}_{\omega l}(r)$) that is independent of r; let us label this integral as $\mathcal{W}_l^{\mathrm{H},>}$. Now the integrals in the remaining terms are of the form

$$\int_{-\infty}^{\infty}\theta(\omega^2 - \mu^2) j_l^{\pm}(\omega)e^{\pm 2i\omega r_*}d\omega, \tag{6.28}$$

where $\theta(\omega^2 - \mu^2)j_l^{\pm}(\omega)$ are integrable functions over $\omega \in \mathbb{R}$. Indeed, $j_l^{\pm}(\omega)$ contain factors such as $A_{\omega l}$, $A^{\mathrm{up}}_{\omega l}$ and $\operatorname{csch}(\pi\omega/\kappa_+)$, which decay exponentially as $|\omega| \to \infty$, while $B_{\omega l} \to 1$ as $|\omega| \to \infty$, and hence $j_l^{\pm}(\omega)$ decay exponentially as $|\omega| \to \infty$. By the Riemann-Lebesgue Lemma, in the limit $r_* \to +\infty$, these integrals must vanish

and hence we must have

$$\mathsf{w}^{\mathrm{H}}_{>}(r) \sim \frac{1}{4\pi^2}\sum_{l=0}^{\infty}(2l+1)\mathcal{W}_l^{\mathrm{H},>}, \qquad r \to r_-, \tag{6.29}$$

which is finite at the inner horizon. The convergence of the l-sum is achieved by construction with the presence of the renormalization counterterms $k^{(1)}_{\omega l}(r_-)$. A similar analysis shows that $\mathsf{w}^{\mathrm{U}}_{>}(r)$ is also finite at the inner horizon. Hence, for massive fields, in the limit as $r \to r_-$, the renormalized vacuum polarization both in the Hartle-Hawking and Unruh states is dominated by its low frequency contribution $\mathsf{w}_{<}(r)$, which is logarithmically divergent at r_-

$$\mathsf{w}^{\mathrm{A}}(r) \sim \mathsf{w}_{<}(r) \sim \log|f|\sum_{l=0}^{\infty}(2l+1)\,h_l(\mu), \quad r \to r_-. \tag{6.30}$$

Let us now evaluate the quantity $h_l(\mu)$ in the massless limit. As already mentioned, $q_l = 0$ in this limit. The expression for $c_l^{(0)}$ can be obtained explicitly for massless fields. In [126], it was shown that

$$a_l^{(0)} = \frac{(-1)^{l+1}(r_+^2 - r_-^2)}{2r_+r_-}, \qquad b_l^{(0)} = \frac{(-1)^{l}(r_+^2 + r_-^2)}{2r_+r_-}, \tag{6.31}$$

and since $q_l = 0$, we have

$$c_l^{(0)} = a_l^{(0)} - b_l^{(0)} = (-1)^{l+1}\frac{r_+}{r_-}, \tag{6.32}$$

which in turn implies, using Eq. (A.6),

$$h_l(0) = 0. \tag{6.33}$$

Hence, for a massless field the coefficient of the leading order term in the asymptotic expansion (6.30) vanishes for all l. There is, in principle, also a subleading $\log(\log|f|)$ divergence as $r \to r_-$ coming from the second term in Eq. (6.18), and so this term has a coefficient proportional to

$$\pi^2 q_l\,\Im\{a_l^{(0)}\} + \kappa_+^2 c_l^{(0)}(c_l^{(1)} + \Im\{a_l^{(0)}\}\Im\{A_l^{(1)}\}). \tag{6.34}$$

In the massless limit, $a_l^{(0)}$ and $b_l^{(0)}$ are purely real while $a_l^{(1)}$ and $b_l^{(1)}$ are purely imaginary, a fact easily deduced from the small frequency expansion of Eq. (6.14). Together with $q_l = 0$, this implies that the expression above vanishes and hence there is no $\log(\log|f|)$ divergence either. The conclusion here is that the vacuum polarization is regular as $r \to r_-$ for massless scalar fields, agreeing with the numerical

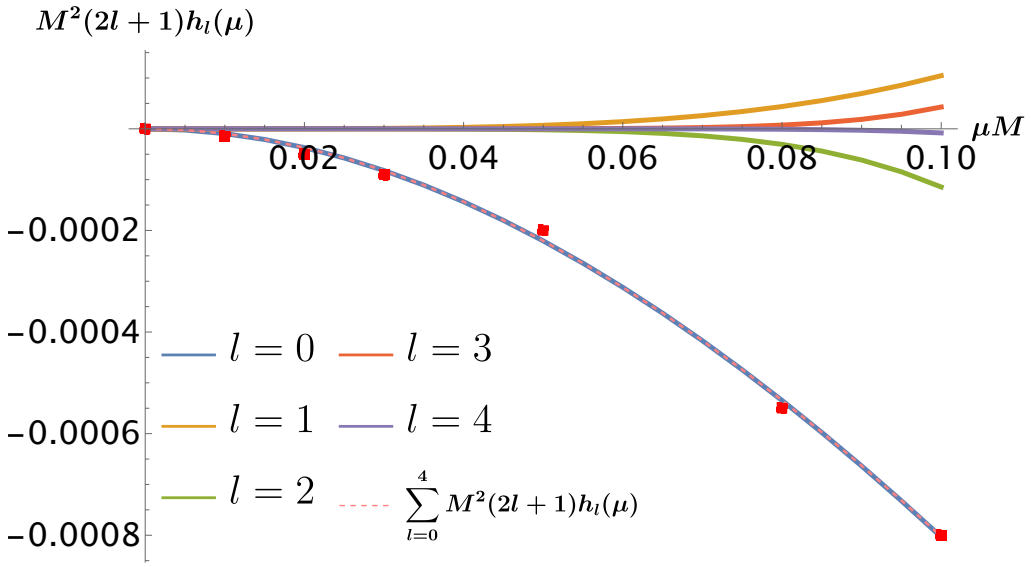


Figure 6.7: *In this figure, the coefficient of the logarithmic divergence $h_l(\mu)$ is plotted as a function of the mass of the scalar field. Note that, for visualization purposes, the $l \geq 1$ modes have been multiplied by a factor $10^{2(2l-1)}$. This figure also shows that the $l = 0$ mode provides the dominant contribution to the coefficient of the logarithmic divergence. The red squares represent the coefficients obtained from the full numerical results by fitting the function $\langle \hat{\Phi}^2 \rangle_{ren}$ near the inner horizon. The small discrepancy with the sum of the numerically obtained coefficients arises from an uncertainty in the fitting process. The coefficients are obtained with the parameter $Q = 0.8M$.*

results.

On the other hand, can we deduce anything about the massive case? Explicit formulae for the q_l and $c_l^{(k)}$ coefficients are difficult to derive since there are no known closed form zero-frequency solutions for the radial equation when $\mu \neq 0$. It is possible to derive analytic approximations for the scattering coefficients in the low-frequency and high-l regime but it is the low-l modes that are the dominant contribution to the coefficient of the logarithm in Eq. (6.30). In Fig. 6.7 we compute the coefficient numerically[1] showing that the coefficient is nonzero for massive fields and that it depends on the mass. Additionally, this figure highlights how the contribution to the coefficient of the logarithmic divergence decreases rapidly with increasing l-modes. Furthermore, as depicted in Fig. 6.8, the coefficient of the logarithmic divergence approaches zero as the mass of the scalar field becomes sufficiently large. In Appendix C.2, we show analytically, through asymptotic matching, that indeed the coefficient vanishes in the large mass regime.

We find it very interesting that the massless and massive field have such different

[1]To obtain numerically q_l and $c_l^{(0)}$, we compute $A_{\omega l}$, $B_{\omega l}$ and $A^{\rm up}_{\omega l}$ for a very small value of ω (i.e. $\bar{\omega}M = 10^{-20}$). Then, assuming Eq. (6.14), we can approximate $a_l^{(0)} \approx \Re\{A_{\bar{\omega} l}\}$, $b_l^{(0)} \approx \Re\{B_{\bar{\omega} l}\}$ and $q_l \approx \bar{\omega}\Im\{A_{\bar{\omega} l}\}$. Similarly, assuming Eq. (6.17), we compute $A_l^{(1)} \approx \frac{A^{\rm up}_{\bar{\omega} l} - (-1)}{\bar{\omega}}$. One can verify the accuracy of this procedure by repeating the calculation for different values of $\bar{\omega}$ and checking that the resulting coefficients remain unchanged to the required number of significant digits.

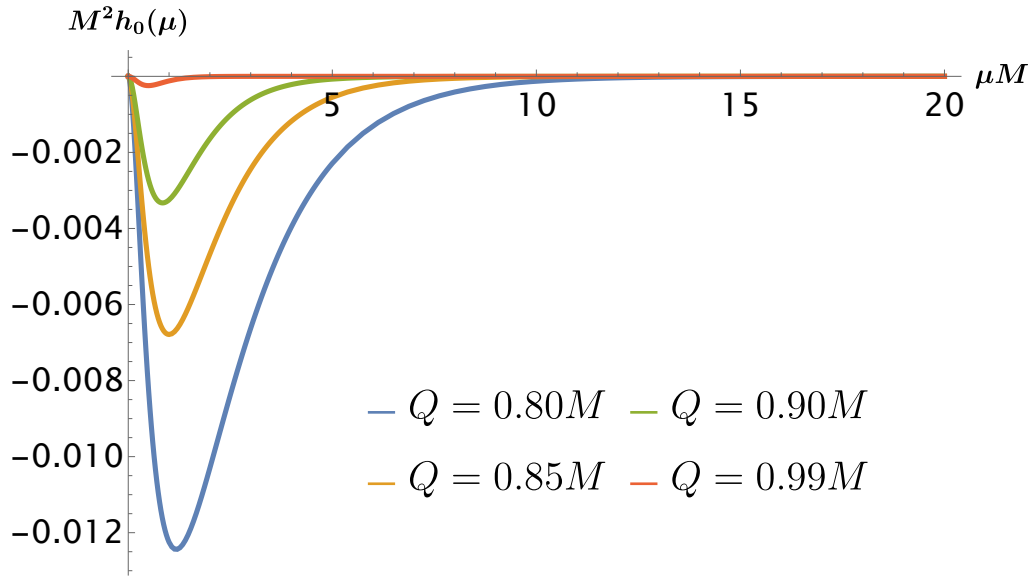


Figure 6.8: *In this figure, the coefficient of the logarithmic divergence $h_0(\mu)$ for the $l = 0$ mode is plotted as a function of the mass of the scalar field. This plot shows that the logarithmic divergence disappears in the large mass regime of the scalar field. Additionally, the magnitude of the coefficient of the logarithmic divergence decreases as the charge of the black hole tends to the extremal value $Q = M$.*

behaviour at the Cauchy horizon, and that the regularity of the massless case is fine-tuned. It would be very interesting to see if there are qualitative differences in the behaviour of the renormalized stress-energy tensors of massive and massless scalar fields near the Cauchy horizon, since this is the quantity that sources the backreaction. This will be the topic of the next Section.

6.4 The RSET on the Cauchy horizon

6.4.1 Analytical results

In this section, we obtain the leading order behaviour of the renormalized stress-energy tensor on the Cauchy horizon, by analysing the asymptotic behaviour (as $r \to r_-$) of the different terms in the components of the RSET. Putting together all the expressions presented in Section 5.3, we can write the relevant components of

the renormalized stress-energy tensor as

$$\begin{aligned}
\langle\hat{T}^{t}{}_{t}\rangle_{\rm ren} &= -\xi\,\mathsf{w}^{;t}{}_{;t} + (\tilde{w})^{t}{}_{t} + (\xi-\tfrac{1}{4})\Box\mathsf{w} + \xi R^{t}{}_{t}\mathsf{w} - \frac{1}{8\pi^2}v_1,\\
\langle\hat{T}^{r}{}_{r}\rangle_{\rm ren} &= \frac{1}{2}\mathsf{w}^{;t}{}_{;t} - (\tilde{w})^{t}{}_{t} + \mathsf{w}^{;\theta}{}_{;\theta} - 2\,(\tilde{w})^{\phi}{}_{\phi} - \xi R\,\mathsf{w} - \mu^2\mathsf{w}\\
&\quad - (\xi-\tfrac{1}{2})\mathsf{w}^{;r}{}_{;r} + (\xi-\tfrac{1}{4})\Box\mathsf{w} + \xi R^{r}{}_{r}\mathsf{w} + \frac{5}{8\pi^2}v_1,\\
\langle\hat{T}^{\theta}{}_{\theta}\rangle_{\rm ren} &= -\xi\,\mathsf{w}^{;\theta}{}_{;\theta} + (\tilde{w})^{\phi}{}_{\phi} + (\xi-\tfrac{1}{4})\Box\mathsf{w} + \xi R^{\theta}{}_{\theta}\mathsf{w} - \frac{1}{8\pi^2}v_1,\\
\langle\hat{T}_{uu}\rangle_{\rm ren} &= \frac{f}{4}\left(\langle\hat{T}^{r}{}_{r}\rangle_{\rm ren} - \langle\hat{T}^{t}{}_{t}\rangle_{\rm ren}\right) - \frac{1}{2}\langle\hat{T}^{r}{}_{t}\rangle_{\rm ren},\\
\langle\hat{T}_{vv}\rangle_{\rm ren} &= \frac{f}{4}\left(\langle\hat{T}^{r}{}_{r}\rangle_{\rm ren} - \langle\hat{T}^{t}{}_{t}\rangle_{\rm ren}\right) + \frac{1}{2}\langle\hat{T}^{r}{}_{t}\rangle_{\rm ren},
\end{aligned} \tag{6.35}$$

where w, $(\tilde{w})^{t}{}_{t}$, $(\tilde{w})^{\phi}{}_{\phi}$ and v_1 are defined in Eqs. (5.80), (5.81), (5.82) and (1.70d), respectively. We have here also introduced the semiclassical flux components $\langle\hat{T}_{uu}\rangle_{\rm ren}$ and $\langle\hat{T}_{vv}\rangle_{\rm ren}$, with u and v being the Eddington-Finkelstein coordinates in the interior defined as in Eq. (5.26). In the Unruh state, the off-diagonal component $\langle\hat{T}^{r}{}_{t}\rangle^{\rm U}_{\rm ren}$ is nonzero and only involves the "in" modes on the exterior [3]. Therefore, it is easily analytically continued into the interior and takes the form

$$\langle\hat{T}^{r}{}_{t}\rangle^{\rm U}_{\rm ren} = \frac{1}{4\pi^2}\sum_{l=0}^{\infty}(2l+1)\int_{\mu}^{\infty}d\omega\frac{\omega}{4r^2}(1-\coth(\pi\omega/\kappa_+))(1-|A^{\rm up}_{\omega l}|^2). \tag{6.36}$$

The asymptotic behavior of $\mathsf{w}^{\rm A}(r)$ was previously analysed in Sec. 6.3.2. An almost identical analysis can be done to obtain the leading order behaviour of $(\tilde{w}^{\rm A})^{\phi}{}_{\phi}$, which involves integrals of the same form as the ones in $\mathsf{w}^{\rm A}(r)$. This analysis yields for both the Hartle-Hawking and Unruh states

$$(\tilde{w}^{\rm A})^{\phi}{}_{\phi}(r) \sim \frac{\log|f|}{2\,r_-^2}\sum_{l=0}^{\infty}(2l+1)l(l+1)h_l(\mu), \quad r\to r_-. \tag{6.37}$$

What remains is to obtain the contribution of $(\tilde{w}^{\rm A})^{t}{}_{t}$. Expanding the Hadamard

parametrix to order $n = 2$ and focusing first on the Hartle-Hawking state yields

$$
\begin{aligned}
(\tilde{w}^{\mathrm{H}})^t{}_t(r) = \frac{1}{4\pi^2|f|}\sum_{l=0}^{\infty}(2l+1)\int_0^{\infty} d\omega \Bigg[& \frac{\omega\coth(\pi\omega/\kappa_+)}{2\,r_-^2}\left(|A_{\omega l}|^2+|B_{\omega l}|^2\right) \\
& + \frac{\omega\mathrm{csch}(\pi\omega/\kappa_+)}{r_-^2}\Re\{A^{\mathrm{up}}_{\omega l}(A_{\omega l}B_{\omega l})\} - \omega^2 k^{(2)}_{\omega l}(r)\Bigg] \\
& + \frac{1}{4\pi^2|f|}\sum_{l=0}^{\infty}(2l+1)\int_0^{\mu} d\omega\,\omega^2\,\Re\left\{j_l^+(\omega)e^{2i\omega r_*}+j_l^-(\omega)e^{-2i\omega r_*}\right\} \\
& + \frac{1}{4\pi^2|f|}\sum_{l=0}^{\infty}(2l+1)\Re\left\{\int_{\mu}^{\infty} d\omega\,\omega^2 j_l^+(\omega)e^{2i\omega r_*}+\int_{\mu}^{\infty} d\omega\,\omega^2 j_l^-(\omega)e^{-2i\omega r_*}\right\} \\
& + \frac{1}{4\pi^2}\Bigg[\mathcal{T}^{(\mathrm{p})}_{10}+\mathcal{D}^{(\mathrm{p})}_{22}+\frac{1}{|f|}(\mathcal{T}^{(\mathrm{p})}_{11}+\mathcal{D}^{(\mathrm{p})}_{21})+\frac{\mathcal{D}^{(\mathrm{r})}_{20}}{|f|^2}+\frac{\mathcal{D}^{(\mathrm{r})}_{21}}{|f|^3}+\frac{\mathcal{D}^{(\mathrm{r})}_{22}}{|f|^4}+\frac{\mathcal{T}^{(\mathrm{r})}_{10}}{|f|^2} \\
& \quad + \left(\mathcal{T}^{(\mathrm{l})}_{10}+\frac{\mathcal{T}^{(\mathrm{l})}_{11}}{|f|}\right)(\log(|f|/(\ell^2\lambda^2))-2\gamma_{\mathrm{E}}+3)\Bigg] + \frac{1}{8\pi^2|f|}\mathcal{T}^{(\mathrm{l})}_{00}(r)\,\lambda^2, \quad r\to r_-,
\end{aligned}
\tag{6.38}
$$

where we implemented a similar splitting as done in Eq. (6.26) and the functions $j_l^{\pm}(\omega)$ are defined as in Eq. (6.27). Focusing first on the integrals with $\omega^2 > \mu^2$ containing factors of the form $e^{\pm 2i\omega r_*}$, we can once again apply the Riemann-Lebesgue lemma. Specifically, these integrals contain now terms of the form

$$
\int_{-\infty}^{\infty}\theta(\omega^2-\mu^2)\,\omega^2 j_l^{\pm}(\omega)e^{\pm 2i\omega r_*}d\omega \tag{6.39}
$$

where $\theta(\omega^2-\mu^2)\,\omega^2 j_l^{\pm}(\omega)$ are integrable functions over $\omega\in\mathbb{R}$. As before, $j_l^{\pm}(\omega)$ contain factors such as $A_{\omega l}$, $A^{\mathrm{up}}_{\omega l}$ and $\mathrm{csch}(\pi\omega/\kappa_+)$, which decay exponentially as $|\omega|\to\infty$, while $B_{\omega l}\to 1$ as $|\omega|\to\infty$, and hence $\omega^2\,j_l^{\pm}(\omega)$ decay exponentially as $|\omega|\to\infty$. Hence, we can use the Riemann-Lebesgue lemma to show that these integrals vanish as $r_*\to\infty$. The corresponding integrals in the regime where $\omega^2<\mu^2$ require a different treatment. In this case, we can implement a small frequency expansion, valid in the asymptotic limit $r_*\to\infty$, similar to that used to obtain Eq. (6.18). Specifically, we introduce the expansions (6.17) and (6.14) for $A^{\mathrm{up}}_{\omega l}$, $A_{\omega l}$ and $B_{\omega l}$ and expand $\coth(\pi\omega/\kappa_+)$ and $\mathrm{csch}(\pi\omega/\kappa_+)$ for small ω, while keeping the factors $e^{\pm i\omega r_*}$ unexpanded. It then follows that

$$
\omega^2\,\Re\left\{j_l^+(\omega)e^{2i\omega r_*}+j_l^-(\omega)e^{-2i\omega r_*}\right\} = \mathcal{O}\left(\omega^j\right)\left(\cos(2\omega r_*)+\sin(2\omega r_*)\right), \quad j\in\mathbb{N}\setminus\{0\}, \tag{6.40}
$$

and hence

$$\int_0^\mu d\omega\, \omega^2\, \Re\left\{j_l^+(\omega)e^{2i\omega r_*} + j_l^-(\omega)e^{-2i\omega r_*}\right\} \to 0, \quad \text{as} \quad r_* \to \infty. \tag{6.41}$$

Thus, we have shown that all the integrals involving terms of the form $e^{\pm 2i\omega r_*}$ vanish in Eq. (6.38), as $r_* \to \infty$. We next consider the integrals of the renormalization counterterms and the analytic terms in Eq. (6.38):

$$\begin{aligned} K_2 :=& \frac{1}{4\pi^2|f|}\sum_{l=0}^{\infty}(2l+1)\int_0^\infty d\omega\,[-\omega^2 k^{(2)}_{\omega l}(r)] \\ &+ \frac{1}{4\pi^2}\Bigg[\mathcal{T}^{(\mathrm{p})}_{10} + \mathcal{D}^{(\mathrm{p})}_{22} + \frac{1}{|f|}(\mathcal{T}^{(\mathrm{p})}_{11} + \mathcal{D}^{(\mathrm{p})}_{21}) + \frac{\mathcal{D}^{(\mathrm{r})}_{20}}{|f|^2} + \frac{\mathcal{D}^{(\mathrm{r})}_{21}}{|f|^3} + \frac{\mathcal{D}^{(\mathrm{r})}_{22}}{|f|^4} + \frac{\mathcal{T}^{(\mathrm{r})}_{10}}{|f|^2} \\ &+ \left(\mathcal{T}^{(\mathrm{l})}_{10} + \frac{\mathcal{T}^{(\mathrm{l})}_{11}}{|f|}\right)(\log(|f|/(\ell^2\lambda^2)) - 2\gamma_{\mathrm{E}} + 3)\Bigg] + \frac{1}{8\pi^2|f|}\mathcal{T}^{(\mathrm{l})}_{00}(r)\,\lambda^2, \quad r \to r_-, \end{aligned} \tag{6.42}$$

where

$$\begin{aligned} k^{(2)}_{\omega l}(r) =& \sum_{a=0}^{2}\sum_{b=0}^{a}\mathcal{D}^{(\mathrm{r})}_{ab}(r)\mathcal{I}_{\omega l}(a,b|r) + \sum_{a=1}^{1}\sum_{b=0}^{a-1}\mathcal{T}^{(\mathrm{r})}_{ab}(r)\mathcal{I}_{\omega l}(a+1,b|r) \\ &+ \sum_{a=0}^{1}\sum_{b=0}^{a}\mathcal{T}^{(\mathrm{l})}_{ab}(r)\mathcal{J}_{\omega l}(a,b\,|r). \end{aligned} \tag{6.43}$$

Working in the limit as $r \to r_-$ and focusing on the leading-order divergent terms in this limit, it can be shown that (we report the details of this calculation in Appendix C.3):

$$K_2 = \frac{1}{4\pi^2|f|}\sum_{l=0}^{\infty}(2l+1)\left[\int_0^\infty d\omega\,\left(-\frac{\omega}{2\,r_-^2}\right) - \frac{\kappa_-^2}{24\,r_-^2}\right] + \mathcal{O}(\log|f|), \quad r \to r_-. \tag{6.44}$$

We note that the quantity K_2, being the leading-order contribution at the Cauchy horizon of the mode-sum representation of the Hadamard counter-terms, is divergent since both the frequency integral and the l-sum diverge. These divergences, however, capture the same behavior present in the mode-sum representation of the Wightman function, such that Eq. (6.38) is free of both large-frequency and large-l divergences. Thus, putting everything together, we find at leading order

$$(\tilde{w}^{\mathrm{H}})^t{}_t(r) \sim \frac{1}{4\pi^2|f|}\sum_{l=0}^{\infty}(2l+1)\,\mathcal{Y}^{\mathrm{H}}_l, \quad r \to r_-, \tag{6.45}$$

where $\mathcal{Y}_l^{\rm H}$ is regular, independent of r and given by

$$\mathcal{Y}_l^{\rm H} = \int_0^\infty d\omega \left[\frac{\omega \coth(\pi\omega/\kappa_+)|A_{\omega l}|^2}{r_-^2} + \frac{\omega \,\mathrm{csch}(\pi\omega/\kappa_+)}{r_-^2} \Re\{A^{\rm up}_{\omega l}(A_{\omega l}B_{\omega l})\} + \frac{\omega \coth(\pi\omega/\kappa_+)}{r_-^2} - \frac{\omega}{2r_-^2} \right] - \frac{\kappa_-^2}{24\, r_-^2}. \tag{6.46}$$

$\mathcal{Y}_l^{\rm H}$ can be simplified further by noting that we can perform the renormalization of the frequency integral in closed form as

$$\int_0^\infty \left[\frac{\omega \coth(\pi\omega/\kappa_+)}{2\, r_-^2} - \frac{\omega}{2\, r_-^2} \right] = \frac{\kappa_+^2}{24\, r_-^2}. \tag{6.47}$$

The final expression is then

$$\mathcal{Y}_l^{\rm H} = \int_0^\infty d\omega\, \omega \left[\frac{\coth(\pi\omega/\kappa_+)|A_{\omega l}|^2}{r_-^2} + \frac{\mathrm{csch}(\pi\omega/\kappa_+)}{r_-^2} \Re\{A^{\rm up}_{\omega l}(A_{\omega l}B_{\omega l})\} \right] + \frac{\kappa_+^2 - \kappa_-^2}{24\, r_-^2}. \tag{6.48}$$

For the Unruh state, an equivalent analysis can be performed, yielding

$$\mathcal{Y}_l^{\rm U} = \mathcal{Y}_l^{\rm H} + \int_\mu^\infty d\omega \frac{\omega\, (|A_{\omega l}|^2 + |B_{\omega l}|^2)}{4\, r_-^2} (1 - \coth(\pi\omega/\kappa_+)) \left(1 - |A^{\rm up}_{\omega l}|^2\right). \tag{6.49}$$

Hence, to leading order, for both the Hartle-Hawking and Unruh states we have

$$(\tilde{w}^{\rm A})^t{}_t(r) \sim \frac{1}{4\pi^2|f|} \sum_{l=0}^\infty (2l+1)\, \mathcal{Y}_l^{\rm A}, \qquad r \to r_-. \tag{6.50}$$

The frequency integrals decay exponentially, since they contain factors such as $A_{\omega l}$, $A^{\rm up}_{\omega l}$, $\mathrm{csch}(\pi\omega/\kappa_+)$ and $(1 - \coth(\pi\omega/\kappa_+))$, which decay exponentially as $|\omega| \to \infty$, while $B_{\omega l} \to 1$ as $|\omega| \to \infty$, thus they converge extremely rapidly. All the l-sums are convergent by construction of the renormalization procedure and, at the inner horizon, only a handful of l-modes are required to obtain accurate results. To summarize, we have shown that for a massive scalar field

$$\begin{aligned} \mathsf{w}^{\rm A}(r) &\sim \mathcal{O}\left(\log|f|\right), \quad r \to r_-, \\ (\tilde{w}^{\rm A})^t{}_t(r) &\sim \mathcal{O}(|f|^{-1}), \quad r \to r_-, \\ (\tilde{w}^{\rm A})^\phi{}_\phi(r) &\sim \mathcal{O}\left(\log|f|\right), \quad r \to r_-, \end{aligned}$$

while in the massless case, since $h_l(0) = 0$, we obtain

$$\begin{aligned}
\mathsf{w}^{\mathrm{A}}(r)|_{\mu=0} &\sim \mathcal{O}\,(1)\,, \quad r \to r_-,\\
(\tilde{w}^{\mathrm{A}})^t{}_t(r)\Big|_{\mu=0} &\sim \mathcal{O}(|f|^{-1}), \quad r \to r_-,\\
(\tilde{w}^{\mathrm{A}})^\phi{}_\phi(r)\Big|_{\mu=0} &\sim \mathcal{O}\,(1)\,, \quad r \to r_-.
\end{aligned}$$

Hence, analysing the expression (6.35) and considering only the terms that contribute to the leading order divergences at the inner horizon for each component of the renormalized stress-energy tensor, we find

$$\begin{aligned}
\langle \hat{T}^t{}_t\rangle_{\mathrm{ren}} &\sim (\tilde{w})^t{}_t + \tfrac{1}{2}\xi\, f'\mathsf{w}' + \xi f \mathsf{w}'' + \mathcal{O}(\log|f|), && r \to r_-,\\
\langle \hat{T}^r{}_r\rangle_{\mathrm{ren}} &\sim -(\tilde{w})^t{}_t + \tfrac{1}{2}\xi f'\mathsf{w}' + \mathcal{O}(\log|f|), && r \to r_-,\\
\langle \hat{T}^\theta{}_\theta\rangle_{\mathrm{ren}} &\sim (\tilde{w})^\phi{}_\phi + \xi R^\theta_\theta \mathsf{w} + \mathcal{O}(1), && r \to r_-.
\end{aligned} \tag{6.51}$$

Introducing the expressions we obtained for w, $(\tilde{w})^t{}_t$, $(\tilde{w})^\phi{}_\phi$ and R^θ_θ we get, to leading order

$$\begin{aligned}
\langle \hat{T}^t{}_t\rangle^{\mathrm{A}}_{\mathrm{ren}} &= -\langle \hat{T}^r{}_r\rangle^{\mathrm{A}}_{\mathrm{ren}} \sim \frac{\mathcal{K}^{\mathrm{A}}}{|f|}, && r \to r_-,\\
\langle \hat{T}^\theta{}_\theta\rangle^{\mathrm{A}}_{\mathrm{ren}} &\sim \mathcal{L}\,\log|f|, && r \to r_-,
\end{aligned} \tag{6.52}$$

where we have defined the radial independent quantities as

$$\mathcal{K}^{\mathrm{A}} = \frac{1}{4\pi^2}\sum_{l=0}^{\infty}(2l+1)\left(\mathcal{Y}^{\mathrm{A}}_l + 8\pi^2\xi\,\kappa_-^2\, h_l(\mu)\right), \tag{6.53}$$

$$\mathcal{L} = \sum_{l=0}^{\infty}(2l+1)\left(\frac{l(l+1)}{2\,r_-^2} + \xi\frac{r_+}{r_-^3}\right) h_l(\mu). \tag{6.54}$$

From these expressions, it is clear that, for both massless and massive scalar fields, the $\langle \hat{T}^t{}_t\rangle_{\mathrm{ren}}$ and $\langle \hat{T}^r{}_r\rangle_{\mathrm{ren}}$ components of the renormalized stress-energy tensor diverge as $|f|^{-1}$ at the inner horizon, while $\langle \hat{T}^\theta{}_\theta\rangle_{\mathrm{ren}}$ diverges logarithmically for massive fields and is finite in the case of massless fields. Additionally, using Eq. (6.52) it can be shown analytically that these components satisfy the conservation equation at leading order.

Next, we compute the semiclassical fluxes for massive fields in the Hartle-Hawking state on the inner horizon (we denote the results on the inner horizon with the superscript $^-$) by introducing Eq. (6.52) into the relevant expressions in Eq. (6.35)

and find

$$\langle \hat{T}^{-}_{uu} \rangle^{\rm H}_{\rm ren} = \langle \hat{T}^{-}_{vv} \rangle^{\rm H}_{\rm ren} = \frac{\mathcal{K}^{\rm H}}{2}. \tag{6.55}$$

We note that, for massless fields, we retrieve the expression in [115]. Rearranging the expressions appropriately, following [115], the computation of the fluxes for the Unruh state is most easily computed from the Hartle-Hawking fluxes as

$$\langle \hat{T}^{-}_{yy} \rangle^{\rm U}_{\rm ren} = \frac{\mathcal{K}^{\rm H}}{2} + \mathcal{J}_{(yy)}, \tag{6.56}$$

where we have defined

$$\mathcal{J}_{(yy)} = \frac{1}{8\pi^2} \sum_{l=0}^{\infty} (2l+1) \int_{\mu}^{\infty} d\omega \frac{\omega}{4r_-^2} (1 - \coth(\pi\omega/\kappa_+))(1 - |A^{\rm up}_{\omega l}|^2) \left(|A_{\omega l}|^2 + \delta^v_y \right). \tag{6.57}$$

This shows that the uu and vv-components do not diverge despite tt and rr diverging in Eq. (6.52) and that they are non-vanishing even in the massless case at the inner horizon, in agreement with [115].

Finally, transforming the results in Kruskal coordinates near the Cauchy horizon

$$\bar{U} = -e^{\kappa_- u}, \quad \bar{V} = e^{\kappa_- v}, \tag{6.58}$$

we obtain at the Cauchy horizon

$$\begin{aligned} \langle T^{-}_{\bar{U}\bar{U}} \rangle^{\rm A}_{\rm ren} &= \frac{e^{-2\kappa_- u}}{\kappa_-^2} \langle T^{-}_{uu} \rangle^{\rm A}_{\rm ren}, \\ \langle T^{-}_{\bar{V}\bar{V}} \rangle^{\rm A}_{\rm ren} &= \frac{e^{-2\kappa_- v}}{\kappa_-^2} \langle T^{-}_{vv} \rangle^{\rm A}_{\rm ren}. \end{aligned} \tag{6.59}$$

Recalling that $\kappa_- < 0$, it is clear that if $\langle T^{-}_{vv} \rangle^{\rm A}_{\rm ren}$ is nonzero, then $\langle T^{-}_{\bar{V}\bar{V}} \rangle^{\rm A}_{\rm ren}$ diverges exponentially at the inner horizon (where $v \to \infty$). These results reflect the ones obtained in [115] for a massless, minimally coupled field. Notably, this divergence is stronger than in the classical scenario, in which one usually finds $\langle T^{-}_{\bar{V}\bar{V}} \rangle^{\rm A}_{\rm ren} \propto v^{-p} e^{-2\kappa_- v}$, where p is a positive integer that depends on the type of perturbation [98, 100, 127]. Thus, when written in terms of Kruskal coordinates $\langle T^{-}_{\bar{V}\bar{V}} \rangle^{\rm A}_{\rm ren} = C/\bar{V}^2$, as $\bar{V} \to 0^+$, with C being a constant that is in general nonzero. In [111], it was shown analytically for quantum scalar fields in RNdS spacetime that, for Hadamard states, $\langle T^{-}_{\bar{V}\bar{V}} \rangle^{\rm A}_{\rm ren}$ diverges at the Cauchy horizon as $\bar{V}^{-2}$. In the same work, it was argued that such a divergence should be sufficient to convert the Cauchy horizon into a strong singularity. Since we find the same type of divergence in the Reissner-Nordström case, this suggests that quantum effects may restore the strong cosmic censorship

in the asymptotically flat Reissner-Nordström black hole. However, recent work in RNdS spacetime indicates that, at least for massless or small-mass scalar fields, correlations of the $\hat{T}_{\bar{V}\bar{V}}$ component of the stress-energy tensor over macroscopic distances are non-negligible at the Cauchy horizon, suggesting a breakdown of the semiclassical Einstein equations [128]. The authors suggest that this may potentially require a treatment beyond semiclassical gravity that accounts for such correlations in the backreaction calculation (see, for instance, [129, 130]).

6.4.2 Numerical results

With expressions (6.55) and (6.56) at hand, it is possible to numerically compute the semiclassical fluxes for both the Hartle-Hawking and Unruh states on the Cauchy horizon for a wide range of parameters, such as the mass of the scalar field, the value of its coupling to the gravitational background, and the charge of the black hole. Specifically, the ω-integrals in $\mathcal{K}^{\rm H}$ and $\mathcal{J}_{(yy)}$ are numerically integrated by interpolating the integrand on a predefined ω-grid on which the coefficients $A^{\rm up}_{\omega l}$, $A_{\omega l}$ and $B_{\omega l}$ have been computed. The coefficient $h_l(\mu)$ is obtained as in Figures 6.7 and 6.8.

In Figure 6.9, we report the semiclassical fluxes on the Cauchy horizon for both quantum states, considering a minimally coupled field with mass in the range $\mu M \in [0, 1/10]$. The fluxes in the two states exhibit similar behavior. The numerical results for a massless field are in agreement with the inner horizon results reported in Fig. 1 of the Supplemental Material of Ref. [115]. As the mass increases, the magnitude of the fluxes also increases, within the range of investigation. The rate of increase is stronger in the Unruh state. Figure 6.10 presents a contour plot of the $\langle \hat{T}^{-}_{uu} \rangle^{\rm H}_{\rm ren}$ component in the Hartle-Hawking state as a function of the scalar field mass and coupling; the corresponding plots for the Unruh state are qualitatively identical. This Figure shows that there are specific combinations of mass and coupling for which the fluxes vanish on the inner horizon, though this requires fine-tuning between the two parameters.

We also produced analogous plots to investigate the dependence of the fluxes on the black hole charge, with particular focus on the near-extremal regime. Figures 6.11 and 6.12 show the results for a massive field with $\mu M = 0.1$. The first figure indicates that the semiclassical fluxes take similar values in both quantum states and vanish in the extremal limit. In addition, comparing Fig. 6.11 with the corresponding figure for a massless field (see Fig. 1 in Ref. [115]), it can be noticed that the fluxes $\langle \hat{T}^{-}_{yy} \rangle_{\rm ren}$ for a massive field change sign twice. Specifically, for $Q/M \gtrsim 0.9925$, the fluxes are positive for a massive field while remaining negative for a massless field. Interestingly, as discussed in [115], the sign of the component

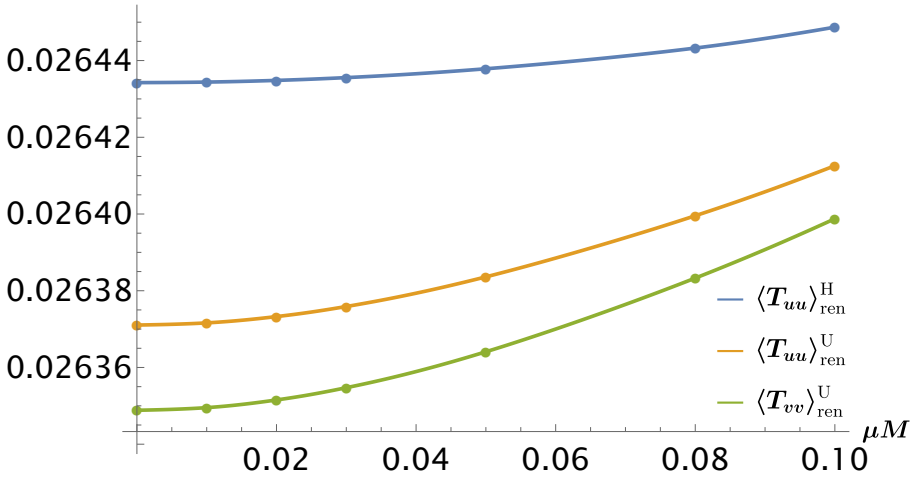


Figure 6.9: *$\langle \hat{T}^{-}_{uu} \rangle^{H}$, $\langle \hat{T}^{-}_{uu} \rangle^{U}$ and $\langle \hat{T}^{-}_{vv} \rangle^{U}$ at the Cauchy horizon for a minimally coupled massive scalar field varying the mass of the scalar field μ. These results were obtained with $Q = 0.8M$ and summing l-modes up to $l = 5$. We expect the results to be accurate to at least the first 5 relevant digits.*

$\langle \hat{T}^{-}_{vv} \rangle_{\rm ren}$ determines the nature of the tidal deformations experienced by an observer infalling towards the ingoing section of the inner horizon (as $v \to +\infty$). In particular, the infalling observer will experience rapid contraction if $\langle \hat{T}^{-}_{vv} \rangle_{\rm ren} > 0$ and expansion if $\langle \hat{T}^{-}_{vv} \rangle_{\rm ren} < 0$ [115]. Therefore, our numerical results suggest that introducing a nonzero mass for the scalar field may change the nature of the discussed tidal deformations in black holes with values of Q close to the extremal limit. The contour plot in Fig. 6.12 further shows that there exist particular combinations of parameters for which the fluxes vanish, even in the non-extremal case. As seen from Eq. (6.59), this is physically significant because a vanishing $\langle \hat{T}^{-}_{vv} \rangle^{\rm A}_{\rm ren}$ flux implies that the RSET component $\langle T^{-}_{\bar{V}\bar{V}} \rangle^{\rm A}_{\rm ren}$ is free of the $1/V^2$ divergence. As a result, in this case, the classical effects would dominate near the Cauchy horizon. As before, the contour plots for the components in the Unruh state are qualitatively identical to those for the Hartle–Hawking state.

6.5 Conclusions

In this Chapter, we investigated the properties of the Hartle-Hawking and Unruh states in the region near the Cauchy horizon of a Reissner-Nordström black hole by computing the RVP and RSET.

In Ref. [119], it was first shown that the renormalized vacuum polarization of massless scalar fields exhibits an unexpected behavior in the vicinity of the inner horizon. Specifically, after some oscillations, the vacuum polarization for both states asymptotes to a finite negative value at the inner horizon. This is surprising when one considers the plot in Fig. 5.7, in which the RVP in both quantum states appears

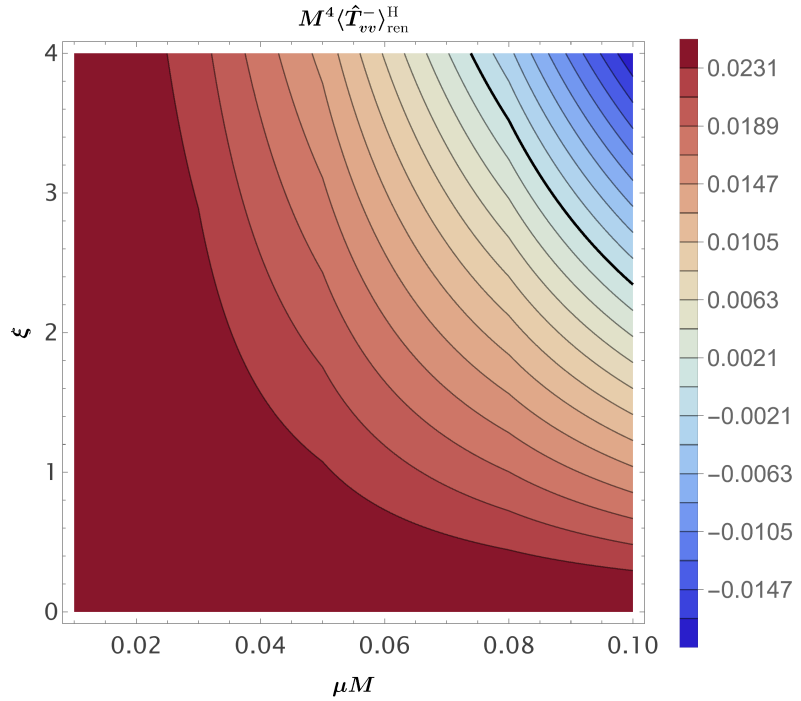


Figure 6.10: *$\langle\hat{T}^-_{uu}\rangle^H$ at the Cauchy horizon for a massive scalar field varying the mass μ and the coupling ξ. The thick black line highlights the combination of parameters for which $\langle\hat{T}^-_{uu}\rangle^H = 0$. These results were obtained with $Q = 0.8M$ and summing l-modes up to $l = 5$.*

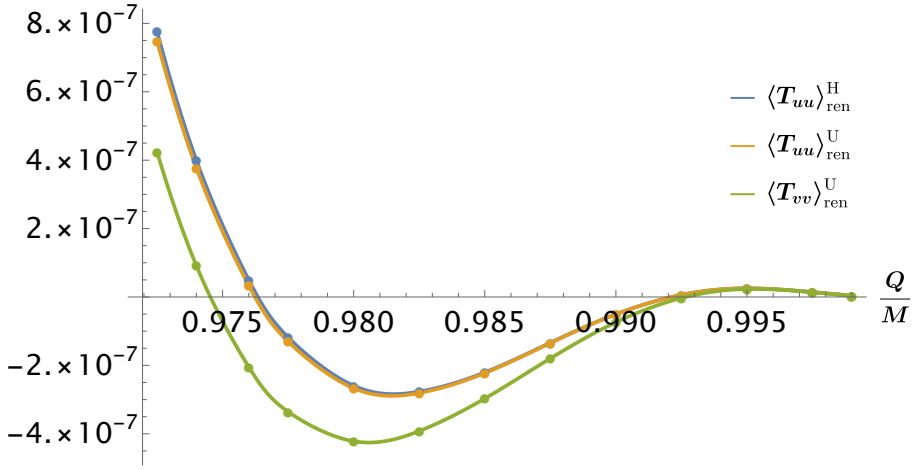


Figure 6.11: *$\langle\hat{T}^-_{uu}\rangle^H$, $\langle\hat{T}^-_{uu}\rangle^U$ and $\langle\hat{T}^-_{vv}\rangle^U$ at the Cauchy horizon for a minimally coupled massive scalar field varying the charge of the black hole Q. These results were obtained with $\mu M = 0.1$ and summing l-modes up to $l = 2$.*

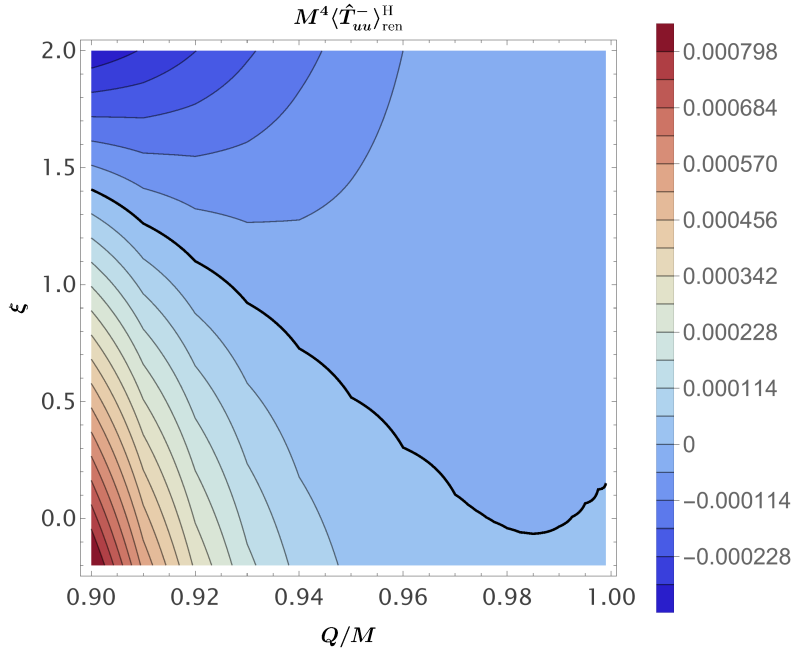


Figure 6.12: *$\langle\hat{T}^-_{uu}\rangle^H$ at the Cauchy horizon for a massive scalar field varying the charge of the black hole Q and the coupling ξ. The thick black line highlights the parameter combination for which $\langle\hat{T}^-_{uu}\rangle^H = 0$. These results were obtained with $\mu M = 0.1$ and summing l-modes up to $l = 2$.*

to diverge as the inner horizon is approached. In the analysis presented in this Chapter, we reproduced the numerical results of [119] for massless scalar fields and found numerical agreement with the corresponding asymptotic values at the inner horizon. As discussed, this required computing quantum effects extraordinarily close to the inner horizon and dealing with related numerical challenges.

In addition, motivated by the surprising results obtained in the massless case near the inner horizon, we performed a similar analysis for massive fields. We emphasize that, to the best of our knowledge, the extended coordinate method is currently the only available method for the direct computation of renormalized expectation values for massive fields. Interestingly, the numerical results suggest that for a massive scalar field, the vacuum polarization exhibits a logarithmic divergence at the inner horizon. This divergence comes with a coefficient that depends on the field mass and on the black hole mass and charge. As the mass of the field decreases or as the charge of the black hole approaches its extremal value ($Q \to M$), the coefficient of the logarithmic divergence decreases.

Furthermore, we carried out an analytical derivation to investigate the behavior of the RVP near the Cauchy horizon. We found that a logarithmic divergence emerges from the small frequency contribution to the integral of the renormalized Wightman function. For massless fields, we showed analytically that the coefficients of the logarithmic divergence and of a sub-leading $\log(\log|f|)$ term vanish, implying that the RVP is finite on the inner horizon and thereby confirming the numerical

results. In the case of massive fields, this coefficient can instead be computed numerically from the low-frequency expansions of the interior and exterior scattering coefficients. The coefficient is found to be non-zero and in agreement with that extracted from the full numerical evaluation of the RVP. Another interesting feature is that the logarithmic divergence appears to be independent of the choice of the quantum state, potentially hinting at universal properties of the semiclassical effects at the inner horizon.

These results for the RVP are an example of a cautionary tale on two separate fronts. First, it is a cautionary tale about extrapolating on the basis of numerical data. One has to carry out a sophisticated analytical derivation to see the behavior of the RVP near the inner horizon, a behavior that is not easily deduced or extrapolated from a blind analysis of the numerics. The second cautionary tale is to assume that massive scalar fields behave the same as massless ones. Given the technical advantage of working with massless fields, it is tempting to do calculations in this context and assume the phenomenology for massive fields is identical. This Chapter provides a counter-example to that reasoning. This is all the more pertinent given the only scalar field we know exists - the Higgs boson - is massive.

Having obtained results for the RVP, the next natural question is whether the RSET components exhibit different properties at the inner horizon depending on the mass of the quantum field. To address this, we derived semi-analytical expressions for the RSET at the inner horizon that involve numerically computed mode-sums. This analysis showed that, at leading order, the energy density and the radial pressure are equal and diverge as $1/|f|$ for both quantum states and for both massless and massive fields. The angular pressures are instead found to be logarithmically divergent for massive fields, while remaining finite in the massless case. In addition, we showed that the semiclassical fluxes $\langle \hat{T}^u{}_u \rangle$ and $\langle \hat{T}^v{}_v \rangle$ remain finite on the Cauchy horizon. This result is consistent with [115], where the fluxes were computed for massless fields. We obtained the semiclassical fluxes numerically in both states over a wide range of parameters, finding numerical evidence that they vanish in the extremal limit. Finally, we discussed how a nonzero $\langle T^-_{vv} \rangle^{\rm A}_{\rm ren}$, when transformed to Kruskal coordinates, gives rise to an exponential divergence at the inner horizon in the $\langle T^-_{\bar{V}\bar{V}} \rangle^{\rm A}_{\rm ren}$ component, thus suggesting that semiclassical effects may induce strong backreaction effects on the background spacetime, potentially acting as the Universe's agent for Cosmic Censorship [111]. Once again, we find it interesting that the qualitative properties of the RSET are independent of the quantum state, as proved for a real scalar field in RNdS in [111], suggesting that these semiclassical effects may be robust under different physical conditions.

The work presented in this Chapter represents a first step towards the computation of the semiclassical backreaction near the Cauchy horizon of spherically

symmetric black holes. A perhaps interesting extension of this work would be to consider charged scalar fields. Recently, the extended coordinate method has been generalized to charged fields propagating on the exterior of spherically symmetric black holes [56], and a line of research to extend such methodology to black hole interiors has been explored during this PhD.

Chapter 7

Conclusions and outlook

In what follows, we summarize the main contributions and achievements of this thesis. In Chapter 2, we generalized the extended coordinate implementation of Hadamard renormalization to the direct computation of the renormalized stress-energy tensor of a quantum scalar field in the Boulware state in static, spherically symmetric spacetimes. In the extended coordinate approach, we express the geometrical short-distance divergence encoded in the Hadamard parametrix as mode sums in the same form as those in the Green's function, and then perform the renormalization mode-by-mode. We treated the Boulware state as a zero-temperature state defined on the Euclidean section of the Lorentzian spacetime. This approach allows the use of Euclidean techniques, which considerably simplify the distributional nature of the singular structure of the Green's function. In the original formulation of the extended coordinate method, the additional assumption that the field is in the Hartle-Hawking state required a periodic identification of the Euclidean time coordinate modulo the inverse Hawking temperature. This periodic identification meant that the continuous frequency spectrum in the mode-sum expression for the Euclidean Green's function was discretized, leading to a simpler analytical and numerical treatment. For zero-temperature states, this periodic identification is not possible, and therefore the frequency spectrum remains continuous. As a result, the regularization parameters that arise when we express the terms in the Hadamard parametrix as mode-sums are not ordinary functions of ω, but generalized functions that must be carefully treated accordingly. One of the positive consequences of this generalization of the extended coordinate method is that this treatment naturally introduces an infrared cutoff in the integrals over ω, such that the final results are independent of the cutoff value. In the AHS approach to renormalization in the Boulware state, the infrared cutoff was introduced in an ad-hoc way to deal with infrared divergences. In our method, it emerges in the derivation of our regularization parameters.

This generalized extended coordinate method works effectively in any static,

spherically symmetric spacetime and for arbitrary field mass or gravitational coupling. This makes it possible to compute renormalized quantities in a variety of spacetimes of interest and over a wide range of field parameters. The extension of the method to the Boulware state opens the window towards obtaining the renormalized stress-energy tensor of scalar fields in previously unexplored situations, particularly in spacetimes that do not admit a Hartle-Hawking state to serve as a reference state in the state-subtraction approach, such as extremal black holes or stellar spacetimes. Furthermore, there is also a computational advantage to a direct Boulware approach, since the state subtraction scheme requires two sets of modes, one for the Lorentzian and one for the Euclidean sectors, while the direct approach only requires the computation of the Euclidean modes.

In Chapter 3, we verified the new method by computing the RSET for a quantum scalar field in the Boulware state on the exterior of a sub-extremal Reissner-Nordström black hole. We compared our results with existing ones obtained with the state subtraction approach [3] and found good agreement. We then implemented the renormalization method to compute the RSET for massless and massive fields on the exterior of an extremal Reissner-Nordström black hole. To the best of the author's knowledge, these are the first results obtained for a massive field. In addition, we assessed the regularity of the Boulware state by calculating the energy density on the horizon as perceived by a freely falling observer. We found numerical evidence of its regularity for both massless and massive fields.

In Chapter 4, we moved away from the black hole context and considered a static, spherically symmetric thin shell joining a Minkowski interior to a Schwarzschild exterior. We considered a quantum scalar field in the Boulware state propagating in this spacetime. We calculated the renormalized vacuum polarization and the RSET numerically in the bulk of the spacetime over a wide range of parameters, with particular focus on the black hole limit. In addition, to investigate their behavior near the shell, we implemented two independent analytical approximations: a WKB approximation for the Euclidean modes and a weak-field approximation valid in the regime of small compactness. The RVP and RSET are divergent on the shell, but these are Casimir-type divergences associated with the presence of the idealized sharp boundary. The power and coefficient of the leading-order divergences at the shell of both RVP and RSET components obtained with the two methods were in agreement with the numerical results. These results were motivated by the desire to better understand semiclassical effects in compact stars. Especially interesting is the role classical energy conditions play in the Buchdahl limit. These energy conditions are violated quantum mechanically and so that begs the question of how compact can an object be in the semiclassical theory. This work is still ongoing, and we hope to report on it soon.

In Chapter 5, we derived the mode-sum representations for Wightman functions in the Unruh and Hartle-Hawking states for massive scalar fields on the interior of a Reissner-Nordström black hole. We then generalized the extended coordinate method to the non-static interior of spherically symmetric black holes, working directly in the Lorentzian framework. This work represents the first-ever application of the extended coordinate method in a Lorentzian spacetime. We showed that, conveniently, the renormalization parameters derived for zero-temperature states on the exterior are essentially those required for the Hartle-Hawking and Unruh states on the interior with a trivial modification. Therefore, we numerically obtained the renormalized vacuum polarization and the RSET for both massless and massive scalar fields on the interior of a Reissner-Nordström black hole. The massless results agree with previous studies [3, 119], while the massive ones are novel.

Finally, in Chapter 6, we focused on the computation of the RVP and RSET in the vicinity of the Cauchy horizon of a Reissner-Nordström black hole. Specifically, we first obtained numerical results for the RVP for both massless and massive fields extraordinarily close to the inner horizon. Interestingly, we found that the RVP diverges logarithmically at the inner horizon for quantum fields with nonzero mass. We then derived analytic expressions for the RVP at the Cauchy horizon. We showed that the coefficient of the logarithmic divergence vanishes analytically in the massless limit, in agreement with [119], as well as for massive fields in the large-mass limit. The numerical evaluation of this coefficient reveals that it is, in general, nonzero for massive fields of relatively small mass. We then obtained semi-analytical leading-order expressions for the RSET components on the Cauchy horizon. When written in terms of the Kruskal coordinates regular at the Cauchy horizon, the component $\langle T^{-}_{\bar{V}\bar{V}}\rangle^{\rm A}_{\rm ren} \propto \bar{V}^{-2}$, with $\bar{V} \to 0^{+}$. In [111], a similar divergence was obtained in RNdS spacetime. The authors of that work further suggest that a divergence of this form could potentially convert the Cauchy horizon into a strong singularity [107], possibly restoring strong cosmic censorship. The qualitative properties of both the RVP and RSET results at the inner horizon are found to be independent of the quantum state. Once again, the massless results at the Cauchy horizon are in agreement with previous studies [115, 119], while the corresponding massive field results are presented here for the first time. We then computed the semiclassical fluxes on the Cauchy horizon numerically over a wide range of scalar field masses, black hole charges, and couplings ξ. We found numerical evidence that the semiclassical fluxes vanish in the black hole extremal limit for both the Hartle-Hawking and Unruh states.

The results obtained in Chapter 6 for the renormalized vacuum polarization near the Cauchy horizon provide us with two different cautionary lessons. First, they suggest that one should be cautious in extrapolating numerical data to infer

behavior beyond the domain in which the data were obtained. In the massless case, by looking at the numerical data in Fig. 5.7, one could have naively deduced that the renormalized vacuum polarization diverges at the Cauchy horizon. We showed analytically that this is not the case. The second cautionary lesson we can learn is that the assumption that massless and massive scalar fields are phenomenologically the same is perhaps not justified in certain scenarios.

The work presented in this thesis may be extended in several directions. An interesting way to extend the work presented in Chapters 5 and 6 on the interior of a Reissner-Nordström black hole would be to consider charged scalar fields. A particularly intriguing question is whether the renormalized scalar condensate for a massive charged scalar field remains finite or diverges at the Cauchy horizon. Addressing this would require extending the method discussed in Sec. 5.2 to obtain the interior propagators for charged scalar fields in the Unruh and Hartle-Hawking states. It would also require generalizing the interior implementation of the extended coordinate method to account for the anti-symmetric part of the Hadamard parametrix that appears when considering charged scalar fields. The treatment of the antisymmetric contribution was discussed in [56], where the extended coordinate method was generalized to charged scalar fields in the Hartle-Hawking state on the exterior of static, spherically symmetric black holes. This procedure may be straightforwardly extended to the interior for computing the renormalized scalar condensate, the renormalized current, and the RSET.

Of particular interest is also the computation of the backreaction near the Cauchy horizon of near-extremal Reissner-Nordström black holes. In Figure 6.11, we showed that, in the near extremal regime, the semiclassical fluxes for massive, minimally coupled, scalar fields exhibit a different sign compared to those obtained in the massless case [115]. The sign of the $\langle \hat{T}^{-}_{vv} \rangle$ component is regarded as one of the main drivers of the backreaction near the Cauchy horizon: if positive, the inner horizon is expected to contract, if negative, it is expected to move outwards [131, 132]. A proper understanding of the fate of the Cauchy horizon in near-extremal black holes in the presence of massive quantum scalar fields requires using our results for the RSET obtained with different masses and couplings to compute the semiclassical backreaction.

Another avenue that could potentially be explored is whether the results near the Cauchy horizon would persist for quantum fields with other spins or in different spacetimes. In the former case, this would require adapting the extended coordinate renormalization scheme. The latter is, instead, for spherically symmetric spacetimes, a possible direct application of the generalized extended coordinate approach developed in this thesis. An interesting avenue would be to study semiclassical backreaction inside a Reissner-Nordström-de Sitter black hole. In this setting, the classical

stability of the Cauchy horizon is parameter dependent [133, 134], potentially challenging the strong cosmic censorship, especially in near extremal regimes [135, 136]. Therefore, the semiclassical backreaction effects in these contexts are particularly relevant. Several works [111–114] have been carried out to assess the semiclassical stability of the Cauchy horizon in RNdS spacetime, suggesting that semiclassical effects may turn the Cauchy horizon into a strong singularity in the Tipler sense [107]. Klein et al. [113] computed the semiclassical current and stress-energy fluxes on the Cauchy horizon for a massive charged scalar field in RNdS spacetime. Their results indicate that a near extremal black hole would be driven away from extremality due to backreaction effects. We showed in Fig. 6.12, that the coupling ξ to the background curvature, which was not considered in [113], plays a significant role in determining the sign of the semiclassical fluxes in the near extremal regime for massive neutral fields in Reissner-Nordström spacetime. A natural extension of our work would therefore be to carry out an extensive analysis of the semiclassical fluxes in the case of an RNdS black hole, considering different couplings and field masses, and to compute the semiclassical backreaction in this context.

Moreover, a long-term objective would be to generalize the extended coordinate prescription to the more astrophysically relevant Kerr black hole, to understand whether the semiclassical effects obtained in spherically symmetric black holes persist beyond spherical symmetry. This extension is challenging for the extended coordinate method, which currently relies on the numerous symmetries of spherically symmetric spacetimes. In this regard, five-dimensional equal-angular-momenta Myers-Perry-AdS black holes [58], which possess additional symmetries, may provide a useful testing ground for generalizing the extended coordinate method beyond spherical symmetry. Moreover, the knowledge acquired in Chapter 2 regarding the careful treatment of the frequency integrals as generalized functions is certainly a transferable resource for the development of the extended coordinate method in the Kerr case.

Beyond black holes, the work presented in Chapter 4 for thin shell spacetimes represents a test case for applying the extended coordinate method to study the semiclassical effects in compact stars. At the classical level, the Buchdahl limit sets an upper bound on the compactness of static, spherically symmetric stellar configurations. The method developed in Chapters 2-4 for computing the RSET provides a powerful tool for exploring the role of the Boulware state in such compact horizonless configurations. Of particular importance is whether the RSET violates some of the assumptions of Buchdahl's theorem. The computation of the semiclassical backreaction in these settings could therefore determine whether quantum effects relax or tighten the classical compactness bound.

Finally, on the computational side, the ultimate goal would be to develop an

open-source semiclassical toolkit by making the *Mathematica* Notebooks for computing accurate renormalized expectation values publicly available. This would require making the Notebooks efficient, accessible, easy to use, and well-documented. Such a toolkit would provide the semiclassical physics community with a powerful, user-friendly computational framework that could facilitate in-depth exploration of the backreaction problem in several contexts and in a relatively straightforward manner.

Appendices

Appendix A

The extended coordinate method for zero-temperature states

A.1 Cut-off independence

There is a subtle cancellation happening between the terms dependent on λ in $\mathcal{J}_{\omega l}(a,b\,|r)$ and the finite terms in Eq. (2.47) which also depend on λ. We can make this cancellation explicit by analyzing the terms in the renormalized vacuum polarization that contain the cutoff, which we refer to as $\mathsf{w}^{(\lambda)}$:

$$\begin{aligned}\mathsf{w}^{(\lambda)} = &\frac{\mathcal{T}^{(\mathrm{l})}_{00}(r)}{8\pi^2}\left[\int_{-\infty}^{\infty} d\omega\,\theta\left(\omega^2-\lambda^2\right)|\omega|^{-1}+\log(\lambda^2)\right]\\ &+\frac{\sqrt{\pi}}{8\pi^2}\sum_{a=1}^{n-1}\sum_{b=0}^{a}\mathcal{T}^{(\mathrm{l})}_{ab}(r)\frac{f^{a-b}2^{2a}}{\Gamma(-a+\frac{1}{2})}\left[a!\int_{-\infty}^{\infty} d\omega\,\theta\left(\omega^2-\lambda^2\right)|\omega|^{-2a-1}-\frac{(a-1)!}{\lambda^{2a}}\right].\end{aligned} \tag{A.1}$$

We have separated the $\mathcal{T}^{(l)}_{00}(r)$ and $a>0$ terms in $\mathcal{J}_{\omega l}(a,b\,|r)$ and used the identity (2.27) to truncate the l sum as well as introduced $k=0$, only condition for these terms being nonzero at coincidence. We can show that the renormalized vacuum polarization is independent on the choice of the cutoff by verifying that

$$\begin{aligned}\frac{\partial}{\partial\lambda}\left(\mathsf{w}^{(\lambda)}\right) =&\frac{\mathcal{T}^{(\mathrm{l})}_{00}(r)}{8\pi^2}\left(-\frac{2}{\lambda}+\frac{2}{\lambda}\right)\\ &+\frac{\sqrt{\pi}}{8\pi^2}\sum_{a=1}^{n-1}\sum_{b=0}^{a}\mathcal{T}^{(\mathrm{l})}_{ab}(r)\frac{f^{a-b}2^{2a}}{\Gamma(-a+\frac{1}{2})}\left(-2\,a!\lambda^{-2a-1}+2\,a!\lambda^{-2a-1}\right)=0,\end{aligned} \tag{A.2}$$

where we made use of

$$\frac{\partial}{\partial\lambda}\left(\theta\left(\omega^2-\lambda^2\right)\right)=-\left(\delta\big(\omega+\lambda\big)+\delta\left(\omega-\lambda\right)\right). \tag{A.3}$$

Similarly, it can be demonstrated that the RSET is also completely independent of the choice of the cutoff.

A.2 Other representations for direct and tail regularization parameters

In this appendix, we report different but equivalent representations for the functions $\mathcal{I}_{\omega l}(a,b\,|r)$ and $\mathcal{J}_{\omega l}(a,b\,|r)$. Above, we have presented the derivation for these expressions in terms of hypergeometric functions. The alternative representations below involve the modified Bessel functions $I_\nu(z)$ and $K_\nu(z)$ and the generalized incomplete gamma function $\Gamma(a,z_0,z_1)=\int_{z_0}^{z_1}t^{a-1}e^{-t}dt$.

$$\begin{aligned}
&\mathcal{I}_{\omega l}(a,b\,|r)=\\
&=\frac{r^{2b+1}f^{-b-1/2}}{(2^b b!)\,(2r^2)^{b+1}}\sum_{p=0}^{b}\frac{(-1)^a 2^p(p)_{2b-2p}}{\Gamma(b-p+1)}\frac{\partial^{2a+p}}{\partial|\omega|^{2a+p}}\left(|\omega|^p I_{l+\frac{1}{2}}\left(\frac{|\omega|r}{\sqrt{f}}\right)K_{l+\frac{1}{2}}\left(\frac{|\omega|r}{\sqrt{f}}\right)\right)\\
&=\frac{1}{2}\frac{(-1)^a}{2^{2b}b!(f)^{b+1/2}r}\sum_{p=0}^{b}\frac{2^p(p)_{2b-2p}}{\Gamma(b-p+1)}\sum_{k=0}^{2a+p}\binom{2a+p}{k}\frac{p!\,|\omega|^{-2a+k}}{(-2a+k)!}\sum_{d=0}^{k}\binom{k}{d}\left(\frac{r}{\sqrt{f}}\right)^k\\
&\quad\times\frac{(-1)^d}{2^k}\sum_{c=0}^{2k-2d}\binom{k-d}{c}I_{l+1/2-k+d+2c}\left(\frac{|\omega|r}{\sqrt{f}}\right)\sum_{n=0}^{2d}\binom{d}{n}K_{l+1/2-d+2n}\left(\frac{|\omega|r}{\sqrt{f}}\right)\\
&=\lim_{x\to-1}\frac{2^l(-1)^{a+b}\,(2r^2)^{a-\frac{1}{2}}}{2\,b!f^{a+b+\frac{1}{2}}}\Bigg\{\sum_{k=1}^{b}\sum_{j=0}^{l}\frac{(-1)^{j+1}j!\binom{l}{j}\binom{\frac{1}{2}(l+j-1)}{l}}{2(-k+j+1)!}\\
&\quad\times\frac{\partial^{b-k}}{\partial x^{b-k}}\left((1-x)^{a+b-\frac{1}{2}}e^{-|\omega|\sqrt{\frac{2(1-x)r^2}{f}}}\right)+\sum_{k=b}^{l}\sum_{j=0}^{k-b}\frac{k!\binom{l}{k}\binom{\frac{1}{2}(k+l-1)}{l}(-1)^{-2b+k-j}}{(k-b)!}\\
&\quad\times\binom{k-b}{j}\left(|\omega|\sqrt{\frac{2r^2}{f}}\right)^{-2a-2k+2j-1}\Gamma\left(2a+2k-2j+1,0,\frac{2r|\omega|}{\sqrt{f}}\right)\Bigg\},
\end{aligned}\tag{A.4}$$

$$
\begin{aligned}
&\mathcal{J}_{\omega l}(a,b\,|r) = \\
&= \sqrt{\pi}(2r^2\rho^2)^{a-b}(a-b)!2^{2a}(-1)^l \sum_{k=0}^{a-b} \frac{\theta\left(\lambda^2-\omega^2\right)(a-k)!k!|\omega|^{2k-2a-1}}{(a-k-b)!\Gamma(k-a+\frac{1}{2})(k+l+1)!(k-l)!(2\rho^2)^k} \\
&\quad + (2r^2)^{a-b}(-1)^b\Gamma(1+a-b)\frac{r}{f^{1/2}} \sum_{k=0}^{a-b+1} \frac{(-1)^k}{2^{a-b+2}}\binom{a-b+1}{k}\frac{(2l+2(a-b)-4k+3)}{(l-k+\frac{1}{2})_{a-b+2}} \\
&\quad \times \frac{\partial^{2b}}{\partial|\omega|^{2b}} I_{l+\frac{3}{2}+a-b-2k}\left(\frac{|\omega|r}{\sqrt{f}}\right) K_{l+\frac{3}{2}+a-b-2k}\left(\frac{|\omega|r}{\sqrt{f}}\right) \\
&= \sqrt{\pi}(2r^2\rho^2)^{a-b}(a-b)!2^{2a}(-1)^l \sum_{k=0}^{a-b} \frac{\theta\left(\lambda^2-\omega^2\right)(a-k)!k!|\omega|^{2k-2a-1}}{(a-k-b)!\Gamma(k-a+\frac{1}{2})(k+l+1)!(k-l)!(2\rho^2)^k} \\
&\quad + (2r^2)^{a-b}(-1)^b\left(\frac{r}{\sqrt{f}}\right)^{2b+1}\Gamma(1+a-b) \sum_{k=0}^{a-b+1} \frac{(-1)^k}{2^{a-b+2}}\binom{a-b+1}{k} \\
&\quad \times \frac{(2l+2(a-b)-4k+3)}{(l-k+\frac{1}{2})_{a-b+2}} \sum_{p=0}^{2b}\binom{2b}{p}\frac{(-1)^p}{2^{2b}} \sum_{q=0}^{4b-2p}\binom{2b-p}{q} I_{l+3/2+a-3b-2k+p+2q}\left(\frac{|\omega|r}{\sqrt{f}}\right) \\
&\quad \times \sum_{n=0}^{2p}\binom{p}{n} K_{l+3/2+a-b-2k-p+2n}\left(\frac{|\omega|r}{\sqrt{f}}\right) \\
&= -\lim_{|\omega'|\to|\omega|} \frac{f^{a-b}}{4\pi} \sum_{k=0}^{a-b} 2^{l+2}(-1)^{a-k}\binom{a-b}{k}\frac{\partial^{2a-2k}}{\partial|\omega'|^{2a-2k}} \sum_{n=0}^{l}\sum_{b=0}^{n}\frac{\pi}{|\omega'|}(-1)^{n-b}\binom{l}{n} \\
&\quad \times \binom{\frac{1}{2}(l+n-1)}{l}\binom{n}{b}\left(\frac{2r^2}{f}\right)^k \left(\frac{\Gamma\left(2(k-b+n+1),0,\frac{2|\omega'|r}{\sqrt{f}}\right)}{\left(\frac{\sqrt{2}|\omega'|r}{\sqrt{f}}\right)^{2(k-b+n+1)}} - \frac{2^{k-b+n}\theta(\lambda^2-\omega^2)}{k-b+n+1}\right).
\end{aligned}
\tag{A.5}
$$

A.3 Hadamard coefficients

Below we list the coefficients $\mathcal{D}^{(\mathrm{p})}_{ab}$, $\mathcal{D}^{(\mathrm{r})}_{ab}$, $\mathcal{T}^{(\mathrm{l})}_{ab}$, $\mathcal{T}^{(\mathrm{r})}_{ab}$ and $\mathcal{T}^{(\mathrm{p})}_{ab}$ to 2nd order.

$$
\begin{aligned}
\mathcal{D}^{(\mathrm{r})}_{00} &= 2,\\
\mathcal{D}^{(\mathrm{r})}_{10} &= -\frac{f\left(r^2 f'' - 2rf' + 2f - 2\right)}{12r^2},\\
\mathcal{D}^{(\mathrm{r})}_{11} &= \frac{f\left(r^2\left(f'^2\right) - 4f\left(rf' + 1\right) + 4f^2\right)}{24r^2},\\
\mathcal{D}^{(\mathrm{r})}_{20} &= \frac{1}{2880r^4}\Bigg(f\Big[-5r^2\left(-f'^2\right)\left(r^2 f'' - 2rf' - 2\right)\\
&\quad - 8f^2\left(3r^3 f^{(3)} - 7r^2 f'' + 19rf' + 10\right)\\
&\quad + f\left(9r^4 f''^2 - 20r^2 f'' + 86r^2 f'^2 + 4rf'\left(3r^3 f^{(3)} - 14r^2 f'' + 20\right) + 4\right) + 76f^3\Big]\Bigg),\\
\mathcal{D}^{(\mathrm{r})}_{21} &= -\frac{1}{2880r^4}\Bigg(f\Big[r^4\Big(f'^2 + f'^4\Big) + r^2 f\Big(-30rf'^3 + f'^2\Big(11r^2 f'' - 30\Big)\Big)\\
&\quad + 4f^3\Big(11r^2 f'' - 52rf' - 40\Big)\\
&\quad - 2f^2\Big(10r^2 f'' - 67r^2 f'^2 + f'\Big(22r^3 f'' - 80r\Big) - 28\Big) + 104f^4\Big]\Bigg),\\
\mathcal{D}^{(\mathrm{r})}_{22} &= \frac{f^2\left(r^2 f'^2 - 4f\left(rf' + 1\right) + 4f^2\right)^2}{1152r^4},\\
\mathcal{D}^{(\mathrm{p})}_{11} &= -\frac{f'}{6r},\\
\mathcal{D}^{(\mathrm{p})}_{21} &= \frac{f\left(-9rf'^2 + 6rf\left(rf^{(3)} - 2f''\right) + 2f'\left(7r^2 f'' + f + 5\right)\right)}{720r^3},\\
\mathcal{D}^{(\mathrm{p})}_{22} &= \frac{7r^2 f'^2 - 10rf' + rf\left(9rf'' + 4f'\right) - 3f^2 + 3}{720r^4},
\end{aligned}
\tag{A.6}
$$

$$
\begin{aligned}
\mathcal{T}^{(\mathrm{l})}_{00} &= \frac{6\mu^2 r^2 - (6\xi-1)\left(r^2 f'' + 4rf' + 2f - 2\right)}{12r^2},\\
\mathcal{T}^{(\mathrm{l})}_{10} &= \frac{1}{480r^4}\Bigg(r^2 f''\left((10\xi(3\xi-1)+1)r^2 f'' - 10(6\xi-1)\left(2\xi+\mu^2 r^2\right)\right)\\
&\quad + 4(5\xi(24\xi-5)+1)r^2 f'^2\\
&\quad + 2rf'\left((5\xi-1)r^3 f^{(3)} + 2\left(60\xi^2 - 5\xi - 1\right)r^2 f'' + 40(1-6\xi)\xi + 10\mu^2(1-12\xi)r^2\right)\\
&\quad + 2rf\Big(r\left((20\xi(3\xi+2)-8)f'' + r\left((5\xi-1)rf^{(4)}(r) + (40\xi-7)f^{(3)}\right)\right)\\
&\qquad\qquad + (80\xi(3\xi-1)+6)f'\Big)\\
&\quad - 40f\xi\left(6\xi + 3\mu^2 r^2 - 1\right) + 4(10\xi(3\xi-1)+1)f^2 + 2\left(15\left(2\xi+\mu^2 r^2\right)^2 - 2\right)\Bigg),\\
\mathcal{T}^{(\mathrm{l})}_{11} &= \frac{f}{480r^4}\Bigg(-2\left(r^2 f'' + 2\right)\left((1-5\xi)r^2 f'' + 10\xi + 5\mu^2 r^2 - 2\right) + 2(1-10\xi)r^2 f'^2\\
&\quad + rf\left((16-80\xi)f' + r\left((12-80\xi)f'' + r\left(rf^{(4)}(r) + (6-20\xi)f^{(3)}\right) + 20\mu^2\right)\right)\\
&\quad + 8(5\xi-1)f^2 + rf'\left((10\xi-1)r^3 f^{(3)} + 4(20\xi-3)r^2 f'' + 20(6\xi-1)\right)\Bigg)\\
\mathcal{T}^{(\mathrm{r})}_{10} &= \frac{f\left(r^2 f'^2 - 4f\left(rf'+1\right) + 4f^2\right)\left((1-6\xi)\left(2 - r\left(rf'' + 4f'\right) - 2f + 2\right) - 6\mu^2 r^2\right)}{576r^4},\\
\mathcal{T}^{(\mathrm{p})}_{10} &= \frac{(f-1)\left((1-6\xi)\left(2 - r\left(rf'' + 4f'\right) - 2f\right) - 6\mu^2 r^2\right)}{144r^4},\\
\mathcal{T}^{(\mathrm{p})}_{11} &= \frac{f\left(rf' - 2f + 2\right)\left((1-6\xi)\left(2 - r\left(rf'' + 4f'\right) - 2f\right) - 6\mu^2 r^2\right)}{144r^4}.
\end{aligned}
\tag{A.7}
$$

A.4 Numerical and analytical parts of the RSET

In this appendix, we give explicit expressions for $\langle\hat{T}^{\alpha}{}_{\beta}\rangle_{\text{numerical}}$ and $\langle\hat{T}^{\alpha}{}_{\beta}\rangle_{\text{analytical}}$ that arise in the split in Eq. (3.13) of the RSET into a numerical and analytical part, which are separately conserved. The numerical part is given by

$$
\langle\hat{T}^{\alpha}{}_{\beta}\rangle_{\text{numerical}} = -\tilde{\mathsf{w}}^{\alpha}{}_{\beta} - (\xi - \tfrac{1}{2})\tilde{\mathsf{w}}^{;\alpha}{}_{;\beta} + (\xi - \tfrac{1}{2})\Box\tilde{\mathsf{w}}\,\delta^{\alpha}{}_{\beta} + \xi\, R^{\alpha}{}_{\beta}\tilde{\mathsf{w}}, \tag{A.8}
$$

where

$$\tilde{\mathsf{w}} = \frac{1}{8\pi^2}\Bigg\{ \int_{-\infty}^{\infty} \sum_{l=0}^{\infty} (2l+1)\left(g_{\omega l}(r) - k_{\omega l}^{(n)}(r)\right) d\omega \\ - \sqrt{\pi} \sum_{a=1}^{n-1} \sum_{b=0}^{a} \mathcal{T}_{ab}^{(\mathrm{l})}(r)\, \frac{(a-1)!2^{2a} f^{a-b}}{\Gamma(-a+\frac{1}{2})\lambda^{2a}} \Bigg\} + \frac{1}{8\pi^2}\mathcal{T}_{00}^{(\mathrm{l})}(r)\log(\lambda^2), \tag{A.9}$$

$$\tilde{\mathsf{w}}^{\tau}{}_{\tau} = \frac{1}{4} f'\, \tilde{\mathsf{w}}' - \frac{1}{8\pi^2 f}\Bigg\{ \int_{-\infty}^{\infty} \sum_{l=0}^{\infty} (2l+1)\omega^2 \left(g_{\omega l} - k_{\omega l}^{(n)}\right) d\omega \\ - \sqrt{\pi} \sum_{\substack{a=0 \\ a\neq 1}}^{n-1} \sum_{b=0}^{a} \mathcal{T}_{ab}^{(\mathrm{l})}(r)\, \frac{a!2^{2a} f^{a-b}}{\Gamma(\frac{1}{2}-a)(a-1)\lambda^{2a-2}} \Bigg\} + \frac{1}{4\pi^2}(\mathcal{T}_{10}^{(\mathrm{l})} + \frac{\mathcal{T}_{11}^{(\mathrm{l})}}{f})\log(\lambda^2), \tag{A.10}$$

$$\tilde{\mathsf{w}}^{\phi}{}_{\phi} = \tilde{\mathsf{w}}^{\theta}{}_{\theta} = \frac{1}{2r} f\, \tilde{\mathsf{w}}' - \frac{1}{16\pi^2 r^2}\Bigg\{ \int_{-\infty}^{\infty} \sum_{l=0}^{\infty} (2l+1) l(l+1)\left(g_{\omega l} - k_{\omega l}^{(n)}\right) d\omega \\ + \sqrt{\pi} \sum_{a=2}^{n-1} \sum_{b=0}^{a} \mathcal{T}_{ab}^{(\mathrm{l})}\, \frac{r^2(a-b)(a-2)!2^{2a} f^{a-b-1}}{\Gamma(\frac{3}{2}-a)\lambda^{2a-2}} \Bigg\} + \frac{1}{4\pi^2}\mathcal{T}_{10}^{(\mathrm{l})}(\log(\lambda^2), \tag{A.11}$$

$$\tilde{\mathsf{w}}^{r}{}_{r} = -\tilde{\mathsf{w}}^{\tau}{}_{\tau} - 2\tilde{\mathsf{w}}^{\phi}{}_{\phi} + \xi\, R\, \tilde{\mathsf{w}} + \mu^2 \tilde{\mathsf{w}}. \tag{A.12}$$

The analytical part is

$$\langle \hat{T}^{\alpha}{}_{\beta} \rangle_{\text{analytical}} = -\bar{\mathsf{w}}^{\alpha}{}_{\beta} - (\xi - \tfrac{1}{2})\bar{\mathsf{w}}^{;\alpha}{}_{;\beta} + (\xi - \tfrac{1}{2})\Box\bar{\mathsf{w}}\, \delta^{\alpha}{}_{\beta} + \xi\, R^{\alpha}{}_{\beta}\bar{\mathsf{w}} - \frac{1}{8\pi^2} v_1 \delta^{\alpha}{}_{\beta}, \tag{A.13}$$

where

$$\bar{\mathsf{w}} = -\frac{1}{8\pi^2}\left\{ \frac{\mathcal{D}_{10}^{(\mathrm{r})}}{f} + \frac{\mathcal{D}_{22}^{(\mathrm{r})}}{f^2} + \mathcal{D}_{11}^{(\mathrm{p})} + \mathcal{T}_{00}^{(\mathrm{l})}(r)(\log(f/\ell^2) - 2\gamma_{\mathrm{E}}) \right\}, \tag{A.14}$$

$$\bar{\mathsf{w}}^{\tau}{}_{\tau} = \frac{1}{4} f'\, \bar{\mathsf{w}}' - \frac{1}{4\pi^2}\Bigg\{ \frac{\mathcal{T}_{10}^{(\mathrm{r})}}{f^2} + \mathcal{T}_{10}^{(\mathrm{p})} + \frac{\mathcal{T}_{11}^{(\mathrm{p})}}{f} + \frac{\mathcal{T}_{10}^{(\mathrm{r})}}{f^2} + \mathcal{D}_{22}^{(\mathrm{p})} + \frac{\mathcal{D}_{21}^{(\mathrm{p})}}{f} + \frac{\mathcal{D}_{20}^{(\mathrm{r})}}{f^2} + \frac{\mathcal{D}_{21}^{(\mathrm{r})}}{f^3} + \frac{\mathcal{D}_{22}^{(\mathrm{r})}}{f^4} \\ + (\mathcal{T}_{10}^{(\mathrm{l})} + \frac{\mathcal{T}_{11}^{(\mathrm{l})}}{f})(\log(f/\ell^2) - 2\gamma_{\mathrm{E}} + 3) \Bigg\}, \tag{A.15}$$

$$\bar{\mathsf{w}}^{\phi}{}_{\phi} = \bar{\mathsf{w}}^{\theta}{}_{\theta} = \frac{1}{2r} f\, \bar{\mathsf{w}}' - \frac{1}{4\pi^2}\Bigg\{ \mathcal{T}_{10}^{(\mathrm{p})} + \frac{\mathcal{T}_{11}^{(\mathrm{l})}}{f} - \frac{\mathcal{T}_{10}^{(\mathrm{r})}}{f^2} + \mathcal{D}_{22}^{(\mathrm{p})} - \frac{\mathcal{D}_{20}^{(\mathrm{r})}}{f^2} - 2\frac{\mathcal{D}_{21}^{(\mathrm{r})}}{f^3} - 3\frac{\mathcal{D}_{22}^{(\mathrm{r})}}{f^4} \\ + \mathcal{T}_{10}^{(\mathrm{l})}(\log(f/\ell^2) - 2\gamma_{\mathrm{E}} + 1) \Bigg\}, \tag{A.16}$$

$$\bar{\mathsf{w}}^{r}{}_{r} = -\bar{\mathsf{w}}^{\tau}{}_{\tau} - 2\bar{\mathsf{w}}^{\phi}{}_{\phi} + \xi\, R\, \bar{\mathsf{w}} + \mu^2 \bar{\mathsf{w}} - \frac{3}{4\pi^2} v_1, \tag{A.17}$$

where explicit expressions for the Hadamard coefficients in terms of f are found in Appendix A.3.

A.5 Regularization of $|\omega|^{-2j-1}$ as a generalized function

In this Appendix, derive the expression in Eq. (2.42) for defining the regularization of $|\omega|^{-2j-1}$ as a generalized function. Let us initially take a test function of compact support $\varphi(\omega)$, then the regularized $|\omega|^{-2j-1}$ can be expressed as

$$\begin{aligned}(|\omega|^{-2j-1},\varphi(\omega)) = \int_0^\infty d\omega\,\omega^{-2j-1}\Big[\varphi(\omega)+\varphi(-\omega)\\ -2\sum_{k=0}^{j-1}\frac{\varphi^{(2k)}(0)}{(2k)!}\omega^{2k}-2\frac{\varphi^{(2j)}(0)}{(2j)!}\omega^{2j}\theta(\lambda-\omega)\Big].\end{aligned} \tag{A.18}$$

where $\theta(z)$ is the step function and λ is an arbitrary inverse length scale. It is convenient to split the integral into three parts

$$\begin{aligned}(|\omega|^{-2j-1},\varphi(\omega)) = \int_0^\lambda d\omega\,\omega^{-2j-1}\Big[\varphi(\omega)+\varphi(-\omega)-2\sum_{k=0}^{j}\frac{\varphi^{(2k)}(0)}{(2k)!}\omega^{2k}\Big]\\ -2\int_\lambda^\infty d\omega\sum_{k=0}^{j-1}\frac{\varphi^{(2k)}(0)}{(2k)!}\omega^{2k-2j-1}+\int_\lambda^\infty d\omega\,\omega^{-2j-1}\Big[\varphi(\omega)+\varphi(-\omega)\Big].\end{aligned} \tag{A.19}$$

The last integral here is simply

$$\int_\lambda^\infty d\omega\,\omega^{-2j-1}\Big[\varphi(\omega)+\varphi(-\omega)\Big] = \big(\theta(\omega^2-\lambda^2)|\omega|^{-2j-1},\varphi(\omega)\big)\,. \tag{A.20}$$

Introducing the Taylor expansions about $\omega = 0$ for $\varphi(\omega)$ and $\varphi(-\omega)$ in the low-frequency integral and simplifying yields

$$\begin{aligned}(|\omega|^{-2j-1},\varphi(\omega)) =& 2\int_0^\lambda d\omega\sum_{k=j+1}^{\infty}\frac{\varphi^{(2k)}(0)}{(2k)!}\omega^{2k-2j-1}-2\int_\lambda^\infty d\omega\sum_{k=0}^{j-1}\frac{\varphi^{(2k)}(0)}{(2k)!}\omega^{2k-2j-1}\\ &+\big(\theta(\omega^2-\lambda^2)|\omega|^{-2j-1},\varphi(\omega)\big)\,.\end{aligned} \tag{A.21}$$

We perform the remaining ω integrals and combine the resulting sums to obtain

$$(|\omega|^{-2j-1},\varphi(\omega)) = 2\sum_{\substack{k=0\\k\neq j}}^{\infty}\frac{\varphi^{(2k)}(0)\lambda^{2k-2j}}{(2k)!(2k-2j)}+\big(\theta(\omega^2-\lambda^2)|\omega|^{-2j-1},\varphi(\omega)\big)\,, \tag{A.22}$$

which can be written as

$$(|\omega|^{-2j-1},\varphi(\omega)) = 2\sum_{\substack{k=0\\k\neq j}}^{\infty}\frac{\lambda^{2k-2j}(-1)^{2k}}{(2k)!(2k-2j)}(\delta^{(2k)}(\omega),\varphi(\omega)) + \left(\theta(\omega^2-\lambda^2)|\omega|^{-2j-1},\varphi(\omega)\right). \tag{A.23}$$

Therefore, we have shown that

$$\frac{1}{|\omega|^{2j+1}} = \frac{\theta(\omega^2-\lambda^2)}{|\omega|^{2j+1}} + 2\sum_{\substack{k=0\\k\neq j}}^{\infty}\frac{\lambda^{2k-2j}\delta^{(2k)}(\omega)}{(2k)!(2k-2j)}, \qquad j>0\in\mathbb{Z}. \tag{A.24}$$

Appendix B

Thin shells

B.1 Hadamard coefficients

Below we list the coefficients $\mathcal{D}^{(\mathrm{p})}_{ab}$, $\mathcal{D}^{(\mathrm{r})}_{ab}$, $\mathcal{T}^{(\mathrm{l})}_{ab}$, $\mathcal{T}^{(\mathrm{r})}_{ab}$ and $\mathcal{T}^{(\mathrm{p})}_{ab}$ to 2nd order.

$$
\begin{aligned}
\mathcal{D}^{(\mathrm{r})}_{00} &= 2, \\
\mathcal{D}^{(\mathrm{r})}_{10} &= \frac{r^2 h f'^2 + r f \left(r f' h' + 2h \left(f' - r f''\right)\right) + f^2 \left(-2rh' + 4h^2 - 4h\right)}{24 r^2 f h^2}, \\
\mathcal{D}^{(\mathrm{r})}_{11} &= \frac{r^2 f'^2 - 4rff' - 4f^2(h-1)}{24 r^2 h}, \\
\mathcal{D}^{(\mathrm{r})}_{20} &= \frac{1}{11520 r^4 f^2 h^4} \Bigg[47 r^4 h^2 f'^4 - 8 r^3 f h f'^2 \left(h \left(14 r f'' + 5 f'\right) - 7 r f' h'\right) \\
&\quad - 4 r f^3 \Big(57 r^2 f' h'^2 - 6 r h \left(9 r f'' h' + f' \left(4 r h'' - 13 h'\right)\right) + 20 h^3 \left(r f'' - 3 f'\right) \\
&\qquad + h^2 \left(f' \left(72 - 10 r h'\right) + 8 r \left(3 r f^{(3)} - 4 f''\right)\right) \Big) \\
&\quad + r^2 f^2 \Big(57 r^2 f'^2 h'^2 - 12 r h f' \left(9 r f'' h' + f' \left(2 r h'' + 3 h'\right)\right) \\
&\qquad + h^2 \left(36 r^2 f''^2 - 4 f'^2 + 8 r f' \left(6 r f^{(3)} + 11 f''\right)\right) \Big) \\
&\quad + 4 f^4 \left(57 r^2 h'^2 + h^2 \left(76 - 20 r h'\right) + 8 r h \left(10 h' - 3 r h''\right) + 4 h^4 - 80 h^3\right) \Bigg], \\
\mathcal{D}^{(\mathrm{r})}_{21} &= \frac{1}{5760 r^4 f h^3} \Bigg[9 r^4 h f'^4 + r^3 f f'^2 \left(11 r f' h' - 2h \left(11 r f'' + 3 f'\right)\right) \\
&\quad + 2 r^2 f^2 f' \left(-33 r f' h' + 20 h^2 f' + h \left(44 r f'' - 68 f'\right)\right) \\
&\quad + 4 r f^3 \left(33 r f' h' + h \left(f' \left(82 - 5 r h'\right) - 22 r f''\right) + 10 h^2 \left(r f'' - 7 f'\right)\right) \\
&\quad - 8 f^4 \left(h \left(26 - 5 r h'\right) + 11 r h' + 14 h^3 - 40 h^2\right) \Bigg], \\
\mathcal{D}^{(\mathrm{r})}_{22} &= \frac{\left(-r^2 f'^2 + 4 r f f' + 4 f^2 (h-1)\right)^2}{1152 r^4 h^2},
\end{aligned}
$$

$$\mathcal{D}_{11}^{(\mathrm{p})} = \frac{fh' - hf'}{12rfh^2},$$

$$\begin{aligned}\mathcal{D}_{21}^{(\mathrm{p})} = \frac{1}{2880r^3f^2h^4}\Bigg[&5r^2h^2f'^3 + 2rfhf'\left(7rf'h' + 11h\left(f' - rf''\right)\right)\\
&- 2f^3\left(10h^2h' + 57rh'^2 + 2h\left(7h' - 12rh''\right)\right)\\
&+ f^2\Big(57r^2f'h'^2 + 20h^3f' - 4h^2\left(5f' - 6r^2f^{(3)}\right)\\
&- 2rh\left(27rf''h' - 4f'\left(5h' - 3rh''\right)\right)\Big).\Bigg],\end{aligned}$$

$$\begin{aligned}\mathcal{D}_{22}^{(\mathrm{p})} = \frac{1}{2880r^4f^2h^4}\Bigg[&-9r^2h^2f'^2 + 4rfh\left(-7rf'h' - 5h^2f' + h\left(3rf'' + 2f'\right)\right)\\
&+ f^2\left(57r^2h'^2 + 4h^2\left(5rh' - 3\right) - 8rh\left(3rh'' + h'\right) + 12h^4\right)\Bigg],,\end{aligned}$$

$$\begin{aligned}\mathcal{T}_{00}^{(\mathrm{l})} = \frac{1}{24r^2f^2h^2}\Bigg[&(6\xi - 1)r^2hf'^2 + (6\xi - 1)rf\left(rf'h' - 2h\left(rf'' + 2f'\right)\right)\\
&+ 4f^2\left((6\xi - 1)rh' + h^2\left(6\xi + 3\mu^2r^2 - 1\right) + (1 - 6\xi)h\right)\Bigg],\end{aligned}$$

$$
\begin{aligned}
\mathcal{T}_{10}^{(1)} = \frac{1}{17280 r^4 f^4 h^5}\Bigg[2\Bigg(& 4\left(135 r^4\mu^4 + 60 r^2(9\xi-1)\mu^2 + 540\xi^2 - 120\xi + 2\right) h^5 \\
& - 80\left(3 r^2(9\xi-1)\mu^2 + 54\xi^2 - 21\xi + 2\right) h^4 \\
& + 4\left(540\xi^2 - 300\xi + 5r\left(9 r^2(12\xi-1)\mu^2 + 216\xi^2 - 60\xi + 4\right) h' + 38\right) h^3 \\
& - 2r\left(\left(2160\xi^2 - 960\xi + 94\right) h' + 9r\left(10(6\xi-1)h'' + r(20\xi-3)h^{(3)}\right)\right) h^2 \\
& + 9 r^2 h'\left(40\left(6\xi^2 + 5\xi - 1\right) h' + 13 r(20\xi-3)h''\right) h + 126 r^3(3-20\xi)h'^3 \Bigg) f^4 \\
- 2r\Bigg(& 20\Big(\left(9 r^2(12\xi-1)\mu^2 + 216\xi^2 - 60\xi + 4\right) f' \\
& + 3r\left(r^2(18\xi-1)\mu^2 + 6\xi(6\xi-1)\right) f''\Big) h^4 + 126 r^3(5\xi-1) f' h'^3 \\
& - 2\Big(f'\left(2160\xi^2 - 960\xi + 15r\left(r^2(18\xi-1)\mu^2 + 6\xi(6\xi-1)\right) h' + 94\right) \\
& + 9r\left(2\left(60\xi^2 + 10\xi - 3\right) f'' + r\left((60\xi-11) f^{(3)} + 2r(5\xi-1) f^{(4)}\right)\right)\Big) h^3 \\
& + r\Big(r\left(72 r(5\xi-1) f'' h'' + h'\left(\left(2160\xi^2 + 1680\xi - 373\right) f'' + 108 r(5\xi-1) f^{(3)}\right)\right) \\
& + 9 f'\left(8\left(75\xi^2 - 5\xi - 1\right) h' + r\left((100\xi-17)h'' + 2r(5\xi-1)h^{(3)}\right)\right)\Big) h^2 \\
& + r^2 h'\left(171 r(1-5\xi) h' f'' + f'\left(117 r(1-5\xi)h'' - 2\left(540\xi^2 + 915\xi - 172\right) h'\right)\right) h \Bigg) f^3 \\
+ r^2 h\Bigg(& 60\left(r^2(18\xi-1)\mu^2 + 6\xi(6\xi-1)\right) f'^2 h^3 + 5 r^2\left(54\xi^2 - 222\xi + 43\right) f'^2 h'^2 \\
& + 2\Big(72\left(15\xi^2 - 15\xi + 2\right) f'^2 + r\left(\left(2160\xi^2 - 2640\xi + 401\right) f'' + 90 r(1-5\xi) f^{(3)}\right) f' \\
& + 10 r^2\left(54\xi^2 - 42\xi + 7\right) f''^2\Big) h^2 \\
& + 2r f'\left(9 f'\left(4(40\xi-7)h' + 5r(5\xi-1)h''\right) - 5r\left(108\xi^2 - 219\xi + 41\right) h' f''\right) h \Bigg) f^2 \\
- 2 r^3 h^2 f'^2\Big(& r\left(-270\xi^2 + 570\xi - 107\right) f' h' + 2h\Big(\left(540\xi^2 - 705\xi + 107\right) f' \\
& + r\left(270\xi^2 - 570\xi + 107\right) f''\Big)\Big) f + r^4\left(270\xi^2 - 930\xi + 179\right) h^3 f'^4 \Bigg],
\end{aligned}
$$

$$
\begin{aligned}
\mathcal{T}_{11}^{(1)} = \frac{1}{17280 r^4 f^3 h^5} \Bigg[& 10(33\xi - 16) r^4 h^3 f'^4 - 2 r^3 f h^2 f'^2 \Big(2(44 - 75\xi) r f' h' \\
& + h \left(4(75\xi - 44) r f'' + 21(30\xi - 7) f' \right) \Big) \\
& - r^2 f^2 h \Bigg(2(89 - 165\xi) r^2 f'^2 h'^2 + 60 \mu^2 r^2 h^3 f'^2 + r h f' \Big((420\xi - 307) r f'' h' \\
& + f' \left(9(20\xi - 9) r h'' + 4(330\xi - 79) h' \right) \Big) \\
& + h^2 \Big(8(15\xi + 8) r^2 f''^2 + (38 - 480\xi) f'^2 \\
& - 6 r f' \left(3(20\xi - 9) r f^{(3)} + (300\xi - 83) f'' \right) \Big) \Bigg) \\
& + r f^3 \Bigg(- 126 r^3 f' h'^3 + r^2 h h' \left(171 r f'' h' + f' \left(117 r h'' + 2(330\xi - 7) h' \right) \right) \\
& + 40 h^4 \left(3\mu^2 r^3 f'' + f' \left(30\xi + 3\mu^2 r^2 - 5 \right) \right) \\
& - 2 r h^2 \Big(r \left(36 r f'' h'' + h' \left(54 r f^{(3)} + (211 - 600\xi) f'' \right) \right) \\
& - 9 f' \left((80\xi - 8) h' + r \left((1 - 20\xi) h'' - r h^{(3)} \right) \right) \Big) \\
& + 4 h^3 \Big(f' \left(-15 \mu^2 r^3 h' + 60\xi - 4 \right) \\
& + 9 r \left((6 - 40\xi) f'' + r \left(r f^{(4)} + (7 - 20\xi) f^{(3)} \right) \right) \Big) \Bigg) \\
& + 2 f^4 \Bigg(126 r^3 h'^3 + 4 h^3 \left(15 r h' \left(6\xi + \mu^2 r^2 - 1 \right) + 420\xi - 76 \right) \\
& + r^2 h h' \left((199 - 1320\xi) h' - 117 r h'' \right) \\
& + 6 r h^2 \left((4 - 60\xi) h' + 3 r \left(r h^{(3)} + (40\xi - 6) h'' \right) \right) + 8 h^5 \left(30\xi + 15 \mu^2 r^2 - 2 \right) \\
& - 40 h^4 \left(48\xi + 3\mu^2 r^2 - 8 \right) \Bigg) \Bigg],
\end{aligned}
$$

$$\mathcal{T}_{10}^{(\mathrm{r})} = \frac{1}{1152r^4f^2h^3}\left(-r^2f'^2+4rff'+4f^2(h-1)\right)$$
$$\times\Bigg((6\xi-1)r^2hf'^2+(6\xi-1)rf\left(rf'h'-2h\left(rf''+2f'\right)\right)$$
$$+4f^2\left((6\xi-1)rh'+h^2\left(6\xi+3\mu^2r^2-1\right)+(1-6\xi)h\right)\Bigg),$$
$$\mathcal{T}_{10}^{(\mathrm{p})} = \frac{1}{288r^4f^2h^3}\Bigg[(h-1)\Big((6\xi-1)r^2hf'^2+(6\xi-1)rf\left(rf'h'-2h\left(rf''+2f'\right)\right)$$
$$+4f^2\left((6\xi-1)rh'+h^2\left(6\xi+3\mu^2r^2-1\right)+(1-6\xi)h\right)\Big)\Bigg],$$
$$\mathcal{T}_{11}^{(\mathrm{p})} = -\frac{1}{288r^4f^2h^3}\Bigg[\left(rf'+2f(h-1)\right)\Big((6\xi-1)r^2hf'^2$$
$$+(6\xi-1)rf\left(rf'h'-2h\left(rf''+2f'\right)\right)$$
$$+4f^2\left((6\xi-1)rh'+h^2\left(6\xi+3\mu^2r^2-1\right)+(1-6\xi)h\right)\Big)\Bigg].$$

B.2 Weak field approximation

In this Appendix, following the procedure outlined in Ref. [88], we derive the terms $\log\left(\frac{-\bar{\Box}}{\nu^2}\right)R^{(1)}$ and $\log\left(\frac{-\bar{\Box}}{\nu^2}\right)R^{\alpha}{}_{\beta}{}^{(1)}(x)$, necessary to compute the VP and RSET in the context of the weak field approximation. Hereafter, we drop the $^{(1)}$ superscript for notational simplicity; all quantities are understood to be linear in M/r_0.

The terms involving the Ricci tensor are most easily obtained by considering the Cartesian components of $R_{\alpha\beta}$, which are derived through the tensor transformation law

$$R'^{\alpha}{}_{\beta} = \frac{\partial x'^{\alpha}}{\partial x^{\delta}}\frac{\partial x^{\gamma}}{\partial x'^{\beta}}R^{\delta}{}_{\gamma}, \tag{B.1}$$

where the Cartesian coordinates are $x'^{\alpha}=\{\tau,x,y,z\}$. We then express the Cartesian

components in terms of spherical coordinates $x^\alpha = \{\tau, r, \theta, \phi\}$

$$
\begin{aligned}
R'^{x}_{\ x} &= \sin^2\theta\cos^2\phi\, R^{r}_{\ r} + \cos^2\theta\cos^2\phi\, R^{\theta}_{\ \theta} + \sin^2\phi\, R^{\phi}_{\ \phi},\\
R'^{y}_{\ y} &= \sin^2\theta\sin^2\phi\, R^{r}_{\ r} + \cos^2\theta\sin^2\phi\, R^{\theta}_{\ \theta} + \cos^2\phi\, R^{\phi}_{\ \phi},\\
R'^{z}_{\ z} &= R^{\theta}_{\ \theta} + \cos^2\theta(R^{r}_{\ r} - R^{\theta}_{\ \theta}),\\
R'^{x}_{\ y} &= \sin^2\theta\sin\phi\cos\phi\, R^{r}_{\ r} + \cos^2\theta\sin\phi\cos\phi\, R^{\theta}_{\ \theta} - \sin\phi\cos\phi R^{\phi}_{\ \phi},\\
R'^{x}_{\ z} &= \sin\theta\cos\theta\cos\phi(R^{r}_{\ r} - R^{\theta}_{\ \theta}),\\
R'^{y}_{\ z} &= \sin\theta\cos\theta\sin\phi(R^{r}_{\ r} - R^{\theta}_{\ \theta}).
\end{aligned}
\tag{B.2}
$$

Introducing the Ricci scalar and tensor into Eq. (4.93) and expressing the integrals in spherical coordinates, yields representations of the nonlocal operators for which the integrations can be carried out straightforwardly

$$
\log\left(\frac{-\bar{\Box}}{\nu^2}\right) R = -\frac{1}{2\pi}\int_0^\infty \mathrm{d}r'\, r'^2 \int_0^\pi \mathrm{d}\theta'\, \sin\theta' \int_0^{2\pi} \mathrm{d}\phi'\, \frac{R(r',\theta',\phi')}{(r^2 + r'^2 - 2rr'\cos\theta')^{3/2}} \tag{B.3}
$$

$$
\log\left(\frac{-\bar{\Box}}{\nu^2}\right) R'^{\alpha}_{\ \beta} = -\frac{1}{2\pi}\int_0^\infty \mathrm{d}r'\, r'^2 \int_0^\pi \mathrm{d}\theta'\, \sin\theta' \int_0^{2\pi} \mathrm{d}\phi'\, \frac{R'^{\alpha}_{\ \beta}(r',\theta',\phi')}{(r^2 + r'^2 - 2rr'\cos\theta')^{3/2}}. \tag{B.4}
$$

Computing the ϕ' integral yields for the Ricci scalar

$$
\frac{1}{\pi}\int_0^{2\pi} \mathrm{d}\phi'\, R(r',\theta',\phi') = 2R, \tag{B.5}
$$

and for the diagonal components of the Ricci tensor

$$
\begin{aligned}
&\frac{1}{\pi}\int_0^{2\pi} \mathrm{d}\phi'\, R'^{\tau}_{\ \tau}(r',\theta',\phi') = 2R^{\tau}_{\ \tau},\\
&\frac{1}{\pi}\int_0^{2\pi} \mathrm{d}\phi'\, R'^{x}_{\ x}(r',\theta',\phi') = \frac{1}{\pi}\int_0^{2\pi} \mathrm{d}\phi'\, R'^{y}_{\ y}(r',\theta',\phi') = R^{r}_{\ r} + R^{\phi}_{\ \phi} + (R^{\theta}_{\ \theta} - R^{r}_{\ r})\cos^2\theta',\\
&\frac{1}{\pi}\int_0^{2\pi} \mathrm{d}\phi'\, R'^{z}_{\ z}(r',\theta',\phi') = 2R^{\theta}_{\ \theta} - 2(R^{\theta}_{\ \theta} - R^{r}_{\ r})\cos^2\theta'.
\end{aligned}
\tag{B.6}
$$

All the off-diagonal components of the Ricci tensor vanish upon integration in ϕ', because of spherical symmetry. To compute the θ' integral we change the integration

variable to $u = \cos\theta'$ and obtain

$$g_1(r) := \int_{-1}^{1} du\,(r^2 + r'^2 - 2rr'\,u)^{-3/2} = \begin{cases} \dfrac{2}{r(r-r')(r+r')} & r' < r, \\ \dfrac{2}{r'(r'-r)(r+r')} & r' > r, \end{cases} \tag{B.7}$$

$$g_2(r) := \int_{-1}^{1} u^2 du\,(r^2 + r'^2 - 2rr'\,u)^{-3/2} = \begin{cases} \dfrac{2(r^2+2r'^2)}{3r^3(r-r')(r+r')} & r' < r, \\ \dfrac{2(2r^2+r'^2)}{3r'^3(r'-r)(r+r')} & r' > r. \end{cases} \tag{B.8}$$

Putting together Eqs. (B.3)–(B.8), we obtain

$$\begin{aligned} \log\left(\frac{-\bar{\Box}}{\nu^2}\right) R &= -\int_0^\infty \mathrm{d}r' r'^2 R\, g_1, \\ \log\left(\frac{-\bar{\Box}}{\nu^2}\right) R'^{\tau}{}_{\tau} &= -\int_0^\infty \mathrm{d}r' r'^2 R^{\tau}{}_{\tau}\, g_1, \\ \log\left(\frac{-\bar{\Box}}{\nu^2}\right) R'^{x}{}_{x} &= -\frac{1}{2}\int_0^\infty \mathrm{d}r' r'^2 \left[(R^{r}{}_{r} + R^{\phi}{}_{\phi})\, g_1 + (R^{\theta}{}_{\theta} - R^{r}{}_{r})\, g_2\right], \\ \log\left(\frac{-\bar{\Box}}{\nu^2}\right) R'^{z}{}_{z} &= -\int_0^\infty \mathrm{d}r' r'^2 \left[R^{\theta}{}_{\theta}\, g_1 - (R^{\theta}{}_{\theta} - R^{r}{}_{r})\, g_2\right]. \end{aligned} \tag{B.9}$$

Introducing Eqs. (4.87) and (4.88) into the previous expressions, the radial integrals are easily computed using the properties of the delta distribution. For instance, for the Ricci scalar, using Eq. (B.7), we can write

$$\begin{aligned} \log\left(\frac{-\bar{\Box}}{\nu^2}\right) R = &- \bar{R}\int_0^r \mathrm{d}r'\, r'^2\, \delta(r'-r_0)\frac{2}{r(r-r')(r+r')} \\ &- \bar{R}\int_r^\infty \mathrm{d}r'\, r'^2\, \delta(r'-r_0)\frac{2}{r'(r'-r)(r+r')}. \end{aligned} \tag{B.10}$$

In the interior of the shell, where $r < r_0$, the first integral vanishes. Conversely, in the exterior, where $r > r_0$, the second integral vanishes. Hence, we find

$$\log\left(\frac{-\bar{\Box}}{\nu^2}\right) R = \begin{cases} -\frac{2\bar{R}\,r_0}{(r_0-r)(r+r_0)}, & r < r_0, \\ -\frac{2\bar{R}\,r_0^2}{r(r-r_0)(r+r_0)}, & r > r_0. \end{cases} \tag{B.11}$$

A similar approach can be used to perform the radial integrals of the Ricci tensor components. The resulting tensor is spherically symmetric and diagonal in Cartesian coordinates, $\log\left(\frac{-\bar{\Box}}{\nu^2}\right) R'^{\alpha}{}_{\beta} = \mathrm{diag}(a,c,c,b)$. In spherical coordinates, it simply transforms to $\log\left(\frac{-\bar{\Box}}{\nu^2}\right) R^{\alpha}{}_{\beta} = \mathrm{diag}(a,b,c,c)$. The components in spherical coordi-

nates are then

$$\log\left(\frac{-\bar{\Box}}{\nu^2}\right) R^{\tau}{}_{\tau} = \begin{cases} -\,r_0\,\bar{R}^{\tau}{}_{\tau}\dfrac{2}{(r_0-r)(r+r_0)}, & r<r_0, \\ -\,r_0^2\,\bar{R}^{\tau}{}_{\tau}\dfrac{2}{r(r-r_0)(r+r_0)}, & r>r_0, \end{cases} \tag{B.12}$$

$$\log\left(\frac{-\bar{\Box}}{\nu^2}\right) R^{r}{}_{r} = \begin{cases} -\,\dfrac{4}{3}\bar{R}^{\theta}{}_{\theta}\dfrac{1}{r_0} - \dfrac{2}{3}\bar{R}^{r}{}_{r}\dfrac{2r^2+r_0^2}{r_0\,(r_0-r)(r+r_0)}, & r<r_0, \\ -\,\dfrac{4}{3}\bar{R}^{\theta}{}_{\theta}\dfrac{r_0^2}{r^3} - \dfrac{2}{3}\bar{R}^{r}{}_{r}\dfrac{r_0^2}{r^3}\dfrac{2r_0^2+r^2}{(r-r_0)(r+r_0)}, & r>r_0, \end{cases} \tag{B.13}$$

$$\log\left(\frac{-\bar{\Box}}{\nu^2}\right) R^{\theta}{}_{\theta} = \begin{cases} -\,\dfrac{2}{3}\bar{R}^{\theta}{}_{\theta}\dfrac{2r_0^2+r^2}{r_0\,(r_0-r)(r+r_0)} - \dfrac{2}{3}\bar{R}^{r}{}_{r}\dfrac{1}{r_0}, & r<r_0, \\ -\,\dfrac{2}{3}\bar{R}^{\theta}{}_{\theta}\dfrac{r_0^2}{r^3}\dfrac{r_0^2+2r^2}{(r-r_0)(r+r_0)} - \dfrac{2}{3}\bar{R}^{r}{}_{r}\dfrac{r_0^2}{r^3}, & r>r_0. \end{cases} \tag{B.14}$$

Appendix C

The Reissner-Nordström interior

C.1 Hadamard Coefficients on the interior

Below we list the Hadamard coefficients $\mathcal{D}^{(\mathrm{p})}_{ab}$, $\mathcal{D}^{(\mathrm{r})}_{ab}$, $\mathcal{T}^{(\mathrm{l})}_{ab}$, $\mathcal{T}^{(\mathrm{r})}_{ab}$ and $\mathcal{T}^{(\mathrm{p})}_{ab}$ to second order. Although in Chapters 5 and 6 we adopted the notation for the radial function $|f|$, in this Appendix, we list the parameters adopting $|f| \to -f$ for easier comparison with the exterior coefficients in Appendix A.3.

$$\mathcal{D}^{(\mathrm{r})}_{00} = 2,$$

$$\mathcal{D}^{(\mathrm{r})}_{10} = \frac{f\left(r^2 f'' - 2rf' + 2f - 2\right)}{12r^2},$$

$$\mathcal{D}^{(\mathrm{r})}_{11} = \frac{f\left(r^2\left(f'^2\right) - 4f\left(rf' + 1\right) + 4f^2\right)}{24r^2},$$

$$\mathcal{D}^{(\mathrm{r})}_{20} = \frac{f}{2880r^4}\Bigg(5r^2 f'^2\left(r^2 f'' - 2rf' - 2\right) - 8f^2\left(3r^3 f^{(3)} - 7r^2 f'' + 19rf' + 10\right)$$
$$+ f\left(9r^4 f''^2 - 20r^2 f'' + 86r^2 f'^2 + 4rf'\left(3r^3 f^{(3)} - 14r^2 f'' + 20\right) + 4\right) + 76f^3\Bigg),$$

$$\mathcal{D}^{(\mathrm{r})}_{21} = \frac{f}{2880r^4}\Bigg(r^4 f'^4 + 4f^3\left(11r^2 f'' - 52rf' - 40\right) + r^2 f f'^2\left(11r^2 f'' - 30rf' - 30\right)$$
$$+ f^2\left(-20r^2 f'' + 134r^2 f'^2 + f'\left(160r - 44r^3 f''\right) + 56\right) + 104f^4\Bigg),$$

$$\mathcal{D}^{(\mathrm{r})}_{22} = \frac{f^2\left(r^2 f'^2 - 4f\left(rf' + 1\right) + 4f^2\right)^2}{1152r^4},$$

$$\mathcal{D}^{(\mathrm{p})}_{11} = -\frac{f'}{6r},$$

$$\mathcal{D}^{(\mathrm{p})}_{21} = -\frac{f\left(-9rf'^2 + 6rf\left(rf^{(3)} - 2f''\right) + 2f'\left(7r^2 f'' + f + 5\right)\right)}{720r^3},$$

$$\mathcal{D}^{(\mathrm{p})}_{22} = \frac{7r^2 f'^2 - 10rf' + rf\left(9rf'' + 4f'\right) - 3f^2 + 3}{720r^4},$$

$$\mathcal{T}^{(\mathrm{l})}_{00} = \frac{6\mu^2 r^2 - (6\xi-1)\left(r^2 f'' + 4rf' + 2f - 2\right)}{12r^2},$$

$$\mathcal{T}^{(\mathrm{l})}_{10} = \frac{1}{480r^4}\Bigg(r^2 f''\left((10\xi(3\xi-1)+1)r^2 f'' - 10(6\xi-1)\left(2\xi+\mu^2 r^2\right)\right)$$
$$+ 4(5\xi(24\xi-5)+1)r^2 f'^2$$
$$+ 2rf'\left((5\xi-1)r^3 f^{(3)} + 2\left(60\xi^2 - 5\xi - 1\right)r^2 f'' + 40(1-6\xi)\xi + 10\mu^2(1-12\xi)r^2\right)$$
$$+ 2rf\left((80\xi(3\xi-1)+6)f' + r\left((20\xi(3\xi+2)-8)f'' + r\left((5\xi-1)rf^{(4)} + (40\xi-7)f^{(3)}\right)\right)\right)$$
$$- 40f\xi\left(6\xi + 3\mu^2 r^2 - 1\right) + 4(10\xi(3\xi-1)+1)f^2 + 2\left(15\left(2\xi+\mu^2 r^2\right)^2 - 2\right)\Bigg),$$

$$\mathcal{T}^{(\mathrm{l})}_{11} = \frac{f}{480r^4}\Bigg(2\left(r^2 f'' + 2\right)\left((1-5\xi)r^2 f'' + 10\xi + 5\mu^2 r^2 - 2\right) + 2(10\xi-1)r^2 f'^2$$
$$- rf\left((16-80\xi)f' + r\left((12-80\xi)f'' + r\left(rf^{(4)} + (6-20\xi)f^{(3)}\right) + 20\mu^2\right)\right)$$
$$+ (8-40\xi)f^2 + rf'\left((1-10\xi)r^3 f^{(3)} + 4\left((3-20\xi)r^2 f'' - 30\xi + 5\right)\right)\Bigg),$$

$$\mathcal{T}^{(\mathrm{r})}_{10} = \frac{f\left(r^2 f'^2 - 4f\left(rf'+1\right) + 4f^2\right)\left((1-6\xi)\left(2 - r\left(rf'' + 4f'\right) - 2f + 2\right) - 6\mu^2 r^2\right)}{576r^4},$$

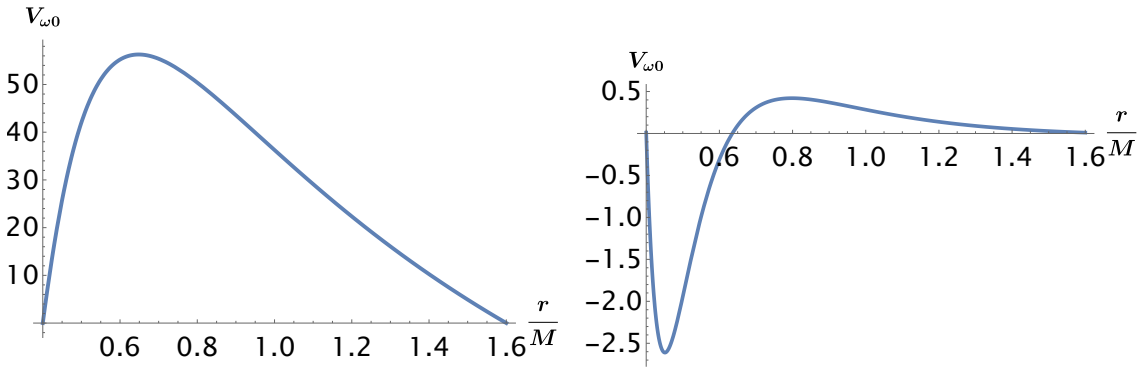
$$\mathcal{T}^{(\mathrm{p})}_{10} = \frac{(f-1)\left((1-6\xi)\left(2 - r\left(rf'' + 4f'\right) - 2f\right) - 6\mu^2 r^2\right)}{144r^4},$$

$$\mathcal{T}^{(\mathrm{p})}_{11} = -\frac{f\left(rf' - 2f + 2\right)\left((1-6\xi)\left(2 - r\left(rf'' + 4f'\right) - 2f\right) - 6\mu^2 r^2\right)}{144r^4}.$$

C.2 Small frequency asymptotics for l=0 in the large mass regime

In this Appendix, we obtain analytic expressions for interior scattering coefficients $A_{\omega 0}$ and $B_{\omega 0}$ and for the exterior $A^{\mathrm{up}}_{\omega 0}$, with $l = 0$, in the low-frequency and large-mass regime. We then use these expressions to show that the coefficient of the logarithmic divergence $h_0(\mu)$ (as defined in Eq. (6.25)) vanishes in the large mass regime, thereby providing analytical evidence to the numerical results reported in Fig. 6.8.

Sela [118] obtained analytical expressions for the low-frequency and large-l scattering coefficients in the interior and exterior of a Reissner-Nordström black hole, using matching asymptotics. This analysis was performed for a massless scalar field, under the assumption that the potential is dominated by the large $\tilde{l} = l + \frac{1}{2}$. Such assumption requires $\tilde{l} \gg \omega M, \frac{r_+}{M}$. At leading order in $\tilde{l}$, the potential in Eq. (5.9)



(a) *Large mass regime, $\mu M = 10$.* ***(b)*** *Small mass regime, $\mu M = 0.2$.*

Figure C.1: *Examples of the potential for the Schrödinger-type equation in the interior of a charged black hole with $M = 1$ and $Q = 0.8M$. Left: large mass regime with $l = 0$, $\omega M = 0.1$, and $\mu M = 10$. Right: small mass regime with $l = 0$, $\omega M = 0.1$, and $\mu M = 0.2$.*

can then be expressed as

$$V_{\omega l}(r) \sim \frac{\tilde{l}^2}{r^4}(r - r_-)(r_+ - r). \tag{C.1}$$

We will employ an analogous treatment to analyse the large mass case for the $l = 0$ mode. Specifically, in the large mass regime, we can write the potential (5.9) as

$$V_{\omega l}(r) \sim \frac{\mu^2}{r^2}(r - r_-)(r_+ - r). \tag{C.2}$$

Thus, in the large-mass regime, and for the $l = 0$ mode, the potential has no turning points on the interior (see also Figure C.1a), making the asymptotic matching easier than in the small-mass case, for which the potential has a non-trivial behavior (see, for instance, Fig. C.1b).

C.2.1 The interior scattering coefficients

In this section, we follow a similar approach to the one outlined in Ref. [118]. We divide the black hole interior into three different regions: the two regions near the horizons and the middle region.

Region A ($r \to r_+$)

Near the event horizon, we expand the potential (5.9) near $r = r_+$ ($r_* \to -\infty$) as

$$V_{\omega 0} \sim \omega^2 + C_+ (r - r_-) = \omega^2 + C_+(r_+ - r_-)e^{-2\kappa_+ r_+}e^{2\kappa_+ r_*}, \quad r_* \to -\infty, \tag{C.3}$$

where we have defined

$$C_+ = \frac{r_+ - r_-}{r_+^4}\left(l^2 + l + \mu^2 r_+^2 + 1 - \frac{r_-}{r_+}\right). \tag{C.4}$$

Introducing this into Eq. (5.7) yields

$$\left\{\frac{d^2}{dr_*^2} + \omega^2 + C_+(r_+ - r_-)e^{-2\kappa_+ r_+}e^{2\kappa_+ r_*}\right\}\psi^{\mathrm{A}}_{\omega l}(r) = 0, \tag{C.5}$$

We need a solution to this equation with the required boundary condition $\psi^{\mathrm{A}}_{\omega l} \sim e^{-i\omega r_*}$ near r_+. This can be written in terms of a Bessel function of the first kind as

$$\psi^{\mathrm{A}}_{\omega l} \sim \left(\frac{C_+ r_+^4}{r_+ - r_-}\right)^{i\omega/(2\kappa_+)} e^{-i\omega r_+}\Gamma(1 - i\omega/\kappa_+)J_{-i\omega/\kappa_+}\left(2\, r_+^2\sqrt{\frac{C_+}{r_+ - r_-}}e^{\kappa_+(r_* - r_+)}\right). \tag{C.6}$$

Now, in the large mass limit and for $l = 0$,

$$r_+^2\sqrt{\frac{C_+}{r_+ - r_-}} \sim \mu\, r_+. \tag{C.7}$$

Additionally, we have that

$$e^{\kappa_+(r_* - r_+)} \sim \left(\frac{r_+ - r}{r_+ - r_-}\right)^{1/2}, \quad r \to r_+. \tag{C.8}$$

Therefore, the solution can be simplified to

$$\psi^{\mathrm{A}}_{\omega 0} \sim (\mu\, r_+)^{i\omega/\kappa_+} e^{-i\omega r_+}\Gamma(1 - i\omega/\kappa_+)J_{-i\omega/\kappa_+}\left(2\mu\, r_+\left(\frac{r_+ - r}{r_+ - r_-}\right)^{1/2}\right). \tag{C.9}$$

Making use of the following connection formula [60]

$$J_\nu(z) = \frac{e^{-i\pi/2}}{\pi}\left[e^{-i\,\nu\,\pi/2}K_\nu\left(z\, e^{-i\pi/2}\right) - e^{i\,\nu\,\pi/2}K_\nu\left(z\, e^{i\pi/2}\right)\right], \tag{C.10}$$

the expression (C.9) can be transformed into a representation involving the modified Bessel functions

$$\psi^{\mathrm{A}}_{\omega 0}(r) \sim p_1^{\mathrm{A}}\, F^{\mathrm{A}}(r) + p_2^{\mathrm{A}}\, F^{\mathrm{A}\,*}(r) \tag{C.11}$$

where

$$F^{\mathrm{A}}(r) = \frac{e^{-i\pi/4}}{\pi} K_{i\omega/\kappa_+}\left(-2i\mu\, r_+\left(\frac{r_+ - r}{r_+ - r_-}\right)^{1/2}\right), \tag{C.12}$$

$$p_1^{\mathrm{A}} = e^{-i\frac{\pi}{4}}(\mu\, r_+)^{i\omega/\kappa_+} e^{-i\omega r_+}\Gamma(1 - i\omega/\kappa_+)\, e^{-\frac{\pi\omega}{2\kappa_+}}, \tag{C.13}$$

$$p_2^{\mathrm{A}} = e^{i\frac{\pi}{4}}(\mu\, r_+)^{i\omega/\kappa_+} e^{-i\omega r_+}\Gamma(1 - i\omega/\kappa_+)\, e^{\frac{\pi\omega}{2\kappa_+}}. \tag{C.14}$$

Region B (The middle region)

In the middle region, we employ the WKB approximation to define a solution

$$\psi^{\mathrm{B}}_{\omega 0}(r) \sim \frac{a_+}{|V_{\omega 0}|^{1/4}}\, e^{i\int\sqrt{V_{\omega 0}(r)}dr_*} + \frac{a_-}{|V_{\omega 0}|^{1/4}}\, e^{-i\int\sqrt{V_{\omega 0}(r)}dr_*}. \tag{C.15}$$

At leading order in μ, we can write

$$V_{\omega 0}(r) \sim \frac{\mu^2}{r^2}(r_+ - r)(r - r_-) \tag{C.16}$$

where we have neglected ω. Under these assumptions, the integral in the exponential can be computed analytically as

$$\int \sqrt{V_{\omega 0}(r)}dr_* = \mu\, y(r), \tag{C.17}$$

where

$$y(r) = -\sqrt{(r_+ - r)(r - r_-)} + \frac{r_+ + r_-}{2}\arctan\left(\frac{r - M}{\sqrt{(r_+ - r)(r - r_-)}}\right). \tag{C.18}$$

Hence, we have

$$\psi^{\mathrm{B}}_{\omega 0}(r) \sim \frac{r^{1/2}}{[(r_+ - r)(r - r_-)]^{1/4}\mu^{1/2}}\left(a_+\, e^{i\mu\, y(r)} + a_-\, e^{-i\mu\, y(r)}\right). \tag{C.19}$$

To obtain the coefficients $a_\pm$, we shall match the solutions in regions I and II. To achieve this we will evaluate $\psi^{\mathrm{B}}_{\omega 0}$ as $r \to r_+$ and $\psi^{\mathrm{A}}_{\omega 0}$ as $r \to -\infty$. Hence, to obtain $\psi^{\mathrm{B}}_{\omega 0}$ as $r \to r_+$ we first take

$$y(r) \sim \left(\frac{r_+ + r_-}{2}\right)\left[\frac{\pi}{2} - 2\left(\frac{r_+ - r}{r_+ - r_-}\right)^{1/2}\right] - [(r_+ - r)(r_+ - r_-)]^{1/2}, \quad r \to r_+. \tag{C.20}$$

Introducing this into Eq. (C.19) and simplifying yields

$$\psi^{\mathrm{B}}_{\omega 0}(r) \sim \frac{r_+^{1/2}}{\mu^{1/2}}[(r_+ - r)(r_+ - r_-)]^{-1/4}\Bigg(a_+\, i^{\frac{\mu(r_+ + r_-)}{2}} e^{-2i\mu r_+\left(\frac{r_+ - r}{r_+ - r_-}\right)^{1/2}} + a_-\,(-i)^{\frac{\mu(r_+ + r_-)}{2}} e^{2i\mu r_+\left(\frac{r_+ - r}{r_+ - r_-}\right)^{1/2}}\Bigg), \quad r \to r_+. \tag{C.21}$$

Additionally, we evaluate $\psi^{\mathrm{A}}_{\omega 0}$ as $r \to -\infty$. Making use of [60]

$$K_\nu(z) \sim \left(\frac{\pi}{2z}\right)^{1/2} e^{-z}, \quad z \to \infty, \tag{C.22}$$

and introducing this into equation (C.11)

$$\psi^{\mathrm{A}}_{\omega 0}(r) \sim \frac{1}{2\sqrt{\pi\mu\, r_+}}\left(\frac{r_+ - r}{r_+ - r_-}\right)^{-1/4} \times \left(p_1^{\mathrm{A}} e^{2i\mu r_+\left(\frac{r_+ - r}{r_+ - r_-}\right)^{1/2}} + p_2^{\mathrm{A}} e^{-2i\mu r_+\left(\frac{r_+ - r}{r_+ - r_-}\right)^{1/2}}\right), \quad r \to -\infty. \tag{C.23}$$

Matching the two asymptotic forms (C.21) and (C.23), we obtain the coefficients

$$\begin{aligned} a_+ &= \frac{(r_+ - r_-)^{1/2}}{2\, r_+\sqrt{\pi}} i^{-\frac{\mu(r_+ + r_-)}{2}} p_2^{\mathrm{A}}, \\ a_- &= \frac{(r_+ - r_-)^{1/2}}{2\, r_+\sqrt{\pi}} (-i)^{-\frac{\mu(r_+ + r_-)}{2}} p_1^{\mathrm{A}}. \end{aligned} \tag{C.24}$$

Region C ($r \to r_-$)

In the region near the Cauchy horizon, we can adopt a similar approach to that used in Region A. Expanding the potential near r_- ($r_* \to \infty$), we find for the radial equation (5.7)

$$\left\{\frac{d^2}{dr_*^2} + \omega^2 - C_-(r_+ - r_-)e^{-2\kappa_- r_-} e^{2\kappa_- r_*}\right\}\psi^{\mathrm{C}}_{\omega l}(r) = 0, \tag{C.25}$$

where

$$C_- = -\frac{r_+ - r_-}{r_-^4}\left(l^2 + l + \mu^2 r_-^2 + 1 - \frac{r_+}{r_-}\right). \tag{C.26}$$

Once again, with $l = 0$ and in the large mass limit,

$$r_-^2\sqrt{-\frac{C_-}{r_+ - r_-}} \sim \mu\, r_-. \tag{C.27}$$

We can write the general solution at leading order in μ near r_- as,

$$\psi^{\rm C}_{\omega 0}(r) \sim p^{\rm C}_1\, F^{\rm C}(r) + p^{\rm C}_2\, F^{\rm C\,*}(r) \tag{C.28}$$

with

$$F^{\rm C}(r) = \frac{e^{-i\pi/4}}{\pi} K_{-i\omega/\kappa_-}\left(-2i\mu\, r_- \left(\frac{r-r_-}{r_+-r_-}\right)^{1/2}\right). \tag{C.29}$$

The coefficients $p^{\rm C}_1$ and $p^{\rm C}_2$ are determined by the matching conditions between regions II and III. We implement a similar approach to that used to match regions I and II. We first take $\psi^{\rm B}_{\omega 0}$ to $r \to r_-$. Specifically, we need

$$y(r) \sim -\left(\frac{r_+ + r_-}{2}\right)\left[\frac{\pi}{2} - 2\left(\frac{r-r_-}{r_+-r_-}\right)^{1/2}\right] - \left[(r_+-r_-)(r-r_-)\right]^{1/2}, \quad r \to r_-. \tag{C.30}$$

Hence, from Eq. (C.19), we obtain

$$\psi^{\rm B}_{\omega 0}(r) \sim \frac{r_-^{1/2}}{\mu^{1/2}}[(r_+-r_-)(r-r_-)]^{-1/4}\Bigg(a_+\,(-i)^{\frac{\mu(r_++r_-)}{2}} e^{2i\mu r_-\left(\frac{r-r_-}{r_+-r_-}\right)^{1/2}} + a_-\, i^{\frac{\mu(r_++r_-)}{2}} e^{-2i\mu r_-\left(\frac{r-r_-}{r_+-r_-}\right)^{1/2}}\Bigg), \quad r \to r_-. \tag{C.31}$$

We then make use of Eq. (C.22) and introduce it into Eq. (C.28) to get the asymptotic form of $\psi^{\rm C}_{\omega 0}(r)$ as $r \to \infty$

$$\psi^{\rm C}_{\omega 0}(r) \sim \frac{1}{2\sqrt{\pi\mu\, r_-}}\left(\frac{r-r_-}{r_+-r_-}\right)^{-1/4} \times \left(p^{\rm C}_1 e^{2i\mu r_-\left(\frac{r-r_-}{r_+-r_-}\right)^{1/2}} + p^{\rm C}_2 e^{-2i\mu r_-\left(\frac{r-r_-}{r_+-r_-}\right)^{1/2}}\right), \quad r \to \infty. \tag{C.32}$$

Comparing the expressions (C.31) and (C.32) yields

$$\begin{aligned} p^{\rm C}_1 &= 2\sqrt{\pi}\, r_-\,(-i)^{\frac{\mu(r_++r_-)}{2}} \frac{a_+}{(r_+-r_-)^{1/2}} \\ &= \frac{r_-}{r_+}(-1)^{\frac{\mu(r_++r_-)}{2}} e^{i\pi/4}(\mu\, r_+)^{i\omega/\kappa_+} e^{-i\omega r_+}\Gamma(1-i\omega/\kappa_+) e^{\pi\omega/(2\kappa_+)}, \\ p^{\rm C}_2 &= 2\sqrt{\pi}\, r_-\, i^{\frac{\mu(r_++r_-)}{2}} \frac{a_-}{(r_+-r_-)^{1/2}} \\ &= \frac{r_-}{r_+}(-1)^{-\frac{\mu(r_++r_-)}{2}} e^{-i\pi/4}(\mu\, r_+)^{i\omega/\kappa_+} e^{-i\omega r_+}\Gamma(1-i\omega/\kappa_+) e^{-\pi\omega/(2\kappa_+)}. \end{aligned} \tag{C.33}$$

Finally, to obtain the interior reflection and transmission coefficients, we must write the solution in a form such that

$$\psi^{\rm C}_{\omega 0}(r) \sim A_{\omega 0} e^{i\omega r_*} + B_{\omega 0} e^{-i\omega r_*}, \quad r_* \to \infty. \tag{C.34}$$

This form can be obtained by rewriting Eq. (C.28) in terms of Bessel functions of the first kind, using again Eq. (C.10),

$$\psi^{\rm C}_{\omega 0}(r) \sim A_{\omega 0}\, p(r) + B_{\omega 0}\, p^*(r). \tag{C.35}$$

with

$$p(r) = (\mu\, r_-)^{-i\omega/\kappa_+} e^{-i\omega r_-} \Gamma(1 - i\omega/\kappa_-) J_{-i\omega/\kappa_-}\left(2\mu\, r_- \left(\frac{r - r_-}{r_+ - r_-}\right)^{1/2}\right), \tag{C.36}$$

and

$$\begin{aligned} A_{\omega 0} = &-\frac{r_-}{r_+}\Gamma\left(1 - \frac{i\omega}{\kappa_+}\right) i^{1-\mu(r_+ + r_-)} (\mu\, r_-)^{\frac{i\omega}{\kappa_-}} (\mu\, r_+)^{\frac{i\omega}{\kappa_+}} e^{-\frac{\pi\omega}{2\kappa_-} - \frac{\pi\omega}{2\kappa_+} - i\omega(r_+ + r_-)} \\ &\times \frac{e^{-\frac{\pi\omega}{\kappa_-}} + e^{\frac{\pi\omega}{\kappa_+}} i^{2\mu(r_+ + r_-)}}{\left(e^{-\frac{2\pi\omega}{\kappa_-}} - 1\right)\Gamma\left(1 + \frac{i\omega}{\kappa_-}\right)}, \\ B_{\omega 0} = &\frac{r_-}{r_+}\Gamma\left(1 - \frac{i\omega}{\kappa_+}\right) i^{1-\mu(r_+ + r_-)} (\mu\, r_-)^{-\frac{i\omega}{\kappa_-}} (\mu\, r_+)^{\frac{i\omega}{\kappa_+}} e^{-\frac{\pi\omega}{2\kappa_-} - \frac{\pi\omega}{2\kappa_+} - i\omega(r_+ - r_-)} \\ &\times \frac{1 + e^{-\frac{\pi\omega}{\kappa_-} + \frac{\pi\omega}{\kappa_+}} i^{2\mu(r_+ + r_-)}}{\left(e^{-\frac{2\pi\omega}{\kappa_-}} - 1\right)\Gamma\left(1 - \frac{i\omega}{\kappa_-}\right)}. \end{aligned} \tag{C.37}$$

C.2.2 The exterior reflection coefficient

A similar approach can be adopted to obtain the $A^{\rm up}_{\omega 0}$ coefficient in the large mass and small frequency regime. Following, once again, the derivation outlined in [118] we can write the radial equation in the limit as $r \to r_+^+$

$$\left\{\frac{d^2}{dr_*^2} + \omega^2 - C_+(r_+ - r_-)e^{-2\kappa_+ r_+} e^{2\kappa_+ r_*}\right\} \psi^{\rm ext}_{\omega l}(r_*) = 0. \tag{C.38}$$

We need a solution that exponentially decays at $r_* \to \infty$ and with asymptotic form $e^{i\omega r_*} + A^{\rm up}_{\omega l} e^{-i\omega r_*}$ at $r_* \to -\infty$. Such solution can be written as

$$\psi^{\rm ext}_{\omega l}(r_*) = \left(\frac{C_+ r_+^4}{r_+ - r_-}\right)^{-i\omega/(2\kappa_+)} \frac{2\, e^{i\omega r_+}}{\Gamma(-i\omega/\kappa_+)} K_{i\omega/\kappa_+}\left(2\, r_+^2 \sqrt{\frac{C_+}{r_+ - r_-}} e^{\kappa_+(r_* - r_+)}\right) \tag{C.39}$$

Near r_+, for $l = 0$ and in the large mass regime,

$$\psi^{\rm ext}_{\omega 0}(r_*) = (\mu\, r_+)^{-i\omega/(2\kappa_+)}\, \frac{2\, e^{i\omega r_+}}{\Gamma(-i\omega/\kappa_+)} K_{i\omega/\kappa_+}\left(2\mu\, r_+ \left(\frac{r-r_+}{r_+-r_-}\right)^{1/2}\right), \quad r \to r_+. \tag{C.40}$$

Now, comparing with the form $e^{i\omega r_*} + A^{\rm up}_{\omega 0} e^{-i\omega r_*}$ as $r_* \to -\infty$ one finds

$$A^{\rm up}_{\omega 0} \sim (\mu\, r_+)^{-2i\omega/\kappa_+} e^{2i\omega r_+} \frac{\Gamma(i\omega/\kappa_+)}{\Gamma(-i\omega/\kappa_+)}. \tag{C.41}$$

Note that in the limit as $\omega \to 0$, $A^{\rm up}_{00} \sim -1$ at leading order.

C.2.3 The coefficient of the logarithmic divergence

Expanding the expressions in Eqs. (C.37) and (C.41) in a series near $\omega = 0$, we obtain the terms needed for the computation of the coefficient of the logarithmic divergence for the $l = 0$ mode:

$$\begin{aligned}
q_0 &= \frac{(r_- - r_+)}{2\pi r_+ r_-} \cos\left(\frac{\pi\mu}{2}(r_+ + r_-)\right), \\
a^{(0)}_0 &= \frac{1}{2\pi r_+ r_-}\Big[\pi\left(r_+^2 - r_-^2\right)\sin\left(\frac{\pi\mu}{2}(r_+ + r_-)\right) + \Big(-2r_-^2\log(\mu\, r_-) \\
&\quad - (2\gamma-1)(r_- - r_+)(r_+ + r_-) + 2r_+^2\log(\mu\, r_+)\Big)\cos\left(\frac{\pi\mu}{2}(r_+ + r_-)\right)\Big], \\
b^{(0)}_0 &= -\frac{1}{2\pi r_+ r_-}\Big[\pi\left(r_+^2 + r_-^2\right)\sin\left(\frac{\pi\mu}{2}(r_+ + r_-)\right) + \Big(2r_-^2\log(\mu\, r_-) \\
&\quad + (2\gamma-1)r_-^2 + 2r_+ r_- + 2r_+^2\log(\mu\, r_+) + (2\gamma-1)r_+^2\Big)\cos\left(\frac{\pi\mu}{2}(r_+ + r_-)\right)\Big], \\
A^{(1)}_0 &= \frac{2ir_+}{r_+ - r_-}\big(r_- + 2r_+\log(\mu\, r_+) + (2\gamma-1)r_+\big), \\
c^{(0)}_0 &= \Re\{a^{(0)}_0\} - \Re\{b^{(0)}_0\} + q_0\Im\{A^{(1)}_0\}.
\end{aligned} \tag{C.42}$$

Introducing these expressions into Eq. (6.25), one can show that the coefficient of the logarithmic divergence $h_0(\mu)$ is identically zero in the large mass limit. This is in agreement with the numerical results reported in Fig. 6.8.

C.3 Near-Cauchy horizon, other expressions

C.3.1 Frequency integrals of the Hadamard renormalization counterterms

Integrals of the form $\int k^{(2)}_{\omega l}(r)\, d\omega$ as $r \to r_-$:

$$\begin{aligned}
&\int_0^\mu \mathcal{I}_{\omega l}(0,0|r) d\omega \sim -\frac{1}{8\, r_-^2} \log|f| + \mathcal{O}(1),\\
&\int_0^\mu \mathcal{I}_{\omega l}(1,0|r) d\omega \sim -\frac{1}{2|f|}\delta_{l,0} + \mathcal{O}(1),\\
&\int_0^\mu \mathcal{I}_{\omega l}(1,1|r) d\omega \sim -\frac{1}{2|f|^2}\delta_{l,0} + \mathcal{O}(1),\\
&\int_0^\mu \mathcal{I}_{\omega l}(2,0|r) d\omega \sim \frac{r_-^2}{|f|^2}\delta_{l,0} - \frac{r_-^2}{3|f|^2}\delta_{l,1} + \mathcal{O}(1),\\
&\int_0^\mu \mathcal{I}_{\omega l}(2,1|r) d\omega \sim \frac{2\, r_-^2}{|f|^3}\delta_{l,0} - \frac{2\, r_-^2}{3|f|^3}\delta_{l,1} + \mathcal{O}(1),\\
&\int_0^\mu \mathcal{I}_{\omega l}(2,2|r) d\omega \sim \frac{3\, r_-^2}{|f|^4}\delta_{l,0} - \frac{r_-^2}{|f|^4}\delta_{l,1} + \mathcal{O}(1),\\
&\int_0^\mu \mathcal{J}_{\omega l}(0,0|r) d\omega \sim -\frac{1}{2} \log|f|\, \delta_{l,0} + \mathcal{O}(1),\\
&\int_0^\mu \mathcal{J}_{\omega l}(1,0|r) d\omega \sim -\, r_-^2\, \log|f|\, \delta_{l,0} + \frac{1}{3}\, r_-^2\, \log|f|\, \delta_{l,1} + \mathcal{O}(1),\\
&\int_0^\mu \mathcal{J}_{\omega l}(1,1|r) d\omega \sim -\frac{r_-^2}{|f|}\delta_{l,0} + \frac{1}{3}\frac{r_-^2}{|f|}\delta_{l,1} + \mathcal{O}(1).
\end{aligned} \tag{C.43}$$

C.3.2 Contribution of the Hadamard renormalization counterterms to $(\tilde{w})^t_t$

In the following expression, we isolate from Eq. (6.38) the contribution coming from the Hadamard renormalization counterterms

$$\begin{aligned}
K_2 :=& \frac{1}{4\pi^2|f|}\sum_{l=0}^{\infty}(2l+1)\int_0^\infty d\omega\, [-\omega^2 k^{(2)}_{\omega l}(r)]\\
&+ \frac{1}{4\pi^2}\Bigg[\mathcal{T}^{(\mathrm{p})}_{10} + \mathcal{D}^{(\mathrm{p})}_{22} + \frac{1}{|f|}(\mathcal{T}^{(\mathrm{p})}_{11} + \mathcal{D}^{(\mathrm{p})}_{21}) + \frac{\mathcal{D}^{(\mathrm{r})}_{20}}{|f|^2} + \frac{\mathcal{D}^{(\mathrm{r})}_{21}}{|f|^3} + \frac{\mathcal{D}^{(\mathrm{r})}_{22}}{|f|^4} + \frac{\mathcal{T}^{(\mathrm{r})}_{10}}{|f|^2}\\
&+ \left(\mathcal{T}^{(\mathrm{l})}_{10} + \frac{\mathcal{T}^{(\mathrm{l})}_{11}}{|f|}\right)(\log(|f|/(\ell^2\lambda^2)) - 2\gamma_{\mathrm{E}} + 3)\Bigg] + \frac{1}{8\pi^2|f|}\mathcal{T}^{(\mathrm{l})}_{00}(r)\, \lambda^2, \quad r \to r_-,
\end{aligned} \tag{C.44}$$

where

$$k^{(2)}_{\omega l}(r) = \sum_{a=0}^{2}\sum_{b=0}^{a} \mathcal{D}^{(\mathrm{r})}_{ab}(r)\mathcal{I}_{\omega l}(a,b|r) + \sum_{a=1}^{1}\sum_{b=0}^{a-1} \mathcal{T}^{(\mathrm{r})}_{ab}(r)\mathcal{I}_{\omega l}(a+1,b|r) + \sum_{a=0}^{1}\sum_{b=0}^{a} \mathcal{T}^{(\mathrm{l})}_{ab}(r)\mathcal{J}_{\omega l}(a,b\,|r). \tag{C.45}$$

To obtain the leading-order contribution to Eq. (C.44) near the Cauchy horizon, it is necessary to evaluate the integrals of the form $\int \omega^2\, k^{(2)}_{\omega l}(r)\, d\omega$ as $r \to r_-$:

$$\begin{aligned}
&\frac{1}{|f|}\int_0^{\bar\Omega} \omega^2\, \mathcal{I}_{\omega l}(0,0|r) d\omega \sim \frac{\bar\Omega^2}{8\, r_-^2\, |f|} + \mathcal{O}(\log|f|),\\
&\frac{1}{|f|}\int_0^{\bar\Omega} \omega^2\, \mathcal{I}_{\omega l}(1,0|r) d\omega \sim \frac{\log|f|}{4\, r_-^2\, |f|} + \mathcal{O}(|f|^{-1}), \quad \text{(Note that: } \mathcal{D}^{(\mathrm{r})}_{10} \sim \mathcal{O}(|f|)),\\
&\frac{1}{|f|}\int_0^{\infty} \omega^2\, \mathcal{I}_{\omega l}(1,1|r) d\omega \sim -\frac{1}{4\, r_-^2\, |f|^2} + \mathcal{O}(1),\\
&\frac{1}{|f|}\int_0^{\infty} \omega^2\, \mathcal{I}_{\omega l}(2,0|r) d\omega \sim \frac{1}{|f|^2}\delta_{l,0} + \mathcal{O}(1),\\
&\frac{1}{|f|}\int_0^{\infty} \omega^2\, \mathcal{I}_{\omega l}(2,1|r) d\omega \sim \frac{1}{|f|^3}\delta_{l,0} + \mathcal{O}(1),\\
&\frac{1}{|f|}\int_0^{\infty} \omega^2\, \mathcal{I}_{\omega l}(2,2|r) d\omega \sim \frac{1}{|f|^4}\delta_{l,0} + \mathcal{O}(1),\\
&\frac{1}{|f|}\int_0^{\bar\Omega} \omega^2\, \mathcal{J}_{\omega l}(0,0|r) d\omega \sim \frac{\lambda^2}{2|f|}\,\delta_{l,0} + \frac{\log|f|}{4\, r_-^2} + \mathcal{O}(1),\\
&\frac{1}{|f|}\int_0^{\infty} \omega^2\, \mathcal{J}_{\omega l}(1,0|r) d\omega \sim \frac{r_-^2\,\lambda^2}{|f|}\delta_{l,0} - \frac{r_-^2\,\lambda^2}{3|f|}\delta_{l,1} - \log|f|\delta_{l,0} + \mathcal{O}(1),\\
&\frac{1}{|f|}\int_0^{\infty} \omega^2\, \mathcal{J}_{\omega l}(1,1|r)\, d\omega \sim \frac{\log|f|}{|f|}\delta_{l,0} + \mathcal{O}(|f|^{-1}), \quad \text{(Note that: } \mathcal{T}^{(\mathrm{l})}_{11} \sim \mathcal{O}(|f|)).
\end{aligned} \tag{C.46}$$

We note that the integrals above that are formally divergent in the frequency have been evaluated up to a generic frequency cutoff $\bar\Omega$. However, at leading order in $|f|$, only $\mathcal{I}_{\omega l}(0,0|r)$ contains divergent frequency contributions. The remaining integrals do not present divergent frequency contributions at leading order in $|f|$.

Introducing the results of the integrals (C.46) and the Hadamard coefficients (in Sec. C.1) into Eq. (C.44), one finds that all analytic contributions diverging as $1/|f|$ or faster are exactly canceled by the integral terms. We therefore obtain the simple

expression

$$K_2 = \frac{1}{4\pi^2|f|}\sum_{l=0}^{\infty}(2l+1)\left[-\int_0^\infty d\omega\,\omega^2\mathcal{D}^{(\mathrm{r})}_{00}\mathcal{I}_{\omega l}(0,0|r)+\frac{\mathcal{D}^{(\mathrm{r})}_{11}}{4r_-^2|f|}\right] + \mathcal{O}(\log|f|), \qquad r\to r_-, \qquad (\text{Note that } \mathcal{D}^{(\mathrm{r})}_{11}\sim\mathcal{O}(|f|)). \tag{C.47}$$

This expression can be further simplified by noting that

$$\omega^2\mathcal{D}^{(\mathrm{r})}_{00}\,\mathcal{I}(0,0|r)\sim\frac{\omega}{2\,r_-^2}+\mathcal{O}(|f|), \qquad r\to r_-, \tag{C.48}$$

and

$$\frac{\mathcal{D}^{(\mathrm{r})}_{11}}{4r_-^2|f|}\sim-\frac{\kappa_-^2}{24\,r_-^2}+\mathcal{O}(|f|), \qquad r\to r_-. \tag{C.49}$$

Therefore, the contribution of the Hadamard renormalization counterterms to Eq. (6.38), at leading order in $|f|$, simplifies to

$$K_2 = \frac{1}{4\pi^2|f|}\sum_{l=0}^{\infty}(2l+1)\left[\int_0^\infty d\omega\,\left(-\frac{\omega}{2\,r_-^2}\right)-\frac{\kappa_-^2}{24\,r_-^2}\right]+\mathcal{O}(\log|f|), \quad r\to r_-. \tag{C.50}$$

References

[1] J. Arrechea, C. Breen, A. Ottewill, L. Pisani, P. Taylor, Renormalized stress-energy tensor for scalar fields in the Boulware state with applications to extremal black holes, *Phys. Rev. D* **2025**, *111*, 085009.

[2] J. Arrechea, C. Breen, A. Ottewill, L. Pisani, P. Taylor, Vacuum polarization and renormalized stress-energy tensor of spherical thin shells, *arXiv preprint arXiv:2607.07583* **2026**.

[3] J. Arrechea, C. Breen, A. Ottewill, P. Taylor, Renormalized stress-energy tensor for scalar fields in Hartle-Hawking, Boulware, and Unruh states in the Reissner-Nordström spacetime, *Phys. Rev. D* **2023**, *108*, 125004.

[4] J. de Boer, B. Dittrich, A. Eichhorn, S. B. Giddings, S. Gielen, S. Liberati, E. R. Livine, D. Oriti, K. Papadodimas, A. D. Pereira, et al., Frontiers of Quantum Gravity: shared challenges, converging directions, *arXiv preprint arXiv:2207.10618* **2022**.

[5] L. Parker, Particle Creation in Expanding Universes, *Phys. Rev. Lett.* **1968**, *21*, 562–564.

[6] L. Parker, Quantized Fields and Particle Creation in Expanding Universes. I, *Phys. Rev.* **1969**, *183*, 1057–1068.

[7] L. Parker, Quantized Fields and Particle Creation in Expanding Universes. II, *Phys. Rev. D* **1971**, *3*, 346–356.

[8] L. E. Parker, The Creation of Particles in an Expanding Universe. Harvard University, **1967**.

[9] A. Ferreiro, J. Navarro-Salas, S. Pla, The birth of gravitational particle creation: the enduring legacy of Leonard Parker's 1966 thesis, *The European Physical Journal H* **2026**, *51*, 4.

[10] S. W. Hawking, Particle creation by black holes, *Communications in mathematical physics* **1975**, *43*, 199–220.

[11] W. G. Unruh, Notes on black-hole evaporation, *Phys. Rev. D* **1976**, *14*, 870–892.

[12] N. D. Birrell, P. C. W. Davies, Quantum Fields in Curved Space, Cambridge Univ. Press, Cambridge, UK, **1984**.

[13] S. A. Fulling, Aspects of quantum field theory in curved spacetime, Cambridge university press, **1989**.

[14] R. M. Wald, Quantum field theory in curved spacetime and black hole thermodynamics, University of Chicago press, **1994**.

[15] L. Parker, D. Toms, Quantum field theory in curved spacetime: quantized fields and gravity, Cambridge university press, **2009**.

[16] V. Mukhanov, S. Winitzki, Introduction to quantum effects in gravity, Cambridge university press, **2007**.

[17] R. M. Wald, General relativity, University of Chicago press, **2010**.

[18] S. W. Hawking, G. F. Ellis, The large scale structure of space-time, Cambridge university press, **1973**.

[19] P. Candelas, D. J. Raine, Feynman propagator in curved space-time, *Phys. Rev. D* **1977**, *15*, 1494–1500.

[20] J. Hadamard, *Lectures on Cauchy's Problem in Linear Partial Differential Equations*, Yale University Press, New Haven, **1923**.

[21] J. L. Synge, Relativity: The General Theory, North-Holland, Amsterdam, The Netherlands, **1960**.

[22] B. S. DeWitt, Dynamical theory of groups and fields, Gordon and Breach, **1965**.

[23] M. R. Brown, A. C. Ottewill, Photon propagators and the definition and approximation of renormalized stress tensors in curved space-time, *Phys. Rev. D* **1986**, *34*, 1776–1786.

[24] M. R. Brown, A. C. Ottewill, The energy-momentum operator in curved space-time, *Proceedings of the Royal Society of London. A. Mathematical and Physical Sciences* **1983**, *389*, 379–403.

[25] Y. Décanini, A. Folacci, Hadamard renormalization of the stress-energy tensor for a quantized scalar field in a general spacetime of arbitrary dimension, *Phys. Rev. D* **2008**, *78*, 044025.

[26] S. M. Christensen, Regularization, renormalization, and covariant geodesic point separation, *Phys. Rev. D* **1978**, *17*, 946–963.

[27] S. M. Christensen, Vacuum expectation value of the stress tensor in an arbitrary curved background: The covariant point-separation method, *Phys. Rev. D* **1976**, *14*, 2490–2501.

[28] B. S. DeWitt, R. W. Brehme, Radiation damping in a gravitational field, *Annals of Physics* **1960**, *9*, 220–259.

[29] S. L. Adler, J. Lieberman, Y. J. Ng, Regularization of the stress-energy tensor for vector and scalar particles propagating in a general background metric, *Annals of Physics* **1977**, *106*, 279–321.

[30] S. L. Adler, J. Lieberman, Trace anomaly of the stress-energy tensor for massless vector particles propagating in a general background metric, *Annals of Physics* **1978**, *113*, 294–303.

[31] R. M. Wald, Trace anomaly of a conformally invariant quantum field in curved spacetime, *Physical Review D* **1978**, *17*, 1477.

[32] R. M. Wald, The back reaction effect in particle creation in curved spacetime, *Communications in Mathematical Physics* **1977**, *54*, 1–19.

[33] K. Sanders, Static Symmetric Solutions of the Semi-Classical Einstein-Klein-Gordon System, *Annales Henri Poincare* **2022**, *23*, 1321–1358.

[34] J. Z. Simon, Higher-derivative Lagrangians, nonlocality, problems, and solutions, *Phys. Rev. D* **1990**, *41*, 3720–3733.

[35] L. Parker, J. Z. Simon, Einstein equation with quantum corrections reduced to second order, *Phys. Rev. D* **1993**, *47*, 1339–1355.

[36] E. E. Flanagan, R. M. Wald, Does back reaction enforce the averaged null energy condition in semiclassical gravity?, *Phys. Rev. D* **1996**, *54*, 6233–6283.

[37] J. B. Hartle, S. W. Hawking, Path-integral derivation of black-hole radiance, *Phys. Rev. D* **1976**, *13*, 2188–2203.

[38] D. G. Boulware, Quantum field theory in Schwarzschild and Rindler spaces, *Phys. Rev. D* **1975**, *11*, 1404–1423.

[39] P. Candelas, Vacuum polarization in Schwarzschild spacetime, *Phys. Rev. D* **1980**, *21*, 2185–2202.

[40] B. S. Kay, R. M. Wald, Theorems on the uniqueness and thermal properties of stationary, nonsingular, quasifree states on spacetimes with a bifurcate killing horizon, *Physics Reports* **1991**, *207*, 49–136.

[41] P. Candelas, K. W. Howard, Vacuum $<\varphi^2>$ in Schwarzschild spacetime, *Phys. Rev. D* **1984**, *29*, 1618–1625.

[42] K. W. Howard, P. Candelas, Quantum Stress Tensor in Schwarzschild Space-Time, *Phys. Rev. Lett.* **1984**, *53*, 403–406.

[43] K. W. Howard, Vacuum $<T_\mu{}^\nu>$ in Schwarzschild spacetime, *Phys. Rev. D* **1984**, *30*, 2532–2547.

[44] P. R. Anderson, W. A. Hiscock, D. A. Samuel, Stress-energy tensor of quantized scalar fields in static black hole spacetimes, *Phys. Rev. Lett.* **1993**, *70*, 1739–1742.

[45] P. R. Anderson, W. A. Hiscock, D. A. Samuel, Stress-energy tensor of quantized scalar fields in static spherically symmetric spacetimes, *Phys. Rev. D* **1995**, *51*, 4337–4358.

[46] A. Levi, A. Ori, Pragmatic mode-sum regularization method for semiclassical black-hole spacetimes, *Phys. Rev. D* **2015**, *91*, 104028.

[47] A. Levi, A. Ori, Versatile Method for Renormalized Stress-Energy Computation in Black-Hole Spacetimes, *Phys. Rev. Lett.* **2016**, *117*, 231101.

[48] A. Levi, A. Ori, Mode-sum regularization of $<\phi^2>$ in the angular-splitting method, *Phys. Rev. D* **2016**, *94*, 044054.

[49] A. Levi, E. Eilon, A. Ori, M. van de Meent, Renormalized Stress-Energy Tensor of an Evaporating Spinning Black Hole, *Phys. Rev. Lett.* **2017**, *118*, 141102.

[50] A. Levi, Renormalized stress-energy tensor for stationary black holes, *Phys. Rev. D* **2017**, *95*, 025007.

[51] P. Taylor, C. Breen, Mode-sum prescription for the vacuum polarization in odd dimensions, *Phys. Rev. D* **2016**, *94*, 125024.

[52] P. Taylor, C. Breen, Mode-sum prescription for vacuum polarization in black hole spacetimes in even dimensions, *Phys. Rev. D* **2017**, *96*, 105020.

[53] P. Taylor, C. Breen, A. Ottewill, Mode-sum prescription for the renormalized stress energy tensor on black hole spacetimes, *Phys. Rev. D* **2022**, *106*, 065023.

[54] N. Zilberman, M. Casals, A. Ori, A. C. Ottewill, Quantum Fluxes at the Inner Horizon of a Spinning Black Hole, *Phys. Rev. Lett.* **2022**, *129*, 261102.

[55] J. Arrechea, PhD thesis, **2023**.

[56] C. Breen, G. Montagnon, P. Taylor, E. Winstanley, Mode-sum prescription for renormalized expectation values for a charged quantum scalar field on a charged black hole, *Phys. Rev. D* **2025**, *111*, 045010.

[57] G. J. Montagnon, PhD thesis, University of Sheffield, **2025**.

[58] A. Monteverdi, E. Winstanley, Quantum scalar field theory on equal-angular-momenta Myers-Perry-AdS black holes, *Phys. Rev. D* **2025**, *112*, 125014.

[59] A. Monteverdi, PhD thesis, University of Sheffield, **2025**.

[60] *NIST Digital Library of Mathematical Functions*, https://dlmf.nist.gov/, Release 1.2.1 of 2024-06-15, F. W. J. Olver, A. B. Olde Daalhuis, D. W. Lozier, B. I. Schneider, R. F. Boisvert, C. W. Clark, B. R. Miller, B. V. Saunders, H. S. Cohl, and M. A. McClain, eds.

[61] S. Hollands, R. Wald, Conservation of the stress tensor in perturbative interacting quantum field theory in curved spacetimes, *Reviews in Mathematical Physics* **2005**, *17*, 227–311.

[62] I. M. Gel'fand, G. E. Shilov, *Generalized Functions, V. 1: Properties and Operations*, (Academic Press, 1964).

[63] P. R. Anderson, W. A. Hiscock, D. J. Loranz, Semiclassical stability of the extreme Reissner-Nordstrom black hole, *Phys. Rev. Lett.* **1995**, *74*, 4365–4368.

[64] P. R. Anderson, W. A. Hiscock, B. E. Taylor, Do Semiclassical Zero Temperature Black Holes Exist?, *Phys. Rev. Lett.* **2000**, *85*, 2438–2441.

[65] D. A. Lowe, Comment on "Do Semiclassical Zero Temperature Black Holes Exist", *Phys. Rev. Lett.* **2001**, *87*, 029001.

[66] P. R. Anderson, W. A. Hiscock, B. E. Taylor, Anderson, Hiscock, and Taylor Reply: *Phys. Rev. Lett.* **2001**, *87*, 029002.

[67] J. Matyjasek, O. B. Zaslavsky, Quantum back reaction of massive fields and selfconsistent semiclassical extreme black holes and acceleration horizons, *Phys. Rev. D* **2001**, *64*, 104018.

[68] P. R. Anderson, A method to compute $<\varphi^2>$ in asymptotically flat, static, spherically symmetric spacetimes, *Phys. Rev. D* **1990**, *41*, 1152–1162.

[69] D. N. Page, Particle emission rates from a black hole: Massless particles from an uncharged, nonrotating hole, *Phys. Rev. D* **1976**, *13*, 198–206.

[70] J. Arrechea, C. Barceló, R. Carballo-Rubio, L. J. Garay, Asymptotically flat vacuum solutions in order-reduced semiclassical gravity, *Phys. Rev. D* **2023**, *107*, 085005.

[71] J. W. York, Black hole in thermal equilibrium with a scalar field: The back-reaction, *Phys. Rev. D* **1985**, *31*, 775–784.

[72] W. A. Hiscock, Gravitational vacuum polarization around static spherical stars, *Phys. Rev. D* **1988**, *37*, 2142–2150.

[73] K. Numajiri, K. Okabayashi, S. Mukohyama, Boulware vacuum vs regularity: Thoughts on anomaly-induced effective action, *Phys. Rev. D* **2025**, *111*, 085024.

[74] P. M. Saffin, Q.-X. Xie, Quantum fields in boson star spacetime, **2026**.

[75] W. Israel, Singular hypersurfaces and thin shells in general relativity, *Nuovo Cim. B* **1966**, *44S10*, [Erratum: Nuovo Cim.B 48, 463 (1967)], 1.

[76] H. A. Buchdahl, General Relativistic Fluid Spheres, *Phys. Rev.* **1959**, *116*, 1027–1034.

[77] E. Poisson, A Relativist's Toolkit: The Mathematics of Black-Hole Mechanics, Cambridge University Press, **2009**.

[78] J. Arrechea, C. Barceló, G. García-Moreno, J. Polo-Gómez, Beyond Buchdahl's limit: bilayered stars and thin-shell configurations, **2024**.

[79] G. Darmois, Les équations de la gravitation einsteinienne, Gauthier-Villars, **1927**, p. 58.

[80] N. Sen, Über die Grenzbedingungen des Schwerefeldes an Unstetigkeitsflächen, *Annalen der Physik* **1924**, *378*, 365–396.

[81] K. Lanczos, Flächenhafte Verteilung der Materie in der Einsteinschen Gravitationstheorie, *Annalen der Physik* **1924**, *379*, 518–540.

[82] K. Schwarzschild, On the gravitational field of a sphere of incompressible fluid according to Einstein's theory, *Sitzungsber. Preuss. Akad. Wiss. Berlin (Math. Phys.)* **1916**, *1916*, 424–434.

[83] A. Urbano, H. Veermäe, On gravitational echoes from ultracompact exotic stars, *JCAP* **2019**, *04*, 011.

[84] D. Deutsch, P. Candelas, Boundary effects in quantum field theory, *Phys. Rev. D* **1979**, *20*, 3063–3080.

[85] M. Benini, C. Dappiaggi, A. Schenkel in Annales Henri Poincaré, *Vol. 19*, Springer, **2018**, pp. 2401–2433.

[86] D. A. R. Dalvit, F. D. Mazzitelli, Running coupling constants, Newtonian potential, and nonlocalities in the effective action, *Phys. Rev. D* **1994**, *50*, 1001–1009.

[87] A. Satz, F. D. Mazzitelli, E. Alvarez, Vacuum polarization around stars: Nonlocal approximation, *Phys. Rev. D* **2005**, *71*, 064001.

[88] A. Boasso, F. D. Mazzitelli, Vacuum polarization in the horizonless Bardeen metric, *Phys. Rev. D* **2025**, *112*, 105016.

[89] A. Barvinsky, G. Vilkovisky, Beyond the Schwinger-Dewitt technique: converting loops into trees and in-in currents, *Nuclear Physics B* **1987**, *282*, 163–188.

[90] A. Barvinsky, G. Vilkovisky, Covariant perturbation theory (II). Second order in the curvature. General algorithms, *Nuclear Physics B* **1990**, *333*, 471–511.

[91] I. G. Avramidi, A covariant technique for the calculation of the one-loop effective action, *Nuclear Physics B* **1991**, *355*, 712–754.

[92] P. O. Mazur, E. Mottola, Gravitational Condensate Stars: An Alternative to Black Holes, *Universe* **2023**, *9*, 88.

[93] J. Arrechea, C. Barceló, R. Carballo-Rubio, L. J. Garay, Ultracompact horizonless objects in order-reduced semiclassical gravity, *Phys. Rev. D* **2024**, *109*, 104056.

[94] I. A. Reyes, G. M. Tomaselli, Quantum field theory on compact stars near the Buchdahl limit, *Phys. Rev. D* **2023**, *108*, 065006.

[95] Y. Matsuo, Interior of Schwarzschild in semiclassical gravity, **2026**.

[96] R. Penrose in Symposium-International Astronomical Union, *Vol. 64*, Cambridge University Press, **1974**, pp. 82–91.

[97] D. Christodoulou in The twelfth marcel grossmann meeting: on recent developments in theoretical and experimental general relativity, astrophysics and relativistic field theories (In 3 volumes), World Scientific, **2012**, pp. 24–34.

[98] W. A. Hiscock, Evolution of the interior of a charged black hole, *Phys. Lett. A* **1981**, *83*, 110–112.

[99] E. Poisson, W. Israel, Internal structure of black holes, *Phys. Rev. D* **1990**, *41*, 1796–1809.

[100] A. Ori, Inner structure of a charged black hole: An exact mass-inflation solution, *Phys. Rev. Lett.* **1991**, *67*, 789–792.

[101] P. R. Brady, J. D. Smith, Black Hole Singularities: A Numerical Approach, *Phys. Rev. Lett.* **1995**, *75*, 1256–1259.

[102] S. Hod, T. Piran, Mass Inflation in Dynamical Gravitational Collapse of a Charged Scalar Field, *Phys. Rev. Lett.* **1998**, *81*, 1554–1557.

[103] L. M. Burko, Structure of the Black Hole's Cauchy-Horizon Singularity, *Phys. Rev. Lett.* **1997**, *79*, 4958–4961.

[104] A. Ori, Structure of the singularity inside a realistic rotating black hole, *Phys. Rev. Lett.* **1992**, *68*, 2117–2120.

[105] P. R. Brady, S. Droz, S. M. Morsink, Late-time singularity inside nonspherical black holes, *Phys. Rev. D* **1998**, *58*, 084034.

[106] A. Ori, Oscillatory Null Singularity inside Realistic Spinning Black Holes, *Phys. Rev. Lett.* **1999**, *83*, 5423–5426.

[107] F. J. Tipler, Singularities in conformally flat spacetimes, *Phys. Lett. A* **1977**, *64*, 8–10.

[108] M. Dafermos, J. Luk, The interior of dynamical vacuum black holes I: The Cˆ0-stability of the Kerr Cauchy horizon, *Annals of Mathematics* **2025**, *202*, 309–630.

[109] N. Birrell, P. Davies, On falling through a black hole into another universe, *Nature* **1978**, *272*, 35–37.

[110] W. A. Hiscock, Quantum-mechanical instability of the Kerr-Newman black-hole interior, *Phys. Rev. D* **1980**, *21*, 2057–2063.

[111] S. Hollands, R. M. Wald, J. Zahn, Quantum instability of the Cauchy horizon in Reissner–Nordström–deSitter spacetime, *Classical and Quantum Gravity* **2020**, *37*, 115009.

[112] S. Hollands, C. Klein, J. Zahn, Quantum stress tensor at the Cauchy horizon of the Reissner–Nordström–de Sitter spacetime, *Phys. Rev. D* **2020**, *102*, 085004.

[113] C. Klein, J. Zahn, S. Hollands, Quantum (Dis)Charge of Black Hole Interiors, *Phys. Rev. Lett.* **2021**, *127*, 231301.

[114] C. Klein, J. Zahn, Renormalized charged scalar current in the Reissner–Nordström–de Sitter spacetime, *Phys. Rev. D* **2021**, *104*, 025009.

[115] N. Zilberman, A. Levi, A. Ori, Quantum Fluxes at the Inner Horizon of a Spherical Charged Black Hole, *Phys. Rev. Lett.* **2020**, *124*, 171302.

[116] N. Zilberman, A. Ori, Quantum fluxes at the inner horizon of a near-extremal spherical charged black hole, *Phys. Rev. D* **2021**, *104*, 024066.

[117] A. Lanir, A. Levi, A. Ori, O. Sela, Two-point function of a quantum scalar field in the interior region of a Reissner-Nordstrom black hole, *Phys. Rev. D* **2018**, *97*, 024033.

[118] O. Sela, Quantum effects near the Cauchy horizon of a Reissner-Nordström black hole, *Phys. Rev. D* **2018**, *98*, 024025.

[119] A. Lanir, A. Ori, N. Zilberman, O. Sela, A. Maline, A. Levi, Analysis of quantum effects inside spherical charged black holes, *Phys. Rev. D* **2019**, *99*, 061502.

[120] W. Israel, Thermo-field dynamics of black holes, *Phys. Lett. A* **1976**, *57*, 107–110.

[121] S. M. Christensen, S. A. Fulling, Trace anomalies and the Hawking effect, *Phys. Rev. D* **1977**, *15*, 2088–2104.

[122] P. Taylor, Regular quantum states on the Cauchy horizon of a charged black hole, *Classical and Quantum Gravity* **2020**, *37*, 045004.

[123] V. Frolov, Vacuum polarization near the event horizon of a charged rotating black hole, *Phys. Rev. D* **1982**, *26*, 954.

[124] J. M. McNamara, Behaviour of scalar perturbations of a Reissner-Nordström black hole inside the event horizon, *Proc. R. Soc. Lond. A* **1978**, *364*, 121–134.

[125] C. Kehle, Y. Shlapentokh-Rothman, A Scattering Theory for Linear Waves on the Interior of Reissner–Nordström Black Holes, *Annales Henri Poincaré* **2019**, *20*, 1583–1650.

[126] Y. Gürsel, I. D. Novikov, V. D. Sandberg, A. A. Starobinsky, Final state of the evolution of the interior of a charged black hole, *Phys. Rev. D* **1979**, *20*, 1260–1270.

[127] E. Poisson, W. Israel, Inner-horizon instability and mass inflation in black holes, *Physical review letters* **1989**, *63*, 1663.

[128] C. Klein, J. Zahn, Long-range correlations of the stress tensor near the Cauchy horizon, *Phys. Rev. D* **2024**, *109*, L061702.

[129] N. Pinamonti, D. Siemssen, Scale-invariant curvature fluctuations from an extended semiclassical gravity, *Journal of Mathematical Physics* **2015**, *56*.

[130] B.-L. B. Hu, E. Verdaguer, Semiclassical and stochastic gravity: Quantum field effects on curved spacetime, Cambridge University Press, **2020**.

[131] T. McMaken, Backreaction from quantum fluxes at the Kerr inner horizon, *Phys. Rev. D* **2024**, *110*, 045019.

[132] J. Arrechea, G. Neri, S. Liberati, Inner horizon instability via the trace anomaly effective action, *Phys. Rev. D* **2025**, *111*, 084036.

[133] F. Mellor, I. Moss, Stability of black holes in de Sitter space, *Phys. Rev. D* **1990**, *41*, 403–409.

[134] P. Brady, E. Poisson, Cauchy horizon instability for Reissner-Nordstrom black holes in de Sitter space, *Classical and Quantum Gravity* **1992**, *9*, 121–125.

[135] P. Hintz, A. Vasy, Analysis of linear waves near the Cauchy horizon of cosmological black holes, *Journal of Mathematical Physics* **2017**, *58*.

[136] V. Cardoso, J. L. Costa, K. Destounis, P. Hintz, A. Jansen, Quasinormal Modes and Strong Cosmic Censorship, *Phys. Rev. Lett.* **2018**, *120*, 031103.